Optimization of the Post-Compression Process of Ultrashort Laser Pulses in Hollow Capillary Fibers

Aurora Crego García

Departamento de F´ısica Aplicada. Área de Óptica
Grupo de Investigación en Aplicaciones del Láser y Fotónica (ALF)
Universidad de Salamanca

A thesis submitted for the degree of
Doctor of Physics at Universidad de Salamanca
supervised by Dr. Julio San Román Álvarez de Lara
and Dr. Enrique Conejero Jarque

Salamanca, June 2021

JULIO SAN ROMÁN ÁLVAREZ DE LARA, Profesor Contratado Doctor del Área de Óptica en el Departamento de F´ısica Aplicada de la Universidad de Salamanca, y ENRIQUE CONEJERO JARQUE, Profesor Titular del Área de Óptica en el Departamento de F´ısica Aplicada de la Universidad de Salamanca, en calidad de codirectores CERTIFICAN:

Que la presente Memoria, "Optimization of the Post-Compression Process of Ultrashort Laser Pulses in Hollow Capillary Fibers/ Optimización del Proceso de Post-Compresión de Pulsos Ultracortos en Fibras Huecas" ha sido realizada bajo su dirección por la doctoranda Aurora Crego Garc´ıa, y dan su consentimiento para la presentación y defensa de la Tesis Doctoral para optar al grado de Doctora en F´ısica con Mención Internacional.

Salamanca, junio de 2021.

“Yo creo que nada sucede por casualidad, ¿sabes?
Que, en el fondo, las cosas tienen su plan secreto, aunque nosotros no lo entendamos.”

Carlos Ruiz Zafón
La sombra del viento

Acknowledgments/Agradecimientos

Después de todo lo vivido en esta etapa de mi vida, me hace mucha ilusión mostrar mi agradecimiento a todos los que de una manera u otra habéis participado en esta aventura conmigo. Siempre he oído decir que una vez llegados a este punto el trabajo más difícil está hecho, pero creo que poner por escrito todo lo que te ronda por la cabeza a estas alturas, no es tarea fácil, así que espero no olvidarme de nadie.

En primer lugar, quiero dar las gracias a mis directores de tesis Julio y Enrique por su interés, confianza y paciencia durante todos estos años. Si he llegado hasta aquí, ha sido porque hace ya unos años (no pongo cifra porque ya son unos cuantos) aceptasteis tutelar el trabajo de fin de grado de una indecisa estudiante a punto de acabar la carrera y que se introdujo desde ese momento de cabeza en el mundo de los láseres. Gracias por todo el conocimiento, ayuda y consejos en muchos ámbitos, que me habéis ofrecido a lo largo de estos años. Habéis sido un gran apoyo para mí, tanto a nivel profesional como personal (no puedo traer cerezas suficientes al despacho para agradecéroslo). Ahora sin ninguna duda, puedo decir que lo más importante de una tesis son los directores que tengas; ¡muchas gracias!

Junto a ellos, quiero agradecer a todos los que forman o formaron parte del grupo de "Aplicaciones del Láser y Fotónica", que cada vez son más, por su acogida y por las charlas, tanto a nivel científico, como cotidianas en los cafés y celebraciones (antes de que el Covid rompiera tan buenas tradiciones). Gracias Íñigo, Nacho y Warein por hacerme partícipe en los experimentos siempre que podíais y así seguir fomentando mi parte de física experimental. Quería agradeceros a todos por las oportunidades, enseñanzas y apoyo que nos habéis ofrecido a los doctorandos para poder crecer profesionalmente durante estos años. Es un gusto y un orgullo haber formado parte de un grupo con tan buen ambiente, tanto entusiasmo y tanto conocimiento; muchísimas gracias. A mis compañeros de camino durante estos años, Roberto y Laura, que habéis soportado mis quejas cuando me atascaba con un programa y también mis chácharas, que sé que las echaréis de menos, gracias por todos los buenos momentos vividos dentro y fuera del despacho.

Esta tesis no habría sido posible sin todos vosotros y todos los que además habéis contribuido siempre para mejorar este trabajo hasta el último momento. Gracias en especial al Prof. Michaël Hemmer y al Prof. Mauro Nisoli por haber aceptado ser los revisores externos de esta tesis. También quería agradecer al Prof. Alexander Gaeta por darme la oportunidad de colaborar con su grupo durante mi estancia en la Universidad de Columbia.

Y en el ámbito personal a todos los buenos amigos que han estado presentes, aunque sea de manera virtual tan de moda en el último año; en especial a Juan Miguel, Paula, Pilar y Ángel. Aunque cada vez estemos más desperdigados, que sigamos compartiendo y celebrando juntos todo lo bueno que nos llegue.

Por último y más importante, a mis padres Jerónimo y María Ángeles, gracias por darme todo y más y por recordarme siempre hacerme valer con esfuerzo y humildad. A mi hermana Bea, gracias por ser mi apoyo y mi ejemplo a seguir. A Miguel Ángel, gracias por tu ayuda en mis momentos de mini-crisis y por tu confianza incondicional en mí, incluso cuando ya dudaba hasta yo. Gracias por estar siempre ahí; parte de esta tesis es gracias a vosotros.

Muchísimas gracias a todos vosotros, y aunque no sea lo típico, gracias Salamanca, por todo lo que me has dado desde que llegué. Parafraseando a Cervantes: ¡Nos volveremos a ver!

Aurora

Contents

List of Publications

Aurora Crego, Enrique Conejero Jarque, and Julio San Roman. Influence of the spatial confinement on the self-focusing of ultrashort pulses in hollow-core fibers. *Scientific Reports*, 9:9546, 12 2019. doi: 10.1038/s41598-019-45940-3. URL https://doi.org/10.1038/s41598-019-45940-3.

Aurora Crego, Enrique Conejero Jarque, and Julio San Roman. Ultrashort visible energetic pulses generated by nonlinear propagation of necklace beams in capillaries. *Opt. Express*, 29(2):929–937, Jan 2021. doi: 10.1364/OE.411338. URL http://www.opticsexpress.org/abstract.cfm?URI=oe-29-2-929.

List of Proceedings

Aurora Crego, Enrique Conejero Jarque, and Julio San Roman. Activation of the self-focusing process in hollow-core fibers: Influence of the spatio-temporal dynamics. In *2019 Conference on Lasers and Electro-Optics Europe and European Quantum Electronics Conference*, page cj_3_2. Optical Society of America, 2019. URL http://www.osapublishing.org/abstract.cfm?URI=CLEO_Europe-2019-cj_3_2.

Aurora Crego, Julio San Roman, and Enrique Conejero Jarque. Visible short-pulses generation by nonlinear propagation of necklace beams in capillaries. *EPJ Web Conf.*, 238:11005, 2020. doi: 10.1051/epjconf/202023811005. URL https://doi.org/10.1051/epjconf/202023811005.

Resumen

El campo de la óptica no lineal lleva activo y en continuo crecimiento desde hace 60 años debido a los nuevos temas de investigación que surgen del estudio de la interacción láser-materia y sus posibles aplicaciones. En concreto, el desarrollo de nuevas fuentes de luz coherentes y ultracortas es de gran relevancia para explorar procesos fundamentales en la ciencia.

Actualmente los pulsos de poco ciclos de duración se pueden generar con técnicas de compresión basadas en efectos auto-inducidos por pulsos de luz intensos. La técnica de post-compresión que mejores resultados ha obtenido, con relación a la energía y a la duración del pulso, es aquella basada en fibra hueca llena de un gas. Las distintas estrategias que se necesitan para aumentar más la energía y conseguir pulsos cada vez más cortos a longitudes de ondas diferentes de las convencionales, conllevan al continuo desarrollo e investigación de esta técnica.

El objetivo de esta tesis es encontrar nuevas propuestas para optimizar esta técnica de post-compresión. El hilo conductor de esta trabajo es el entendimiento de los efectos espacio-temporales no lineales que aparecen durante la propagación de distintos tipos de haces en la fibra hueca, intentando encontrar una solución al problema de escalado de la energía.

En la introducción se presentará un breve resumen del desarrollo y los avances conseguidos con esta y otras técnicas en la actualidad. Las bases teóricas sobre la propagación no lineal de pulsos láser en fibra hueca se desarrollarán en el Capítulo 2. Se explicarán los distintos efectos espacio-temporales no lineales que aparecen en la propagación del pulso láser en la fibra y la ecuación de ondas no lineal. Los modelos numéricos implementados se detallarán en el Capítulo 3, se han utilizado tres modelos distintos, (1+1)D, (2+1)D y (3+1)D, entre los cuales, el (1+1)D y el (3+1)D se han desarrollado en este trabajo.

Comenzaremos con el estudio de los efectos espacio-temporales no lineales que aparecen en la propagación del modo fundamental de una fibra hueca y la influencia del confinamiento espacial del sistema como posibles factores que limitan el proceso de

post-compresión, todo ello desarrollado en el Cap´ıtulo 4. En este mismo cap´ıtulo, identificaremos los l´ımites de energ´ıa para evitar efectos no lineales que desfavorecen el proceso de auto-compresión [Crego et al., 2019].

En los siguientes cap´ıtulos estudiaremos diferentes estrategias para conseguir pulsos ultracortos y energéticos. Primero, investigaremos la propagación no lineal de haces estructurados en fibra hueca. La ventaja de este tipo de haces es que se puede aumentar la energ´ıa de entrada del pulso ya que la intensidad está distribuida en un área mayor dentro del núcleo de la fibra. En particular, en el Cap´ıtulo 5 estudiaremos la propagación de haces con polarización que var´ıa espacialmente, conocidos como haces vectoriales. La propagación no lineal de estos haces ha resultado complicada tanto teórica como experimentalmente. En el Cap´ıtulo 6, investigaremos la propagación no lineal de otro tipo de haz estructurado, los haces tipo "necklace" con un número diferente de cuentas o lóbulos, los cuales pueden llevar más energ´ıa que el modo fundamental de la fibra hueca. El resultado principal de este estudio será la generación de haces ultracortos y energéticos en el visible con una alta eficiencia [Crego et al., 2021].

En Cap´ıtulo 7, estudiaremos la posibilidad de obtener pulsos ultracortos y energéticos a diferentes longitudes de onda mediante el proceso de generación de ondas dispersivas en la fibra hueca. En concreto, investigaremos la evolución de la energ´ıa y de la duración del pulso durante el proceso de generación de la onda dispersiva para poder obtener simultáneamente pulsos de pocos ciclos de duración y alta energ´ıa.

Finalmente, en el Cap´ıtulo 8 resumiremos los principales resultados obtenidos en este trabajo y hablaremos de las posibles perspectivas y l´ıneas de investigación.

Chapter 1

Introduction

The field of nonlinear optics is 60 years old, and it is still growing due to the new topics that continuously emerge from the study of light-matter interactions and possible applications. In particular, the development of new coherent ultrabroadband light sources is of great importance to explore fundamental phenomena in science.

Few-cycle pulses can be generated nowadays with pulse compression techniques based on self-action effects of intense light pulses. The most successful post-compression technique able to reach the high-energy few-cycle regime is the hollow capillary fiber (HCF) compressor. The different strategies to scale up the output energy and to obtain ultrashort pulses at different wavelengths than the conventional infrared lead to further investigation of this technique.

The aim of this thesis is to find new approaches to optimize this post-compression technique. The conducting line followed in this study is the understanding of the nonlinear spatio-temporal effects that appear during the propagation of different types of beams in the HCF, attempting to find a solution to the energetic up-scaling problem.

A brief overview of the developments and the state-of-the-art of post-compression techniques is given in the present chapter. The theoretical foundations of the nonlinear propagation of laser pulses in HCFs are explained along Chapter 2. We will explain the different nonlinear effects that appear during the propagation in the HCF and the nonlinear wave equation. We have developed different numerical models, (1+1)D, (2+1)D and (3+1)D, and their implementation is explained in Chapter 3. In particular, the (1+1)D and (3+1)D models have been developed in the frame of this thesis.

The starting point of this thesis is the study of the spatio-temporal nonlinear effects that appear during the propagation of the fundamental mode of a HCF and the influence of the spatial confinement and of the system as possible limiting factors for an efficient

post-compression process, explained here in Chapter 4. In that chapter we will identify the energy limits to avoid detrimental effects in propagation that worsen the output pulse [Crego et al., 2019].

In the following chapters we will study different strategies to obtain ultrashort and energetic pulses. First, we will investigate the nonlinear propagation of structured beams in the HCF. The advantages of this type of beams are that the input energy can be higher since the intensity is distributed in a larger area within the core of the HCF. In particular, in Chapter 5 we will study the propagation of beams with spatially varying polarization, or vector beams. The nonlinear propagation of this type of beams has proven to be complicated both theoretically and experimentally. In Chapter 6, we will explore the nonlinear propagation of another type of structured beams, necklace beams with different number of beads, which were thought to be able to carry more energy than the fundamental mode. The main result will be the generation of ultrashort visible energetic pulses with a high efficiency [Crego et al., 2021].

In Chapter 7 we will explore the possibility of obtaining ultrashort and energetic pulses at different wavelengths by means of the dispersive wave generation process in HCF. In particular, we will study the evolution of the energy and the pulse duration during the generation process of the dispersive wave in order to obtain a high-energy few-cycle pulse.

Finally, we will summarize the main results obtained in this work and we will give an outlook of possible future research lines on the subject in Chapter 8.

1.1 A Brief History of Nonlinear Propagation of Ultrashort Laser Pulses

The demonstration of the laser by Ted Maiman paved the way to new research topics and several applications in a wide variety of scientific fields over the last 60 years [Maiman, 1960]. One of them was the study of the nonlinear response of materials to light, only possible due to the high power and coherent laser light available from that moment on. From the invention of the laser to the present day, the field of nonlinear optics has grown rapidly.

One year after the invention of the laser, the first laser-based experiments in nonlinear optics were performed. The first demonstration of this nonlinear response was made by Franken et al. in 1961 with the experimental generation of the second harmonic using a ruby laser (632 nm) [Franken et al., 1961]. However, the nonlinear effects in

these experiments were very weak and the phase-matching was missing, but with the significantly more intense pulsed laser beams, obtained by Q-switching [Hellwarth, 1961, McClung and Hellwarth, 1962] or mode-locking techniques [Hargrove et al., 1964], these nonlinear effects set an upper limit on the laser beam power to prevent material damage. Together with these studies many more were carried out, reporting the first self-trapping of dielectric waveguide modes due to the optical Kerr effect in 1964 by Chiao et al. when trying to explain the experimental observation of damage tracks in glass [Chiao et al., 1964]. They contemplated the propagation without spreading of a high-intensity beam in a dielectric material to explain the effect observed. This optical Kerr effect was already defined as a third order nonlinear effect that induces an intensity-dependent variation in the refractive index of the medium in the form, $n = n_L + n_{NL}I$, where n_{NL} is the nonlinear refractive index and I the pulse intensity [Boyd, 2020].

The invention and continuous development of the laser also motivated the search for new applications. The most important one was the development of optical fibers with low attenuation by Kao and Hockham in 1966, becoming a suitable tool for communications [Kao and Hockham, 1966]. One of the main advantages of these devices is that they facilitated the propagation of high-intensity pulses over long interaction lengths, which enhanced the nonlinear response using low input peak powers. In subsequent years, the studies on different nonlinear effects in optical fibers continued. Stolen et al. first observed in 1972 the stimulated Raman and Brillouin emissions in glass-fiber optical waveguides [Stolen et al., 1972]. In 1973 Hasegawa and Tappert proposed the theoretical transmission of a temporal soliton in a dielectric fiber [Hasegawa and Tappert, 1973]. They mentioned the possibility of compensating the pulse stretching, associated to the spectral broadening induced by the nonlinear intensity dependence of the refractive index, with the temporal pulse compression induced by the anomalous dispersion response, which is the base of post-compression setups to reduce the pulse duration. This theoretical proposal was confirmed experimentally in 1985 using a single mode silica fiber and a mode-locked laser of 7 ps pulse duration, with which they reported the compression of a laser pulse down to 6 ps when they increased the input pulse power [Mollenauer et al., 1980]. The first femtosecond laser pulses using a combination of saturable gain in a dye laser medium and a saturable dye absorber were obtained by Shank and Ippen in 1974 [Shank and Ippen, 1974].

Besides short laser pulses, the interest in intense broad-band continuum light sources for spectroscopy applications was also a matter of great interest. First continuum generation by different nonlinear effects in an optical fiber was reported by Lin and Stolen in 1976, obtaining a much more intense and wider bandwidth source for spectroscopy than the available laser sources at that moment [Lin and Stolen, 1976]. In this case, the dominant nonlinear effects which contribute to the spectrum broadening were stimulated Raman

scattering and self-phase modulation, so that the continuum generation was produced on the red side of the central wavelength. Some years later, they also observed the first spectrum broadening by self-phase modulation alone in optical fibers, using a single mode silica fiber and mode-locked argon laser pulses [Stolen and Lin, 1978]. Since the spectrum broadening generated was due to the self-phase modulation effect alone, the continuum was generated both above and below the central wavelength. With this technique, in the early 1980s, post-compressed laser pulses were observed in different experiments after broadening the spectrum in an optical fiber through self-phase modulation effect [Fujimoto et al., 1984, Halbout and Grischkowsky, 1984, Shank et al., 1982, Tomlinson et al., 1984], generating the shortest pulses of 6 fs of duration in less than a decade [Fork et al., 1987]. These results were a revolution for ultrafast science due to the temporal pulse duration achieved but obtaining compressed pulses from optical fibers with energies above the nanojoule level was challenging. Despite the good efficiency and the good beam quality obtained with the optical fibers, some parts of the system struggle with power levels above a few hundred watts. Besides, they have limitations on the core diameter in the single-mode regime and the material choice. These limitations, together with the new nonlinear phenomena available with the generation of more intense and shorter laser pulses thanks to the Chirped Pulse Amplification technique proposed by Strickland and Mourou in 1985 [Strickland and Mourou, 1985], motivated the research of new fiber designs.

An important progress in energy scaling was made possible by the invention of microstructured fibers or photonic crystal fibers [Knight et al., 1996]. The design of their internal microstructured geometry gives an exceptional control in the dispersion and makes possible to obtain a single mode propagation in the full optical range. Certain types of photonic crystal fibers present a hollow core, thus the wave-guiding is not achieved by total internal reflection between a high-index core and a low-index cladding as in optical fibers. Instead, it is based in the photonic bandgap effect due to the periodic refractive index structure of the cladding. Since the core of photonic crystal fibers can be solid but also filled with air or liquid, they also present a higher damage threshold compared to the standard optical fibers. They can be fabricated with an extremely small core (with a section of a few μm^2) so light is confined in this small region, which enhances the nonlinearity even more than in standard optical fibers. The first demonstration of the enhanced nonlinearity in solid-core photonic crystal fibers was reported in 2000, with the supercontinuum spectrum broadening from the visible (400 nm) to the mid-infrared (1600 nm) [Ranka et al., 2000], confirmed also by others experiments in tapered standard optical fibers [Birks et al., 2000]. In 2002, the first broad-band photonic crystal fiber with hollow core was demonstrated by Benabid et al. with low loss for almost two-octave bandwidth [Benabid et al., 2002]. Recently a seven-octave

high-brightness light source using an anti-resonant-reflection photonic crystal fiber has been reported, demonstrating the feasibility of photonic crystal fibers as a technology capable of generating sub-3-fs, energetic and tunable laser sources [Ugaitz et al., 2021]. Although photonic crystal fibers present interesting properties compared to standard optical fibers, the propagation losses are generally larger than in standard optical fibers.

With the Chirped Pulse Amplification technique, it was possible to obtain pulses of a few tens of femtoseconds of duration. However, the interest in even more energetic few-cycle laser pulses for different applications, such as harmonic generation, motivated the investigation of new techniques to obtain these ultrashort and energetic pulses. Although photonic crystal fibers were an important step forward and hollow-core photonic crystal fibers enabled a higher pulse energy, it is necessary to follow a different strategy in order to obtain pulses in the millijoule level.

1.1.1 Post-Compression Techniques

A compressor is a device used to reduce the duration of an ultrashort laser pulse by linear or/and nonlinear techniques. In standard post-compression schemes, the spectrum of the pulse is first broadened by the nonlinear interaction between the laser pulse and the nonlinear medium, while the temporal pulse shape barely changes. In this nonlinear process, the pulse spectrum broadens while the spectral phase changes simultaneously, resulting in a pulse much longer than the corresponding transform limited duration. To flatten the spectral phase, post-compression schemes are usually followed by a phase compensation setup with a prism pair, a grating pair [Treacy, 1969, 1968] or the most commonly used chirped mirrors [Szipõcs and Kõházi-Kis, 1997, Szipõcs et al., 1994].

There have been several reports on the compression of laser pulses in the last years and some of the methods developed are filamentation, post-compression in bulk media, post-compression in optical fibers and HCFs, multiple-plate compression and soliton self-compression, among others. In the case of filamentation, the interplay between Kerr effect, ionization and linear effects leads to a plasma filament in solids, liquids or gases [Couairon and Mysyrowicz, 2007]. With this technique it is possible to obtain short pulses and a supercontinuum spectrum during the pulse propagation. However, related to the energy scaling, only filamentation in gases is possible [Hauri et al., 2004], where pulses up to 200 µJ [Goulielmakis et al., 2008] and shorter than 4 fs [Steingrube et al., 2012] have been achieved at 800 nm. In the mid-infrared, the generation of subterawatt few-cycle pulses through filamentation has also been reported [Mitrofanov et al., 2016]. Although pulse compression through filamentation has obtained successful results, the complex spatio-temporal coupling leads to a non-uniform temporal compression and

only the central part of the beam, with a small fraction of the total energy, can be used as a short pulse source. Post-compression in bulk media was first reported in 1988 by Rolland and Corkum obtaining pulses of tens of femtoseconds on the microjoule level [Rolland and Corkum, 1988]. They propagated a laser beam through a quartz plate shorter enough to avoid self-focusing and then they compressed it with a grating pair. Although it is possible to obtain more energetic pulses in the subpetawatt level at present, it is difficult to obtain few-cycle duration [Mironov et al., 2020]. Another strategy is the multiple-plate compression technique which consists in a series of plates where the spacing and the thickness of the plates can be modified depending on the pulse energy to obtain a high compression ratio [Lu et al., 2014, 2019]. The pulse peak power is above the critical power in the plate, so the beam starts to self-focus inducing an important spectral broadening. The thickness of the plate is small enough to avoid beam collapse, thus the beam focuses behind the plate in air and then it basically diverges due to diffraction. The next plate is placed at the distance where the beam is large enough to repeat the process. The disadvantage of this technique is the energy scaling (sub-millijoule regime).

The most widely used method to generate these ultrashort and energetic pulses that we are going to study in this work, is through gas-filled hollow capillary fibers (HCFs). The interaction of laser pulses with gas media is of great importance since they present a higher damage threshold than other nonlinear media, and even when the gas is ionized due to the pulse interaction, it does not become permanently damaged like bulk materials. For these reasons, HCFs and hollow-core photonic crystal fibers, made from a single hollow core in a solid cladding and filled with gas or liquid, have been a successful tool in experiments in the last decades. Another main advantage of these devices is that the nonlinearity and the dispersion of the system can be easily tuned without additional fabrication steps just changing the gas pressure. Although there are hollow-core photonic crystal fibers that use this technology and they have a low attenuation and a low bend loss compared with standard HCFs [Azhar et al., 2013, Cregan et al., 1999], the latter are useful when propagating intense (millijoule-scale) laser pulses over lengths of a few meters in large core HCF (r_F >100 μm), which is the research topic of this work.

1.1.2 Pulse Post-Compression in Hollow Capillary Fibers

The main difference between hollow capillary fibers (HCFs) and photonic crystal fibers is that HCF do not present a microstructured cladding, which makes them a weakly guiding multimode system because the core presents a smaller refractive index than the cladding. In this case, the guiding relies on grazing-incidence reflection, and it is very sensitive to bending. Another difference is the core size, HCFs present a larger

core than photonic crystal fibers, which enables the up-scaling of the pulse energy but at the same time enhances the multimode propagation regime. There is a schematic comparison of HCFs and photonic crystal fibers in Fig. 1.1. While HCFs were already used in experiments back in the 1970s [Ippen, 1970, Miles et al., 1977], they went on to form the basis of intense few-cycle laser pulse compressors in ultrafast science.

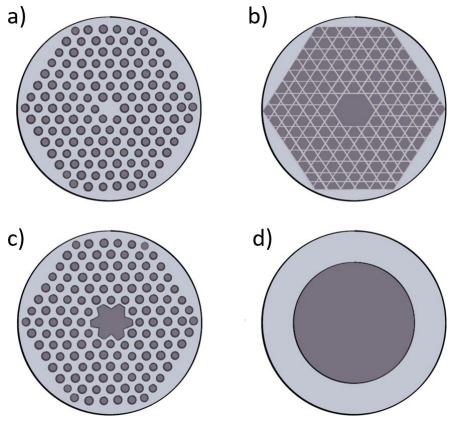

Figure 1.1: Schematic representation of different photonic crystal fibers with solid and hollow core (a,b,c) and a standard hollow capillary fiber (HCF) (d).

A relevant contribution in ultrafast laser science occurred in 1996 when Nisoli et al. reported the generation of 10 fs pulses with 240 μJ energy using for the first time a HCF [Nisoli et al., 1996]. The energy of the generated few-cycle pulses were more than three orders of magnitude higher than the post-compressed pulses obtained in former experiments. This was possible due to the low nonlinearity of the gas medium inside the HCF and the increment of the core diameter up to 140 μm. They later improved this result compressing a 20-fs laser pulse down to 4.5 fs [Nisoli et al., 1997]. Although HCFs present a limit in the input pulse energy to avoid detrimental nonlinear effects, like self-focusing and plasma [Conejero Jarque et al., 2018], the output pulses are essential for generating isolated attosecond pulses via high-order harmonic processes in noble gases [Corkum, 1993].

Over the last decades, several advances have been achieved related to the pulse duration and energy scaling in HCF compressors. The main requirements to obtain a shorter pulse duration are the possibility of expanding the spectral broadening keeping the single-mode operation and the development of ultrabroadband dispersive delay lines for dispersion compensation. By using short input pulses of around 20 fs and keeping the nonlinearities low, it is possible to obtain sub-2-cycle pulses with 1 mJ [Schweinberger et al., 2012]. Further energy scaling up to 1.9 mJ [Anderson et al., 2011] can be achieved using circularly polarized light since the nonlinearity decreases by a factor of

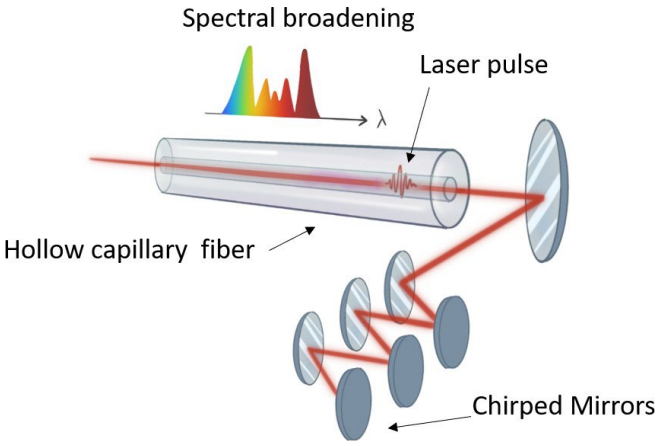

Figure 1.2: Hollow capillary compressor setup.

2/3 [Ghimire et al., 2005]. The implementation of a novel spectral broadening technique consisting of a two-stage HCF arrangement allowed the achievement of ultrashort and high-power laser pulses [Nisoli et al., 2002]. With this technique Schenkel at al. reported a 3.8 fs pulse of 0.35 mJ from a Ti:sapphire laser [Schenkel et al., 2003], but also, related to the energy scaling, Hädrich et al. reported an infrared 6-fs pulse at an unprecedented average power of 216 W [Hädrich et al., 2016].

Related to the energy scaling, it is necessary to avoid gas ionization at high intensities since it can lead to undesirable nonlinear effects. Therefore, ionization sets an upper limit on the input peak intensity of the pulse which restricts the HCF core size. Once the core size is chosen, to obtain the desire spectral broadening one can change the pressure or the HCF length to enhance the nonlinearity. The gas pressure also presents a restriction to avoid the critical value for which self-focusing takes place and the HCF length is limited to 1 m to avoid the bending, setting an upper limit in the input energy itself. The solution to this many-parameters problem was proposed in 2008 by Nagy et al. with the utilization of flexible HCF, whose ends can be pulled to keep the fiber straight [Nagy et al., 2008]. Another strategy to increase the input energy apart from increasing the HCF length, is using pressure gradients inside the HCF, which was introduced by Midorikawa's group. To avoid self-focusing and ionization of the gas medium at the HCF entrance, they apply the gas at the output side and flows to the entrance through the fiber, but this reduces the interaction length [Suda et al., 2005]. A different alternative is the utilization of hollow-planar waveguides to increase the mode area [Nurhuda et al., 2006]. This made possible to reach the terawatt level at sub-15 fs duration, but the beam profile cannot be controlled properly resulting in an inhomogeneous spectral broadening [Arnold et al., 2010]. Combining all the methods mentioned above for energy scaling it

is possible to obtain compressed pulses of 3.8 fs and 6.1 mJ with a peak power of 1.2 TW [Nagy et al., 2020].

An alternative method to obtain high-energy pulse compression avoiding the ionization of the medium, consists in the propagation of long input pulses of a few hundred of femtoseconds, but to compress them to the few-cycle regime it is necessary a large compression ratio. One of the possible ways to obtain few-cycle pulses with this method is to use molecular gases taking advantage of the non-instantaneous nonlinear Raman response related to the alignment of molecules in the field direction, enhancing the red side of the spectrum [Wahlstrand et al., 2011]. This technique can be improved to obtain a two-octave spectrum and a compression factor of 45, by matching the input pulse duration to the time constant of the delayed Raman response [Beetar et al., 2020].

1.1.3 Pulse Soliton Self-Compression in Hollow Capillary Fibers

An alternative nonlinear compression technique would be the soliton self-compression dynamics during nonlinear propagation. With this technique it is possible to obtain few-cycle pulses with multi-octave spanning spectra without needing further phase compensation. However, the self-compression dynamics is highly dependent on the input pulse and HCF parameters: under some circumstances, a high-intensity laser pulse propagates in the anomalous dispersion regime inside the HCF. Since the dispersion and the self-phase modulation effect induce group velocity dispersion with opposite signs inside the HCF, they can be balanced resulting in a stable optical soliton. The maximum possible compression is limited by higher-order linear and nonlinear effects, like higher-order dispersion terms, self-steepening and Raman response, which can cause the soliton fission [Voronin and Zheltikov, 2008].

The first experimental demonstration of self-compression dynamics in a hollow waveguide was reported by Wagner et al. in 2004. They compressed down to 13 fs an initial 30-fs pulse from a Ti:sapphire laser after the propagation inside a hollow waveguide filled with argon at low pressure [Wagner et al., 2004]. This technique has been studied in detail for infrared pulses in filaments [Kretschmar et al., 2014], bulk material [Shumakova et al., 2016] and photonic crystal fibers [Ermolov et al., 2019, Joly et al., 2011]. Recent results about a much larger energy soliton self-compression in HCFs were reported by Travers' group. They demonstrated that standard HCFs also present negative dispersion just choosing the fiber and laser parameters carefully [Travers et al., 2019]. The linear dispersion experimented by the laser pulse depends on the gas dispersion and the HCF contributions, while the nonlinear response depends not only on the gas properties, but also on the mode confinement. Travers's group scaled the soliton effects to the

multi-millijoule energy and terawatt peak power level, orders of magnitude above optical fibers and photonic crystal fibers. They observed experimentally the self-compression of a previously post-compressed 10-fs laser pulse down to 1.2 fs in a 3 m flexible HCF with 125 µm inner radius filled with 0.4 bar of helium. In addition, they generated tunable few-cycle ultraviolet pulses by changing the pressure of the gas. This effect is observed at the maximum compression point, when the soliton fission occurs and some energy is resonantly transferred from the soliton to a certain frequency in the normal dispersion region in a phase-matching process [Akhmediev and Karlsson, 1995, Karpman, 1993]. This emitted radiation propagates linearly and its wavelength can be tuned changing the gas pressure inside the HCF. This effect, named dispersive wave generation process, sets the foundations for a new topic in nonlinear optics.

This dispersive wave is a result of the interplay between the anomalous dispersion that the pulse experiences during the propagation, and the nonlinear effects, leading to a soliton formation and a self-compression process. Thus, it is possible to achieve an ultrashort pulse with a high intensity peak. In addition, this self-compression process is accompanied by an important spectral expansion or shed of energy to a certain frequency in the normal dispersion regime, produced under perfect phase matching conditions, separated from the soliton spectrum [Akhmediev and Karlsson, 1995], usually known as dispersive wave emission.

1.1.4 State-of-the-Art

During the last few years, the race towards the generation of ultrashort and energetic laser pulses has achieved several milestones. In this subsection we briefly outline the best compression results related to the different techniques in terms of compressed pulse duration, pulse energy, peak power, compression factor and average power. In general, these parameters are limited by physical laws or technical issues, so their improvement is quite demanding.

The shortest pulses and the highest peak powers are generated by propagating short pulses from Ti:sapphire lasers (blue markers in Fig. 1.3) in HCFs and flexible HCFs (SF-HCF) [Bohman et al., 2010, Nagy et al., 2020, Ouillé et al., 2020], while the highest average powers are obtained with ytterbium-based systems (orange markers in Fig. 1.3) [Hädrich et al., 2016, Russbueldt et al., 2019]. If we compare the compression methods, the multi-pass cell technique (MPC) is the only one above sub-3-cycle operation [Balla et al., 2020], but together with HCFs, they generate the highest pulse energy and average power [Hädrich et al., 2016, Lücking et al., 2014, Nagy et al., 2019, Russbueldt et al., 2019]. It should be noted that the HCF is one of the most successful post-compression

techniques being able to reach the high-energy few-cycle regime (red area in in Fig. 1.3 left) with above-mJ and sub-3-cycle pulses [Bohman et al., 2010, Nagy et al., 2020]. It is possible to obtain higher energies in planar waveguides [Jarnac et al., 2014] and using weakly ionized gases [Hort et al., 2015]. Recently, the post-compression of sub-30 fs pulses at the terawatt level for an ytterbium laser system has been reported in HCFs filled with liquid, which presents an important advance [Fan et al., 2021].

According to the compression ratio the cascaded setups present a larger compression ratio, even though they are more complex than single stage compressors. The compression factors obtained in single-stage setups based on multi-pass cells (MPC) [Balla et al., 2020, Kaumanns et al., 2018] or very long flexible HCFs [Nagy et al., 2019] filled with molecular gases [Beetar et al., 2020], are more than 2 times larger than in a 1 m standard HCF [Hädrich et al., 2013]. In cascaded setups like multi-pass cells [Balla et al., 2020], hollow-core photonic crystal fibers (HC-PCF) [Köttig et al., 2020] or HCFs [Hädrich et al., 2016], it is possible to obtain a compression factor between 3-7 times larger than in a 1 m standard HCF. These results were reported in the near infrared, but since the period of the optical cycle decreases at shorter wavelengths, the development of short new wavelength sources is an important topic. Although the compression of ultraviolet pulses was demonstrated in 1999 using HCFs through parametric frequency mixing when propagating the fundamental and the second harmonic [Durfee et al., 1999], the highest-energy few-cycle pulses in the ultraviolet range were obtained through the dispersive wave generation process in a flexible HCF [Travers et al., 2019].

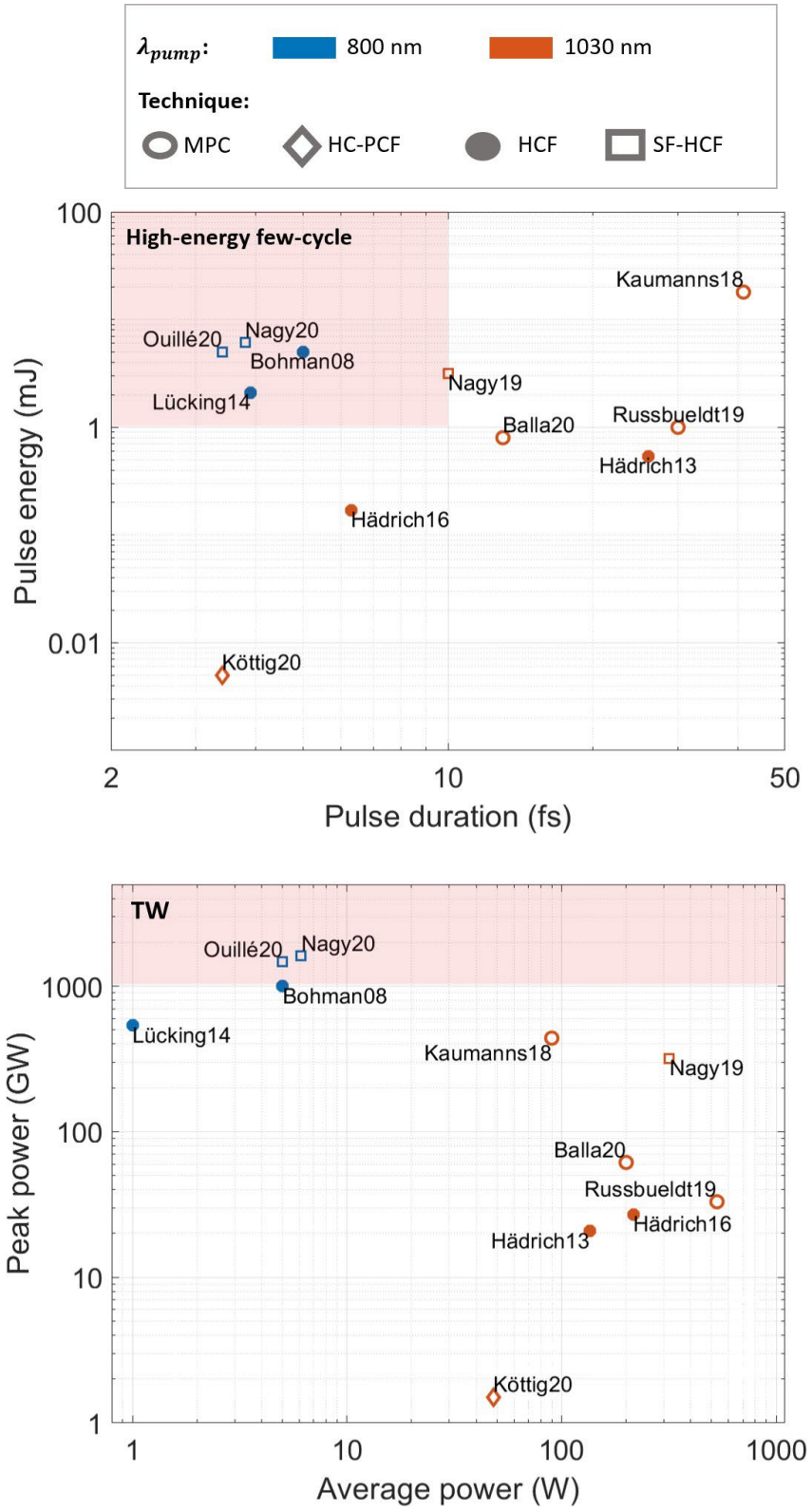

Figure 1.3: Top panel shows the output pulse energy versus the output pulse duration in compression experiments with different techniques. Bottom panel shows the output peak versus average power achieved by different post compression techniques (Fig. based on Ref. [Nagy et al., 2021]).

Chapter 2

Pulse Propagation in Hollow Capillary Fibers

2.1 Pulse Propagation Equation for Nonlinear Media

In the present section we derive the equation that governs the pulse nonlinear propagation in hollow capillary fibers (HCFs). This equation is relevant to describe the propagation of an ultrashort laser pulse through a nonlinear and dispersive medium.

Let us begin considering Maxwell's equations in the International System of Units [Agrawal, 2013].

$$\nabla \cdot \mathbf{D} = \rho \tag{2.1}$$

$$\nabla \cdot \mathbf{B} = 0 \tag{2.2}$$

$$\nabla \times \mathbf{E} = -\frac{\partial \mathbf{B}}{\partial t} \tag{2.3}$$

$$\nabla \times \mathbf{H} = \mathbf{J} + \frac{\partial \mathbf{D}}{\partial t} \tag{2.4}$$

where $\mathbf{E}$ and $\mathbf{H}$ are the electric and the magnetic field respectively, and $\mathbf{D}$ and $\mathbf{B} = \mu_0 \mathbf{H}$ are the electric and magnetic flux densities, E_0 and μ_0 being the vacuum permittivity and the vacuum permeability. The current density vector $\mathbf{J}$ and the charge density ρ represent the sources for the electromagnetic field. The electric flux density can be expressed in terms of the electric field and the polarization vector $\mathbf{P}$ as $\mathbf{D} = E_0 \mathbf{E} + \mathbf{P}$. We can obtain the wave equation that governs the nonlinear pulse propagation from Maxwell's equations by taking the curl of Eq. 2.3

$$\nabla \times (\nabla \times \mathbf{E}) = -\frac{\partial}{\partial t}(\nabla \times \mathbf{B}) = -\frac{\partial}{\partial t}(\nabla \times \mu_0 \mathbf{H}) = -\frac{\partial}{\partial t}\left(\mu_0 \mathbf{J} + \mu_0 \frac{\partial \mathbf{D}}{\partial t}\right) \tag{2.5}$$

We can simplify this equation considering the propagation in a neutral and homogeneous medium such as $\nabla\cdot\mathbf{D} = \nabla\cdot(\varepsilon_0\mathbf{E}+\mathbf{P}) = 0$. We can use this approximation if the medium is isotropic and electrically neutral ($\rho = 0$) [Boyd, 2020]. Femtosecond pulses are the subject under consideration in this study, so even at high pulse intensities that can ionize the medium, we can assume that the positive and negative charges in the medium do not have enough time to separate on such a short time scale, and the average local charge remains zero. Then $\nabla\times(\nabla\times\mathbf{E}) = \nabla(\nabla\cdot\mathbf{E}) - \nabla^2\mathbf{E} = -\nabla^2\mathbf{E}$ using Eq. 2.1. We can rewrite this equation as

$$\nabla^2\mathbf{E} - \frac{1}{c^2}\frac{\partial^2\mathbf{E}}{\partial t^2} = \mu_0\frac{\partial}{\partial t}\mathbf{J} + \mu_0\frac{\partial^2}{\partial t^2}\mathbf{P} \tag{2.6}$$

Equation 2.6 describes the propagation of an electromagnetic field in a homogeneous and isotropic medium, where the relation $\varepsilon_0\mu_0 = 1/c^2$ was used, c being the speed of light in vacuum. Since we are working with dielectric materials, we are interested in the induced polarization vector $\mathbf{P}$, related to the density current of bound charges, so the current density associated with free charges is zero ($\mathbf{J} = 0$).

$$\nabla^2\mathbf{E} - \frac{1}{c^2}\frac{\partial^2\mathbf{E}}{\partial t^2} = \frac{1}{\varepsilon_0 c^2}\frac{\partial^2}{\partial t^2}\mathbf{P} \tag{2.7}$$

From Eq. 2.7 we deduce that the polarization acts as a source of the electromagnetic field. If the intensity of the electromagnetic field applied to a dielectric material is high, the response of this material to light becomes nonlinear. The origin of this nonlinear response is related to the anharmonic motion of bound electrons under the interaction with the applied field. As a result, the total polarization $\mathbf{P}$ includes the linear and nonlinear response.

$$\mathbf{P}(\mathbf{r}, \theta, t, z) = \mathbf{P}^L(\mathbf{r}, \theta, t, z) + \mathbf{P}^{NL}(\mathbf{r}, \theta, t, z) \tag{2.8}$$

$\mathbf{P}^L$ being the linear part and $\mathbf{P}^{NL}$ the nonlinear part, which are related to the electric field by

$$\mathbf{P} = \mathbf{P}^L + \mathbf{P}^{NL} = \varepsilon_0\chi^{(1)}\cdot\mathbf{E} + \varepsilon_0\left(\chi^{(2)}:\mathbf{EE} + \chi^{(3)}\vdots\mathbf{EEE} + \ldots\right) \tag{2.9}$$

where $\chi^{(j)}(j = 1, 2, \ldots)$ is the jth order susceptibility. In general, $\chi^{(j)}$ is a tensor of rank $j + 1$, so all the field combinations are possible. The linear susceptibility $\chi^{(1)}$ represents the principal contribution to $\mathbf{P}$ and the high-order terms of the susceptibility correspond to the nonlinear polarization contribution. To study the propagation of short laser pulses inside a HCF, both dispersive and nonlinear effects must be considered. We can write Eq. 2.7 as

$$\nabla^2\mathbf{E} - \frac{1}{c^2}\frac{\partial^2\mathbf{E}}{\partial t^2} = \frac{1}{\varepsilon_0 c^2}\frac{\partial^2}{\partial t^2}\mathbf{P}^L + \frac{1}{\varepsilon_0 c^2}\frac{\partial^2}{\partial t^2}\mathbf{P}^{NL} \tag{2.10}$$

where we assume that $\mathbf{P}^{NL}$ is treated as a small perturbation to $\mathbf{P}^{L}$, since the changes in the refractive index due to the nonlinear effects are $< 10^{-6}$ [Boyd, 2020]. We also assume that the electric field maintains the polarization along the propagation inside the HCF so that a scalar approach is valid. If we express Eq. 2.10 as a function of the displacement field $\mathbf{D} = \varepsilon_0\mathbf{E} + \mathbf{P}^{L} + \mathbf{P}^{NL}$.

$$\mathbf{D} = \mathbf{D}^{L} + \mathbf{P}^{NL} \tag{2.11}$$

$$\nabla^2\mathbf{E} - \frac{1}{\varepsilon_0 c^2}\frac{\partial^2\mathbf{D}^{L}}{\partial t^2} = \frac{1}{\varepsilon_0 c^2}\frac{\partial^2}{\partial t^2}\mathbf{P}^{NL} \tag{2.12}$$

Since the pulse is going to propagate through a cylindrical HCF filled with gas as nonlinear medium, the Laplace operator has the form $\nabla^2 = \frac{\partial^2}{\partial z^2} + \frac{\partial^2}{\partial r^2} + \frac{1}{r}\frac{\partial}{\partial r} + \frac{1}{r^2}\frac{\partial^2}{\partial \theta^2}$ in cylindrical coordinates. In Eq. 2.12 the nonlinearity of the medium acts as a source term in the right-hand side of the equation. We can express both the electric field $\mathbf{E}$ and the polarization $\mathbf{P}^{NL}$ as

$$\begin{aligned}\mathbf{E}(\mathbf{r}, \theta, t, z) &= \mathbf{A}(\mathbf{r}, \theta, t, z)e^{i(k_0 z - \omega_0 t)} + c.c\\ \mathbf{P}^{NL}(\mathbf{r}, \theta, t, z) &= \mathbf{p}^{NL}(\mathbf{r}, \theta, t, z)e^{i(k_0 z - \omega_0 t)} + c.c\end{aligned} \tag{2.13}$$

where ω_0 is the central frequency of the pulse, $k_0 = n_0\omega_0/c$ is the wavevector, with n_0 the linear refractive index of the medium at ω_0, $n_L(\omega_0)$, and $\mathbf{E}$ and $\mathbf{P}^{NL}$ represent non-plane waves with complex time- and space-dependent varying amplitudes, $\mathbf{A}(\mathbf{r}, \theta, t, z)$ and $\mathbf{p}^{NL}(\mathbf{r}, \theta, t, z)$. The field quantities in terms of their Fourier transforms can be expressed as

$$\begin{aligned}\mathbf{E}(\mathbf{r}, \theta, \omega, z) &= \frac{1}{2\pi}\int \mathbf{E}(\mathbf{r}, \theta, t, z)e^{i\omega t}dt\\ \mathbf{D}^{L}(\mathbf{r}, \theta, \omega, z) &= \frac{1}{2\pi}\int \mathbf{D}^{L}(\mathbf{r}, \theta, t, z)e^{i\omega t}dt\\ \mathbf{P}^{NL}(\mathbf{r}, \theta, \omega, z) &= \frac{1}{2\pi}\int \mathbf{P}^{NL}(\mathbf{r}, \theta, t, z)e^{i\omega t}dt\end{aligned} \tag{2.14}$$

We assume that $\mathbf{D}^{(L)}(\mathbf{r}, \theta, \omega, z)$ and $\mathbf{E}(\mathbf{r}, \theta, \omega, z)$ are related by the linear dispersion relation [Boyd, 2020]

$$\mathbf{D}^{L}(\mathbf{r}, \theta, \omega, z) = \varepsilon_0\chi^{(1)}(\omega)\mathbf{E}(\mathbf{r}, \theta, \omega, z) \tag{2.15}$$

where $\chi^{(1)}$ is the linear relative permittivity, a dielectric complex scalar quantity in the case of a dissipative and isotropic medium. By introducing expressions 2.13-2.15 in Eq. 2.12, we obtain the Helmholtz equation in the frequency domain

$$\nabla^2\mathbf{E}(\mathbf{r}, \theta, \omega, z) + \left(\frac{\omega}{c}\right)^2 \varepsilon^{(1)}(\omega)\mathbf{E}(\mathbf{r}, \theta, \omega, z) = -\frac{\omega^2}{\varepsilon_0 c^2}\mathbf{P}^{NL}(\mathbf{r}, \theta, \omega, z) \tag{2.16}$$

where we define the complex refractive index of the medium as $n^2(\omega) = \chi^{(1)}(\omega)$. We can

make this simplification assuming low losses inside the HCF in the wavelength region of interest, so the imaginary part of $\mathbb{E}(\omega)$ is small compared to the real part. We will include the losses later in a perturbative way.

To derive a wave equation for the envelopes $\mathbf{A}(\mathbf{r}, \theta, t, z)$ and $\mathbf{p}^{NL}(\mathbf{r}, \theta, t, z)$, we represent them in terms of the Fourier transforms of $\mathbf{A}(\mathbf{r}, \theta, t, z)$ and $\mathbf{p}^{NL}(\mathbf{r}, \theta, t, z)$, which are given by

$$\begin{aligned} \mathbf{A}(\mathbf{r}, \theta, \omega, z) &= \int_{-\infty}^{\infty} \mathbf{A}(\mathbf{r}, \theta, t, z) e^{i\omega t} dt \\ \mathbf{p}^{NL}(\mathbf{r}, \theta, \omega, z) &= \int_{-\infty}^{\infty} \mathbf{p}^{NL}(\mathbf{r}, \theta, t, z) e^{i\omega t} dt \end{aligned} \tag{2.17}$$

and they are related to $\mathbf{E}(\mathbf{r}, \theta, \omega, z)$ and $\mathbf{P}^{NL}(\mathbf{r}, \theta, \omega, z)$ by

$$\mathbf{E}(\mathbf{r}, \theta, \omega, z) = \mathbf{A}(\mathbf{r}, \theta, \omega - \omega_0, z) e^{ik_0 z} + \mathbf{A}^*(\mathbf{r}, \theta, \omega + \omega_0, z) e^{-ik_0 z} \quad \mathbf{A}(\mathbf{r}, \theta, \omega - \omega_0, z) e^{ik_0 z} \tag{2.18}$$

$$\begin{aligned} \mathbf{P}^{NL}(\mathbf{r}, \theta, \omega, z) = \mathbf{p}^{NL}(\mathbf{r}, \theta, \omega - \omega_0, z) e^{ik_0 z} + \mathbf{p}^{NL*}(\mathbf{r}, \theta, \omega + \omega_0, z) e^{-ik_0 z} \\ \mathbf{p}^{NL}(\mathbf{r}, \theta, \omega - \omega_0, z) e^{ik_0 z} \end{aligned} \tag{2.19}$$

With these expressions the wave equation 2.16 becomes

$$\nabla^2 \quad \mathbf{A}(\mathbf{r}, \theta, \omega - \omega_0, z) e^{ik_0 z} \quad + k(\omega)^2 \mathbf{A}(\mathbf{r}, \theta, \omega - \omega_0, z) e^{ik_0 z} = -\frac{\omega^2}{E_0 c^2} \mathbf{p}^{NL}(\mathbf{r}, \theta, \omega - \omega_0, z) e^{ik_0 z} \tag{2.20}$$

where $k(\omega) = n_L(\omega)\omega/c$. The Laplace operator can be expressed as $\nabla^2 = \partial^2/\partial z + \nabla^2_{\perp}$, where $\nabla^2_{\perp} = \frac{\partial^2}{\partial r^2} + \frac{1}{r}\frac{\partial}{\partial r} + \frac{1}{r^2}\frac{\partial^2}{\partial \theta^2}$ is the transverse Laplacian in cylindrical coordinates. The approximation of considering the evolution of the pulse envelope alone is valid down to single-cycle pulses, as long as the slowly evolving wave approximation is applicable [Brabec and Krausz, 1997].

We assume that the complex amplitude $\mathbf{A}(\mathbf{r}, \theta, t, z)$ evolves slowly in z over a wavelength since the fast variations are in the complex exponentials (see 2.13), $|\partial^2 A/\partial z^2| << 2k|\partial A/\partial z|$, so the highest-order derivatives may be neglected. Taking the slowly evolving wave approximation we can neglect the term $\partial^2/\partial z^2$ in the Laplace operator in Eq. 2.20 and for simplicity we use $A(r, \theta, \omega, z)$ and $p^{NL}(r, \theta, \omega, z)$)

$$2ik_0 \frac{\partial}{\partial z} \mathbf{A}(\mathbf{r}, \theta, \omega, z) + \nabla^2_{\perp} \mathbf{A}(\mathbf{r}, \theta, \omega, z) + (k(\omega)^2 - k_0^2) \mathbf{A}(\mathbf{r}, \theta, \omega, z) = -\frac{\omega^2}{E_0 c^2} \mathbf{p}^{NL}(\mathbf{r}, \theta, \omega, z) \tag{2.21}$$

$$\begin{aligned} \frac{\partial}{\partial z} \mathbf{A}(\mathbf{r}, \theta, \omega, z) - \frac{i}{2k_0} \nabla^2_{\perp} \mathbf{A}(\mathbf{r}, \theta, \omega, z) - \frac{i}{2k_0} (k(\omega)^2 - k_0^2) \mathbf{A}(\mathbf{r}, \theta, \omega, z) = \\ = \frac{i}{2k_0} \frac{\omega_2}{E_0 c^2} \mathbf{p}^{NL}(\mathbf{r}, \theta, \omega, z) \end{aligned} \tag{2.22}$$

The nonlinear polarization term includes several contributions from second, third and higher orders, as can be seen in Eq. 2.9. Since these effects are perturbative in the range of intensities considered in this work, only the first contributions will be significant. The second-order susceptibility $x^{(2)}$ is responsible for second-harmonic generation, optical rectification and sum-frequency generation. However, it is nonzero only for media that lack an inversion symmetry at the molecular level. In gases $x^{(2)}$ vanishes and the first contribution to the nonlinear polarization that they present is $x^{(3)}$. The third-order susceptibility $x^{(3)}$ is responsible of third-harmonic generation, four-wave mixing and nonlinear refraction effects, among others.

The general expression for the third-order nonlinear polarization in the time domain to study the third-order nonlinear effects in waveguides is [Agrawal, 2013]

$$\mathbf{P}^{NL}(\mathbf{r}, \theta, t) = E_0 \int_{-\infty}^{\infty} x^{(3)}(t-\tau_1, t-\tau_2, t-\tau_3) \cdot \times \mathbf{E}(\mathbf{r}, \theta, \tau_1)\mathbf{E}(\mathbf{r}, \theta, \tau_2)\mathbf{E}(\mathbf{r}, \theta, \tau_3) d\tau_1 d\tau_2 d\tau_3 \tag{2.23}$$

where $x^{(3)}$ is a tensor and all the field combinations are possible, and τ represents the delay between the medium response and the applied field. Due to the complexity of this expression, it is necessary to make several approximations. First of all, not all the nonlinear effects considered here are relevant to our discussion, such us third-order harmonic generation or four-wave mixing. Most nonlinear effects in waveguides are a consequence of the nonlinear refraction. In this case, the refractive index of the medium in the presence of an intense laser beam does not only depend on its frequency but also on the space- and time-dependent intensity $I(r, t)$ of the laser [Chiao et al., 1964, Couairon and Mysyrowicz, 2007].

$$n = n_L + n_{NL} I \tag{2.24}$$

where n_L is the linear part and n_{NL} is the nonlinear part of the refractive index, related to the third order susceptibility $x^{(3)}$. Considering only the effects associated to a self-induced change in the refractive index, the expression of the third-order susceptibility is

$$x^{(3)}(t-\tau_1, t-\tau_2, t-\tau_3) = x^{(3)} R(t-\tau_1)\delta(t-\tau_2)\delta(\tau_1-\tau_3) \tag{2.25}$$

$R(t)$ being the nonlinear response function normalized in a manner similar to the delta function, i. e. $\int_{-\infty}^{\infty} R(t)dt = 1$, and it should include the electronic and vibrational contributions. The nonlinear polarization in the time domain for self-induced effects in waveguides becomes [Agrawal, 2013]

$$\mathbf{P}^{NL}(\mathbf{r}, \theta, t) = E_0 x^{(3)} \mathbf{E}(\mathbf{r}, \theta, t) \int_{-\infty}^{\infty} R(t-\tau_1)|\mathbf{E}(\mathbf{r}, \theta, \tau_1)|^2 d\tau_1 \tag{2.26}$$

where we assume that the electric field and the induced polarization vectors point along the same direction. We assume that $R(t)$ obeys the causality condition $R(t) = 0$ for $t - \tau_1 < 0$, so the nonlinear polarization only depends on the past values of the electric field. In general, the functional form of $R(t)$ can be written as

$$R(t - \tau_1) = (1 - f_R)\delta(t - \tau_1) + f_R \cdot h_R(t - \tau_1) \tag{2.27}$$

where the first term is the instantaneous electronic response and the second term is the retarded vibrational response. We will explain in detail the terms f_R and h_R below.

We can transform Eq. 2.26 into the frequency domain by introducing the Fourier transforms

$$\mathbf{P}^{NL}(\mathbf{r}, \theta, t) = 3E_0\chi^{(3)} \left(\int_{-\infty}^{\infty} \mathbf{E}(\mathbf{r}, \theta, \omega_1) e^{-i\omega_1 t} \frac{d\omega_1}{2\pi} \right) \left(\int_{-\infty}^{\infty} \mathbf{C}(\mathbf{r}, \theta, \omega_2) e^{-i\omega_2 t} \frac{d\omega_2}{2\pi} \right) \tag{2.28}$$

where $\mathbf{C}(\mathbf{r}, \theta, \omega_2)$ is the Fourier transform of $\mathbf{C}(\mathbf{r}, \theta, t) = \int_{-\infty}^{\infty} R(t - \tau_1)|\mathbf{E}(\mathbf{r}, z, \tau_1)|^2 d\tau_1$. The factor 3 comes from the possible combinations of the three electric fields to generate the Kerr effect. The nonlinear polarization in the frequency domain is the following

$$\mathbf{P}^{NL}(\mathbf{r}, \theta, \omega) = 3E_0\chi^{(3)} \int_{-\infty}^{\infty} \mathbf{E}(\mathbf{r}, \theta, \omega - \omega_2)\mathbf{C}(\mathbf{r}, \theta, \omega_2) \frac{d\omega_2}{2\pi} \tag{2.29}$$

2.1.1 Nonlinear Spatial Effects: Self-Focusing

In the case of a monochromatic laser beam, i.e. a sufficiently long laser pulse with central frequency ω_0 and a narrow spectrum, we can neglect the temporal dependence because only the spatial effects are significant during the propagation. In addition, to observe the instantaneous spatial response we only take into account the spatial and longitudinal dimensions and assume cylindrical symmetry, so we can simplify $A(r, \theta, \omega, z) = A(r, z)\delta(\omega)$. For the case of a material with an instantaneous third-order response, we can derive the polarization amplitude from Eq. 2.26

$$\mathbf{p}^{NL}(\mathbf{r}) = 3E_0\chi^{(3)}|\mathbf{A}(\mathbf{r}, z)|^2\mathbf{A}(\mathbf{r}, z) \tag{2.30}$$

$\chi^{(3)} = 2/3 n_L n_{NL}$ being the third-order susceptibility [Boyd, 2020] and the dimensions of $|A(r, z)|^2$ are W/cm^2. Introducing this expression in Eq. 2.22

$$\begin{aligned} \frac{\partial}{\partial z}\mathbf{A}(\mathbf{r}, z) - \frac{i}{2k_0}\nabla_\perp^2\mathbf{A}(\mathbf{r}, z) - \frac{i}{2k_0(r)}\left(k(r)^2 - k_0(r)^2\right)\mathbf{A}(\mathbf{r}, z) = \\ = i\frac{\omega_0}{c}n_{NL}(r)|\mathbf{A}(\mathbf{r}, z)|^2\mathbf{A}(\mathbf{r}, z) \end{aligned} \tag{2.31}$$

where in the case of a monochromatic beam $k = k_0$. We can express $k(r) = k^R(r) + ia(r)/2$ [Brabec and Krausz, 1997], k^R being the propagation constant and $a(r)$ the linear absorption due to the gas and the propagation losses due to the HCF. Assuming that the leaks are low and the absorption of the gas is negligible at the wavelengths considered here, and hence so is the dispersion that would come from this absorption, then $k^R >> a$ and we can neglect the terms a^2. We have included the radial dependence in k_0, k^R, a, n_L and n_{NL} since we consider the possibility of inhomogeneous media, like a step-index fiber.

$$\frac{\partial}{\partial z}\mathbf{A}(\mathbf{r},z) - \frac{i}{2k_0(r)}\nabla_\perp^2\mathbf{A}(\mathbf{r},z) - \frac{i}{2k_0(r)}\left(k^R(r)^2 - k_0(r)^2\right)\mathbf{A}(\mathbf{r},z) + \frac{a(r)}{2}\mathbf{A}(\mathbf{r},z) = \\ = i\frac{\omega_0}{c}n_{NL}(r)|\mathbf{A}(\mathbf{r},z)|^2\mathbf{A}(\mathbf{r},z) \tag{2.32}$$

where $\nabla_\perp^2 = \frac{\partial^2}{\partial r^2} + \frac{1}{r}\frac{\partial}{\partial r}$ assuming cylindrical symmetry. We have assumed $k^R(r)/k_0(r) \approx 1$ since the imaginary part of k is small in the absorption term. In Eq. 2.32 we can identify which effects change the field amplitude during the propagation. The second term on the left-hand side represents the diffraction of the pulse and the nonlinear term on the right-hand side represents the optical Kerr effect. The consequence of this nonlinear intensity-dependent term is the self-focusing of the beam towards the highest intensity regions, usually its central part [Kelley, 1965]. This process is activated when a laser beam with peak power above a critical value, called critical power (P_{cr}) [Marburger, 1975], propagates through a material for which n_{NL} is positive. As a result, the medium acts as a positive lens and the beam self-focuses, as can be seen in Fig. 2.1. This process is of great practical importance, because if the intensity of the laser beam is high enough, it can damage the material. Moreover, it is the principal effect in the filamentation process in materials.

We can use Eq. 2.32 to model the self-focusing dynamics of a laser beam propagating inside a HCF. The numerical model is described in Section 3.1 and the phenomenology of the role of the self-focusing dynamics on the propagation inside the HCF and the results are discussed in detail in Chapter 4.

2.1.2 Nonlinear Spatio-Temporal Effects

Since we are in a context of short pulses, we also need to study the temporal nonlinear effects in addition to the spatial effects. For this reason, we include the temporal dependence in the field amplitude and calculate the second order derivative in time of the

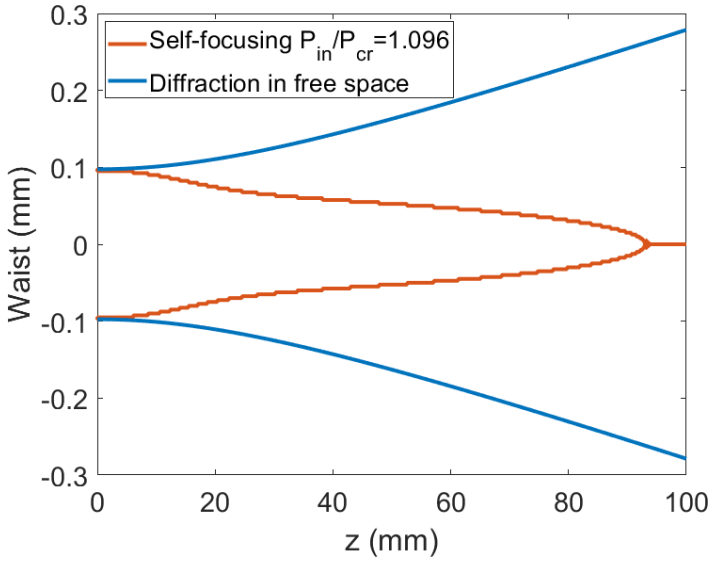

Figure 2.1: Self-focusing of a beam in air by optical Kerr effect due to the intensity-dependent refractive index of the medium. When the peak power of the beam exceeds a critical value, (P_{cr}) self-focusing overcomes diffraction (orange solid line) in the propagation dynamics. The blue solid line represents the free space propagation of the beam when diffraction dominates the propagation dynamics.

nonlinear polarization that appears on the right-hand side of Eq. 2.12 using Eq. 2.13.

$$\frac{\partial^2}{\partial t^2}\mathbf{P}^{NL}(\mathbf{r},\theta,t,z) = -\omega_0^2\left(1+\frac{i}{\omega_0}\frac{\partial}{\partial t}\right)^2 \mathbf{p}^{NL}(\mathbf{r},\theta,t,z)\; e^{i(k_0 z-\omega_0 t)} + c.c. \tag{2.33}$$

We rewrite Eq. 2.20 as

$$\left(\frac{\partial^2}{\partial z^2} + 2ik_0\frac{\partial}{\partial z} + \nabla_\perp^2\right)\mathbf{A}(\mathbf{r},\theta,\omega,z) + (k(\omega)^2 - k_0^2)\mathbf{A}(\mathbf{r},\theta,\omega,z) = \\ = -\frac{\omega^2}{E_0 c^2}\left(1+\frac{\omega}{\omega_0}\right)^2 \mathbf{p}^{NL}(\mathbf{r},\theta,\omega,z) \tag{2.34}$$

where $k(\omega) = n(\omega)\omega/c$ and $n(\omega)$ is the complex refractive index. Since $k(\omega)$ is the propagation constant it represents the linear response including all the dispersion terms and the absorption. We can approximate $k(\omega)$ as a power series in the frequency difference $\omega - \omega_0$ as

$$k(\omega) = k_0(\omega_0) + k_1(\omega-\omega_0) + D(\omega) \tag{2.35}$$

$$D(\omega) = \sum_{m\geq 2}^{\infty}\frac{1}{m!}k_m(\omega-\omega_0)^m \tag{2.36}$$

where D represents the higher-order dispersion terms, $k_m = (\partial^m k/\partial\omega^m)_{\omega=\omega_0}$ and $k_1 = (\partial k/\partial\omega)_{\omega=\omega_0} = 1/v_g(\omega_0)$ is the reciprocal of the group velocity v_g. The first order term, k_0, can be expressed as $k_0 = k_0^R + ia/2$. In Eq. 2.35, k_0^R and k_m represent the complete linear dispersion response and a represents the linear absorption considered only to the

first order, since in our study the absorption is small. If we introduce these expressions in the Eq. 2.34 and we convert the equation to the time domain, then we obtain

$$\left(\frac{\partial^2}{\partial z^2} + 2ik_0\frac{\partial}{\partial z} + \nabla_\perp^2 + (k_0^R)^2 - k_0^2 - \frac{a^2}{4} - k_1^2\frac{\partial^2}{\partial t^2} + \tilde{D}^2 + i\beta_0 a + 2ik_1 k_0^R\frac{\partial}{\partial t} - ak_1\frac{\partial}{\partial t} + \right.$$
$$\left. + iaD + 2ik_1 D\frac{\partial}{\partial t} + 2k_0^R D\right)\mathbf{A}(\mathbf{r},\theta,t,z) = -\frac{\omega_0^2}{E_0 c^2}\left(1 + \frac{i}{\omega_0}\frac{\partial}{\partial t}\right)^2 \mathbf{p}^{NL}(\mathbf{r},\theta,t,z) \tag{2.37}$$

The differential operator $\tilde{D}$ is written as follows

$$\tilde{D}(t) = \sum_{m\geq 2}\frac{1}{m!}k_m\left(i\frac{\partial}{\partial t}\right)^m \tag{2.38}$$

Using a frame moving with the pulse, $T = t - k_1 z$ and $z = z$, Eq. 2.37 becomes

$$\left(\frac{\partial^2}{\partial z^2} - 2k_1\frac{\partial}{\partial z}\frac{\partial}{\partial T} + k_1^2\frac{\partial^2}{\partial T^2} + 2ik_0\left(\frac{\partial}{\partial z} - k_1\frac{\partial}{\partial T}\right) + \nabla_\perp^2\right)\mathbf{A} + \left((k_0^R)^2 - k_0^2 - \frac{a^2}{4} - \right.$$
$$\left. - k_1^2\frac{\partial^2}{\partial T^2} + \tilde{D}^2 + ik_0^R a + 2ik_1 k_0^R\frac{\partial}{\partial T} - ak_1\frac{\partial}{\partial T} + ia\tilde{D} + 2ik_1\tilde{D}\frac{\partial}{\partial T} + 2k_0^R\tilde{D}\right)\mathbf{A} =$$
$$= -\frac{\omega^2}{E_0 c^2}\left(1 + \frac{i}{\omega_0}\frac{\partial}{\partial T}\right)^2 \mathbf{p}^{NL} \tag{2.39}$$

Now we group terms together and we assume that $k_0^R \approx k_0$, since the imaginary part of the refractive index is very small in our case. We can drop all the terms D^2, a^2 and $\partial^2/\partial z^2$ because they are invariably small.

$$-\frac{i}{2k}\nabla_\perp^2 + \left(\frac{\partial}{\partial z} + \frac{a}{2} - i\tilde{D}\right)\left(1 + i\frac{k_1}{k_0}\frac{\partial}{\partial T}\right)\mathbf{A} = \frac{ik_0}{2E_0 n_0^2}\left(1 + \frac{i}{\omega_0}\frac{\partial}{\partial T}\right)^2 \mathbf{p}^{NL} \tag{2.40}$$

The ratio $k_1/k_0 = v_g^{-1}/(n_L\omega_0/c) = n_g/(n_L\omega_0)$ can be approximated to $1/\omega_0$ ignoring dispersion [Boyd, 2020]. So this equation can be written as (for simplicity we write $z = z$)

$$\frac{\partial}{\partial z} - \frac{i}{2k_0}\nabla_\perp^2\left(1 + \frac{i}{\omega_0}\frac{\partial}{\partial T}\right)^{-1} - iD + \frac{a}{2}\mathbf{A}(\mathbf{r},\theta,t,z) =$$
$$= \frac{ik_0}{2E_0 n_0^2}\left(1 + \frac{i}{\omega_0}\frac{\partial}{\partial T}\right)\mathbf{p}^{NL}(\mathbf{r},\theta,t,z) \tag{2.41}$$

or

$$\left(\frac{\partial}{\partial z} - \frac{i}{2k_0}\nabla_\perp^2 T^{-1} - i\tilde{D} + \frac{a}{2}\right)\mathbf{A}(\mathbf{r},\theta,t,z) = \frac{ik_0}{2E_0 n_0^2}\tilde{T}\mathbf{p}^{NL}(\mathbf{r},\theta,t,z) \tag{2.42}$$

where $\tilde{T}$ is an operator defined as $\tilde{T} = 1 + \frac{i}{\omega_0}\frac{\partial}{\partial T}$. This is a general expression of the nonlinear propagation equation. It includes the linear effects that appear in the propagation, the diffraction, the spatio-temporal coupling (which improves the model above the slowly envelope approximation) and the high-order dispersion terms through $\tilde{D}$. The spatial widening of the beam due to diffraction is represented by the transverse Laplacian, while the temporal distortion of the pulse due to the material dispersion is included in $\tilde{D}$. Related to the nonlinear dynamics, the self-steepening effect is represented by the differential operator $\tilde{T}$ in the right-hand side and the linear space-time coupling is represented by the inverse of the same differential operator on the left-hand side. By considering this linear spatio-temporal coupling, we do not neglect the term $\partial^2/\partial z \partial t$ that appears in Eq. 2.39, so we impose the slowly varying amplitude approximation in the propagation direction z, but not in time, which is useful in the case of ultrashort pulses (this approximation is known as the slowly evolving wave approximation, SEWA) [Couairon and Mysyrowicz, 2007].

It is usually stated that envelope pulse propagation description is limited to those regimes that can be described as quasi-monochromatic. However, the nonlinear envelope equation (NEE), which corresponds to Eq. 2.42 and was derived by Brabec and Krausz [Brabec and Krausz, 1997], is valid for ultrashort, broad-band spectrum laser pulses due to different "correction terms" beyond the slowly varying envelope approximation. This equation can manage pulses with broad spectrum and fast temporal features, even though the field is described through its envelope.

2.1.2.1 Self-Phase Modulation and Self-Steepening

The subsequent step is to assume a material with purely electronic instantaneous third-order response. In that case, according to Eq. 2.26 the polarization amplitude takes the form

$$\mathbf{p}^{NL}(\mathbf{r}, \theta, t, z) = 3\varepsilon_0 \chi^{(3)} |\mathbf{A}(\mathbf{r}, \theta, t, z)|^2 \mathbf{A}(\mathbf{r}, \theta, t, z) \tag{2.43}$$

$\chi^{(3)} = 2/3 n_L n_{NL}$ being the third-order susceptibility, so $|\mathbf{A}(\mathbf{r}, \theta, t, z)|^2$ is expressed in W/cm^2 [Boyd, 2020]. Introducing this expression in Eq. 2.41, we describe the nonlinear phase acquired during the propagation.

$$\left(\frac{\partial}{\partial z} - \frac{i}{2k_0} \nabla_{\perp}^2 \tilde{T}^{-1} - i\tilde{D} + \frac{a}{2} \right) \mathbf{A}(\mathbf{r}, \theta, T, z) = i \frac{\omega_0}{c} \frac{n_L n_{NL}}{n_0} \tilde{T} |\mathbf{A}(\mathbf{r}, \theta, T, z)|^2 \mathbf{A}(\mathbf{r}, \theta, T, z) \tag{2.44}$$

a being the linear absorption that, in the case of a HCF, includes the propagation losses due to the gas absorption and to the HCF confinement, as we will see in Section 2.2. The refractive index n_0 is defined as $n_0 = n_L(\omega_0)$. The term on the right-hand side of

the equation describes the self-phase modulation and self-steepening effects. Self-phase modulation is a fundamental effect in post-compression schemes due to the effective spectral broadening. This effect is a consequence of the optical Kerr effect, similarly to self-focusing, and it also appears due to the nonlinear contribution to the refractive index, n_{NL}, which induces a change in the temporal phase of the pulse during the propagation. Let us consider the case of a laser pulse whose shape is described by $E(t, z) = E_0(t, z)e^{i(kz-\omega_0 t)}$, $E_0(t, z)$ being the envelope, $k = n_L\omega_0/c$ and ω_0 the central frequency. If this laser pulse is intense, then it will experience self-phase modulation which leads to a change in the refractive index as a function of the pulse intensity $n = n_L + n_{NL}I(t)$.

$$E(t, z) = E_0(t, z)e^{i(n_L \frac{\omega_0}{c} z + n_{NL} I(t) \frac{\omega_0}{c} z - \omega_0 t)} \tag{2.45}$$

So the phase φ of the electric field experiences a new temporal modulation induced by the pulse itself. This time-varying phase induces an instantaneous frequency of the pulse $\omega(t)$

$$\omega(t) = -\frac{d}{dt}\varphi(t, z) = \omega_0 - n_{NL}\frac{\omega_0}{c} z \frac{\partial}{\partial t} I(t) \tag{2.46}$$

This instantaneous frequency shifts through the propagation of the pulse in the nonlinear medium leading to the formation of new spectral components and to a spectral broadening of the laser pulse. According to Eq. 2.46, the new spectral components are created on the slope of the pulse envelope: the leading edge of the pulse ($\partial I/\partial t > 0$) shifts to the red side, while the trailing edge ($\partial I/\partial t < 0$) shifts to the blue side of the spectrum, which leads to a positively chirped pulse after the propagation in the nonlinear medium. The maximum broadening can be determined by the highest slope of the pulse. In addition, there are points with the same slope, which means that the same spectral components are created at different times leading to spectral fringes with different period depending on the time difference. In the peak of the pulse there is no spectral shift ($\partial I/\partial t = 0$) so this region contributes to the central wavelength. Since the pulse energy is proportional to the integral of both the pulse shape and the spectrum, the steeper the slope is, the less energy it contains which is distributed in a broader spectral region, as it is observed in the blue side of the spectrum on the right of Fig. 2.2 [Nagy et al., 2021].

The differential operator on the right-hand side of Eq. 2.44 describes the self-steepening effect. This effect can be understood like an intensity dependence of the group velocity, $v_g = d\omega/dk = c/(n_L + \omega dn/d\omega)$ [Boyd, 2020]. In general, the nonlinear refractive index, n_{NL}, is positive and as the pulse envelope propagates with the group velocity, the peak of the pulse with high intensity slows down with respect to the wings of the pulse. As a result, the slope of the leading edge decreases while the slope of the trailing edge

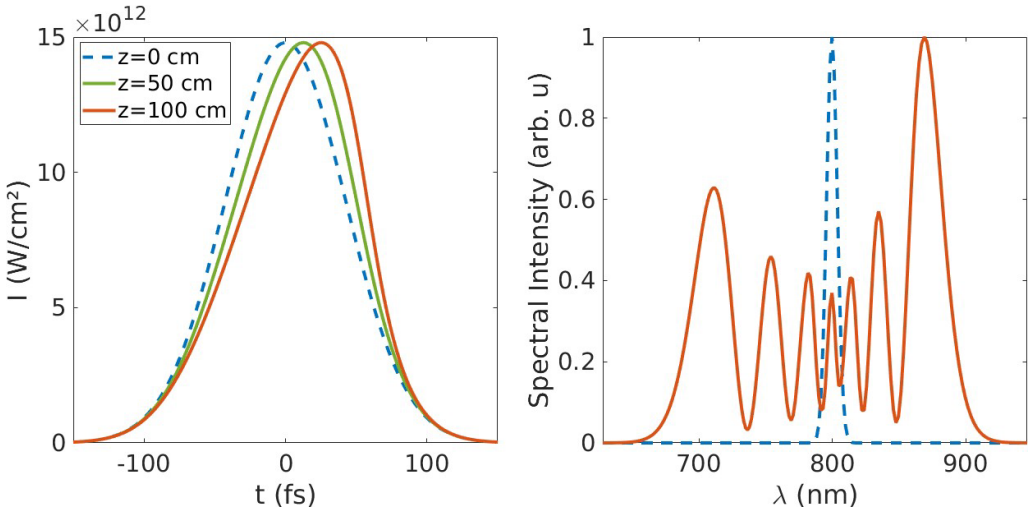

Figure 2.2: Self-phase modulation and self-steepening effects in a nonlinear propagation. The initial intensity and spectrum are represented in blue dashed lines. Self-phase modulation is responsible of the spectrum broadening and modulates its structure, while self-steepening is responsible of the slowdown of the intensity peak and the asymmetry of the spectrum.

becomes steeper, which can lead to an optical shock wave. This temporal asymmetry due to self-steepening leads to an asymmetry in the spectrum. Since the slope is higher in the trailing edge of the pulse, there is a larger spectral broadening in the blue side of the spectrum, containing less energy than the red side, as Fig. 2.2 illustrates.

2.1.2.2 Delayed Raman Response

If we now assume a material with molecular response, which is slower than the electronic response, we have to consider the non-instantaneous response of the third-order susceptibility. Taking this into account, the Kerr term has an instantaneous part and a delayed part. We have to use the general form of the nonlinear polarization, as defined in Eq. 2.26 [Agrawal, 2013] and the polarization amplitude takes the form

$$\mathbf{p}^{NL}(\mathbf{r}, \theta, t, z) = 3E_0 x^{(3)} \mathbf{A}(\mathbf{r}, \theta, t, z) \int_{-\infty}^{\infty} R(t - \tau_1) |\mathbf{A}(\mathbf{r}, \theta, \tau_1, z)|^2 d\tau_1 \tag{2.47}$$

$x^{(3)} = 2/3 n_L n_{NL}$ being the third-order susceptibility, so $|\mathbf{A}(\mathbf{r}, \theta, t, z)|^2$ is expressed in W/cm² [Boyd, 2020]. Introducing this expression in Eq. 2.41

$$\begin{aligned} \left(\frac{\partial}{\partial z} - \frac{i}{2k_0} \nabla_\perp^2 \tilde{T}^{-1} - i\tilde{D} + \frac{a}{2} \right) \mathbf{A}(\mathbf{r}, \theta, T, z) = \\ = \frac{\omega_0}{c} \frac{n_L n_{NL}}{n_0} \tilde{T} \mathbf{A}(\mathbf{r}, \theta, T, z) \int_{-\infty}^{\infty} R(T - \tau_1) |\mathbf{A}(\mathbf{r}, \theta, T, z)|^2 d\tau_1 \end{aligned} \tag{2.48}$$

where n_0 is defined as the linear refractive index at ω_0, $n_L(\omega_0)$. As can be seen in Eq. 2.27, the Raman effect of a molecular gas contributes with a fraction f_R and a temporal response $h_R(t)$ to the nonlinear response. In the particular case of gases, which we will study in this work, this term can be expressed as $R(T-t) = (1-f_R)\delta(T-t) + f_R/\tau_K \exp(-(T-t)/\tau_K)$, f_R being the ratio between the self-phase modulation and the Raman effect, and τ_K the characteristic time for the Raman response [Conejero Jarque et al., 2018].

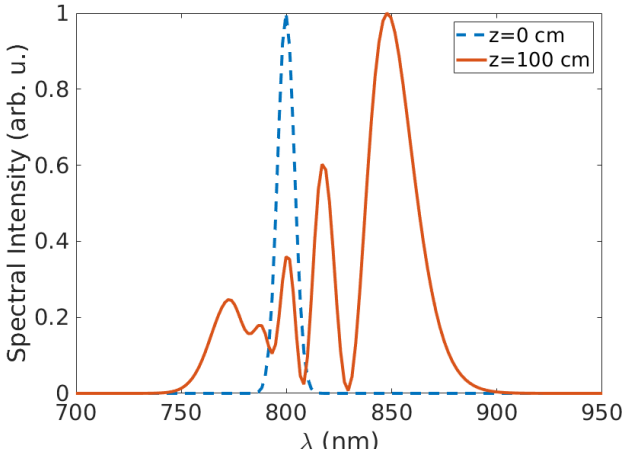

Figure 2.3: Pulse spectrum modulated by the Raman response when propagating through air. The initial spectrum is represented in blue dashed line and the final spectrum in orange solid line. There is a red shift in the spectrum due to the Raman effect.

In the latter equation, the terms on the left-hand side are the diffraction, the space-time coupling, the dispersion and the linear absorption. On the right-hand side we describe the self-phase modulation and the Raman delayed response, both affected by self-steepening. Because of the delayed Raman response, the pulse spectrum suffers a red shift as the pulse propagates inside the HCF (see Fig. 2.3), a phenomenon referred to as the self-frequency shift [Mitschke and Mollenauer, 1986]. This is due to the fact that Raman effect is the result of light interaction with the vibrations of the molecules. The Raman scattering is an inelastic scattering process in which a medium absorbs a photon and emits a new one with slightly different frequency. Usually the frequency of the emitted photon is lower than the frequency of the one absorbed. The energy difference is accounted for by a vibrational energy (see Fig. 2.4). When this process is stimulated by the light intensity, it can be described as a nonlinear third order process in a similar way as the optical Kerr effect, as we have presented.

The new lower frequencies components are called the Raman Stokes components, which are generated from the ground level. There are also Raman anti-Stokes components, but they are much weaker than the Stokes components because they consist of a transition

from an excited level to the ground level and, at low temperatures, the population in the ground level is larger (as sketched in Fig. 2.4). Of course, if the intensity of the Raman Stokes component is large enough, the re-emitted photon can be scattered again at a lower energy, and so on, which means that the process can cascade generating a broadband spectrum at longer wavelengths.

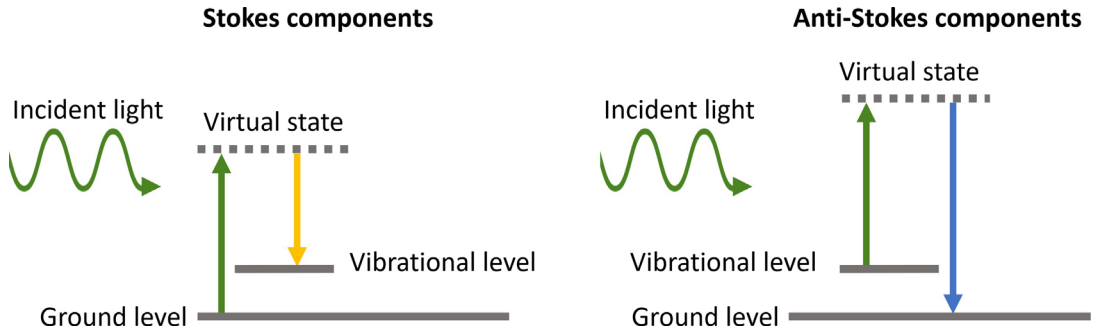

Figure 2.4: Left panel: an incident photon (green) can be absorbed by the nonlinear medium and scattered with lower energy (Stokes components (yellow and orange)). Right panel: an incident photon (green) can be absorbed by the nonlinear medium and scattered with higher energy (anti-Stokes components (blue and purple)). In the process there is a molecular transition between different energy states.

2.1.3 Ionization Effects: Plasma Generation and Multiphoton Absorption

When the intensity of the pulse reaches $10^{13} - 10^{14}$ W/cm^2, it is enough to ionize the molecules or atoms of the medium inside the core of the HCF. These intensity values can be reached when the pulse propagates inside the HCF by the self-focusing of the beam, for example, leading to the ionization of the medium and the generation of plasma. The way of introducing the effects of the ionization in the models presented in the previous subsections is by means of the plasma current density $\mathbf{J_p}$ associated with the ionized medium [Brabec and Krausz, 2000, Couairon et al., 2002].

$$\nabla^2\mathbf{E} - \frac{1}{c^2}\frac{\partial^2\mathbf{E}}{\partial t^2} = \frac{1}{E_0}\left(\frac{\partial^2}{\partial t^2}\mathbf{P}^L + \frac{\partial^2}{\partial t^2}\mathbf{P}^{NL}\right) + \frac{\partial\mathbf{J_p}}{\partial t} \tag{2.49}$$

$$\frac{\partial\mathbf{J_p}}{\partial t} = -\frac{\sigma}{2}(1 + i\omega_0\tau_c)\rho\mathbf{E} - \frac{W(|\mathbf{E}|^2)U_i}{2I}(\rho_a - \rho)\mathbf{E} \tag{2.50}$$

where U_i is the ionization potential of the gas, $\rho(r, \theta, t, z)$ is the density of free electrons, τ_c is the collision time (relaxation time) and σ is the cross section for the inverse Bremsstrahlung, which is written as follows [Couairon et al., 2011]

$$\sigma = \frac{\omega_0}{n_L(\omega)c\rho}\frac{\omega_0\tau_c}{1 + \omega_0^2\tau_c^2} \tag{2.51}$$

$\rho_c = E_0 m_e \omega_0^2 / e^2$ being the value of the critical plasma density above which the plasma becomes opaque for the frequency ω_0, and m_e and e are the electron mass and charge, respectively. The first term of Eq. 2.50 is the contribution of free electrons moving away

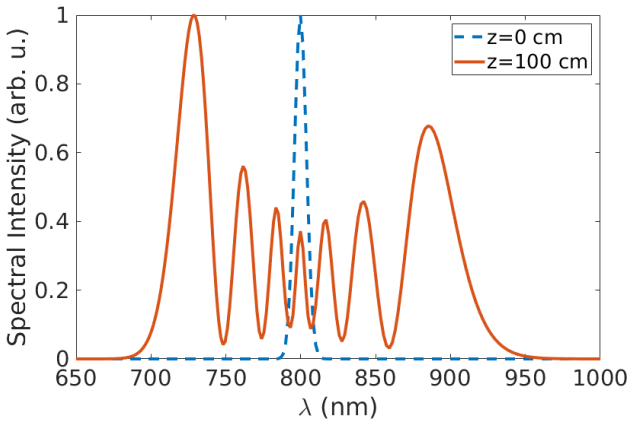

Figure 2.5: Pulse spectrum modulated by self-phase modulation in argon. The initial spectrum is represented in blue dashed line and the final spectrum in orange solid line. Due to the effect of the ionization the spectrum presents a blue shift.

from the atom after the ionization process [Couairon and Bergé, 2000] . The real part of this first term represents the absorption of light by the generated plasma itself, while the imaginary part leads to plasma defocusing and blue shifting of the laser spectrum typically observed in ionized gases [Bloembergen, 1973], as can be seen in Fig. 2.5. The second term accounts for the absorption related to the ionization process. The parameter $W(|E|^2)$ is the ionization rate, which depends on the ionization potential (U_i), the laser intensity and the central pulse frequency, and it is able to describe the ionization in the multiphoton and tunnelling regime. We use the model of Perelomov-Popov-Terent'ev (PPT model) to calculate the ionization rates since it is valid for a wider intensity range compared to other ionization models [Couairon and Mysyrowicz, 2007, Couairon et al., 2011, Perelomov et al., 1966]. Both plasma defocusing and absorption prevent beam collapse when self-focusing dominates the propagation.

Including these terms, the complete nonlinear wave equation for ultrashort pulses is the following [Couairon and Mysyrowicz, 2007]

$$\left(\frac{\partial}{\partial z} - \frac{i}{2k_0}\nabla_\perp^2 T^{-1} - iD + \frac{\alpha}{2}\right)\mathbf{A}(r,\theta,T,z) = N(|A|^2, A, \rho) \tag{2.52}$$

where the nonlinear effects mentioned above are included in

$$N(|A|^2, A, \rho) = N_{Kerr}(|A|^2, A) + N_{ioniz}(A, \rho) + N_{abs}(|A|^2, A, \rho) \tag{2.53}$$

$$N_{Kerr}(|A|^2, A) = i\frac{\omega_0 n_L n_{NL}}{c\ n_0}\left(1+\frac{i}{\omega_0}\frac{\partial}{\partial T}\right)\left(\int_{-\infty}^{T} R(T-t)|A(r,\theta,T,z)|^2 dt\right)\mathbf{A}(r,\theta,T,z) \tag{2.54}$$

$$N_{ioniz}(A,\rho) = -i\frac{\sigma}{2}\omega_0\tau_c\left(1+\frac{i}{\omega_0}\frac{\partial}{\partial T}\right)^{-1}\rho(r,\theta,T)\mathbf{A}(r,\theta,T,z) \tag{2.55}$$

$$N_{abs}(|A|^2, A, \rho) = -\frac{W(|A(r,\theta,T,z)|^2)U_i}{2|A(r,\theta,T,z)|^2}(\rho_{at}-\rho)\mathbf{A}(r,\theta,T,z) - \frac{\sigma}{2}\left(1+\frac{i}{\omega_0}\frac{\partial}{\partial T}\right)^{-1}\rho(r,\theta,T)\mathbf{A}(r,\theta,T,z) \tag{2.56}$$

Equation 2.56 includes the losses due to the ionization process (first term) and the losses due to the plasma absorption (second term). Equation 2.52 is solved simultaneously with the equation describing the evolution of the density of electrons

$$\frac{\partial\rho}{\partial t} = W(|A|^2)(\rho_{at}-\rho) \tag{2.57}$$

$W(|A|^2)$ being the ionization rate calculated with the PPT model [Perelomov et al., 1966] and ρ_{at} is the atomic density of the medium.

The most important parameters related to the ionization process are the central frequency ω_0, the peak amplitude of the pulse A_0 and the ionization potential of the gas U_i. The relation among these parameters through the Keldysh adiabaticity parameter, Γ, indicates the ionization regime [Keldysh, 1965]: Multiphoton ionization, tunnelling ionization and barrier suppression ionization.

$$\Gamma = \frac{\omega_0(2m_eU_i)^{1/2}}{eA_0} \tag{2.58}$$

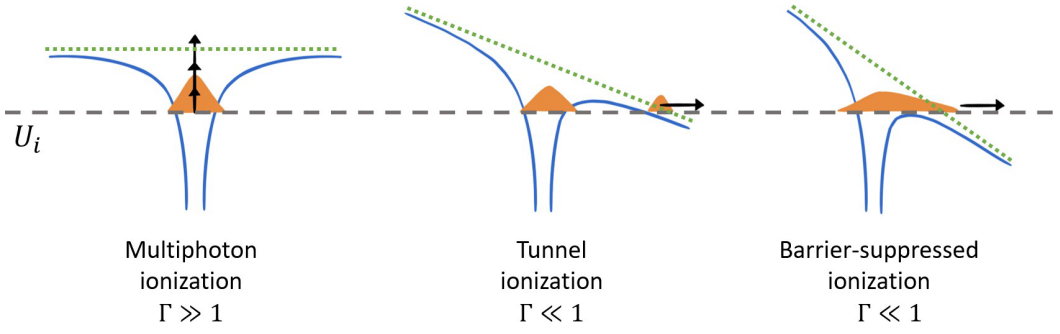

Figure 2.6: Scheme of different ionization regimes depending on the external electric field applied.

Multiphoton ionization is the dominant process when $\Gamma \gg 1$, which happens for high

frequencies or weak fields ($I \leq 10^{13}$ W/cm^2). In this case, a certain number of photons, K, are absorbed by an electron, which passes to the continuum with a kinetic energy given by $K\hbar\omega_0 - U_i$. On the other hand, in the case of low frequencies and moderate intensity fields ($I \geq 10^{14}$ W/cm^2), then $\Gamma \ll 1$, which means that we are in the tunnelling ionization regime. The intense field modifies the atomic or molecular potential forming a potential barrier through which the electron can pass via tunnelling effect. The limiting case of tunnelling is the barrier suppression ionization, which occurs when the amplitude of the field is sufficiently high that the potential barrier lies underneath the ionization potential level. A scheme of these ionization regimes is represented in Fig. 2.6.

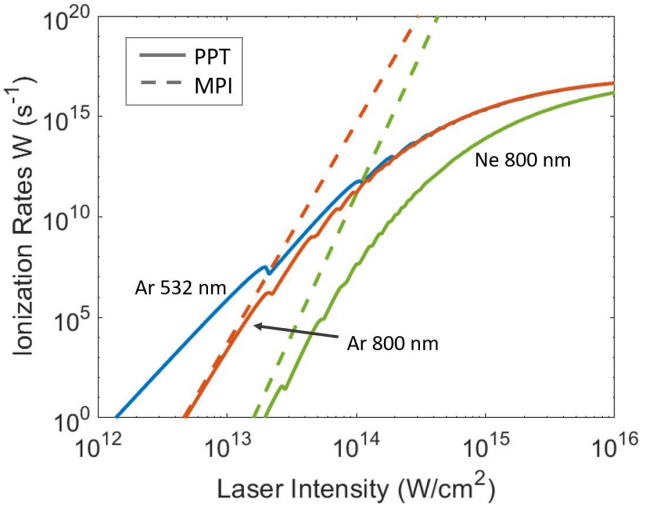

Figure 2.7: Ionization rates for argon at 532 nm (blue line) and 800 nm (orange line), and for neon at 800 nm (green line) with the multiphoton ionization model (MPI) and the PPT model.

As stated before, the PPT model that we use to calculate the ionization rates describes both the multiphoton regime, valid for $I \gg 10^{13}$ W/cm^2, and the tunnel regime for $I \gg 10^{14}$ W/cm^2. There are other ionization models that also work well in the multiphoton regime (MPI model) or in the tunnelling ionization regime (ADK model [Ammosov et al., 1986]), but since in this thesis we use laser intensities in the intermediate regime, we use the PPT model as the best approximation. Figure 2.7 shows the ionization rates for argon and neon computed from the PPT model (solid line) and from the multiphoton ionization (dashed line).

2.2 Hollow Capillary Fiber Spatial Modes

In this section we will introduce the spatial modes of the hollow capillary fiber (HCF) that we will use to study the propagation of a laser pulse though such HCF. In general,

solving the nonlinear propagation equation in three dimensions is quite time-consuming. For this reason, we use the decomposition of the electric field in the spatial eigenmodes of the HCF, which is faster, as we will explain in Chapter 3. In the following subsections we will present the field configurations and the complex propagation coefficients of the different spatial eigenmodes of the HCF that we will study in this thesis.

We consider a dielectric and cylindrical HCF and we assume that if the wavelength is smaller than the core radius ($\lambda << r_F$) and the HCF does not present curvature, the light propagates essentially within the core by grazing incidence reflections at the inner surface, so there is little energy flux into the cladding [Marcatili and Schmeltzer, 1964]. The field in the cladding is weak, and the index difference between the core and the cladding is high enough that any coupling on the femtosecond time scale from the cladding back to the core is negligible, as done in previous studies [Homoelle and Gaeta, 2000, Tempea and Brabec, 1998]. We also assume that $|k_z/k - 1| \ll 1$, which means that the axial propagation constant of each mode (k_z) is nearly equal to that of free space, so only modes with low losses are supported.

There are three types of spatial modes supported by this cylindrical HCF: transverse circular electric modes, transverse circular magnetic modes and hybrid modes. We will distinguish between different spatial modes with two integers, p and q, where $|p|$ is the number of periods of each field component in the azimuthal direction and q the number of maxima and minima of each field component in the radial direction. The expression of the electric field for the different spatial modes in the core of the HCF is written as follows [Marcatili and Schmeltzer, 1964]

1. Circular electric modes TE_{0q} ($p = 0$)

If $(E_{0q})_z = 0$ and $(E_{0q})_r = 0$ everywhere, the electric field has only a tangential component $(E_{0q})_\theta$ that can be approximately expressed as

$$(E_0)_\theta = J_1\left(u_{0q}\frac{r}{r_F}\right)\exp(i(k_z z - \omega t)) \tag{2.59}$$

where u_{pq} is the qth root of the J_{p-1} Bessel function, r_F is the core radius and k_z is the complex propagation constant of the spatial mode we consider. The result is a transverse circular electric mode (TE_{0q}, $q = 1, 2, ...$) in which the electric field lines are transverse concentric circumferences centered on the propagation axis.

These spatial modes, which belong to the so-called vector beam family of the optical beams, present azimuthal polarization and a singularity in the propagation axis. As a consequence of this spatially varying polarization, the spatial intensity distribution has a doughnut shape profile. Figure 2.8 shows a representation of the first two spatial modes

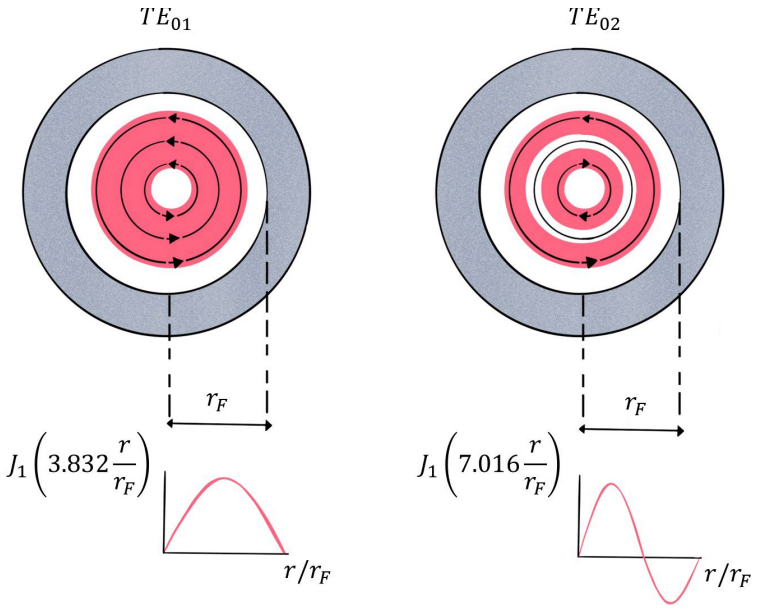

Figure 2.8: First two circular electric modes TE_{01} and TE_{02} [Marcatili and Schmeltzer, 1964].

of the family, TE_{01} and TE_{02} modes [Marcatili and Schmeltzer, 1964], where vectors represent the polarization direction of the local field. In Chapter 5 we will study the features of the propagation of this type of beams inside the HCF.

2. Circular magnetic modes TM_{0q} ($p = 0$)

If $(E_{0q})_\theta = 0$ everywhere, the other two components of the electric field can be approximately expressed as

$$\begin{aligned}(E_{0q})_r &= J_1\left(u_{0q}\frac{r}{r_F}\right)\exp(i(k z - \omega t)) \\ (E_{0q})_z &= i\frac{u_{0q}}{kr_F}\frac{J_0}{J_1}\left(u_{1q}\frac{r}{r_F}\right)\exp(i(k_z z - \omega t))\end{aligned} \tag{2.60}$$

where, again, u_{pq} is the qth root of the J_{p-1} Bessel function, r_F is the core radius, k is the free wavevector in the gas and k_z is the complex propagation constant of the spatial mode we consider. The result is a transverse circular magnetic mode (TM_{0q}, $q = 1, 2, ...$) in which the electric field lines are radial lines.

The longitudinal component of these modes is very small since $\lambda << r_F$, so we can neglect it and the electric field is almost transverse. These spatial modes, also named vector beams as the TE_{0q} modes, present radial polarization and a singularity in the

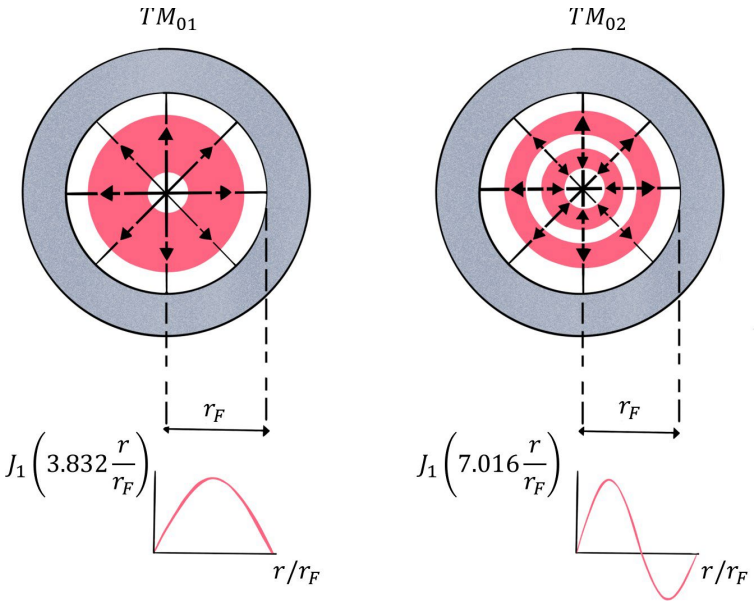

Figure 2.9: First two circular magnetic modes TM_{01} and TM_{02} [Marcatili and Schmeltzer, 1964].

propagation axis. As the TE_{0q} modes, the spatial intensity distribution of the circular magnetic modes has a doughnut shape profile. Figure 2.9 shows a representation of the first two spatial modes [Marcatili and Schmeltzer, 1964]. In Chapter 5 we will study the propagation of this kind of beams inside the HCF and try to find the differences in the propagation dynamics between TE_{0q} and TM_{0q} modes.

3. Hybrid modes EH_{pq} $(p \neq 0)$

In this case all field components are present and the approximated expressions for each field component are

$$
\begin{aligned}
(E_{pq})_\theta &= \left[J_{p-1}\left(u_{pq}\frac{r}{r_F}\right) + i\frac{u_{pq}^2}{2n_L k r_F}\sqrt{v^2-1}\,J_p\left(u_{(p+1)q}\frac{r}{r_F}\right)\right]\cos(p\theta)\exp(i(k_z z-\omega t)) \\
(E_p)_r &= \left[J_{p-1}\left(u_{pq}\frac{r}{r_F}\right) + i\frac{u_{pq}}{2kr}\sqrt{v^2-1}\,J_p\left(u_{(p+1)q}\frac{r}{r_F}\right)\right]\sin(p\theta)\exp(i(k_z z-\omega t)) \\
(E_{pq})_z &= -\left[i\frac{u_{pq}}{k r_F} J_p\left(u_{(p+1)q}\frac{r}{r_F}\right)\right]\sin(p\theta)
\end{aligned}
\tag{2.61}
$$

where u_{pq} are the qth root of the J_{p-1} Bessel function of the first kind of order $p-1$, r_F is the core radius, n is the refractive index of the nonlinear medium filling the core, v is the ratio between the refractive index of the external and internal medium, k is the free

wavevector in the gas and k_z is the complex propagation constant of the spatial mode we consider.

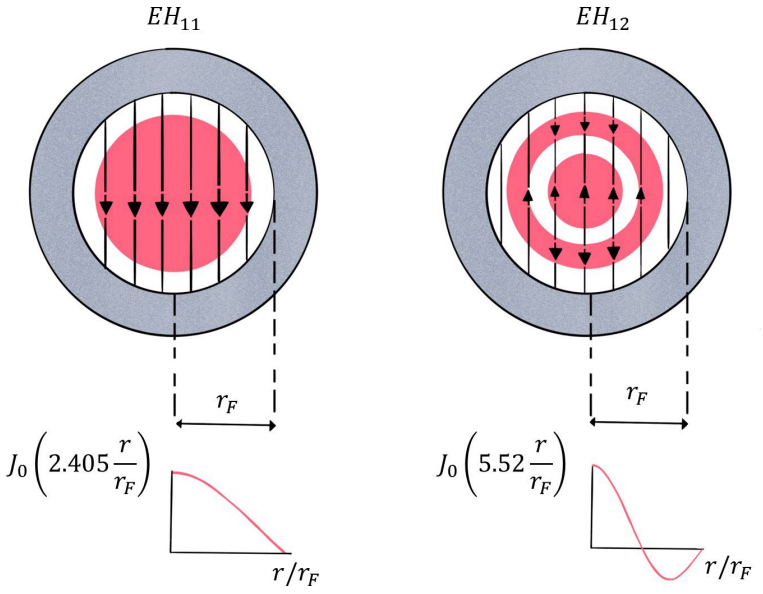

Figure 2.10: First two hybrid modes EH_{11} and EH_{12} [Marcatili and Schmeltzer, 1964].

These are the hybrid modes, indicated as EH_{pq}. The terms that depend on kr_F can be neglected since we assume $\lambda << r_F$, thus the hybrid modes are almost transverse and the imaginary part of the radial and azimuthal component can be neglected too.

These hybrid modes present a uniform linear polarization, a maximum of intensity on the propagation axis and the higher-order modes ($q > 1$) present concentric intensity rings. Figure 2.10 shows a representation of the first two spatial modes of these EH_{1q} modes, EH_{11} and EH_{12} [Marcatili and Schmeltzer, 1964]. Among the hybrid modes of the first order, EH_{11} mode is called the fundamental spatial mode and it is the most frequently used in standard post-compression setups. In Chapter 4 and Chapter 7 we will study the propagation of this kind of beams inside the HCF.

For core radius sufficiently larger than the wavelength, which is the subject of study in this work, we can approximate the expressions for the field components of the different spatial modes as

1. Circular electric modes TE_{0q} $(p = 0)$

$$(E_{0q})_\theta = J_1 \left(u_{0q} \frac{r}{r_F} \right) \tag{2.62}$$

2. Circular magnetic modes TM_{0q} $(p = 0)$

$$(E_{0q})_r = J_1\left(u_{0q}\frac{r}{r_F}\right) \tag{2.63}$$

3. Hybrid modes EH_{pq} $(p \neq 0)$

$$\begin{aligned}(E_{pq})_\theta &= J_{p-1}\left(u_{pq}\frac{r}{r_F}\right)\cos(p\theta)\\ (E_{pq})_r &= J_{p-1}\left(u_{pq}\frac{r}{r_F}\right)\sin(p\theta)\end{aligned} \tag{2.64}$$

These simpler expressions are the ones that we have used to simulate the propagation of the spatial modes inside the HCF.

4. Necklace Beams

These spatial modes are a composition of two degenerate hybrid modes: $EH_{(-|p|)q} + EH_{(|p|+2)q}$, both with the same complex propagation coefficient, as we will see below. If these two hybrid modes are added, we obtain a new family of linearly polarized modes. Its spatial amplitude can be represented by a radially dependent Bessel function of the first kind with a sinusoidal azimuthal dependence.

$$EH_{(-|p|)q} + EH_{(|p|+2)q} = J_{p+1}\left(u_{(p+2)q}\frac{r}{r_F}\right)\sin((p+1)\theta) \tag{2.65}$$

where r_F is the core radius and u_{pq} represent the q-th root of the J_{p-1} Bessel function. Necklace beams are a type of structured laser beams with amplitude and phase rotational symmetry around the propagation axis. There are different families of necklace beams in a HCF depending on the number of rings and beads they present (see Fig. 2.11). Although the spatial structure of these modes seems complex, their generation has already been demonstrated [Grow et al., 2007]. We will study the nonlinear propagation of these type of modes in Chapter 6 to see if we can obtain any benefit by using such structured modes.

Propagation and absorption coefficients

The propagation and absorption coefficients of each pq-mode are the real and imaginary parts of the axial complex propagation coefficient k_z for a HCF

$$k_z(\omega) = \beta_{pq}(\omega) + i\alpha_{pq}(\omega) \tag{2.66}$$

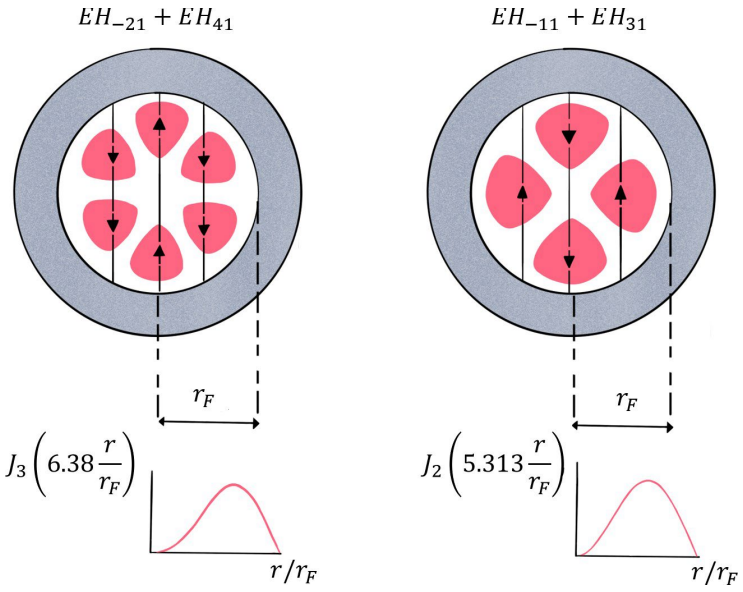

Figure 2.11: Two necklace beams with 6 and 4 beads [Marcatili and Schmeltzer, 1964].

the expression for β_{pq} and a_{pq} being the following [Marcatili and Schmeltzer, 1964]

$$\beta_{pq}(\omega) = \mathrm{Re}(k_z(\omega)) = n_L(\omega)\frac{2\pi}{\lambda}\left(1 - \frac{1}{2}\left(\frac{u_{pq}\lambda}{2\pi r_F\, n_L(\omega)}\right)^2\right)$$
$$a_{pq}(\omega) = \mathrm{Im}(k_z(\omega)) = \left(\frac{u_{pq}}{2}\right)^2 \frac{\lambda^2}{n_L(\omega)^2 r_F^3} \tag{2.67}$$

where $n_L(\omega)$ is the linear refractive index of the medium in the core and λ is the central wavelength in vacuum ($\lambda = 2\pi c/\omega$). The expression for v_p depends on the chosen spatial mode as follows

$$v_p = \begin{cases} \frac{\sqrt{1}}{v^2-1} & TE_{0q} \\ \sqrt{\frac{v^2}{v^2-1}} & TM_{0q} \\ \frac{1}{2}\sqrt{\frac{(v^2+1)}{v^2-1}} & EH_{pq} \end{cases}, \tag{2.68}$$

where v is the ratio between the refractive index of the cladding and the core. These expressions can be used as the propagation constant k^R and the absorption coefficient a defined in the wave equations in the previous section, where the absorption depends on the frequency in this case. Special attention should be paid to the expression of β_{pq} in Eq. 2.67. An important topic in nonlinear pulse compression is the dispersion experienced by laser pulses during the propagation inside the gas-filled HCF. We can note that carefully choosing the pulse wavelength, the core radius or the spatial modes coupled to the HCF, the group velocity dispersion can be negative ($\partial^2\beta_{pq}/\partial\omega^2 < 0$), thus entering in the anomalous dispersion regime. This great variety of parameters will play an important role in this work, since in the anomalous dispersion region new

features arise from the interplay between the second order dispersion (or group velocity dispersion) and self-phase modulation. These two effects can cooperate in such a way that the pulse propagates as an optical soliton and it can self-compress during the propagation, as we will see in Chapter 7. On the other hand, the attenuation constant is proportional to λ^2/a^3. This allows us to decrease the losses by choosing large core radii, but this will reduce the negative contribution of β_{pq} at the same time and enhance the multimode propagation regime. Seeing the expression for a_{pq} in Eq. 2.67, we realize that high-order modes present higher losses.

Lately, there has been an increasing interest in nonlinear multimode systems. The presence of different spatial modes and its interaction have led to the observation of new optical effects and the theoretical challenge of understanding their collective dynamics [Wright et al., 2015].

Chapter 3

Numerical Methods

The aim of this chapter is to develop a numerical model to study the nonlinear propagation of a femtosecond laser pulse along a gas-filled hollow-core capillary (HCF) through the nonlinear propagation equation presented in Section 2.1. This nonlinear partial differential equation (Eq. 2.42), cannot be described analytically in most of the cases, and a numerical solution of the nonlinear propagation equation is necessary to understand the nonlinear effects that affect propagation of the pulse. For this reason, we have developed different numerical models according to the effects that we are interested in or the spatial profile of the input beam.

Several numerical methods can be used to solve the nonlinear propagation equation. The easiest one to implement, and the one we have chosen in this work, is a split-step scheme in which the linear terms (diffraction, dispersion and absorption) and the nonlinear terms are solved separately [Agrawal, 2013]. Although in general, diffraction, dispersion and nonlinearity act together through the propagation along the HCF, with the split-step method we can obtain an approximate solution by assuming that linear and nonlinear effects act independently in a small longitudinal step size. To solve the linear and nonlinear part, we use a variety of numerical models like finite-difference scheme, Fourier space, Runge-Kutta algorithm,... and we will indicate which one we use in the following sections.

In this chapter, we shall present different numerical models for the nonlinear propagation equation, but its expression is adapted according to the dimensions and symmetries that we assume. We have divided this chapter in three sections where we explain the numerical model used to solve the propagation equation in different circumstances. In the first section we will introduce our one-dimensional numerical model, developed in the frame of this thesis, to study the nonlinear propagation of a laser beam considering only the spatial dynamics of the beam during the propagation. We solve the linear part

using a finite-difference scheme and the nonlinear part as an intensity-dependent phase. In the second section, we include the temporal effects and we model the complete spatio-temporal dynamics during the propagation of the pulse with a two-dimensional model. This model was developed by the "Aplicaciones del Lâser y Fotônica" research group in the University of Salamanca, and it has been adapted to the different spatial modes we will study in this thesis. We solve the linear part making use of the decomposition of the electric field into the spatial modes of the HCF and a Runge-Kutta algorithm in the time domain to solve the nonlinear part. In the third section we model the complete spatio-temporal dynamics in the case of pulses with a structured beam profile with a three-dimensional model, also developed in the frame of this thesis. We solve the equation mixing techniques used in the models presented in the two previous sections. We solve the linear part using a finite-difference scheme and the nonlinear part with a Runge-Kutta algorithm in the time domain.

3.1 The Time-Independent Model (1+1)D

The first numerical model we have developed is time-independent, useful for the understanding of the self-focusing dynamics in HCF, which is a purely spatial effect. In the literature, the early numerical studies on the self-focusing dynamics solved a propagation equation including only the diffraction and self-focusing effects and neglecting any time-dependent term [Kelley, 1965]. In accordance with this approach, we have developed a time-independent model ((1+1)D model) based on the nonlinear propagation equation obtained in Subsection 2.1.1 (Eq. 2.32) to study the spatial dynamics of a monochromatic laser beam inside the HCF and how the spatial confinement influences the propagation dynamics. The notation (1+1)D refers to the fact that we only take into account the radial transverse dimension r plus the propagation dimension z. We assume linear polarization so the envelope is a scalar quantity $A(r, z)$. The nonlinear propagation equation for the spatial envelope $A(r, z)$ of the laser beam assuming cylindrical symmetry and neglecting the temporal dynamics is written as follows

$$\frac{\partial}{\partial z}A(r,z) = \frac{i}{2k_0(r)}\left(\frac{\partial^2}{\partial r^2} + \frac{1}{r}\frac{\partial}{\partial r} + \left(n_R(r)\right)^2 - k_0(r)^2\right)A(r,z) - \frac{a(r)}{2}A(r,z) + i\frac{\omega_0}{c}\bar{n}_{NL}(r)|A(r,z)|^2A(r,z) \tag{3.1}$$

where $k_0(r) = n_0(r)\omega_0/c$, ω_0 being the laser frequency and n_0 the linear refractive index in ω_0. The linear absorption of the spatial mode propagating inside the HCF is $a(r) = 2\alpha(r)_{pq}$, defined in Eq. 2.67, $n_L(r)$ is the transverse structure of the linear refractive index, calculated by the corresponding Sellmeier equation at ω_0, and $n_{NL}(r)$ is the transverse structure of the nonlinear contribution to the refractive index of the

gas inside the HCF, also calculated at ω_0. In this case, $k^R(r) = n_L^R(r)\omega_0/c$ represents the propagation constant at the different HCF structures (the core and the cladding), each of them with their own refractive index. Both contributions to the refractive index and k^R and a show radial dependence since we are including the optical linear response of the core and the cladding of the HCF.

The amplitude of the laser beam $A(r, z)$ has initially, at $z = 0$, the radial dependence of a HCF mode, so it can be expressed as $A(r, 0) = F(r)$, $F(r)$ being the modal field distribution, and z is the propagation coordinate. The intensity $|A(r, z)|^2$ has units of W/m² so that the product $n_{NL}(r)|A(r, z)|^2$ is dimensionless. Equation 3.1 is solved numerically using a standard split-step method [Agrawal, 2013]. To understand this method, we write Eq. 3.1 in the form of the two terms that govern the beam propagation, $\hat{L}$ and $\hat{N}$.

$$\frac{\partial A(r,z)}{\partial z} = \hat{L}A(r,z) + \hat{N}(|A^2|, A) \tag{3.2}$$

The linear part of the propagation equation, $\hat{L}$, represents the diffraction and the absorption of the input spatial mode propagating inside the HCF. The nonlinear part, $\hat{N}$, represents the self-focusing process induced by the optical Kerr effect on the propagation [Couairon et al., 2011].

$$\hat{L} = \frac{i}{2k_0(r)}\left(\frac{\partial^2}{\partial r^2} + \frac{1}{r}\frac{\partial}{\partial r} + \left(n^R(r)\right)^2 - k_0(r)\right)^2 - \frac{a(r)}{2} \tag{3.3}$$

$$\hat{N}(|A|^2, A) = i\frac{\omega_0}{c} n_{NL}(r)\,|A(r,z)|^2\,A(r,z) \tag{3.4}$$

With the split-step method we solve Eq. 3.2 in two steps. In the first step, the linear operator $\hat{L}$ is discretized with a finite-difference scheme for the derivatives in z and r. The resulting system of equations is solved using a Crank-Nicolson algorithm [Couairon et al., 2011, Crank and Nicolson, 1947] .

$$\begin{aligned} \frac{\partial A}{\partial z} &= F\left(A, r, z, \frac{\partial A}{\partial r}, \frac{\partial^2 A}{\partial r^2}\right) \\ \frac{\bar{A}_i^{j+1} - A_i^j}{\Delta z} &= \frac{1}{2}\left(F_i^{j+1} + {}^{j}\right) \end{aligned} \tag{3.5}$$

where the i subscript refers to the radial points in the grid and the j superscript refers to the longitudinal points in the propagation direction. The equation for the Crank–Nicolson method is a combination of the forward difference at the point j and the backward difference at point $j + 1$ for the longitudinal coordinate. With this algorithm we solve the unknown envelope at the point $j + 1$, $\bar{A}_i^{j+1}$, only including the linear effects. Discretizing the equation above, we obtain a matrix equation of the form

$$B\bar{A}^{j+1} = CA^j \tag{3.6}$$

where B and C are both tridiagonal matrices. We use Neumann boundary conditions in $r = 0$, $\partial A/\partial r = 0$, and since there is a singularity in $r = 0$, we apply L'Hôpital

$$\lim_{r\to 0}\left(\frac{1}{r}\frac{\partial A}{\partial r}\right)_{r=0} = \frac{\partial^2 A}{\partial r^2} \tag{3.7}$$

We apply Dirichlet boundary conditions at the end of the radial grid, the cladding edge, and to avoid reflections we implemented an absorber at the end of the radial grid. To be sure that the absorber was acting properly, we compared the propagation using the absorber with the propagation in a HCF with a very large cladding to avoid reflections. Thus the matrices B and C are the following

$$B = \begin{bmatrix} 1+4a-a\xi & -4a & 0 & \dots & 0 \\ -a(1-\frac{\Delta r}{2}) & 1+2a-a\xi & -a(1+\frac{\Delta r}{2}) & \dots & 0 \\ \vdots & \vdots & \ddots & \vdots & \vdots \\ 0 & 0 & \dots & -a(1-\frac{\Delta r}{2}) & 1+2a-a\xi \end{bmatrix} \tag{3.8}$$

$$C = \begin{bmatrix} 1-4a+a\xi & 4a & 0 & \dots & 0 \\ a(1\frac{\Delta r}{2}) & 1-2a+a\xi & a(1+\frac{\Delta r}{2}) & \dots & 0 \\ r & \vdots & \ddots & \vdots & \vdots \\ 0 & 0 & \dots & a(1-\frac{\Delta r}{2}) & 1-2a+a\xi \end{bmatrix} \tag{3.9}$$

where $a = i\Delta z/4k_0\Delta r^2$ and $\xi = \Delta r^2((k^R)^2 - k^2)_0$ Δz and Δr being the longitudinal and radial step sizes, respectively. We use a uniform grid for both coordinates, with transversal and longitudinal step sizes. Since the Crank-Nicolson method is unconditionally stable but not always converges to the correct solution, different step-sizes have to be implemented to find the final solution.

In the second step, the nonlinearity acts individually and it is solved as an exponential operator $\exp(\Delta z\hat{N})$, which means introducing an intensity-dependent phase factor $i\gamma|A|^2$, γ being the nonlinear parameter defined as $\gamma = \frac{\omega_0}{c} n_{NL}$

$$\begin{aligned} \frac{\partial A}{\partial z} &= i\gamma|A^2|A \\ A^{j+1} &= \exp(i\gamma|\bar{A}^{j+1}|^2\Delta z)\bar{A}^{j+1} \end{aligned} \tag{3.10}$$

$\bar{A}^{j+1}$ being the solution obtained when solving linear part with the Crank-Nicolson algorithm. As we have mentioned before, we have implemented an absorbing grid to avoid artificial reflections at the end of the spatial grid. The numerical absorber we use is sufficiently smooth to avoid reflections from the absorber itself. The numerical expression of the absorber is $\cos^{1/8}\frac{|r^0-r|\pi}{2d}$, where r_0 is the point where the absorber begins and d is the length of the absorber [He et al., 2007].

We will use this numerical model in Chapter 4 to study the self-focusing dynamics of a laser beam propagating inside a HCF. The parameters used in the simulation will be specified in Chapter 4 according to the laser beam and the nonlinear medium used in the propagation.

3.2 The Time-Dependent Model (2+1)D

Since HCFs are multimode systems, it is not surprising that their multimode nature could be relevant to fully understand the pulse dynamics during the propagation inside the HCF. In the (1+1)D model presented in Section 3.1 we model the diffraction solving the transverse Laplacian, so we do not take into account the full dynamics of the different spatial modes. However, if the pulse intensity is sufficiently high, the nonlinear propagation through the HCF induces an important energy transfer between different spatial modes [Homoelle and Gaeta, 2000]. In addition, considering the short pulse duration of the laser beams, the dispersion and nonlinear temporal effects could also play an important role in the propagation. For this reason, we use a numerical model that includes the temporal dynamics and instead of solving the radial effects directly, it decomposes the electric field into the spatial modes considering only the spatial structure in the core of the HCF. Since these are leaky modes, the propagation losses of each mode are also included in the model.

To observe the influence of the temporal effects and the role of the spatial modes, we use a more complete description of the pulse propagation using a time-dependent model ((2+1)D model) that includes the spatial and temporal dynamics of the pulse. We refer to this model as (2+1)D model, meaning two dimensions, the radial r and the temporal T dimensions, plus the propagation dimension z. We assume linear polarization so the envelope is a scalar quantity $A(r, T, z)$. Considering cylindrical symmetry again, the propagation equation for the temporal envelope of the pulse, $A(r, T, z)$, is the one obtained in Eq. 2.52, where we include the spatio-temporal dynamics and the effects related to the ionization of the medium.

$$\frac{\partial}{\partial z} - \frac{i}{2k_0}\nabla_T^2\left(1 + \frac{i}{\omega_0}\frac{\partial}{\partial T}\right)^{-1} - iD + \frac{a}{2}\Big] A(r, T, z) = N(|A|^2, A, \rho) \tag{3.11}$$

where $\nabla_T^2 = \frac{\partial^2}{\partial r^2} + \frac{1}{r}\frac{\partial}{\partial r}$, $k_0 = n\,\omega_0/c$ and n is the linear refractive index at ω_0 the central frequency. The linear n_L and nonlinear n_{NL} refractive indices will also depend on the gas pressure. We have included the losses of each spatial mode propagating inside the HCF though the absorption coefficient $a = 2\alpha_{pq}$ defined in Eq. 2.67. Now n_L and n_{NL}, the linear and nonlinear refractive indices of the gas filling the HCF, do not show

radial dependence as in the previous model in Section 3.1, since we are simulating only the core of the HCF. Once more, we write Eq. 3.11 in the form of the two terms that govern the beam propagation, $\hat{L}$ and $\hat{N}$.

$$\frac{\partial A(r, T, z)}{\partial z} = \hat{L}A(r, T, z) + \hat{N}(|A^2|, A, \rho) \tag{3.12}$$

where $A(r, T, z)$ can be expressed initially as $A(r, T, 0) = F(r)e^{-T^2/(T_0)^2}$, $F(r)$ being the initial modal field distribution. Equation 3.12 is solved again with a split-step method. This model was developed by the "Aplicaciones del Laser y Fotónica" research group and it is described in detail in reference [Conejero Jarque et al., 2018]. In this case, the linear part is solved decomposing the input pulse in the family of spatial modes of the HCF, and the nonlinear part is solved by means of a fourth-order Runge-Kutta algorithm [Press et al., 2007] in the time domain. The nonlinear operator includes self-focusing, self-phase modulation, self-steepening, Raman, ionization and the losses due to the ionization process and plasma absorption. The model uses a finite number of modes, N, for the modal decomposition, usually thirty, which are enough to model the beam dynamics (in all our simulations, we have checked that the energy transferred to the highest modes is almost negligible).

To solve the linear part we start from the premise that we already know the pulse envelope $A(r, T, z)$ in a certain point but our goal is to obtain $A(r, T, z + \Delta z)$. The envelope can always be expressed as the combination of different spatial modes in the Fourier domain

$$A(r, \omega, z) = \sum_{q=1}^{N} c_q(\omega, z)F_q(r) \tag{3.13}$$

where $A(r, \omega, z)$ represents the Fourier Transform of $A(r, T, z)$ and $F_q(r)$ is the family of p-spatial modes propagating inside the HCF (the modes TE_{0q}, TM_{0q} and EH_{pq} with $q = 1, 2, 3...$). The coefficients of the decomposition, c_q, are calculated by doing the inverse Hankel Transform of the spatial beam distribution in the core of the HCF [Guizar-Sicairos and Gutiérrez-Vega, 2004].

$$c_q(\omega, z) = \frac{1}{r_F^2 J_p^2(u_{(p-1)q})} \int_0^{r_F} A(r, \omega, z)J_{(p-1)}\left(u_{(p-1)q}\frac{r}{r_F}\right) rdr \tag{3.14}$$

where r_F is the core radius and u_{pq} are the q^{th}-zeros of the J_p Bessel function of the first kind of order p. When dealing with hybrid modes, we will be using the family of spatial modes with $p = 1$, while when studying the nonlinear propagation of TE- or TM-modes, we will use the family of the spatial modes with $p = 2$.

In the first part of the Eq. 3.12, the operator $\hat{L}$, represents the linear propagation effects: diffraction, absorption and also dispersion, that we solve using the propagation

and absorption coefficients of each mode, $\beta_{pq}(\omega)$ and $a_{pq}(\omega)$ in the frequency domain as defined in Eq. 2.67 [Marcatili and Schmeltzer, 1964].

$$A(r, \omega, z + \Delta z) = \sum_{q=1}^{N} c_q(\omega, z) F_q(r) exp(i(\beta(\omega)_{pq} + ia(\omega)_{pq})\Delta z)) \tag{3.15}$$

In this case, the spatio-temporal coupling is included in the propagation constant of each mode β_{pq}, as a correction to the dispersion relation $k(\omega)$ in free space [Rothenberg, 1992].

The nonlinear part, $\hat{N}$, not only includes self-focusing but also self-phase modulation, self-steepening, Raman, the ionization and all the losses related to that process.

$$\hat{N} = (\hat{N}_{Kerr} + \hat{N}_{ioniz} + \hat{N}_{abs}) \tag{3.16}$$

The analytical expression that we use for each term is standard and can be found in Eqs. 2.54-2.56 [Couairon and Mysyrowicz, 2007]. Equation 3.16 is solved simultaneously with the evolution of the density of electrons $\frac{\partial \rho}{\partial t} = W(|A|^2)(\rho_{at} - \rho)$. To solve the nonlinear operator, we use a fourth-order Runge-Kutta algorithm in the time domain. The evolution of the free-electron density is also solved with a fourth-order Runge-Kutta method, using the rates obtained from the PPT model [Couairon and Mysyrowicz, 2007, Perelomov et al., 1966].

We will use this numerical model in Chapter 4 to study the influence of the temporal effects and the multimode nature in the self-focusing dynamics of a laser pulse inside a HCF. In Chapter 5 we will study the nonlinear propagation of vector beams inside the HCF and in Chapter 7 we will study the dispersive wave generation also with this model. The parameters used in the simulations will be specified in each chapter according to the laser pulse and the nonlinear medium used in the propagation.

3.3 The Non-Cylindrical Symmetry Model (3+1)D

In this work we also study the nonlinear propagation dynamics of laser beams without cylindrical symmetry, such as necklace beams, through gas-filled HCF. For this reason, we need to modify the previous models to include the azimuthal dependence in the spatio-temporal dynamics. We have developed a (3+1)D model, three dimensions that include the two transverse dimensions (radial r and azimuthal θ) and the temporal dimension T, plus the propagation dimension z. We assume linear polarization so the envelope is a scalar quantity $A(r, \theta, T, z)$. The propagation equation for the envelope of the pulse in cylindrical coordinates, $A(r, \theta, T, z)$, is again Eq. 2.52 but including now

the azimuthal coordinate:

$$\frac{\partial}{\partial z} - \frac{i}{2k_0}\nabla_T^2\left(1 + \frac{i}{\omega_0}\frac{\partial}{\partial T}\right)^{-1} - iD + \frac{a}{2}\Big] A(r, \theta, T, z) = N(|A|^2, A, \rho) \tag{3.17}$$

where $\nabla_T^2 = \frac{\partial^2}{\partial r^2} + \frac{1}{r}\frac{\partial}{\partial r} + \frac{1}{r^2}\frac{\partial^2}{\partial \theta^2}$As the previous models, this equation is also solved with a split-step method.

$$\frac{\partial A(r, \theta, T, z)}{\partial z} = \hat{L}A(r, \theta, T, z) + \hat{N}\left(|A|^2, A, \rho\right) \tag{3.18}$$

where $A(r, \theta, T, z)$ can be expressed initially as $A(r, \theta, T, 0) = F(r, \theta)e^{-T^2/(T_0)^2}$, $F(r, \theta)$ being the modal field distribution. The first term, $\hat{L}$, represents the linear effects, namely the diffraction, the linear losses and the dispersion of the laser beam in the HCF. The expression that we have used for these effects in this case is:

$$\hat{L} = \frac{i}{2k_0}\left(\frac{\partial^2}{\partial r^2} + \frac{1}{r}\frac{\partial}{\partial r} + \frac{1}{r^2}\frac{\partial^2}{\partial \theta^2}\right)\left(1 + \frac{i}{\omega_0}\frac{\partial}{\partial T}\right)^{-1} - \frac{a}{2} + \sum_{m=2}\frac{i^{m+1}}{m!}k_m\frac{\partial^m}{\partial T^m} \tag{3.19}$$

where $k_0 = n_0\omega_0/c$ and n_0 is the linear refractive index at ω_0, $a = 2a_{pq}$ is the absorption coefficient of the input spatial mode obtained from [Marcatili and Schmeltzer, 1964] and $k_m = (\partial^m k/\partial\omega^m)_\omega$, $k = n_L(\omega)\omega/c$ being the dispersion relation of the gas, where $n_L(\omega)$ is represented by the corresponding Sellmeier equation.

The second term, $\hat{N}$, represents the most significant nonlinear effects, such as self-phase modulation (and self-focusing), self-steepening, Raman, ionization, and the losses due to the ionization process and plasma absorption. The expressions that we have used for these effects are Eqs. 2.54-2.56, the same we use in the (2+1)D model in Section 3.2: $\hat{N} = (\hat{N}_{Kerr} + \hat{N}_{ioniz} + \hat{N}_{abs})$. This model is a 3D extension of the model presented in Ref. [Fibich and Gaeta, 2000] and in the previous sections, enhanced to study the nonlinear propagation of beams without cylindrical symmetry through gas-filled HCFs.

We solved Eq. 3.18 by using a split-step method [Agrawal, 2013]. Although it is possible to perform a mode decomposition for beams without cylindrical symmetry like these ones, it is quite time-consuming since we should consider spatial modes from different families and the coupling between them. Hence, we decided to directly solve the Laplacian operator. We solve the linear part at different steps, the dispersion is solved as an exponential operator evaluated in the Fourier domain using the Fast Fourier Transform (FFT) algorithm [Frigo and Johnson, 2005].

$$A(r, \theta, \omega, z + \Delta z) = exp(\Delta z D(i\omega))A(r, \theta, \omega, z) \tag{3.20}$$

where $D(T) = \sum_{m=2}^{\infty} \frac{i^{m+1}}{m!} k_m \frac{\partial^m}{\partial T^m}$ and $D(i\omega)$ is obtained just replacing the differential operator $\frac{\partial}{\partial T}$ by $-i\omega$. The evaluation of Eq. 3.20 is straightforward and relatively fast using FFT algorithm.

The azimuthal dependence is solved also in the Fourier space, which involves replacing the differential operator $\frac{\partial^2}{\partial \theta^2}$ by $-l^2$, where l is the orbital angular momentum. The diffraction term in Eq. 3.19 is then $\frac{i}{2k_0}\left(\frac{\partial^2}{\partial r^2} + \frac{1}{r}\frac{\partial}{\partial r} - \frac{l^2}{r^2}\right)$ and it can be solved now using a Crank-Nicolson algorithm, as in Section 3.1, applied to each spectral component, which allow us to consider also the spatio-temporal coupling effect. The matrix equation has the same form as in Eq. 3.6. Since the azimuthal term presents another singularity at $r = 0$, we avoid this point and start the simulation in $\Delta r/2$. We apply again the Neumann boundary conditions on axis, so $(\partial A/\partial r)_{r=0} = 0$. In this (3+1)D model we only simulate the propagation in the core of the HCF assuming that the light is confined inside the core and it does not escape into the cladding, so we apply the Dirichlet boundary condition at the core edge, where $A = 0$ if $r = r_F$. The matrices B and C in this case are the following

$$B = \begin{bmatrix} 1 + a\left(1 + \Delta r^2 \frac{l^2}{r^2} + \frac{\Delta r}{2}\right) & -a\left(1 + \frac{\Delta r}{2}\right) & 0 & \dots & 0 \\ -a\left(1 - \frac{\Delta r}{2}\right) & 1 + 2a + a\Delta r^2 \frac{l^2}{r^2} & -a\left(1 + \frac{\Delta r}{2}\right) & \dots & 0 \\ \vdots & \vdots & \ddots & \dots & \vdots \\ 0 & 0 & \dots & & \end{bmatrix} \tag{3.21}$$

$$C = \begin{bmatrix} 1 - a\left(1 + \Delta r^2 \frac{l^2}{r^2} + \frac{\Delta r}{2}\right) & a\left(1 + \frac{\Delta r}{2}\right) & 0 & \dots & 0 \\ a\left(1 - \frac{\Delta r}{2}\right) & 1 - 2a - a\Delta r^2 \frac{l^2}{r^2} & a\left(1 + \frac{\Delta r}{2}\right) & \dots & 0 \\ \vdots & \ddots & \ddots & \dots & \vdots \\ 0 & 0 & \dots & 0 & 0 \end{bmatrix} \tag{3.22}$$

where $a = i\Delta z/4k_0\Delta r^2$. We have included the angular momentum obtained from the Fourier transform of the azimuthal coordinate in the terms of the diagonal. The terms in the superdiagonal and subdiagonal are identical to the ones in the matrix of the (1+1)D model (see 3.1) except in the first row.

The rest of the terms that appear in Eq. 2.52, included in the nonlinear part, are solved with a fourth-order Runge-Kutta algorithm in the time domain as in the (2+1)D model in Section 3.2.

We will use this numerical model in Chapter 6 to study the nonlinear propagation of structured beams inside the HCF, in particular necklace beams with different number of beads. The parameters used in the simulation will be specified in Chapter 6 according to the laser pulse and the medium used in the propagation.

Chapter 4

Energy Limit in Post-Compression Schemes: Study on Self-Focusing Dynamics

One of the first nonlinear effects that appears when a laser beam propagates through a nonlinear medium is the optical Kerr effect. This effect consists in the dependence of the refractive index on the intensity of the beam, as shown in Eq. 2.24 . The main consequence of this effect, in the spatial domain, is the self-focusing of the beam towards the highest intensity regions, usually its central part [Kelley, 1965].

$$n(r) = n_L + n_{NL} I(r) \tag{4.1}$$

where n_L and n_{NL} are the linear and nonlinear refractive indices, respectively. In most of the media, the nonlinear refractive index, n_{NL}, is positive so the refractive index increases where the intensity of the beam is higher, which means that the medium acts as a positive lens modifying its own propagation due to the nonlinear response of the medium.

The theory of self-focusing was developed in 1965 by Talanov [Talanov, 1965], proposing the nonlinear propagation equation to obtain the numerical results on self-focusing and the concept of the self-focusing distance, which has been usually defined as the distance where a beam will self-focus and collapse at beam axis [Boyd, 2020, Chiao et al., 2009]. Since this initial work, several important contributions and reviews have been made. The self-focusing process is of great importance in a wide variety of contexts such as in the formation of the Townes soliton [Chiao et al., 1964, Moll et al., 2003, Ruiz et al., 2005], in the design of laser resonators to prevent the presence of hot spots (local self-focusing

processes) [Gobbi and Reali, 1984], as a natural limit in the intensity up-scaling of fiber amplifiers [Farrow et al., 2006], as the initial step of the filament formation [Braun et al., 1995], as a limit in some post-compression schemes [Conejero Jarque et al., 2018] or in the material processing context [Lapointe and Kashyap, 2017], where the self-focusing process triggers other higher order nonlinear effects that worsen the output result.

It is well-known from the literature that for input peak powers above a threshold value, called critical power (P_{cr}), the self-focusing dynamics is activated. This fundamental parameter was defined already in the early self-focusing studies [Chiao et al., 1964] and, since then, its definition has been revisited many times due to its dependence with the spatial profile [Fibich and Gaeta, 2000, Fibich and Ilan, 2000], the temporal and non-paraxial dynamics [Fibich and Papanicolaou, 1997, McAllister et al., 1968], the focusing geometry [Cheng et al., 2015], the spatial impurities [Fibich et al., 2005], the influence of the Raman effect [Chen et al., 2013], etcetera. All these dependencies are an indication of the rich and complex interplay between self-focusing and other linear and nonlinear effects, which is the reason why it is still an active research topic.

Another important concept in the study of self-focusing dynamics is the collapse distance (z_c). There are different models and formulas to estimate its value depending on different parameters, such as the beam waist, the input power and the critical power of the medium. In the case of a free propagating beam several similar formulas have been proposed in different studies [Boyd, 2020, Chiao et al., 2009, Fibich and Ilan, 2000, Marburger, 1975].

The self-focusing process in waveguides (optical fibers, photonic crystal fibers and hollow capillary fibers (HCFs)) has been studied theoretically obtaining contradictory results. Tempea and Brabec reported that the critical power in HCFs is substantially higher (5 times) than the critical power in free space [Tempea and Brabec, 1998]. Some years later, Fibich and Gaeta obtained essentially the opposite result, the critical power was slightly lower for the fundamental mode propagating inside the HCF, the EH_{11} mode, than for a free Gaussian beam propagating in bulk media [Fibich and Gaeta, 2000]. Similarly, Farrow and co-workers observed stationary solutions in a fiber amplifier for peak powers below the critical power of a free Gaussian beam, suggesting a decrease of the real critical power in the fiber, although concluded that the critical power in a step-index fiber was nearly the same than in free space [Farrow et al., 2006]. Finally, self-focusing below the critical power of a free Gaussian beam was also observed in photonic crystal fibers [Köttig et al., 2017], suggesting again a different behaviour between a free and a spatially confined propagation [Homoelle and Gaeta, 2000].

In this chapter we will study the self-focusing dynamics of a beam propagating in a HCF, which is the most usual technique to compress laser pulses in the near infrared

down to the few-cycle regime [Nisoli et al., 1996, Silva et al., 2018]. During the post-compression process, a fundamental criterion in controlled pulse propagation in HCFs is that the input peak power should be below the critical power of self-focusing to avoid the coupling between modes and the ionization of the medium, which increases the losses and worsens the beam quality and the output result [Conejero Jarque et al., 2018]. These limitations set an upper limit in the energy scaling. However, there are some strategies to scale up the energy: using HCF with a larger core radius or using longer wavelengths due to the scaling of the critical power with the wavelength, although the ionization threshold is lower.

We will try to gain some insight into this problem comparing the self-focusing dynamics of free beams and beams propagating in a HCF using two different theoretical models of the nonlinear propagation equation, the (1+1)D and the (2+1)D models explained in Chapter 3. We will see with both numerical models that the collapse distance z_c of the fundamental mode inside the HCF, EH_{11}, is remarkably different than in free space due to the influence of the spatial confinement of the HCF, specially for peak powers slightly higher than the critical power of the fundamental mode of the HCF.

Moreover, the (2+1)D model that includes the temporal dynamics, shows that the spatial collapse can appear also for pulses with peak power below the critical power P_{cr}, the temporal pulse evolution and the interference between different spatial modes in the HCF being the two main ingredients of this complex propagation. We also study the dependence of the self-focusing dynamics with different parameters, such as the HCF radius, the pulse duration, the laser wavelength or the gas pressure. In the last part of this chapter we discuss how the self-focusing dynamics, accompanied by other higher order nonlinear terms, would manifest in a real experiment, demonstrating that pure self-focusing studies help to identify the energy limit of the HCF post-compression scheme.

4.1 Spatial Collapse: Critical Power and Collapse Criterion

It is well-known from the literature that self-focusing sets an upper limit on the beam power that can be propagated through a Kerr medium. For powers above a threshold value, called critical power, self-focusing overcomes diffraction during the propagation and the beam undergoes spatial collapse [Kelley, 1965, Marburger, 1975] with the peak intensity reaching high values that can damage or ionize the medium. Among the different expression for the critical power, in this work we use the following definition as

a reference [Fibich and Gaeta, 2000]

$$P_{cr} = N_{cr}\frac{\lambda_0^2}{4\pi n_L n_{NL}} \tag{4.2}$$

where λ_0 is the wavelength in free space and N_{cr} is a constant that depends on the beam shape as $N_{cr} = \int |F(r)|^2 r dr$, $F(r)$ being the spatial beam distribution, which is assumed to have cylindrical symmetry [Fibich and Gaeta, 2000]. In the case of the Townes profile [Chiao et al., 1964], for which diffraction and self-focusing are balanced, this constant is $N_{cr} \approx 1.86225$. Beams with another spatial profile undergo collapse when their peak power exceeds a threshold usually larger than the critical power for the Townes soliton. In the case of a Gaussian beam propagating in bulk media, the critical power is slightly higher ($N_{cr} = 1.8962$). However, in the case of the fundamental mode propagating in the HCF, the EH_{11} mode, the critical power is the same as the critical power for the Townes profile ($N_{cr} = 1.86225$) [Fibich and Gaeta, 2000]. The reason for this behaviour is that the spatial confinement of the HCF prevents the shedding of energy towards the cladding, keeping it confined in the core. We will use this value of the critical power of the fundamental mode EH_{11} in the HCF as a reference in this work.

There are different theoretical models that propose an expression for the collapse distance z_c of free propagating Gaussian beams when the input peak power is above the critical power. According to the theory, collapse occurs when the beam intensity becomes infinity at a certain distance and the whole beam shrinks to a single point. Here we briefly summarize the most usual models for the collapse distance:

• In the case of Marburger's model, the collapse distance for a Gaussian beam propagating in free space is described by a semi-empirical formula [Dawes and Marburger, 1969, Marburger, 1975]

$$z_c = \frac{0.367 z_R}{\sqrt{(P_{in}/P_{cr})^{1/2} - 0.852} - 0.0219} \tag{4.3}$$

where z_R is the diffraction length (or Rayleigh length) of the beam, defined as $z_R = \pi w_0^2/\lambda$, $\lambda = \lambda_0/n_L$ being the wavelength in the medium and w_0 the initial beam waist. This expression is valid for Gaussian beams with moderate input powers in purely Kerr media [Couairon and Mysyrowicz, 2007].

• In another model proposed by Chiao et al., they defined a collapse distance taking into account the interplay between the nonlinearity and the diffraction as [Chiao et al., 2009]

$$z_c = \frac{2 z_{NL} z_R}{\sqrt{1 - 2 z_{NL}/z_R}} \tag{4.4}$$

where $z_{NL} = n_L/(kn_{NL}|A_0|^2)$ is the nonlinear distance, $k = n_L(\omega)\omega/c$ and $|A_0|^2$ being the initial pulse intensity. The authors observed that the expression gives a z_c two times larger than the one obtained in the numerical simulations when $z_R \gg z_{NL}$.

• A different approach introduced by Boyd [Boyd, 2020] discerns two expressions for the collapse distance valid at different power regimes.

$$z_c = \frac{2n_L w_0^2}{\lambda_0} \frac{1}{\sqrt{P/P_{cr}}} \quad (P \gg P_{cr}) \tag{4.5}$$

This expression considers only the effect of self-focusing and it is valid when the peak power is considerable higher than the critical power and self-focusing overcomes diffraction.

In the case of lower peak powers, the diffraction effect is not negligible and must be also taken into account. The collapse distance can be expressed as

$$z_c = \frac{2n_L w_0^2}{\lambda_0} \frac{1}{\sqrt{P/P_{cr} - 1}} \quad (P \geq P_{cr}) \tag{4.6}$$

• The last model we present here was proposed by Fibich and Ilan [Fibich and Ilan, 2000] to predict the collapse of a free propagating Gaussian beam, which consists in a correction to the formula presented by Marbuger and Dawes (Eq. 4.3)

$$z_c = 0.634 z_R \left(\frac{P}{P_{cr}} - 1 \right)^{-0.6346} \tag{4.7}$$

One of the main issues when numerically studying the self-focusing process is the collapse criterion, which determines the propagating distance at which the spatial collapse takes place. Looking into the literature, one finds that to identify the self-focusing dynamics and the beam collapse, some authors use the beam spatial width evolution [Farrow et al., 2006, Hesketh et al., 2012] while others use the field amplitude or intensity evolution [Fibich and Gaeta, 2000, Fibich et al., 2005]. This type of field amplitude criterion is not adequate for our problem, as we are dealing with beams propagating inside HCFs, whose spatial modes are intrinsically leaky. The absorption losses inherent to the HCF would affect those spatial collapses occurring at short distances in a different way than those occurring at long distances, although both beams would present similar spatial dynamics and widths. Moreover, the peak intensity depends on the spatial size of the beam, so it provides an idea of the spatial collapse, but it also depends on the temporal dynamics. Our spatio-temporal simulations show important pulse compression dynamics that induces a rise of the peak intensity, as we will see in the following sections. While

the peak intensity mixes the spatial and the temporal dynamics, the spatial width is a purely spatial parameter.

For these reasons we prefer to use a beam width criterion and define the spatial collapse in the numerical simulations when the spatial width, measured as the full width at half maximum (FWHM) from the peak intensity, drops below 0.1 times the initial beam waist. With this collapse criterion we can compare our collapse distances obtained from the simulations with one of the collapse models presented in Eqs. 4.3-4.7 to validate it.

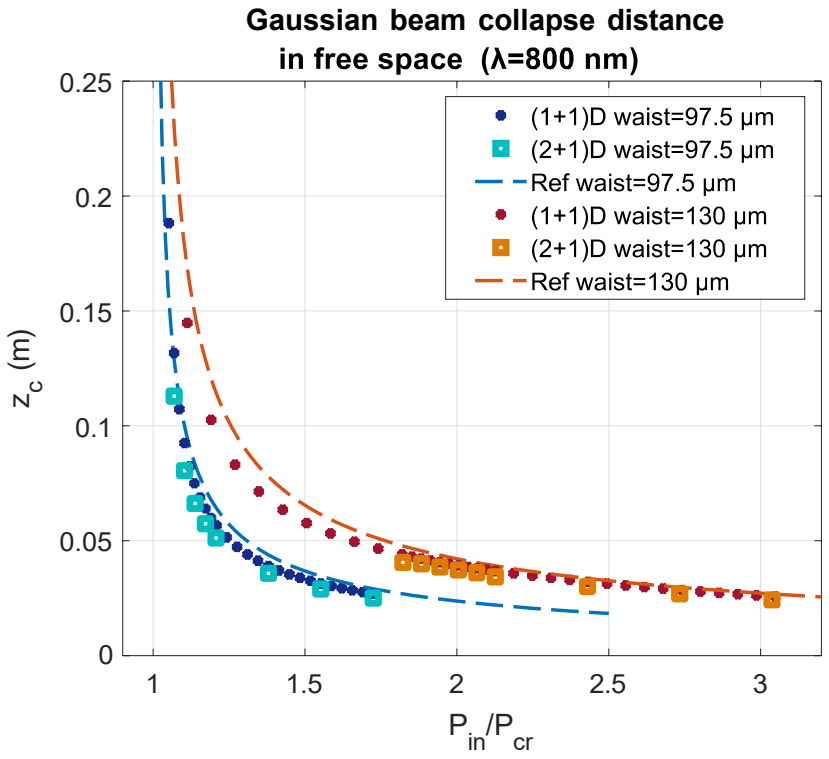

Figure 4.1: Collapse distances (z_c) obtained for a free propagating Gaussian beam with two different initial beam waists (97.5μm and 130μm) using the collapse criterion of 0.1 times of the initial waist. The dots represent the z_c obtained with the (1+1)D model and the square markers are obtained with the (2+1)D model. The dashed lines represent the free-space propagation formula used as a reference (Eq. 4.7) [Fibich and Ilan, 2000].

For this purpose, we have propagated a free Gaussian beam with both numerical models and compared the numerical collapse distances obtained using our collapse criterion, with those predicted by the free-space propagation formula proposed in Eq. 4.7, which is the most precise prediction compared to the numerical simulations. We have plotted the comparison in Fig. 4.1, where the dashed lines represent the free-space propagation formula (Eq. 4.7) used as a reference, and the markers are the numerical collapse distances obtained with both numerical models. The agreement is fairly good, which demonstrates that our collapse criterion is suitable to study the self-focusing dynamics.

A different collapse criterion could change the quantitative results, the collapse distances, but qualitative results, the collapse tendency or dynamics, would remain the same.

4.2 Self-Focusing Dynamics in Hollow Capillary Fibers

To study the collapse process in HCFs we have used two of the numerical models explained in Chapter 3. The first model we use is the time-independent model (1+1)D (Subsection 3.1), which focuses on the spatial dynamics including only the diffraction and the self-focusing effects. It should be noted that this analysis of self-focusing does not represent the actual physics since other nonlinear effects will interplay with self-focusing, but it helps us to isolate and understand the self-focusing dynamics in HCFs, as had been done in previous self-focusing studies [Fibich and Gaeta, 2000, Kelley, 1965].

As we want to study the self-focusing process in the post-compression context, we need to verify the possible influence of the evolution of the temporal structure of the pulse, which could be relevant for pulses in the femtosecond regime. For this reason, we also use the time-dependent model (2+1)D (Subsection 3.2), which includes the complete spatio-temporal dynamics of a laser pulse propagating in a HCF. This second model includes the diffraction and self-focusing effects together with the dispersion, self-phase modulation and self-steepening, but we do not include the ionization, in order to be able to compare these results with those obtained with the (1+1)D model.

In a real experiment, self-focusing should be avoided because it leads to the ionization of the medium. The plasma causes a reduction of the refractive index that defocuses the beam and prevents beam collapse [Chiao et al., 1964]. In the last part of this chapter, we will add the ionization of the medium to the (2+1)D model to see how self-focusing affects the general dynamics in a more realistic way.

4.2.1 The Time-Independent Model ((1+1)D Model)

To understand how the self-focusing dynamics is affected by the spatial confinement induced by the HCF, we have simulated the nonlinear propagation of the fundamental spatial mode of a HCF, the EH_{11} mode, with the (1+1)D model. The initial condition used to solve numerically Eq. 3.2 (see Subsection 3.1) is

$$A(r, z=0) \propto \begin{array}{ll} J_0\left(u_{11} r / r_F\right) & r \leq r_F \\ 0 & r > r_F \end{array}, \tag{4.8}$$

u_{11} being the first zero of the Bessel J_0 function and r_F the HCF core radius. We simulate the propagation of the EH_{11} hybrid mode centered at 800 nm in a HCF with core radius r_F and filled with argon at 1 bar, so $n_L = 1.0003$ [Zhang et al., 2008] and $n_{NL} = 1.74 \cdot 10^{-23}$ (m²/W) in the core [Couairon et al., 2008], and $n_L = 1.4533$ [Malitson, 1965] and $n_{NL} = 3.2 \cdot 10^{-20}$ (m²/W) in the fused silica cladding [Boyd, 2020].

Using the collapse criterion already defined, we will compare the collapse distances obtained numerically from the propagation of the EH_{11} mode inside the HCF, with the free-space collapse distances for a Gaussian beam predicted by the free-space propagation formula in Eq. 4.7 that we use as a reference. To apply this formula we choose the waist of the Gaussian beam that best fits the fundamental mode of the HCF ($w_0 = 0.65 r_F$), its z_R and the critical power corresponding to the EH_{11} mode with $N_{cr} = 1.86225$. Figure 4.2 shows the numerical collapse distances (dots) obtained with the (1+1)D model and the prediction obtained through the free-space propagation formula used as a reference (dashed lines) for different input pulse energies and two HCF core radius (150 µm and 200 µm).

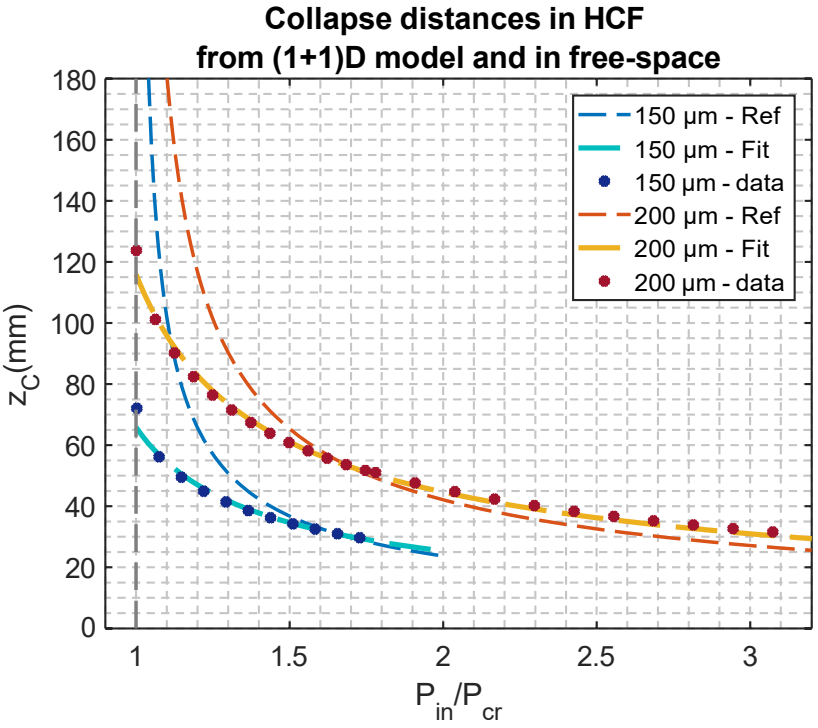

Figure 4.2: Collapse distances (z_c) for the EH_{11} mode at 800 nm as a function of the input peak power and of the core radius of the HCF. Dots represent the z_c obtained from the (1+1)D numerical model for HCFs of 150 µm and 200 µm core radius, solid lines are obtained from the estimation formula (Eq. 4.9) and dashed lines correspond to the prediction from the free-space propagation formula in Eq. 4.7 used as a reference. P_{cr} is the critical power for the fundamental mode of the HCF as defined in 4.2

From the observation of Fig. 4.2 we arrive at two important conclusions: first, we do not observe spatial collapse for peak powers below the critical power, which is consistent with the self-focusing theory [Marburger, 1975]. Second, and maybe the most important observation, the tendency of the collapse distances in the HCF is different from those obtained from the free-space propagation predicted by Eq. 4.7, especially when the input peak power is close to the critical power ($P_{in} \approx P_{cr}$) for the two HCFs. The collapse distances are shorter in the HCF than in free space, which means that the critical power in the HCF should be lower than in free space, in agreement with previous references [Fibich and Gaeta, 2000, Köttig et al., 2017]. Surprisingly, the collapse distances in the HCF disappear abruptly at the critical power, instead of diverging when getting close to this threshold value (P_{cr}) as occurs in the case of free-space propagation. This new behavior can be explained with the reduction of diffraction and the small losses induced by the spatial confinement of the HCF. At moderate input peak powers, diffraction, absorption and self-focusing interact during the propagation in a different manner than in free space. However, at high input peak powers, where the self-focusing term overcomes the absorption and the diffraction during the propagation, the difference between the collapse distances in the HCF and in free space notably reduces. The conclusion obtained from the (1+1)D model is clear: the spatial confinement of the beam limits its diffraction and prevents the shedding of the energy, which favors the self-focusing dynamics during the propagation, specially for peak powers close to the critical power.

Since the free-space propagation formula (Eq. 4.7) does not predict the collapse distances in the case of a propagation inside the HCF, we try to find a new expression. Fitting our numerical results we can obtain a simple formula to predict the collapse inside the HCF:

$$z_c = 0.625 z_R \left(\frac{P_{in}}{P_{cr}} - 0.715 \right)^{-0.6346} \qquad (P \geq P_{cr}) \tag{4.9}$$

P_{cr} and z_R being the critical power and the diffraction length corresponding to the EH_{11} mode with $N_{cr} = 1.86225$. This expression is just a correction of the free-space propagation formula reported by Fibich and Ilan (Eq. 4.7). We have plotted the results obtained from Eq. 4.9 as solid lines in Fig. 4.2 to show the agreement between numerical and analytical results.

4.2.2 The Time-Dependent Model ((2+1)D) Model

A more complete description of the nonlinear pulse propagation dynamics in the HCF is simulated with the time-dependent model, (2+1)D model, that includes spatial and temporal dynamics (Eq. 3.12 of the Subsection 3.2). The temporal effects included in this case are dispersion, self-phase modulation and self-steepening. The Raman response

is not included because the gas filling the HCF is argon, which does not have vibrational response. Since we are studying the spatial nonlinear process, to better identify the collapse dynamics, we have not taken into account the gas ionization inside the HCF, that would inhibit it. Otherwise, it would not be possible to compare the results obtained from the (1+1)D model, which does not include ionization either. In fact, neither the effect of the plasma induced by the pulse nor the losses related to the ionization process or the presence of the plasma are included. This is a standard procedure applied in many previous self-focusing studies to isolate the spatial dynamics [Fibich and Papanicolaou, 1997, Hesketh et al., 2012, Kelley, 1965]. Obviously the self-focusing process will eventually activate ionization in a real scenario, changing the spatio-temporal evolution of the beam. Such an intense nonlinear propagation introduces a very complex spectral phase that makes the output pulse not useful for post-compression and, for this reason, we are interested in the regime where the beam is approaching the blow up instead of in the blow up itself [Hesketh et al., 2012].

In this case we simulate the propagation of the EH_{11} mode, centered at 800 nm, coupled to a HCF with 150 µm core radius and filled with 1 bar of argon. Since the linear refractive index now presents a dependence with the frequency, we use the expression in Ref. [Zhang et al., 2008].

$$n_L(\omega, p) = 1 + p\left(10^{-8}\left(12236.13 + \frac{1232158.1}{90.7 - 1/\lambda^2}\right)\right). \tag{4.10}$$

where p is the gas pressure in bar and λ is the wavelength in micrometers. The nonlinear refractive index is proportional to the gas pressure ($n_{NL} \cdot p$). This expression presents a resonance at 105 nm. To prevent the divergence of the beam when the pulse spectrum broadens to the ultraviolet, we use a numerical absorber and we use the same value of the linear refractive index for wavelengths smaller than 110 nm. A similar equation is used to calculate the lineal refractive index of the cladding, which in our case is fused silica, [Malitson, 1965]. The losses during the propagation are included in the imaginary part of the complex propagation coefficient, $a_1 q$, as defined in Eq. 2.67.

With the collapse criterion we have chosen, we obtain again the collapse distances with the (2+1)D numerical model for different input pulse durations. In Fig. 4.3, the different markers show the collapse distances obtained numerically for different input pulse durations (triangles for 30 fs, dots for 50 fs and circles for 100 fs), the dashed line represents the formula for free-space propagation that we use as a reference (Eq. 4.7) and we also show our new fit (Eq. 4.9) with a solid line.

The more remarkable observation is that the simulations from the (2+1)D model present collapses when the input peak power is below the critical power. We can distinguish two

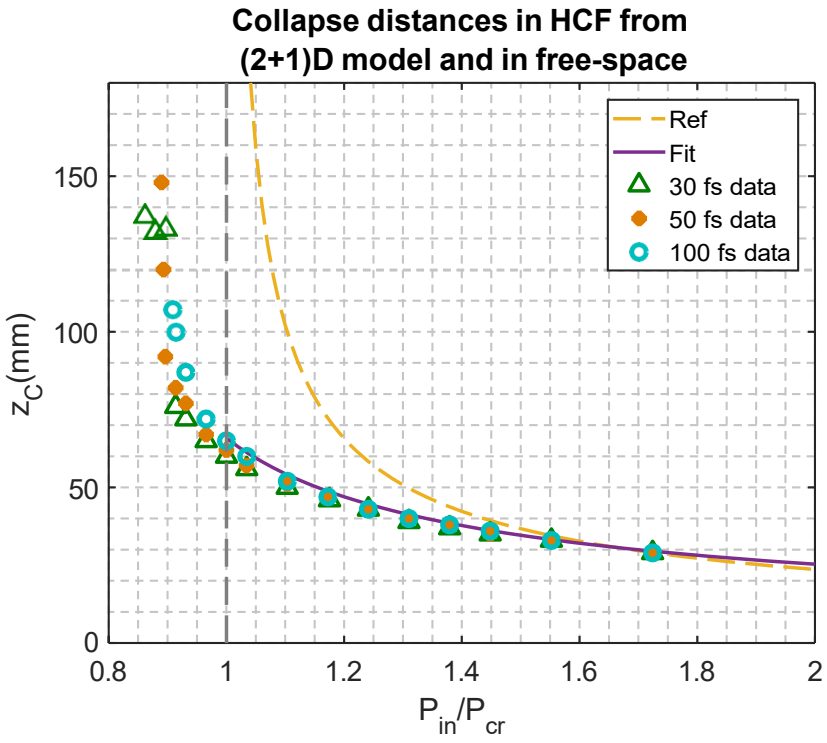

Figure 4.3: Collapse distances (z_c) of the EH_{11} mode at 800 nm as a function of the input power and pulse duration for a HCF with core radius 150μm. Markers represent the z_c obtained from numerical (2+1)D simulations for different laser pulse duration, the dashed line represents the collapse distances predicted by Eq. 4.7 in free space, while the solid line corresponds to the fit obtained from the (1+1)D model (Eq. 4.9).

different regions in Fig. 4.3: the high peak power region ($P_{in} > P_{cr}$) and the new low peak power region ($P_{in} < P_{cr}$), where only the (2+1)D numerical model presents spatial collapses. In the high peak power region, both (1+1)D and (2+1)D numerical models present basically the same collapse tendencies, which demonstrates that for high-power pulses the self-focusing process weakly depends on the input pulse duration. For these cases self-focusing overcomes diffraction, absorption, and also all the temporal effects, dominating the propagation of the beam. All the collapse distances in this regime are well described by the (1+1)D model represented by the estimation formula Eq. 4.9.

4.2.2.1 Role of the Spatial Modes in the Self-Focusing Dynamics: a Multimode Self-Compression

The collapse dynamics observed in the low peak power region in Fig. 4.3 is much more rich and complex than in the high peak power region. First, we should recall that there are already several references that present self-focusing for peak powers below the critical value [Farrow et al., 2006, Hesketh et al., 2012, Köttig et al., 2017], all of them related with multimode guiding systems.

Hollow capillary fibers are also multimode systems and it is not surprising that their multimode nature could be relevant to understand the self-focusing dynamics observed in the simulations, which is the interpretation given by Brabec and Krausz [Brabec and Krausz, 1997]. Although we assume that at the HCF entrance the beam is purely coupled into the fundamental mode, the EH_{11} hybrid mode, self-focusing induces an important energy transfer from the fundamental mode towards higher-order spatial hybrid modes of the type EH_{1q}, since the field is linearly polarized and keeps always the cylindrical symmetry [Homoelle and Gaeta, 2000, Nurhuda et al., 2006]. These higher-order spatial modes, besides activating the self-focusing process due to their narrower spatial distribution (see Fig. 2.10), might present an anomalous dispersion response, which means that they could temporally self-compress. To understand the rich spatio-temporal dynamics that one could expect from this (2+1)D model, we present in Table 4.1 the values of the group velocity and the group velocity dispersion (GVD) at 800 nm for the first four hybrid spatial modes of a HCF with 150 μm core radius and filled with argon at 1 bar of pressure.

$\lambda = 800$ nm	EH_{11}	EH_{12}	EH_{13}	EH_{14}
v_g (nm/fs)	299.71	299.707	299.702	299.695
GVD (fs²/m)	15.17	-10.02	-55.34	-120.80

Table 4.1: Group velocity and GVD values for the EH_{11} mode and first three excited hybrid modes at 800 nm in a HCF with 150 μm core radius and filled with argon at 1 bar.

Figure 4.4 shows the pulse on-axis temporal intensity distribution of a 30 fs pulse with $P_{in} = 0.93P_{cr}$ at 800 nm (right column) and the on-axis intensity distribution of the first seven spatial modes (EH_{1q}, q from 1 to 7, left column), at three different propagation distances inside the HCF. At the beginning ($z = 0$ mm) only the fundamental mode EH_{11} contributes (Fig. 4.4 top left), but as the pulse propagates through the HCF the self-focusing induces an energy transfer to higher-order spatial modes that mainly occurs in the most intense part of the pulse (Fig. 4.4 middle left, see the initial intensity distribution shown for comparison with a black dashed line). Since the energy transfer between the fundamental and the higher-order modes occurs at the peak intensity, the generated modes are shorter and their spectrum should be broader. It seems like there is a compression effect in the energy transfer process itself. The new generated spatial modes send energy back to the fundamental mode during their propagation, inducing an interference in the fundamental mode (Fig. 4.4 bottom left). At $z = 70$ cm, which is close to the collapse distance (72 mm for this case), almost all the spatial modes contribute in the trailing part of the pulse simultaneously generating a high interference

peak, as can be seen in the evolution of the on-axis temporal intensity distribution of the pulse (Fig. 4.4 bottom right).

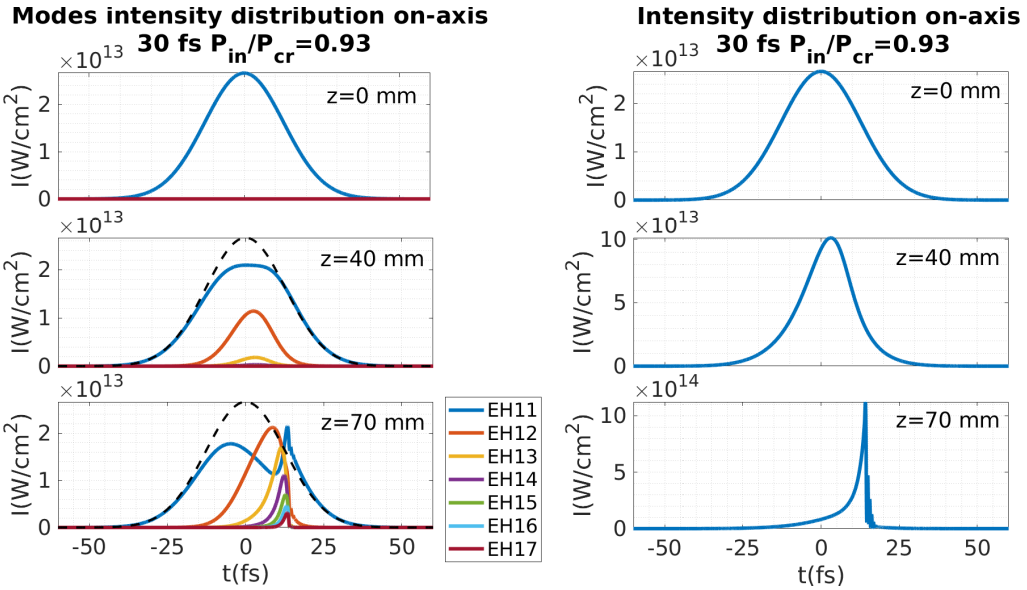

Figure 4.4: Left column shows the on-axis temporal intensity distribution of different spatial modes and right column shows the on-axis temporal intensity distribution of a 30 fs pulse at 800 nm with $P_{in} = 0.93P_{cr}$, propagating in a 150 µm core radius HCF filled with 1 bar of Ar at three propagation distances. The left column includes the intensity distribution of the fundamental mode at z=0 mm with a dashed line for comparison.

Figure 4.4 demonstrates how the particular nonlinear mixture of the different spatial modes distorts the temporal intensity distribution in such a way that it shows an unexpected self-compression process, and a subsequent increase of the peak intensity. Note that the self-compression occurs even when most of the population is in the fundamental mode, which has a normal dispersion response. The key point of this dynamics is the nonlinear energy transfer between the different spatial modes. This self-compression dynamics presents some features of a standard solitonic self-compression [Köttig et al., 2017, López-Zubieta et al., 2018b, Travers et al., 2011], which appears clearly for the higher-order spatial modes and that is translated into the whole pulse through the mode superposition process. The self-compressed pulse has a long front tail, with the peak of the pulse located at the trailing part. Moreover, our simulations indicate the emission of a dispersive wave with the presence of some amplitude oscillations in the trailing part of the pulse (see Ref. [Travers et al., 2011]). This oscillations are a consequence of the interference between the self-compressed pulse and the dispersive wave generated. We will study in detail the generation of dispersive waves in Chapter 7. In our case this interference between the self-compressed pulse and the dispersive wave is clearly visible around $t = 15$ fs as shown in Fig. 4.5. This figure shows a time zoom of the same

temporal structure of the bottom right plot in Fig. 4.4, where we can see the clean interference pattern.

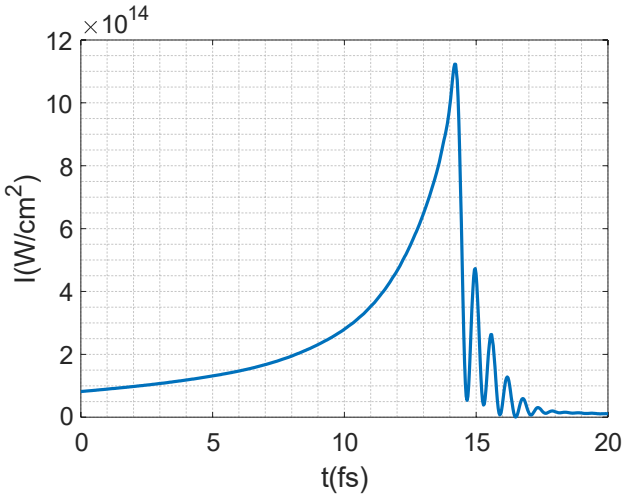

Figure 4.5: We show a zoom of the temporal oscillations in the last graph of the right column of Fig. 4.4, which are a consequence of the interference between the dispersive wave and the self-compressed pulse.

One may wonder how it is possible a compression rather than a pulse stretching since different spatial modes have different group velocities, as shown in Table 4.1. It is true that the different group velocity of each spatial mode could limit the pulse compression, although that effect is clearly not enough for the pulses used in our simulations, as shown in the left column of Fig. 4.4. In that figure one can see how the different modes are delayed in time due to the different group velocities but that delay is not sufficient to avoid the coupling of the different modes in the trailing side of the pulse and its final compression. Moreover, Fig. 4.4 shows that the spatial modes are "locked" in time with each other through the nonlinear coupling, as also observed in Ref. [López-Zubieta et al., 2018a], which reduces the modal stretching of the pulse.

4.2.2.2 Self-Focusing Dynamics in the Low Power and High Power Regimes

In this subsection we will examine if the multimode dynamics and self-compression process explained above is related to the collapses observed in the low peak power region. As shown in Fig. 4.3 the tendency of the collapse distance in the low peak power region is completely different than in the high peak power region. While in the high peak power region we have obtained a quite smooth tendency, increasing the collapse distance continuously when getting close to the critical power, the low peak power region ($P < P_{cr}$) presents a discrete tendency (specially visible for the shortest pulses).

Regarding the spatial dynamics, the presence of higher-order spatial modes also induces oscillations in the beam spatial width, as shown in [Hesketh et al., 2012], that could eventually produce the spatial collapse of the beam when the peak power is moderate. This complex spatio-temporal nonlinear evolution explains the collapses in the low peak power region shown in Fig. 4.3 and the different collapse tendencies depending on the pulse duration.

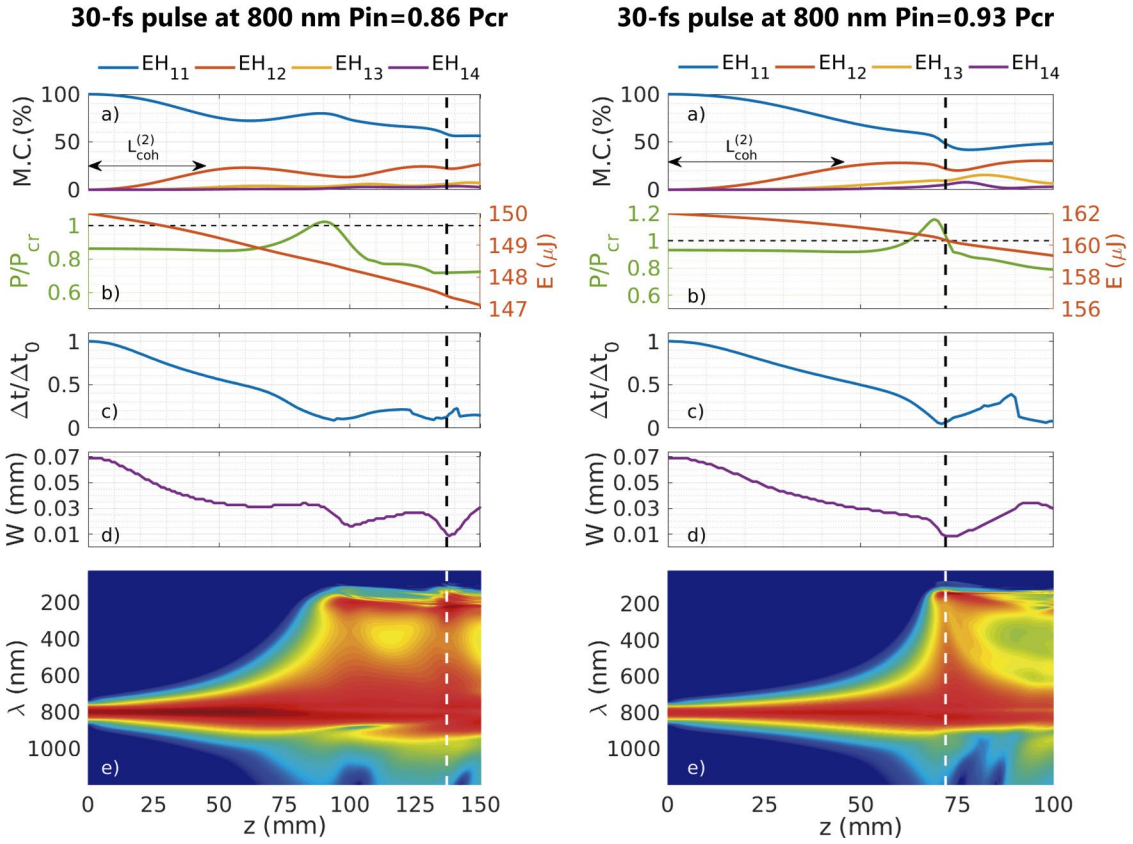

Figure 4.6: Left column corresponds to the propagation of a 30 fs pulse at 800 nm, with 150 μJ input energy and P_{in} = 0.86P_{cr}, propagating in a 150 μm core radius HCF filled with 1 bar of Ar. Right column corresponds to the same propagation but with 162 μJ input energy and P_{in} = 0.93P_{cr}. Each column shows the evolution of the percentage mode contribution (M.C.) of the first four spatial modes (a), the evolution of the peak power and the pulse energy, indicating the P_{cr} with a horizontal dashed line, (b), the evolution of the on-axis pulse duration (c), the evolution of the spatial width (d) and the evolution of the on-axis spectrum (log scale) (e) with the propagation distance. A vertical dashed line indicates the collapse distance, 137 mm (left) and 72 mm (right). The shortest pulse duration obtained would be 2.7 fs (left) and 1.5 fs (right). The coherence length between EH_{11} and EH_{12} is represented by a black arrow. Note the different length of the z-coordinate for each case.

To unveil the origin of these collapse tendencies in the low peak power region we show in Fig. 4.6 a complete set of plots for two different collapses that summarizes the observed phenomenology. Each column of Fig. 4.6 corresponds to the propagation of a 30 fs pulse at 800 nm, with 150 μJ (P_{in} = 0.86P_{cr}, left) and 162 μJ (P_{in} = 0.93P_{cr}, right) of input

energy, propagating in a 150 μm core radius HCF filled with 1 bar of Ar. Each column shows the evolution of the percentage contribution of the first four spatial modes (a), the evolution of the peak power and the pulse energy (b), of the on-axis pulse duration (c), of the spatial width (d) and of the on-axis spectrum (in log scale) (e), with the propagation distance. The vertical dashed lines indicate the collapse distance for each case (137 mm (left), 72 m (right)).

The first important thing to note is that there is an important self-compression, as commented before and shown in Fig. 4.6 (c), which induces an increase of the peak power (shown in Fig. 4.6 (b)). Therefore, although the input peak power is below the critical power P_{cr}, the collapse always occurs after the peak power has surpassed the critical value during the propagation inside the HCF, as one would expect. We have observed in our simulations that the collapse happens if the peak power is above the critical value in a certain position, but the collapse does not occur necessarily at the first self-focus episode of the beam (4.6 left). The self-focusing is an accumulative process, so even though the peak power is above the critical value, if the accumulated nonlinear phase is not high enough, the pulse might self-focus yet not collapsing at that point but at a longer distance.

As pointed out earlier, this process is similar to a solitonic process. The self-compression is accompanied by a dispersive wave generation [Travers et al., 2019] (see Fig. 4.6 (c,e)), that occurs simultaneously with the spatial collapse, as can be seen in Fig. 4.6 (d). The complex nonlinear coupling between the spatial and the temporal dynamics is also corroborated by the evolution of the population of the different spatial modes forming the pulse (see Fig. 4.6 (a)). Another important fact is the oscillatory nature of the spatial collapse (Fig. 4.6 (d)) in contrast with the free-space monotonous catastrophic collapse. This is in agreement with other self-focusing studies in multimode confined media [Hesketh et al., 2012].

Regarding the oscillatory nature of the collapse, it is well-known that the transfer of energy between two spatial modes shows an oscillatory behavior related to a characteristic coherence length, $L_{coh} = \pi/(\beta_{1a} - \beta_{1b})$, where β_{1a} and β_{1b} represent the propagation coefficient of each mode [Tempea and Brabec, 1998]. This coherence length indicates the distance at which the transfer of energy from the first spatial mode towards the second spatial mode is maximum. In our case, the pulse is composed by a mixture of several modes, each of them with its own propagation coefficient, which makes this oscillatory behavior more difficult to identify. Nevertheless, we can use these coherence lengths to remark once more the multimode nature of the self-focusing dynamics in the low peak power region and to estimate the collapse distances.

In the HCF one can define the coherence length between the fundamental, EH_{11} mode, and the higher-order EH_{1q} mode as $L_{coh}^{(q)} = \pi/(\beta^{(11)}(\omega_0) - \beta^{(1q)}(\omega_0))$, where $\beta^{(1q)}(\omega_0)$ represents the propagation coefficient of the qth-spatial mode in the HCF at the central frequency ω_0. At $L_{coh}^{(2)}$, which in the parameters of Figure 4.6 (a) is 45 mm, the energy transferred from the fundamental mode to the EH_{12} mode should be maximum, in the case of pure two-mode system. Figure 4.6 (a) shows that we are not exactly in this pure case because the maximum transfer of energy to the second spatial mode appears at slightly longer distances. So the collapse, if it takes place, should occur between $L_{coh}^{(2)}$ and $2L_{coh}^{(2)}$, where the energy is transferred back to the fundamental mode. This would be the first possible collapse region, that we will show below in Fig. 4.7.

From $L_{coh}^{(2)}$ there are two possible scenarios depending on the input peak power: one scenario in which the self-focusing dominates the evolution before reaching $2L_{coh}^{(2)}$, and the spatial collapse takes place between $L_{coh}^{(2)}$ and $2L_{coh}^{(2)}$ (between 45 and 90 mm), the first possible collapse region. This spatial collapse, shown in Fig. 4.6 (right), is accompanied by an important self-compression process and the subsequent generation of a dispersive wave at a wavelength around 140 nm, all these effects occurring almost simultaneously. In the other scenario, the self-focusing process is arrested by other terms (diffraction, absorption and dispersion), as occurs in Fig. 4.6 (left). In this case the pulse reaches $2L_{coh}^{(2)}$, where the energy transferred to the second spatial mode is returned back to the fundamental and, therefore, the spatial collapse cannot occur yet, but in the next possible collapse region.

The second scenario commented above, which does not show a spatial collapse between $L_{coh}^{(2)}$ and $2L_{coh}^{(2)}$, could undergo collapse in a second coherence cycle when the energy is transferred again from the fundamental mode to the second spatial mode. This second collapse process should occur between $3L_{coh}^{(2)}$ and $4L_{coh}^{(2)}$ (135 mm and 180 mm). Although the case represented in Fig. 4.6 (left) undergoes collapse at 137 mm, it is clear that it reaches the spatial collapse in a second coherence cycle and the collapse is linked again to a second dispersive wave generation process. The evolution of the contribution of the different spatial modes indicates that the collapse distance does not correspond well with the estimation obtained from the coherence length $L_{coh}^{(2)}$. We should define the second collapse region in a more complex way.

To understand the collapses at longer distances and to obtain a better estimation, we have to take into account not only the second mode, but also the third mode EH_{13}. In that case, following the same reasoning used before, one estimates that the pulse would have a second chance to collapse between $2L_{coh}^{(2)} + (L_{coh}^{(2)} + L_{coh}^{(3)})/2$ and $2L_{coh}^{(2)} + (L_{coh}^{(2)} + L_{coh}^{(3)})$, which in our case is between the propagation distances 121 and 152 mm, which is the second possible collapse region as observed in Fig. 4.6 (left). This oscillatory dynamics,

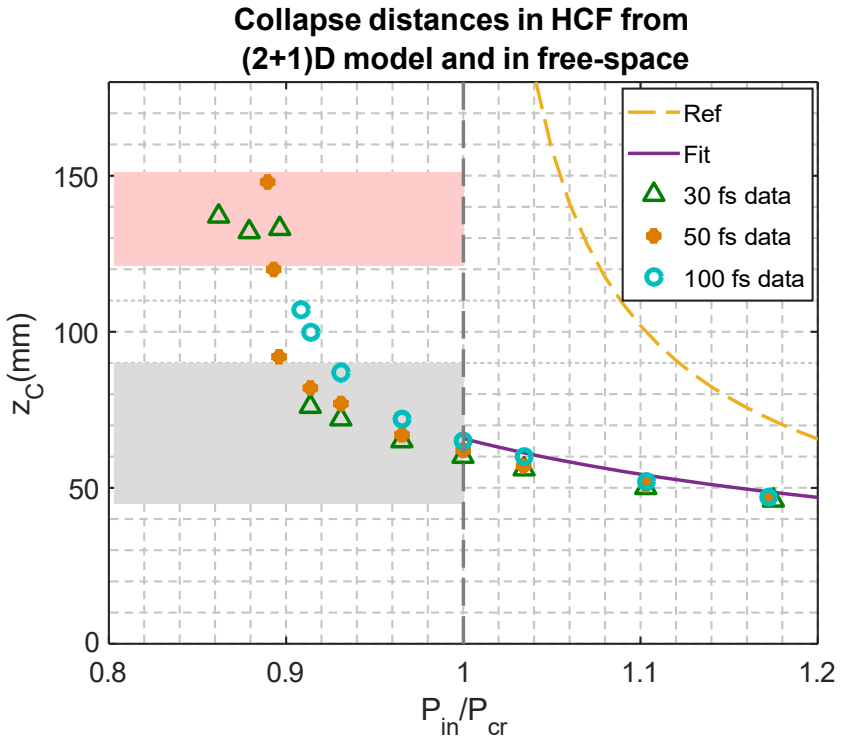

Figure 4.7: Collapse distances (z_c) of the EH_{11} mode at 800 nm in the low peak power region for a HCF with core radius 150μm. Markers represent the z_c obtained from numerical (2+1)D simulations for different laser pulse duration. The shadowed rectangles represent the two first possible collapse regions as described in the text.

related to the periodic energy transfer between the different spatial modes, demonstrates the multimode nature of the self-focusing process and is the reason why we observe discrete collapse distance regions.

To better visualize this discrete collapse behavior we have indicated in Fig. 4.7 these two regions in which the spatial collapse could take place. These regions are related to the energy transfer and the coherent lengths between the fundamental mode EH_{11} and the higher-order spatial modes. The grey shadowed rectangle is defined as the first possible collapse region, resulting from the interplay between the first two spatial modes, and it goes from $L^{(2)}_{coh}$ to $2L^{(2)}_{coh}$ (from 45 mm to 90 mm). The pink shadowed rectangle is defined as the second possible collapse region, considering the interplay between the first three spatial modes, and it goes from $2L^{(2)}_{coh} + (L^{(2)}_{coh} + L^{(3)}_{coh})/2$ to $2L^{(2)}_{coh} + (L^{(2)}_{coh} + L^{(3)}_{coh})$ and corresponds to the collapse distances between 121 mm and 152 mm. Although the spatial beam collapse is driven by more than three spatial modes, these regions estimate quite well the collapse regions, specially for the shortest pulses.

It is clear from Fig. 4.7 that this discrete collapse behaviour is specially significant for short pulses, while the collapse behaviour for longer pulses (100 fs) presents a smoother

collapse tendency. In the following section we will give an explanation of the origin of these differences.

The behaviour in the high peak power region is less rich in the sense that the self-focusing dominates the rest of spatio-temporal effects that are included in the (2+1)D model and the collapse dynamics is clean, with no oscillatory behaviour. We have observed in the high peak power region, for all the different pulse durations that we used, a very similar dynamics to that presented in the right column of Fig. 4.6. Indeed, the higher input peak power cases show such a strong self-focusing process, leading to a short collapse distance, and, as a consequence, the shortest pulse duration is a bit longer than those obtained in the low peak power region but always below 3 fs. This is the main difference between the self-focusing dynamics in the low peak power region and in the high peak power region.

One may ask if the appearance of high-order modes during the self-focusing process, especially in the low peak power region, would affect the total beam spatial profile in the far field and if it will be very different from the high peak power region.

For this reason we show in Fig. 4.8 the time integrated far field of the beam at the collapse distance at two different power regimes, one from the low peak power region and another from the high peak power region in log scale (top row) and in linear scale (bottom row). Figure 4.8 (left) corresponds to the far field of a 30 fs pulse with input energy 162 μJ input energy and $P_{in} = 0.93P_{cr}$. In this case, at the collapse distance (72 mm) the modes contribution of the first four spatial modes is the following: 48.17% of EH_{11}, 21.94% of EH_{12}, 9.52% of EH_{13} and 5.18% of EH_{14}. Figure 4.8 (right) corresponds to the far field of the same pulse but with input energy 270 μJ input energy and $P_{in} = 1.55P_{cr}$. Here, the collapse distance is 33 mm and the modes contribution of the first four spatial modes in this case is: 26.26 % of EH_{11}, 23.76% of EH_{12}, 14.10% of EH_{13} and 9.46% of EH_{14}. Note that the sum of the different modes contribution explicit here is not 100% since we only take into account the first four modes of the thirty we use in the simulations.

As can be observed in Fig. 4.8, the differences between the far field for the two power regimes are very small despite the particular modes contribution in each case, which makes difficult the identification of the self-focusing dynamics by observing directly the far field distributions even with this simplified pure self-focusing model. In the bottom row of Fig. 4.8 we show the far field of the input beam (blue line) for comparison. We can see that the beam at the collapse distance presents slightly larger divergence (orange line).

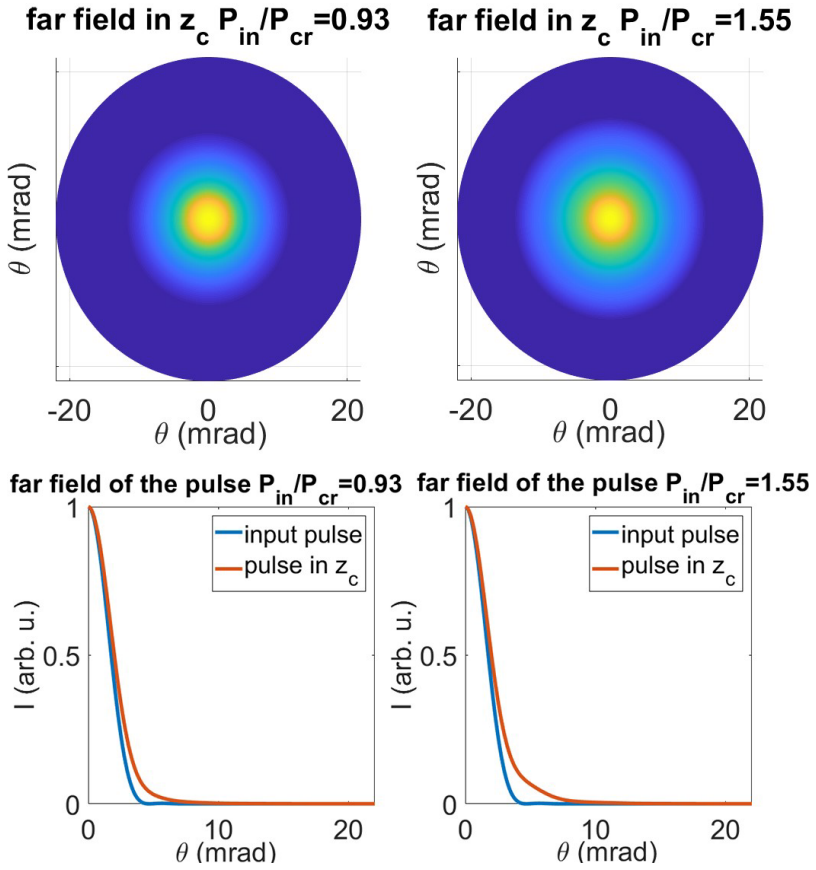

Figure 4.8: Far field of the field at the collapse distance z_C for a 30-fs pulse at 800 nm with $P_{in} = 0.93P_{cr}$ (left column) and with $P_{in} = 1.55P_{cr}$ (right column) in log scale (top row) and in linear scale (bottom row). In the bottom row we show the far field of the input beam for comparison.

4.2.3 Influence of the Parameters of the Input Laser Pulse and the Filling Gas on the Self-Focusing Dynamics

It is interesting to analyze how the properties of the laser pulse, like the pulse duration or central wavelength, and the gas inside the HCF affect the self-focusing dynamics we have presented before.

4.2.3.1 Input Pulse Duration

It is true that the dependence of the collapse distance with the pulse duration in the low peak power region, shown in Fig. 4.7, is not very significant but the dynamics of the collapse process is different. Figure 4.7 shows that for the lowest input peak power cases we observe collapse for the 30-fs pulse but not for the 100-fs pulse. The key point to understand this difference is that self-steepening is very active for shorter pulses but not for longer pulses, so the shorter pulses suffer more nonlinear interaction.

To see the differences on the nonlinear propagation due to the pulse duration we show in Fig. 4.9 the dynamics of a 100-fs pulse with P_{in}/P_{cr} = 0.93 (left) compared with the same input peak power case for a 30-fs pulse shown in Fig. 4.6 (right). The 100-fs pulse presents very similar dynamics to that shown by the 30-fs pulse, but not in the cases of very low input peak powers. Comparing the evolution of a 30-fs pulse in Fig. 4.9 (right) and a 100-fs pulse in Fig. 4.9 (left), with the same input peak power, we can observe that the main difference here is that the spatial collapse takes place at a longer distance for the 100-fs pulse, but showing very similar spatio-temporal dynamics. The minimal pulse duration we obtain is also similar: 1.9 fs for the 100-fs pulse and 1.5 fs for the 30-fs pulse.

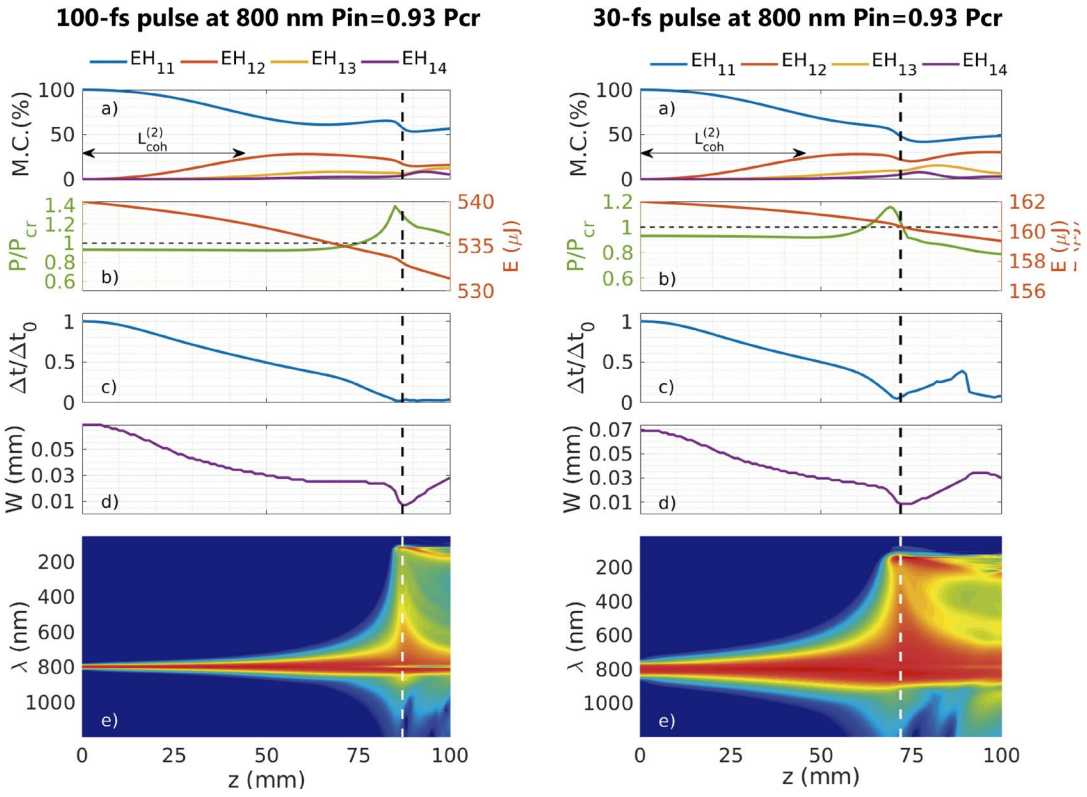

Figure 4.9: Left column corresponds to the propagation of a 100 fs pulse at 800 nm with P_{in} = 0.93P_{cr}, in a 150 μm core radius HCF filled with 1 bar of Ar. Right column corresponds to the propagation of a 30 fs pulse at 800 nm with P_{in} = 0.93P_{cr}, in the same HCF. Each plots shows the evolution of the percentage mode contribution (M.C.) of the first four spatial modes (a), the evolution of the peak power and the pulse energy, indicating the P_{cr} threshold with a horizontal dashed line, (b), the evolution of the on-axis pulse duration (c), the evolution of the spatial width (d) and the evolution of the on-axis spectrum (log scale) (e) with the propagation distance. A vertical dashed line indicates the collapse distance at 87 mm (left) and 72 mm (right). The minimal pulse duration would be 1.9 fs (left) and 1.5 fs (right). Note the different length of the z-coordinate for each case.

As mentioned previously, the self-steepening induces a strong accumulation of the energy at the trailing part of the pulse, increasing the amount of nonlinear effect. Shorter pulses

experience a stronger self-steepening so, the 30-fs pulses take advantage of activating this nonlinear term while the 100-fs pulses are not able to do it. In Fig. 4.10 we show the comparison of the mode population for $P_{in} = 0.93P_{cr}$ for a 30-fs pulse (solid lines) and a 100-fs pulse (dashed lines). Left panel of Fig. 4.10 shows the propagation of both pulses taking into account the self-steepening effect, while in the right panel of Fig. 4.10 the self-steepening effect is neglected for the 30-fs pulse, showing a longer collapse distance. In accordance, we can observe that the energy transfer between the spatial modes when self-steepening is neglected is very similar to the 100-fs pulse modes dynamics.

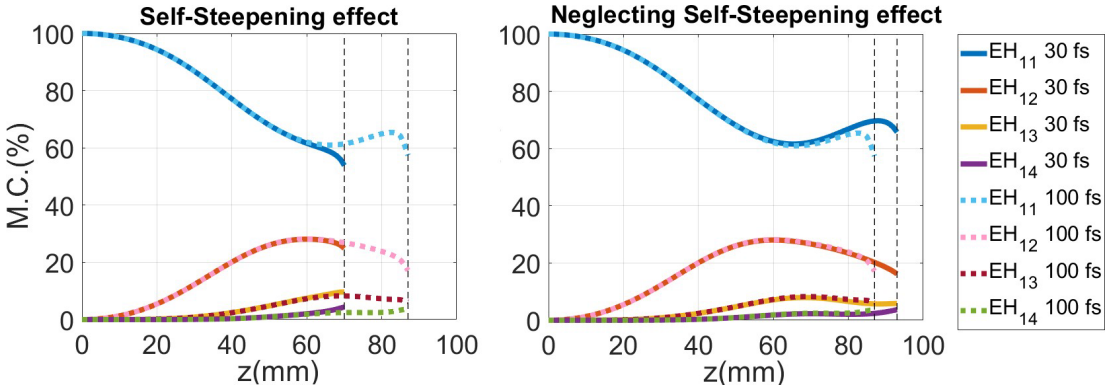

Figure 4.10: Comparison of the mode contribution of the first four spatial modes for a 100-fs pulse and a 30-fs pulse to observe the effect of self-steepening in the self-focusing dynamics (P_{in}/P_{cr} = 0.93 at 1 bar of Ar). We have performed two simulations, including the self-steepening in the simulation of the 30-fs pulse (left) or neglecting it (right). Grey dashed vertical lines indicate the collapse distance in each case.

4.2.3.2 Central Wavelength of the Laser

Another important parameter is the central wavelength of the laser pulse. For instance, ultrashort ytterbium-based laser systems have gained a lot of interest in recent years due to their high average power levels which make them useful in scientific as well as industrial applications, and the compression of Yb-based pulses is a current hot topic in the field (see, for instance, [Beetar et al., 2018, 2019, Jeong et al., 2018, Lavenu et al., 2017, 2018, 2019]). Taking into account that the anomalous dispersion response of the gas increases with the wavelength [López-Zubieta et al., 2018a], as shown in Table 4.2, the fundamental mode at 1030 nm is closer to the zero-dispersion, and the higher-order modes present a larger anomalous dispersion response than in the 800 nm case. Therefore, one expects to observe a stronger self-compression process for the Yb-doped than for the Ti:sapphire laser and, therefore, an earlier spatial collapse.

We have performed simulations for the wavelength of an Yb-doped source, 1030 nm. In particular, we have studied the propagation of a 30 fs laser pulse, centered at 1030 nm,

λ = 1030 nm	EH_{11}	EH_{12}	EH_{13}	EH_{14}
v_g (nm/fs)	299.710	299.706	299.698	299.686
GVD (fs^2/m)	3.40	-50.36	-147.11	-286.79

Table 4.2: Group velocity and GVD values for the fundamental and first three excited modes at 1030 nm in a HCF with 150 µm core radius and filled with argon at 1 bar.

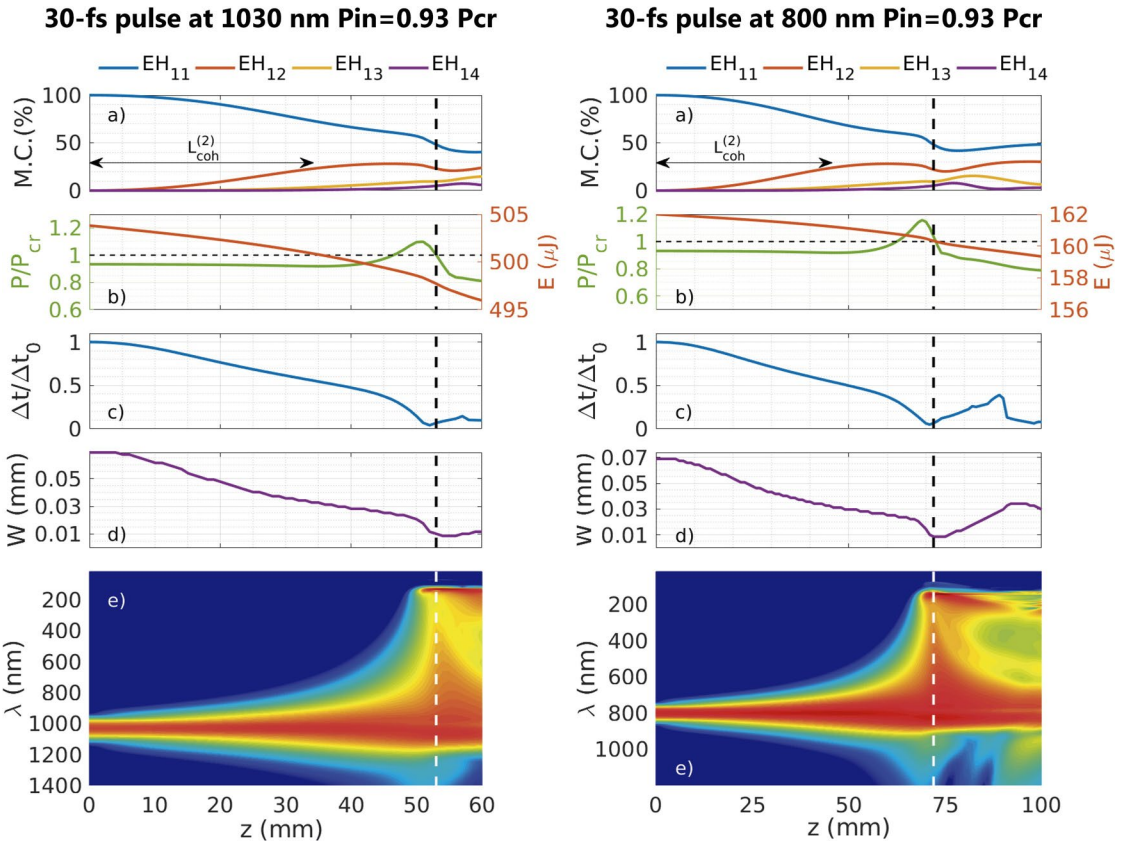

Figure 4.11: Left column corresponds to the propagation of a 30 fs pulse at 1030 nm with P_{in} = 0.93P_{cr}, propagating in a 150 µm core radius HCF filled with 1 bar of Ar. Right column corresponds to the propagation of a 30 fs pulse at 800 nm with P_{in} = 0.93P_{cr}, propagating in the same HCF. Each plot shows the evolution of the percentage mode contribution (M.C.) of the first four spatial modes (a), the evolution of the peak power and the pulse energy, indicating the P_{cr} threshold with a horizontal dashed line, (b), the evolution of the on-axis pulse duration (c), the evolution of the spatial width (d) and the evolution of the on-axis spectrum (log scale) (e) with the propagation distance. A vertical dashed line indicates the collapse distance at 53 mm (left) and 72 mm (right). The minimal pulse duration would be 1.2 fs (left) and 1.5 fs (right). Note the different length of the z-coordinate for each case.

with P_{in}/P_{cr} = 0.93 through a HCF with 150 µm core radius filled with 1 bar of Ar. For the case of the Yb-based pulses we use a $n_{NL} = 0.93 \cdot 10^{23}$ m²/W for the argon in the core given in [Lavenu et al., 2018]. We compare this case at 1030 nm in Fig. 4.11 (left) with the same propagation dynamics of a 30 fs pulse at 800 nm with P_{in}/P_{cr} = 0.93 through the same HCF, Fig. 4.11 (right). The collapse occurs at 53 mm in the 1030 nm case and at 72 mm in the 800 nm case. Except for the collapse distance, that is

shorter in the case of 1030 nm as expected, the general self-focusing dynamics is very similar for both wavelengths. In both cases, although the input peak power is below the critical power, the collapse occurs once the peak power surpasses the critical value. The self-focusing dynamics is also accompanied by the self-compression of the pulse and at the collapse distance a dispersive wave is generated at 136 nm for the 1030 nm case and at 145 nm in the 800 nm case. The black arrows in the first panel represents the coherence length, $L_{coh}^{(2)}$, between the fundamental mode EH_{11} and the EH_{12} mode. In the case of 1030 nm $L_{coh}^{(2)}$ corresponds to 35 mm and in the 800 nm case, $L_{coh}^{(2)}$ is 45 mm.

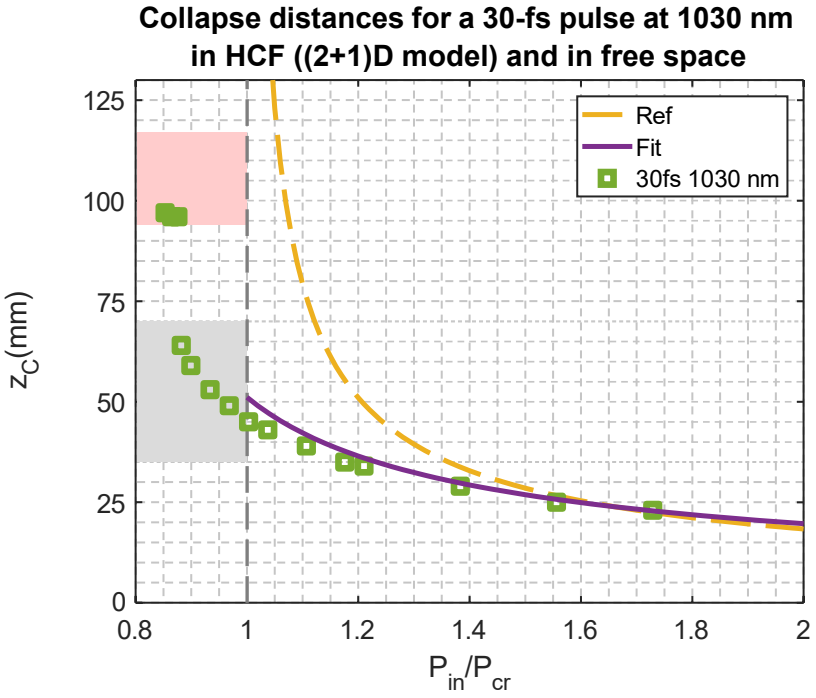

Figure 4.12: Collapse distances (z_c) of the EH_{11} mode as a function of the input power for a HCF with core radius 150µm. The markers represent the z_c obtained from (2+1)D simulations for a 30-fs pulse at 1030 nm, the dashed line shows the collapse distances predicted by the free space formula and the solid line corresponds to the fit obtained from the (1+1)D model (Eq. 4.9). The gray and pink areas represent the collapse regions according to L_{coh}. The gray area goes from 35 to 70 mm and the pink area goes from 94 to 117 mm.

To corroborate this similarity in the collapse dynamics between the 1030 nm and 800 nm, we have done a series of calculations for the Yb-doped fiber laser to see if we find the same collapse distance trend obtained for the Ti:sapphire laser. We have performed simulations with the (2+1)D model for different input peak powers as done in the 800 nm and calculated the collapse distances using the same collapse criterion. In Fig. 4.12 we represent the collapse distances z_c obtained for the 1030 nm case (square markers) and it shows again that the self-focusing dynamics at different central wavelengths are very similar, with almost the same tendency, but at shorter distances. Moreover, our fit equation (Eq. 4.9) obtained for the (1+1)D model at 800 nm, also provides an excellent

agreement only adapting the P_{cr} for 1030 nm (solid line). We have also plotted the gray and pink areas corresponding to the first two possible collapse regions for this situation, as done in the 800 nm case in Fig. 4.7, recovering again a good prediction for the collapse distances. The gray shadowed area represents the first possible collapse region which corresponds to the collapse distances between $L^{(2)}_{coh}$ and $2L^{(2)}_{coh}$ (35 to 70 mm). The pink area represents the second possible collapse region between $2L^{(2)}_{coh} + (L^{(2)}_{coh} + L^{(3)}_{coh})/2$ and $2L^{(2)}_{coh} + (L^{(2)}_{coh} + L^{(3)}_{coh})$, which corresponds to the collapse distances between 94 mm and 117 mm. These results demonstrate the consistency of the dynamics of the spatial collapse in a HCF explained before.

4.2.3.3 Gas Pressure

Gas pressure is another parameter which has an important role in nonlinear propagation in HCFs because it affects both linear dispersion and nonlinear coupling [Conejero Jarque et al., 2018, Jeong et al., 2018]. One of the main advantages of post-compression schemes is that the nonlinearity of the gas can be controlled just changing the pressure of the gas filling the HCF. Varying the pressure, one can obtain the desirable spectral broadening and at the same time avoid reaching the critical power for which self-focusing takes place.

In order to study the possible use of the pressure as a control parameter to locate the collapse at a desired distance, we have performed a pressure scan for a 30 fs Ti:Sa laser pulse with fixed input energy propagating inside a HCF with core radius 150μm filled with argon using the (2+1)D model without ionization. The optimal fiber length should be slightly below the collapse distance, so that the pulse does not collapse but gets close to that point. In order to find the appropriate effective length of the HCF, one typically changes the input pulse energy, the gas type or pressure inside the HCF. Here we perform the pressure scan for two different input energies, 162 μJ and 204 μJ.

The results shown in Fig. 4.13 (left) demonstrate that gas pressure is indeed an excellent parameter to tune the spatial collapse position. As the pressure increases, the nonlinearity also increases and the critical power decreases, so the beam collapses at shorter distances. For gas pressures below 1 bar we do not observe collapse since we enter in the $P_{in} << P_{cr}$ region. At high pressures, the collapse distances for different input energies are almost the same, since the nonlinearity is high and self-focusing overcomes diffraction. At low pressures, the difference between the collapse distances for the two input energies is more significant due to the balance between the self-focusing and the diffraction effects in this regime. The lower pressure together with a lower nonlinearity

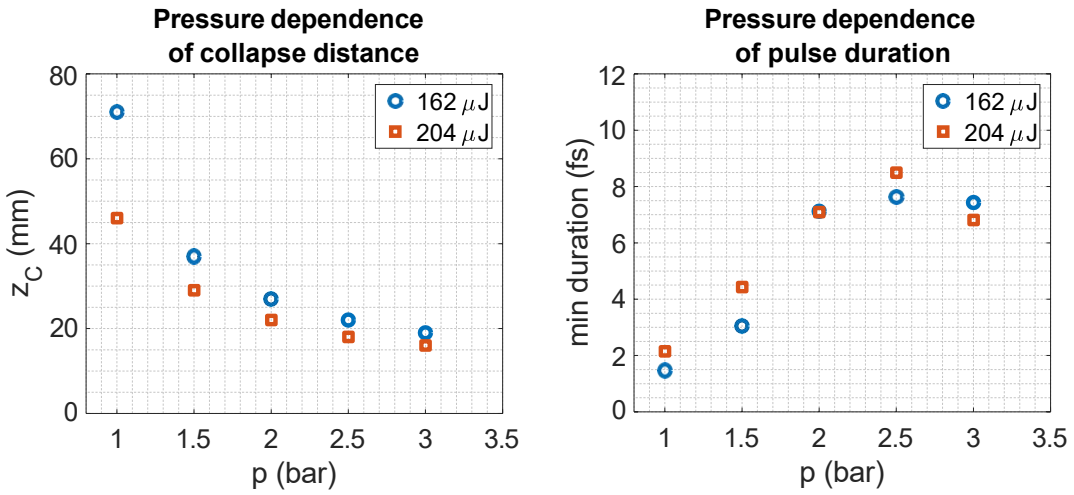

Figure 4.13: This figure shows the collapse distances (left) and minimum pulse duration at this distance inside the HCF (right) for a 30-fs pulse centered at 800 nm with fixed input energy (162 µJ (blue circles) and 204 µJ (orange squares)). Both panels represent the dependence of the collapse distance and pulse duration with the pressure inside the HCF.

leads to longer collapse distances at low input energies, because the nonlinearity needs a longer propagation inside the HCF until it is strong enough for collapse.

Moreover, to have an idea of how the temporal dynamics changes during this pressure scan we show the shortest pulse obtained for each case in Fig. 4.13 (right). One can observe that the lower the pressure, i.e. the lower the nonlinearity, the more necessary is the temporal self-compression effect to achieve the nonlinear spatial collapse. If we increase the pressure, the nonlinearity increases and therefore, the pulse collapses at shorter distances and the minimal pulse duration achieved is longer, since the pulse has undergone less self-compression.

Let us remark that these simulations cannot be directly compared with real experiments because we have not included all the nonlinear effects needed to have a realistic model. The model used in this chapter, so far, is devoted to study the self-focusing process in a HCF, isolated from other spatial nonlinear interactions, and it is not designed to make direct comparisons with experiments. We propose, nevertheless, to use our simplified model to predict the regime where high spatial nonlinear processes, such as the self-focusing and the ionization, would be relevant in a real experiment and the spectral nonlinear phase acquired due to the high spatial nonlinear effects will be observable at the end of a longer HCF.

4.3 The Trace of the Self-Focusing Process in a Real Experiment: the Time-Dependent Model ((2+1)D) including Ionization

All the results presented before in this chapter have been obtained with models which do not include the effects of the generated plasma in the HCF, in order to isolate the spatial dynamics of the self-focusing process. Therefore, one cannot compare directly those results with experiments, where other high nonlinear effects such as the gas ionization eventually prevent the spatial collapse. In this section we will add the gas ionization, the losses due to the ionization process and due to the plasma absorption to the (2+1)D model (see Section 3.2 in Chapter 3) in order to prove that the collapse dynamics shown before is an useful tool to find out the energy limit of a standard HCF post-compression setup.

The parameters used in this new simulation are the same as in the previous ones. Related to the ionization, the critical density ρ_c depending on the central wavelength ω_0, the collision time τ_c, the atomic density ρ_{at} depending on the gas pressure p and the ionization potential U_i are presented in the following table:

ρ_{at}= $2.7 \cdot 10^{19}$ p(bar) cm^{-3}	τ_c=350 fs
ρ_c=$3.14208 \cdot 10^{20}\omega_0^2$ cm^{-3}	U_i=15.76 eV

Table 4.3: Parameters for the ionization of argon, the gas used in the simulations according to [Couairon and Mysyrowicz, 2007]. The critical density ρ_c depends on the central wavelength ω_0 and the atomic density ρ_{at} depends on the gas pressure p.

We propagate a 30-fs pulse centered at 800 nm with $P_{in} = 0.93P_{cr}$ in a 150 µm core radius HCF filled with 1 bar of Ar including ionization. Figure 4.14 shows the complete dynamics, including the ionization effects (left), and the comparison for the same conditions shown but without ionization as in Fig. 4.6 (right). The ionization arrests both the spatial collapse and the self-compression dynamics. It is clear that the beam collapse does not occur for this particular input power, although according to the spatial width, the beam still self-focuses but is not able to achieve the collapse due to the appearance of the plasma (see the peak plasma density shown in Fig. 4.14 (d)). As a consequence of the arrest of the spatial dynamics, the temporal self-compression slows down, and the peak power does not increase as in the pure self-focusing case. Also, the self-phase modulation is much less effective showing a narrower spectral broadening. Although these new simulations bring more nonlinear terms into play, they mutually counteract, making difficult to identify them by simply observing the energy or spatial structure of the output pulse.

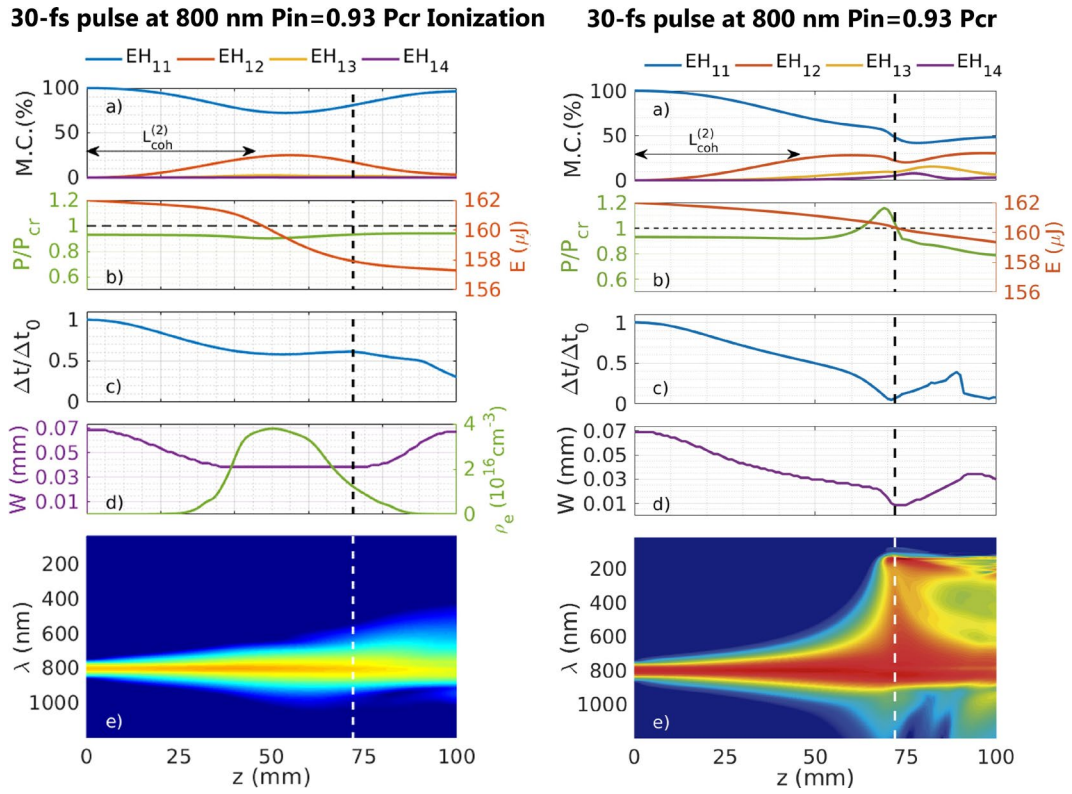

Figure 4.14: Left column corresponds to the propagation of a 30 fs pulse at 800 nm with P_{in} = 0.93P_{cr} including ionization, propagating in a 150 μm core radius HCF filled with 1 bar of Ar. Right column corresponds to the same propagation without ionization. Each plot shows the evolution of the percentage mode contribution (M.C.) of the first four spatial modes (a), the evolution of the peak power and the pulse energy, indicating the P_{cr} threshold with a horizontal dashed line, (b), the evolution of the on-axis pulse duration (c), the evolution of the spatial width and the plasma density if it is the case (d) and the evolution of the on-axis spectrum (log scale) (e) with the propagation distance. A vertical dashed line indicates the collapse distance (72 mm) obtained with the pure self-focusing model (without ionization)

As expected, the results when including the ionization are different, the beam does not collapse according to our criterion, although the self-focusing is the effect responsible for the activation of the ionization and therefore a key nonlinear effect. We do know that the collapse of the beam into a single point cannot be observed in a real experiment due to the ionization of the gas. Therefore, we do not propose nor expect a direct observation of the self-focusing dynamics of the beam inside the HCF. However, nobody could affirm with certainty, according to the beam size, the spectrum or even the energy at the end of the HCF, that the self-focusing was a relevant nonlinear process in the case shown in the right panel of Fig. 4.14. For this reason, the self-focusing is such an invisible effect in complex experiments, and there have been studies during the last fifty years to understand it, studying it isolated from other effects. We propose that if our self-focusing simulations indicate that the beam collapses in the HCF, a real experiment will show the self-focusing dynamics in an indirect way.

The best way to realize that this propagation presents strong nonlinear dynamics is through the complex nonlinear phase of the pulse acquired when the self-focusing triggers other high nonlinear processes such as ionization during the propagation in the HCF. For example, one could use the d-scan [Miranda et al., 2012], which is a technique to compress and perform a complete measurement of the pulse, including the phase information. It is well-known that the d-scan trace is a perfect tool to optimize a standard HCF post-compression setup [Conejero Jarque et al., 2018].

To achieve the optimum stable and shortest output pulse the d-scan trace must present a long, flat and smooth structure, in many cases slightly tilted due to the third order dispersion acquired during the nonlinear propagation. Figure 4.15 shows different d-scan traces of the output field of a 30-fs pulse at 800 nm with an initial EH_{11} mode spatial structure, after the propagation inside a 200 mm long and 150 μm core radius HCF filled with 1 bar of argon for three different input powers. Despite Fig. 4.14 (left) shows the propagation dynamics with the ionization during 100 mm inside the HCF for a better comparison with the no ionization case (Fig. 4.14 (right)), it is clear from the FWHM evolution (Fig. 4.14 (c left)) that the self-compression process has not achieved the optimal minimum pulse duration at this distance compared to the case without ionization. For this reason, we obtain the d-scan trace at a longer distance inside the HCF (200 mm) trying to reach the possible optimal output pulse.

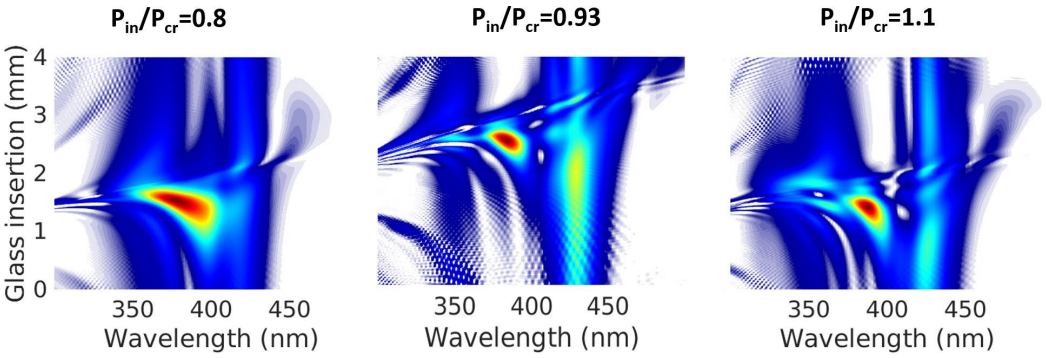

Figure 4.15: D-scan traces of the output field after the propagation (including ionization) inside a 20 cm long and 150 μm core radius HCF filled with 1 bar of argon of an input 30-fs pulse at 800 nm with an initial EH_{11} mode spatial structure. The values of the input powers are P_{in}/P_{cr} = 0.8 (left), P_{in}/P_{cr} = 0.93 (middle) and P_{in}/P_{cr} = 1.1 (right).

During the propagation all the nonlinear spatio-temporal effects have been taken into account together with the gas ionization. In Fig. 4.15 we show the d-scan traces for different values of the input powers are P_{in}/P_{cr} = 0.8 (left), P_{in}/P_{cr} = 0.93 (middle) and P_{in}/P_{cr} = 1.1 (right). The two cases with moderate and high input powers (middle and right) show spatial collapse, according to the pure self-focusing simulation (without ionization), and they also show structured d-scan traces, useless for post-compression

applications. Only the P_{in}/P_{cr} = 0.8 case, which does not undergo collapse according to the pure self-focusing simulations, shows a nice d-scan trace, close to the optimum, with a pulse duration of 5 fs after the post-compression. Figure 4.15 demonstrates that the isolated self-compression study is a solid tool to identify the energy limits of the standard HCF self-compression setup, which are those that do not present spatial collapse.

4.4 Conclusions

As we stated in the introduction, the aim of this work is to gain some insight into the energy limits of the post-compression schemes. In this sense, we try to find the limits to avoid the activation of undesirable high order nonlinear effects (such as spatial collapse or noticeable ionization) that distort the output spectral phase making it useless for post-compression applications. The study presented in this chapter is valid in any power region, specially in the high-power region, since it helps to find the optimal length of the HCF for each input peak power used before the strong spatial dynamics overcomes the propagation.

In this study on the self-focusing dynamics in HCFs, we have demonstrated that the spatial confinement of the fundamental spatial mode EH_{11} in a HCF plays a key role in the self-focusing process. This spatial confinement minimizes the diffraction and enhances the self-focusing of the beam. We have identified two different power regions related to the self-focusing process in the HCF: for input peak powers slightly greater than the critical power, the collapse appears at shorter distances than in the free space case and independently of the pulse duration. This means that the critical power in the HCF is slightly lower for the fundamental mode than for a free beam propagating in bulk media, in agreement with previous studies [Fibich and Gaeta, 2000]. For input peak powers below the critical power, we have obtained spatial collapses induced mainly by the energy transfer between spatial modes. The interplay between the spatial modes explains the appearance of discrete collapse regions that we have numerically observed. We have also observed that the superposition of the higher-order spatial modes and the fundamental mode leads to a self-compression process and the self-focusing of the beam.

Regarding the interplay between the spatial modes, since the energy transfer between the fundamental and the higher-order modes occurs at the peak intensity, the generated modes are shorter and their spectrum should be broader. This process can be understood as a compression effect in the energy transfer process itself, which could be a promising compression technique for further development.

In this low peak power region the spatial collapse is more complex and depends not only on the peak power but also on the input pulse duration. We have found that in the case of short pulses the self-steepening effect plays an important role enhancing the nonlinearity and thus the self-focusing of the beam.

In addition, we have studied the dependence of the self-focusing dynamics with different parameters. We have found that the collapse behaviour, explained at the 800 nm case, is observed again when changing the pump wavelength, which underlines the consistency of the obtained results. Moreover, we have explored the tunability of the spatial collapse position with the gas pressure, obtaining shorter collapse distances for higher pressures.

The spatial collapse dynamics explained here can be used to identify the energy limits when up-scaling the standard post-compression schemes based on HCFs.

Chapter 5

Propagation of Vector Beams in Hollow Capillary Fibers

Vector beams are a type of beams which show a spatially varying polarization (see Section 2.2). As a consequence, they have a singularity on the optical axis and a doughnut-shaped intensity distribution. Vector beams with radial and azimuthal polarization have become an interesting tool to control light-matter interactions, high-harmonic generation [Hernández-Garc´ıa et al., 2017], particle acceleration [Wen et al., 2019], microscopy and processing due to their special properties [Zhan, 2009]. For instance, radial vector beams present a non-vanishing longitudinal electric field component, which allows to focus light significantly tighter, demanding less peak power to achieve high longitudinal intensities [Dorn et al., 2003]. The azimuthally polarized field also presents interesting features, it can generate a strong magnetic field on the optical axis while the electric field is purely transverse [Blanco et al., 2019, Guclu et al., 2016]. For this reason, the possibility of generating an ultrashort pulse with these features has been studied over the last decades. As we have already mentioned, the most usual post-compression technique to achieve these few-cycle laser pulses in the near infrared is the nonlinear propagation of a laser pulse inside a HCF.

There are several methods to generate vector beams: through the combination of two orthogonally polarized beams, such as two linearly polarized beams or two circularly-polarized beams [Tidwell et al., 1990], using liquid crystal modulators [Stalder and Schadt, 1996], segmented wave plates [Machavariani et al., 2007] and more. The post-compression of high-energy few-cycle radially polarized pulses in gas-filled HCF with peak powers of 85 GW has already been demonstrated [Carbajo et al., 2014], but the

polarization is converted from linear to radial or azimuthal after the spectral broadening in the HCF with the fundamental mode EH_{11} and before the temporal compression. Although the efficiency is higher and the losses are lower at least before the compression stage, a broadband polarization mode converter is needed. The possibility of direct spectral broadening of the radially polarized pulses in the HCF and the subsequent post-compression was studied numerically later, arguing that this method is more advantageous [Wang et al., 2017]. The spectral broadening in this case is not limited to the bandwidth of the plate so it is possible to generate structured beams with non-conventional wavelengths. The coupling and the propagation of vector beams in photonic crystal fibers has also been demonstrated, but only at low energies (few microjoules) [Ishaaya et al., 2009]. Recently, the propagation and post-compression of 50-fs radially polarized pulses at 1.8 μm in a HCF has been reported [Kong et al., 2019]. The radially polarized beam is coupled into a krypton-filled HCF of 20 cm long and 150 μm diameter and then post-compressed with a fused silica plate down to 15 fs with 60 μJ. Moreover, the spectral broadening of vector beams by using the multipass cell technique and the subsequent post-compression down to sub-5 fs has also been theoretically studied as a promising technique [Cao et al., 2019].

Vector beams propagating inside a HCF are represented in different ways in the literature. On the one hand, Marcatili's model is the most frequently used [Marcatili and Schmeltzer, 1964]. The radially polarized vector beam which propagates in the hollow capillary fiber (HCF) corresponds to the TM_{0q} mode, while the azimuthally polarized vector beam corresponds to the TE_{0q} mode, where q denotes the number of concentric rings they show. In this model, explained in Section 2.2, the energy propagates essentially within the core of the HCF and the transverse electric field of the vector beams is represented as a Bessel function of the first kind $J_1\,(u_{01}r/r_F\,)$, while the longitudinal component can be neglected. In this case each spatial mode presents its own propagation and attenuation coefficient to model the energy loss during its propagation (see Eqs 2.67). On the other hand, there are other models in which the losses into the cladding are treated using different boundary conditions for the radial and azimuthal polarization [Andreasen and Kolesik, 2013]. Using these core-cladding boundary conditions, the resulting spatially polarized HCF mode cannot be represented as any kind of Bessel function [Wang et al., 2017]. Within this different theoretical approach, numerical simulations showed that 40-fs pulses can be post-compressed down to sub-9 fs pulses at 800 nm, although the spectrum was not spatially homogeneous.

In this chapter we will study the propagation of vector beams through a gas-filled HCF to explore the spectral broadening and the propagation features that these pulses present. We will use the (2+1)D model that performs a mode decomposition. In the first section of this chapter we will study the propagation features of vector beams and the interplay

between the higher-order spatial modes. We will explore different propagation schemes changing the parameters of the laser and the HCF, such as pulse duration, input energy, constant pressure inside the HCF and even implementing pressure gradients. In the second section we will try to couple experimentally the vector beams to the HCF and analyze the spatial mode at the output, which will be useful to validate our numerical simulations when comparing with other theoretical approaches. A complete numerical study of the propagation of these beams in HCFs could be useful for the optimization of the compression process, even considering the possibility of a direct self-compression of these beams in the HCF, which would simplify this post-compression scheme.

5.1 Nonlinear Propagation Dynamics of Vector Beams in Hollow Capillary Fibers

We will study the propagation of vector beams inside a HCF filled with gas with the (2+1)D model presented in Section 3.2. Although the polarization of these modes varies spatially, the local polarization is linear and we can express the beam with only one polarization component, so we can use the (2+1)D model to study the propagation of vector beams in gas-filled HCFs. As we have already explained, the (2+1)D model is based in mode decomposition of the laser pulse in the HCF core into an approximation of the modal fields using Marcatili's model. The electric field on the propagation axis is zero $E(r = 0) = 0$ and it is confined within the core $E(r > r_F) = 0$, r_F being the core radius. The leaky nature of the spatial modes is included by the absorption coefficient of each mode a_{pq} defined in Eq. 2.67. The initial condition to solve numerically Eq. 3.12 in this case is

$$A(r, z = 0) \propto \begin{cases} J_1(u_{01} r / r_F) & r \leq r_F \\ 0 & r > r_F \end{cases}, \tag{5.1}$$

where $u_{01} = 3.8317$ is the first zero of the Bessel J_1 function and r_F is the HCF core radius. The complete expression of the component of the electric field amplitude in the core of the HCF is then:

$$E(r, \theta, t, z = 0) = J_1\left(u_{01} \frac{r}{r_F}\right) e^{-t^2/t_0^2}, \tag{5.2}$$

t_0 being the input pulse duration. We propagate a 100-fs laser pulse, centered at 800 nm, with 1 mJ input energy through a HCF with 150 µm core radius and filled with argon (we use the linear and nonlinear refractive indexes as in Eq. 4.10 and $n_{NL} = 1.74 \cdot 10^{-23} \cdot p$ (m^2/W), where p is the gas pressure [Couairon et al., 2008]). These laser and HCF parameters are the same parameters of the laser system available in the laser facility in the University of Salamanca, so that we can compare our simulations with experimental

results. For the parameters chosen in the simulations, the input vector beam (TE_{01} or TM_{01}) propagates in the normal dispersion regime, since the zero-dispersion wavelength is 1092 nm. Although in the simulations the input beam is a pure vector beam, as defined in Eq. 5.1, we have already seen in Chapter 4 that it is possible to have an energy transfer to higher-order modes during the propagation, especially if the nonlinearity is high. These higher-order modes may present an anomalous dispersion response, so we can expect a complex propagation dynamics.

To gain a better understanding of the spatio-temporal dynamics that we will obtain with the (2+1)D model, we present in Table 5.1 the values of the group velocity and the group velocity dispersion (GVD) at 800 nm for the first four vector beams (TE or TM since the propagation coefficient is the same for both) in a HCF with 150 μm core radius and filled with argon at a pressure of 1.25 bar. The only difference between the radial and the azimuthal polarized vector beams is the absorption coefficient (see Eq. 2.67).

λ = 800 nm	TE_{01}/TM_{01}	TE_{02}/TM_{02}	TE_{03}/TM_{03}	TE_{04}/TM_{04}
v_g (nm/fs)	299.689	299.685	299.679	299.671
GVD (fs^2/m)	11.37	-23.87	-79.26	-154.80

Table 5.1: Group velocity and GVD values for the first four vector beams HCF spatial modes at 800 nm in a HCF with 150 μm core radius and filled with argon at 1.25 bar.

We numerically propagate the vector beams inside the Ar-filled HCF at 1.25 bar and we observe that with these parameters the differences between the TE_{01} and TM_{01} mode are negligible despite the different absorption they present. In Fig. 5.1 we show the comparison of the evolution of the energy for both vector beams (left), both at the radial position of maximum intensity ($r = 1.84 r_F / u_{01}$), and the spectral intensity distribution in log scale of the TM_{01} mode (center) and of the TE_{01} mode (right) after propagating 50 cm inside the HCF. The spatial dynamics is not important even though we are above the critical power of a Gaussian beam ($P = 1.7 P_{cr}$), as defined in Eq. 4.2. We observe neither self-compression nor dispersive wave generation despite the high input energy. The output spectrum at 50 cm corresponds to a Fourier Limit of 17 fs, which is a compression ratio of 6. This could be a suitable regime for post-compression schemes with vector beams, although still far from the few-cycle pulse duration. However, if we would like to obtain a broader spectrum or even achieve the generation of the dispersive wave (as we will study in the next chapters for different beams), we need to increase the nonlinearity. We have performed a scanning over different parameters such as the energy, the duration of the pulse and the gas pressure looking for the self-compression of vector beams in HCF. Since the differences between the TE_{01} mode and the TM_{01} mode

are hardly noticeable, we will study only the propagation of the TE_{01} mode (azimuthal polarization) in the following simulations.

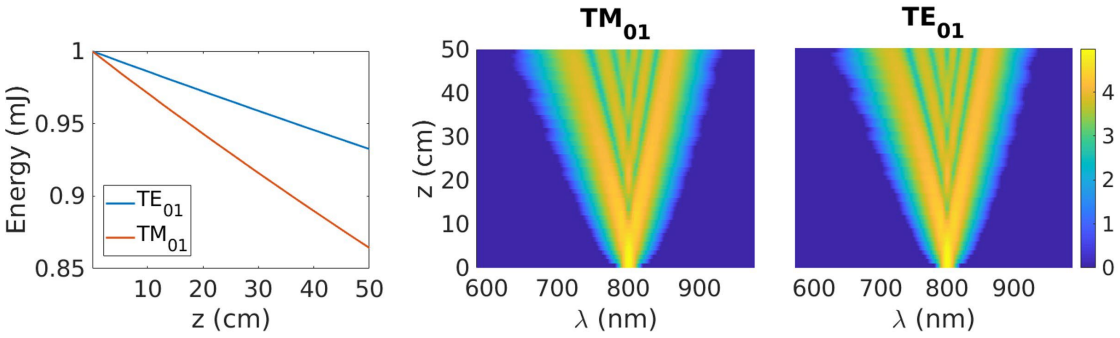

Figure 5.1: Evolution of the energy for both types of vector beams at 1.25 bar (left) and evolution of the spectral intensity distribution at the point of maximum intensity in log scale (arb. u.) of the TM_{01} mode (center) and the TE_{01} mode (right) during the propagation in the HCF.

To achieve a higher nonlinearity we can increase the input pulse energy or the gas pressure. The limit input pulse energy in our laser system is 1 mJ, so we decided to increase the pressure in the simulations. In Fig. 5.2 we present the propagation dynamics of a 100-fs and 1 mJ TE_{01} mode at 2 bar of argon, parameters that are experimentally accessible. In the top left panel in Fig. 5.2 we show the evolution of the spectral intensity distribution at the point of maximum intensity in log scale, in the top right panel we show the evolution of the temporal intensity distribution at the point of maximum intensity and also in log scale, in the bottom left panel we show the evolution of the beam waist and in the bottom right panel we show the mode contribution during the propagation in the HCF.

Looking at the whole set of plots in Fig. 5.2, it is clear that the spatio-temporal dynamics is complex in this parameter regime. In this case, the beam is breaking in many substructures, specially in the rear part of the pulse (see top right panel of Fig. 5.2). This type of evolution is understood as a modulational instability and was called soliton shower to remark the high number of substructures in which the pulse breaks during the nonlinear propagation [Russell et al., 2014]. The soliton shower appears at the rear part of the pulse due to the relevant role of the ionization in this process, which usually affects more the rear part than the front part of the pulse. From the spectral point of view (see top left panel of Fig. 5.2), the soliton shower in the temporal domain results in an important spectral broadening in the blue side but grown from noise, which induces this typical noisy temporal and spectral pulse structure. In a pure soliton shower generation regime, as the one presented in [Russell et al., 2014, Tani et al., 2013], one expects to find a supercontinuum generation process, but we only have an important spectrum broadening with traces of a dispersive wave, which means that we are entering

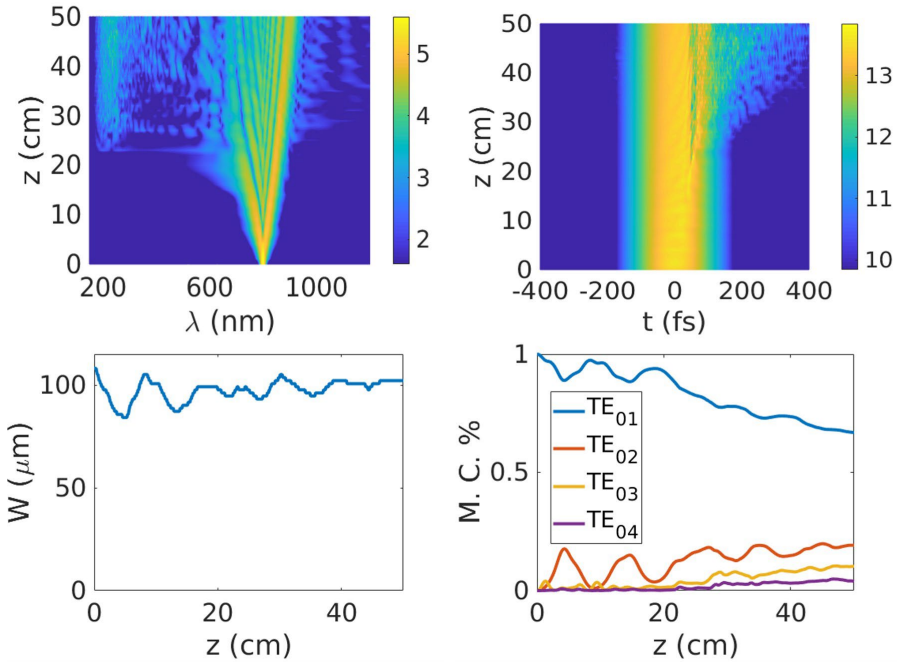

Figure 5.2: Evolution of the spectral (top left) intensity distribution in log scale (arb. u.) and evolution of the temporal (top right) intensity distribution (W/cm^2) at the point of maximum intensity, of the beam waist (bottom left) and of the mode contributions (bottom right) of the TE_{01} mode at 2 bar.

this high-nonlinear regime. To better understand how high the nonlinearity is we can calculate the soliton order defined as

$$N^2 = L_D / L_{NL} \tag{5.3}$$

where $L_D = t_0^2/(|\beta_2|)$ is the dispersion length, $L_{NL} = c/(\omega_0 n_{NL} I_0)$ is the nonlinear length, t_0 is the input pulse duration, $|\beta_2|$ is the group velocity dispersion (GVD) and I_0 is the input laser intensity [Agrawal, 2013]. From this expression we can deduce that N is an indication of the importance of the self-phase modulation and dispersion effects during the propagation along the HCF. If $N \gg 1$ the nonlinearity overcomes dispersion and it dominates the propagation. In this case the soliton order is $N \approx 80$, so it is clear that the nonlinear effects during the propagation are important, which is in agreement with the high nonlinear regime observed in Fig. 5.2.

There is one more thing that we should remark regarding this simulation: the input pulse lies in the normal dispersion region. This could be surprising because in most of the cases, this soliton shower regime is observed when the pulse lies in the anomalous region [Russell et al., 2014, Tani et al., 2013]. In fact, as we will see in Chapter 7, the dispersive wave is understood as a phase-matched energy transfer from a soliton in the anomalous region towards some particular wavelength in the normal dispersion region. So one may wonder how could the soliton shower and the dispersive wave appear in our case since the

pulse is in the normal dispersion region. We believe that the appearance of the high-order spatial modes during the propagation, all of them presenting an anomalous dispersion response, is crucial. The right bottom panel of Fig. 5.2 shows the contribution of the first four spatial modes, where we can see an important coupling between the fundamental mode (TE_{01})and the first excited mode, (TE_{01}). After some propagation distance in the HCF, where there is a coherent interaction between these two modes showing relatively clean oscillations in their populations, the contribution of the excited mode flattens (after 20 cm). This change of the population evolution of the excited state coincides with the appearance of the blue frequencies and the soliton shower generation. We believe that these effects are all connected and linked with ionization and the presence of higher spatial modes and their own nonlinear propagation dynamics.

As commented above, the presence of higher-order modes is of great importance to understand the propagation dynamics. To explore another interesting consequence of the mixture of spatial modes that appear during the nonlinear propagation in the HCF, we can examine the spatio-temporal intensity profile of the pulse during the propagation. Figure 5.3 shows the spatio-temporal intensity profile (W/cm²) of the full pulse (top left),

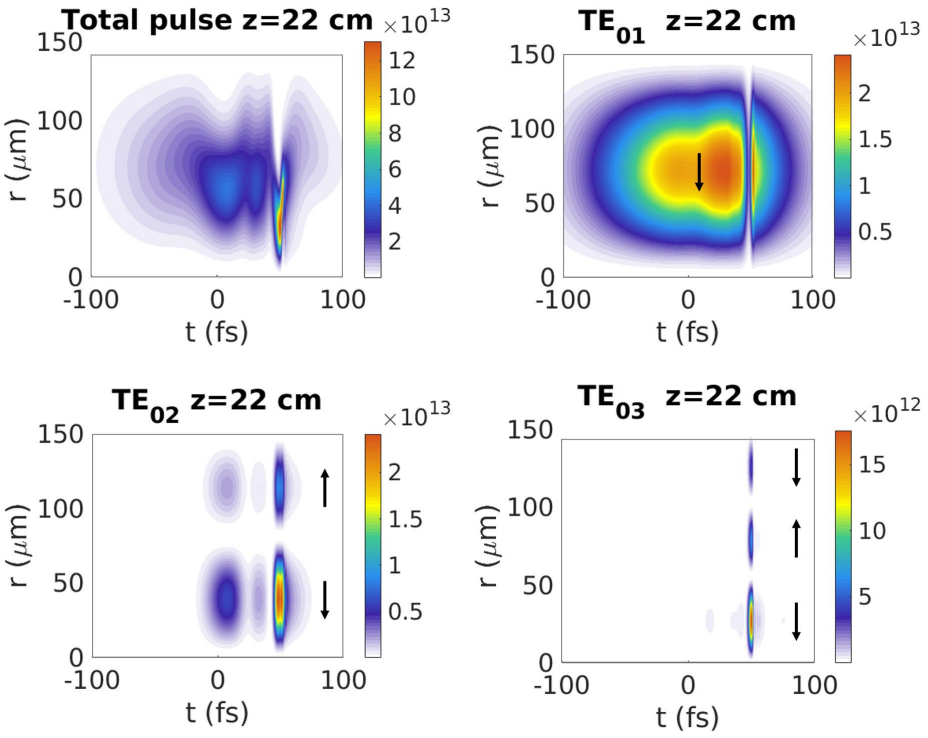

Figure 5.3: Spatio-temporal intensity profile (W/cm^2) of the pulse (top left), of the input spatial mode TE_{01} (top right) and of the first two excited modes, TE_{02} (bottom left) and TE_{03} (bottom right), at 22 cm inside the HCF for a 100-fs pulse. Black arrows represent the sign of the polarization of each ring.

of the first spatial mode TE_{01} contribution (top right) and of the first two excited modes, TE_{02} (bottom left) and TE_{03} (bottom right) contributions, 22 cm inside the HCF just

before the soliton shower regime starts. The higher-order modes TE_{02} and TE_{03} present two and three concentric intensity rings, respectively. In the top left panel we can see that the pulse exhibits a quite complex spatio-temporal intensity distribution. Although the total pulse basically has a single ring structure, its intensity peak is located in the inner part of the ring and at the trailing part of the pulse. However, in the outer part of the ring the pulse presents an important temporal leading pedestal. To understand this complex structure we have to consider the polarization distributions of the different spatial modes. The input TE_{01} mode in Fig. 5.3 (top right) transfers energy to the higher-order modes, leading to an important depletion of the fundamental mode around 50 fs. Thus, the higher-order spatial modes must have a significant contribution around that temporal region, as we can see in the two bottom panels of Fig. 5.3. Nevertheless, as the higher-order modes have several spatial rings, we have to consider the polarization direction (the sign of the electric field, that we have represented as black arrows in the figure) when adding all the contributions. As the different spatial rings of the higher-order modes alternate the sign of the field, we could find situations where the sum of the different contributions cancel each other. At the inner part of the pulse around 50 fs, the first spatial rings of the TE_{02} and TE_{03} modes (the closest to r = 0 μm) have the same sign to the polarization of the input TE_{01} mode and the constructive superposition of all of them results in the high intensity peak of the pulse. However, at the outer part of the pulse at 50 fs, the second spatial ring of the TE_{02} mode, that is placed between 90 and 140 μm, and the second spatial ring of the TE_{03} mode, that is placed between 64 and 96 μm, have the opposite sign to the polarization of the TE_{01} mode. In this case the destructive superposition of all of them leads to a decrease of the intensity of the pulse (top left) in this region (between 60 and 120 μm). These destructive interferences between the fundamental mode and the second ring of the TE_{02} mode are also presented around 0 and 30 fs, at the outer part of the beam. As a consequence of the constructive interference between the three first modes, the pulse presents a single ring structure. All these interference patterns appear at the rear part of the pulse because the higher-order modes have a lower group velocity. This means that they will be located at the rear part of the fundamental mode and they will eventually walk off if the propagation is long and clean enough. In any case, this nonlinear propagation generates a non-uniform broadening, showing a quite different temporal and spectral structure in the inner and in the outer part of the ring.

One may ask if the higher-order spatial modes could walk off the fundamental mode completely under some circumstances. In order to explore this possibility we have developed new simulations with shorter pulses, for which the walk off dynamics should be more relevant. In this case, we have simulated the propagation of a TE_{01} mode of 30 fs centered at 800 nm, inside the HCF of 150 μm core radius and filled with argon at 2

bar. We have to decrease the input pulse energy to avoid a strong ionization, so we use 0.3 mJ as input energy in this case. The same dynamics is obtained for shorter input pulses but at shorter distances inside the HCF. Figure. 5.4. shows the spatio-temporal intensity profile (W/cm²) of the pulse (top left), of the input spatial mode TE_{01} (top right) and of the first two excited modes, TE_{02} (bottom left) and TE_{03} (bottom right), at 7 cm inside the HCF for this short pulse, before the soliton shower regime.

It becomes evident that with these parameters, vector beams present a strong and complex nonlinear dynamics which complicates their propagation in HCF and prevent the achievement of a broad spectrum for few-cycle pulses post-compression. The interplay between the higher-order spatial modes is clearly the main origin of this very complex propagation dynamics.

A different approach that can be useful to obtain a smoother propagation dynamics could be using pressure gradients inside the HCF. This technique is widely used in post-compression schemes. A positive pressure gradient, where the pressure increases along the HCF, could be very useful to avoid a strong ionization and self-focusing effect at the entrance [Carbajo et al., 2014, Nagy et al., 2019, Suda et al., 2005]. In such a situation, the spectrum broadens gradually along the propagation due to the moderate increase of the nonlinearity. However, if the losses are high, the intensity of the pulse

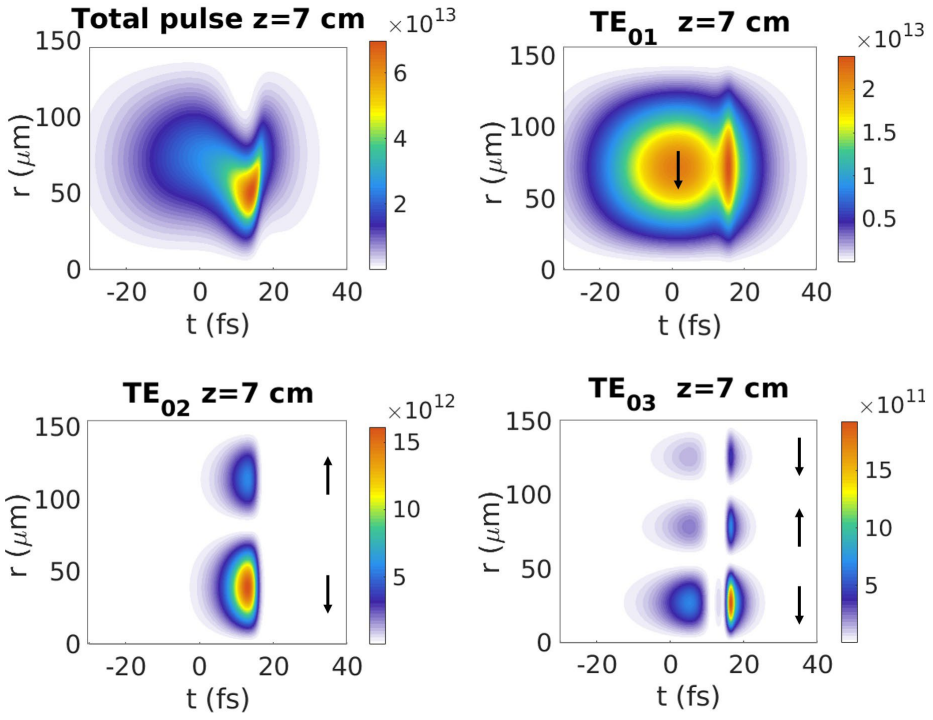

Figure 5.4: Spatio-temporal intensity profile (W/cm²) of the pulse (top left), of the input spatial mode TE_{01} (top right) and of the first two excited modes, TE_{02} (bottom left) and TE_{03} (bottom right), at 7 cm inside the HCF for a 30-fs pulse. Black arrows represent the sign of the polarization of each ring.

will be low when reaching higher pressures and the efficiency of the nonlinear interaction would decrease. Another option is the implementation of a negative pressure gradient, especially useful for ultra-broadband spectrum [Brahms et al., 2019, Mak et al., 2013, Wan and Chang, 2021]. This way the main nonlinear effects occur at the HCF entrance and then the pulse experiences less dispersion along the propagation, which is important when generating short pulses in the ultraviolet due to the dispersive wave emission. Also, the coupling between the spatial modes is less effective in the later stage of the compressor,

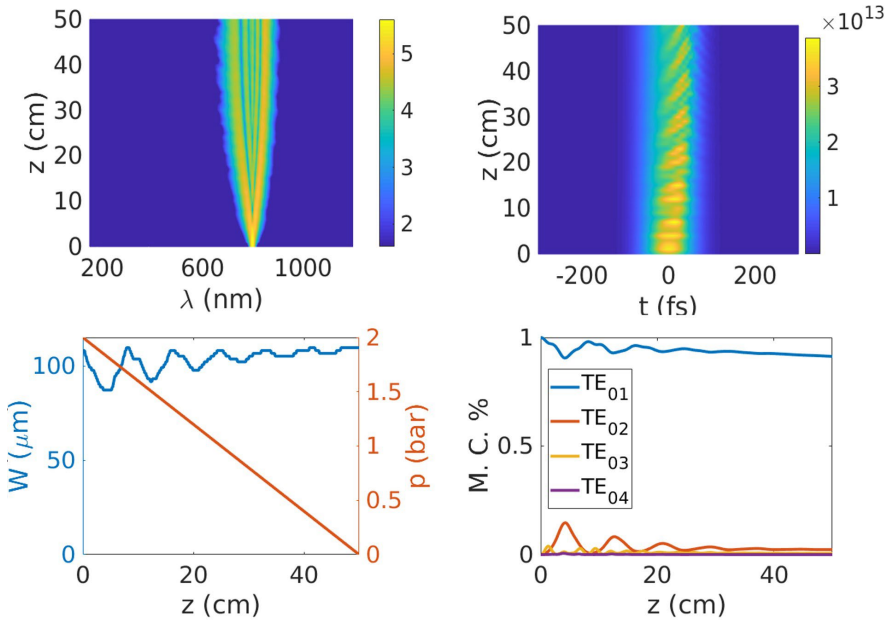

Figure 5.5: Evolution of the spectral (top left) intensity distribution in log scale (arb. u.) and of the temporal (top right) intensity distribution (W/cm^2) at the point of maximum intensity, of the beam waist and pressure gradient (bottom left) and the mode contribution (bottom right) of the TE_{01} mode at a pressure gradient from 2 to 0 bar for a 100-fs pulse.

With this idea in mind, we have propagated the same 100-fs pulse, but this time there is a negative pressure gradient from 2 to 0 bar inside the HCF. We implement a simple linear gradient $p(z) = p_0/L(L + z)$, where p_0 is the pressure at the input and L is the HCF length. We show in Fig. 5.5 the new dynamics obtained in this case. In the top left (right) panel we show the evolution of the spectral (temporal) intensity distribution in log scale, in the bottom left panel we show the evolution of the beam waist and the pressure gradient, and in the bottom right panel we show the mode contributions during the propagation in the HCF. It is evident that the dynamics is smoother now and the nonlinear propagation is not able to enter in the soliton shower regime, as in the constant pressure case.

We can examine again the spatio-temporal intensity profile of the pulse and its decomposition in the spatial modes 22 cm inside the HCF, the same point as in the constant pressure case (see Fig. 5.4). Figure 5.6 shows the spatio-temporal intensity profile (W/cm²) of the pulse (top left), of the input spatial mode TE_{01} (top right) and of the first two excited modes, TE_{02} (bottom left) and TE_{03} (bottom right), 22 cm inside the HCF. The obtained pulse presents basically the same complex and inhomogeneous spatio-temporal structure as in the constant pressure case, although in this case the interaction is moderately nonlinear, so all the propagation dynamics shown here is smoother.

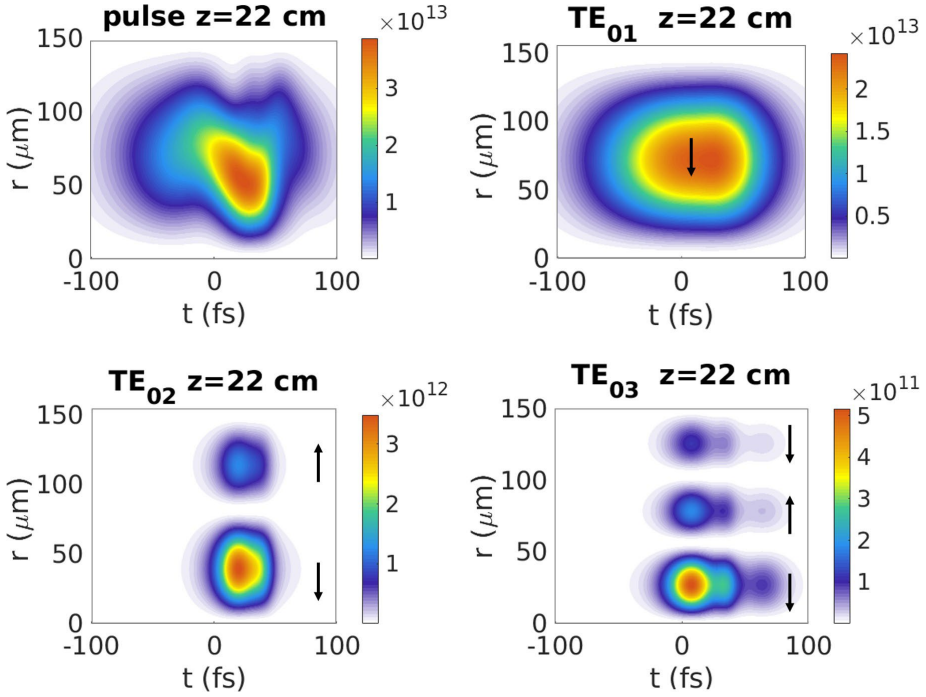

Figure 5.6: Spatio-temporal intensity profile (W/cm²) of the pulse (top left), of the input spatial mode TE_{01} (top right) and of the first two excited modes, TE_{02} (bottom left) and TE_{03} (bottom right), at 22 cm inside the HCF for a 100-fs pulse propagating in a negative pressure gradient from 2 to 0 bar. Black arrows represent the sign of the polarization of each ring.

We use the same type of pressure gradient for the 30-fs pulse but with 0.2 mJ input energy and an initial pressure of 2.8 bar, which is the maximum pressure experimentally accessible in the laser facility in the University of Salamanca. The main difference from the 100-fs case can be seen in the spectrum.

Figure 5.7 shows the spatio-spectral intensity profile of the pulse (left), of the input spatial mode TE_{01} (center) and of the first excited mode, TE_{02} (right), at the HCF output (100 cm in this case). We can see that the spectrum of the pulse is broad, from 550 to 1100 nm, and it shows the typical modulation from the spectral broadening by the self-phase modulation effect with a higher spectral intensity in the infrared. The

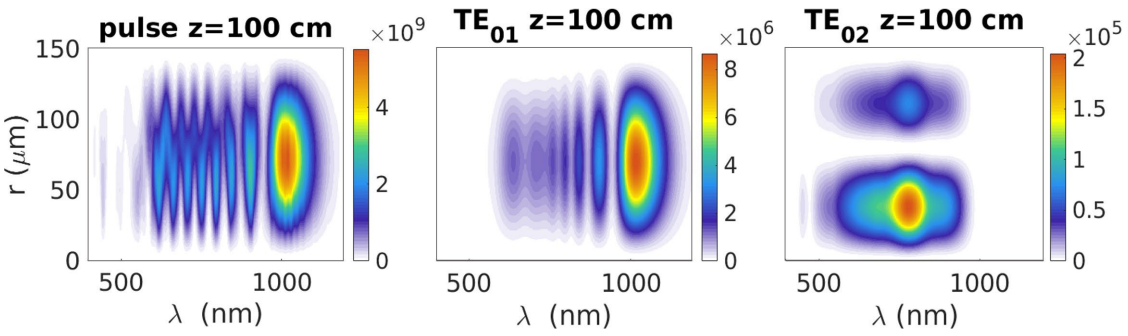

Figure 5.7: Spatio-spectral intensity profile (arb. units) of the pulse (left), of the input spatial mode TE_{01} (center) and of the first excited mode, TE_{02} (right), at 100 cm inside the HCF for a 30-fs pulse propagating in a decreasing pressure gradient from 2.8 to 0 bar.

spectrum of the TE_{01} mode (center) shows similar features, with a clean self-phase modulated spectrum.

On the other hand, the spectrum of the TE_{02} mode (right) is centered at 800 nm and expands to the visible band with the expected double ring spatial structure.

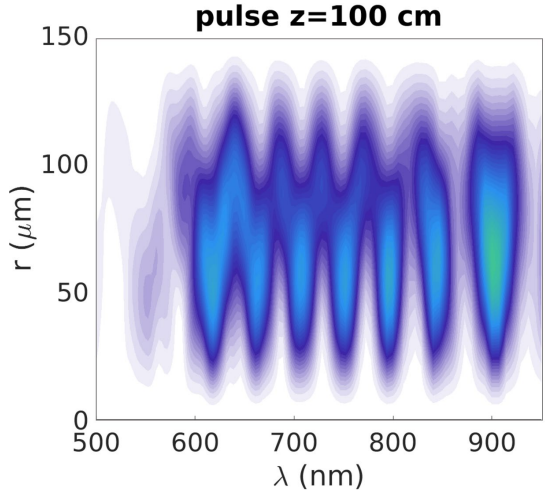

Figure 5.8: Zoom of the spectral modulations of the pulse shown in Fig. 5.7 (left). The spectrum shows spatial inhomogeneity due to the interplay of the spatial modes.

Apart from the significantly wider spectral broadening, the most interesting feature in this case is the interplay of the spatial modes that produces a spatial inhomogeneity in the spectrum (see Fig. 5.8, where we show a zoom of the spectrum of the pulse at 100 cm.). If we look at the spectrum at two different radii, 50 and 120 μm for instance, we can see that the spectrum in the region between 600-850 nm is complementary: the maxima for smaller radii correspond to minima for larger radii, and vice versa. In center and right panels of Fig. 5.7 we show the spectrum of the TE_{01} mode and of the TE_{02} mode, respectively. We can see that this curious spatio-spectral distribution is produced by the two spatial rings of the TE_{02} mode, which have opposite signs

of the electric field and interfere constructively or destructively with the field of the fundamental mode. As a consequence, at different radii the spectral composition of the beam varies, in this particular case, is complementary, which could be interesting for spectroscopy experiments.

To explore the possibility of obtaining a supercontinuum spectrum by adding these complementary spectral contributions, which would allow us to obtain few-cycle vector beam pulses, we have integrated the spectrum over all radii *r*. Figure 5.9 shows the resulting integrated spectrum which goes from 550 to 1100 nm approximately. The integrated spectrum is still quite modulated due the different weight of the spectrum at different radii. Moreover, the integrated spectrum shows a relatively noisy spectrum in the high frequency region (for wavelengths below 500 nm). By looking at the spectrum of the fundamental mode (center panel of Fig. 5.7) we can see that it has no signal in that blue region, which again indicates that all that noisy blue part belongs to the higher spatial modes.

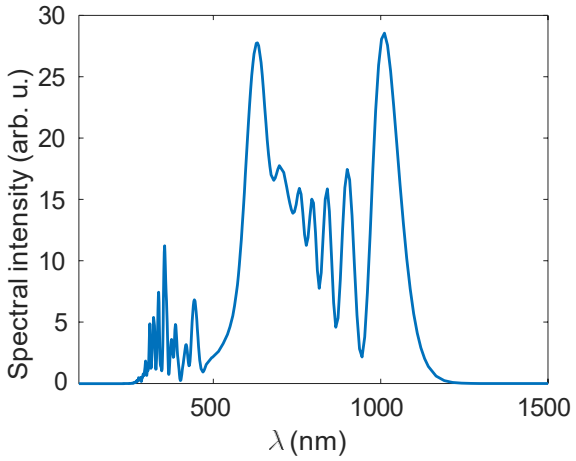

Figure 5.9: Spectral intensity profile of the 30-fs pulse integrated over all radii after propagating in a 1m HCF with a decreasing pressure gradient from 2.8 to 0 bar.

For completeness, we tried several pressure gradients schemes: linear, step, symmetric and asymmetric, but the results obtained were all similar to the cases presented here. in summary, the results from the nonlinear propagation of vector beams with the (2+1)D models show a very complex dynamics where the higher-order spatial modes have a relevant role in the propagation. The possibility of building ultrashort laser beams with such complex spatio-spectral structures is very attractive, although the complex nonlinear modal coupling and interferences indicate that the coupling and propagation of vector beams through a HCF in a real experiment could be challenging.

5.2 Experimental Propagation of Vector Beams in Hollow Capillary Fibers

5.2.1 Coupling Vector Beams in the Hollow Capillary Fiber: Evaluating the Polarization State and the Spatial Profile

As mentioned above, there are different approaches to represent vector beams numerically. Apart from the numerical model we have used in the previous section based on Marcatili's modes [Marcatili and Schmeltzer, 1964], there are other numerical models that establish different boundary conditions to take into account the loss of light into the cladding. This correction in principle is needed for longer wavelengths ($\lambda > 4\mu$m) where the approximation of Marcatili's model breaks down and losses are greater ([Andreasen and Kolesik, 2012] details the propagation model with these boundary conditions). According to this model, there are two possible choices as boundary conditions for the propagation of vector beams in HCFs. First, the electric field on the propagation axis is zero $E(r = 0) = 0$ as in our (2+1)D model. Second, the electric field at the interface of gas and cladding $E(r = r_F)$ has a different value depending on the vector beam propagating inside the HCF [Andreasen and Kolesik, 2013]

$$\begin{aligned} E^{TM}(r = r_F) &= \frac{4E_1 - E_2}{3 - 2ik_{cl}\Delta r/n_c^2} \\ E^{TE}(r = r_F) &= \frac{4E_1 - E_2}{3 - 2ik_{cl}\Delta r} \end{aligned} \tag{5.4}$$

where E_1 and E_2 are the electric fields in the HCF core at Δr and $2\Delta r$ from the core-cladding interface, and n_{cl} and k_{cl} are the linear refractive index and wavenumber of the cladding, respectively. With these boundary conditions the HCF spatial mode differs from Marcatili's modes, not corresponding to any known HCF spatial modes described in terms of Bessel functions [Wang et al., 2017].

To find out the spatial profile of the fundamental mode with these boundary conditions, we propagate a vector beam with an input modal distribution as defined in 5.1 with the time-independent (1+1)D model with the boundary conditions detailed in Eq. 5.4. The linear propagation of the input field under these conditions will converge to a new stable mode profile at the HCF output, which one should interpret as the new spatial profile of the fundamental mode in the HCF when using this numerical approach.

We propagate a laser beam with an input $J_1(u_{01}r/r_F)$ spatial profile centered at 800 nm through a HCF with 150μm of core radius filled with argon at 1 bar. In Fig. 5.10 we show the comparison between the spatial mode obtained at the end of the HCF with the boundary conditions in Eq. 5.4, labeled in the figure as TM_{01} and TE_{01}, and the

J_1 Bessel function from the Marcatili's model (yellow line). We can see that the stable spatial profile after the linear propagation deviates significantly from the input J_1 Bessel function and it is consistent with Ref. [Wang et al., 2017].

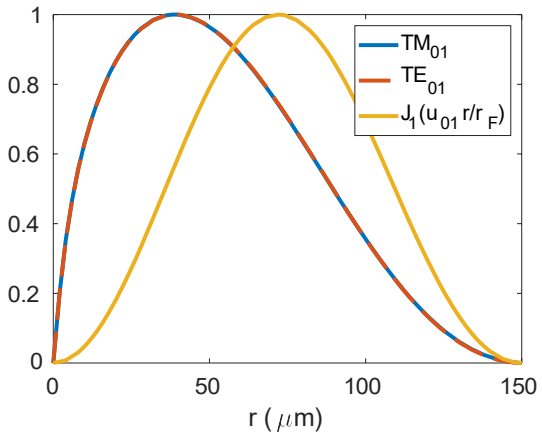

Figure 5.10: Comparison of the $J_1(u_{01}r/r_F)$ function (yellow line) with the stable radially polarized TM_{01} and azimuthally polarized TE_{01} beams resulting from the linear propagation inside the HCF with the other boundary conditions from Eq. 5.4.

In order to gain some insight into which is the real spatial profile of the spatial mode of the vector beams inside the HCF, we have performed an experiment trying to solve the actual disagreement between the numerical models. The experiment was realized in collaboration with the experimental group of Aplicaciones del Láser y Fotónica research group. A schematic experimental layout is shown in Fig. 5.11: A femtosecond linearly polarized Gaussian pulse from a Ti:Sapphire laser system with 100 fs pulse duration, centered at 800 nm, operating at a repetition rate of 1 kHz and ~ 0.7 mJ input energy, is converted into a radial or azimuthal infrared vector beam using a s-waveplate, courtesy of R. Drevinskas, A. Cerkauskaite and P. G. Kazansky from the University of Southampton. These s-waveplates are retarder elements based on the inscription of nanogratings in silica glass using a femtosecond laser. They can induce birrefrigence and the orientation of the optical axis varies spatially.

By rotating the polarization of the beam before the s-waveplate by 90° it is possible to switch between radially and azimuthally polarized beam. To control the input beam polarization we use a half-wave plate before the s-waveplate. After the conversion we couple the vector beam inside a 75 cm long, 150 μm core radius HCF in vacuum. At the HCF output we place a linear polarizer and a CCD to analyze the beam polarization distribution.

In Fig. 5.12 we show the measured spatial intensity distribution at the output of the HCF (left panels). We can observe that both azimuthal (TE_{01} (top)) and radial (TM_{01} (bottom)) vector beams are conserved during the propagation, although they seem very

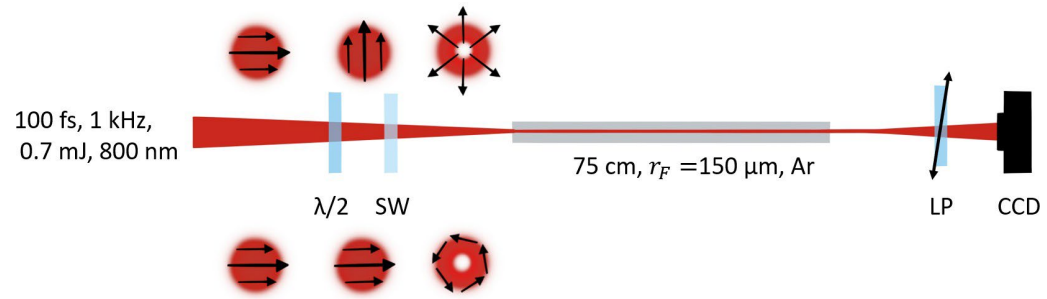

Figure 5.11: Experimental layout: a linearly polarized Gaussian pulse is converted to a radially or azimuthally polarized beam with a s-waveplate (SW). A half-wave plate ($\lambda/2$) rotates the polarization before the SW. The pulses are then coupled into a HCF (150 µm core radius).

sensitive to the HCF alignment. The intensity distribution shown in the left panels has the typical doughnut shape at the output of the HCF.

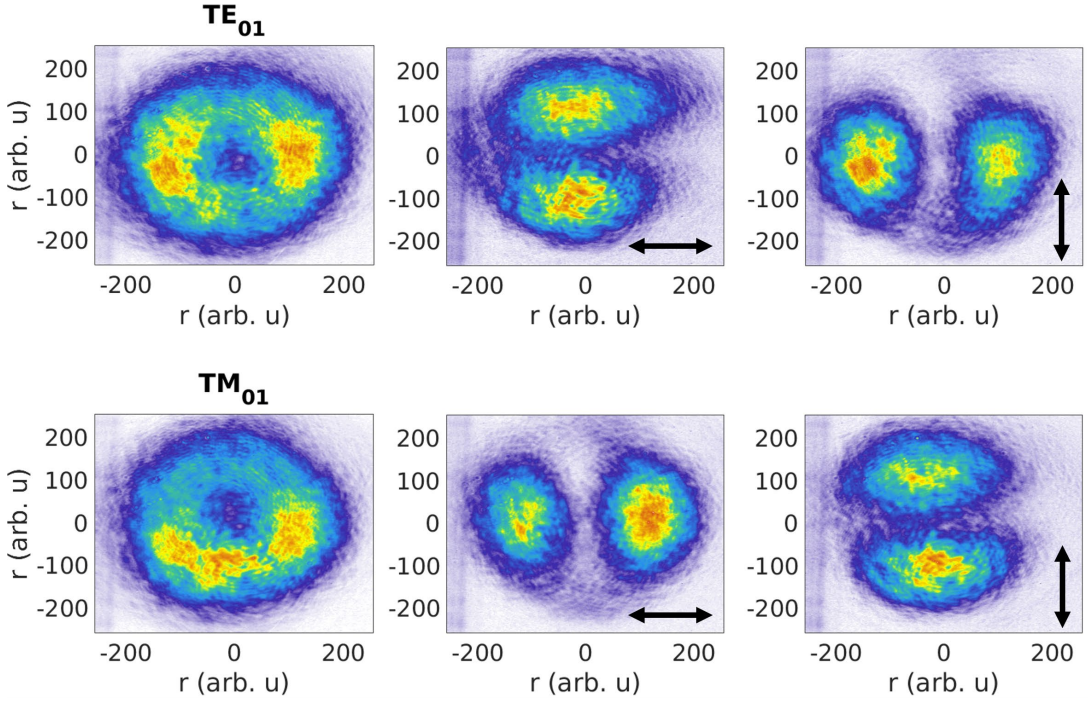

Figure 5.12: Spatial intensity distribution of azimuthal (TE_{01} (top)) and radial (TM_{01} (bottom)) vector beams. Center and right panels show the intensity distribution after placing a linear polarizer in horizontal and vertical directions (see black arrows).

We have checked that the polarization distribution is maintained after the propagation in each case. Center and right panels of Fig. 5.12 show the intensity distribution when placing the analyzer after the HCF output. The intensity profile in this case has two lobes that rotate with the orientation of the analyzer, which is indicated by black arrows.

We can see that the polarization is maintained quite well, which means that these HCF spatial modes are indeed vector beams after linear propagation in the HCF.

With these spatial intensity distributions we can now determine which numerical model suits well with the real spatial profile of vector beams inside our HCF. We have calculated the average intensity profile from each measured spatial intensity distribution and then we have compared it to the Bessel function J_1 truncated to its first root. Figure 5.13 shows the comparison of the radially and azimuthally polarized beam average intensity profile (blue lines) with the $J_1(u_{01}r/r_F)$ function (yellow dashed line). The agreement between the $J_1(u_{01}r/r_F)$ Bessel function and the experimental data is remarkable, so we conclude that the Marcatili's modes represent properly the propagation of the radial and azimuthal spatial modes inside the HCF, and the energy losses into the cladding in this parameter regime are negligible.

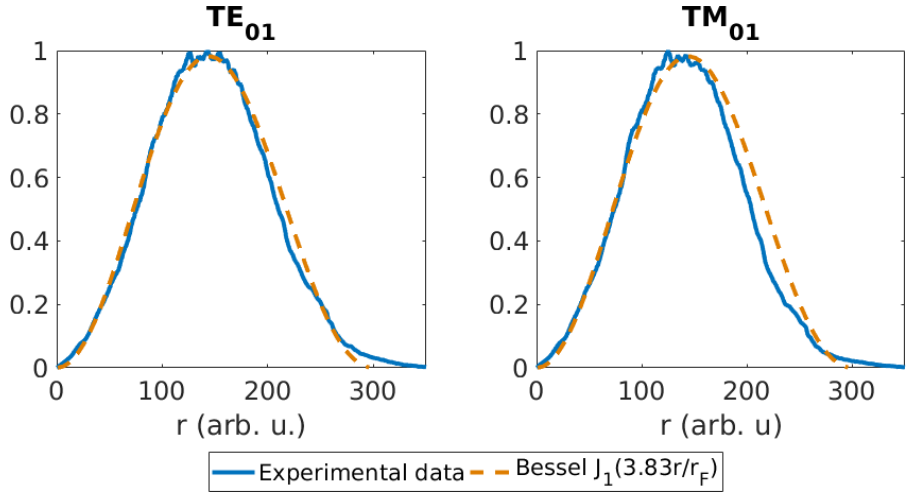

Figure 5.13: Comparison of the calculated average spatial intensity from the experimental data for the azimuthal (TE_{01} (left)) and radial (TM_{01} (right)) vector beams with the $J_1(3.83r/r_F)$ Bessel function (yellow dashed lines).

5.2.2 First Nonlinear Propagation Experimental Results

Now that we are able to successfully couple vector beams into the HCF in vacuum, the next step is to verify if the spatial profile and the polarization distributions are still maintained after a nonlinear propagation regime and if the output spectrum is wide enough for a few-cycle pulse compression.

With this purpose, we fill the HCF with argon and increase the pressure inside up to 2.8 bar, which is the maximum pressure accessible in the experiment. In this case the input energy is $\approx$ 0.4 mJ since almost half of the laser energy is lost in the s-waveplate during the conversion to the vector beam. Figure 5.14 shows the comparison of the experimental

spectrum measured at the HCF output with the spectrum obtained from the (2+1)D model simulations propagating 60 cm inside the HCF. The input pulse energy in the simulations in this case is 0.1 mJ, which is a 25% of the input energy in the experiment. With the simulated spectrum, the Fourier Limit of the output pulse would be 26.4 fs and 27.7 fs for the TE_{01} and for the TM_{01} mode, respectively.

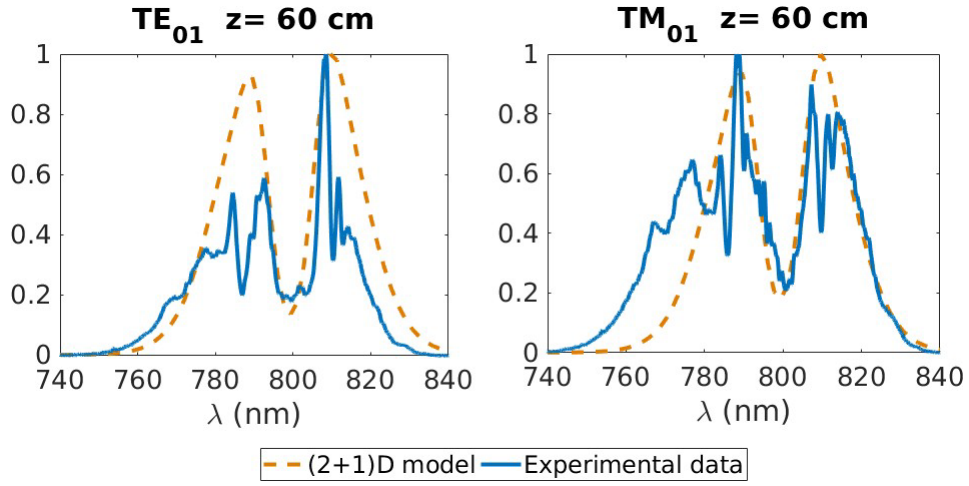

Figure 5.14: Comparison of the measured spectrum at the HCF output for each vector beam (blue lines) with the spectral intensity profile at 60 cm in the HCF obtained from the simulations with the (2+1)D model (yellow dashed line) at 2.8 bar of argon.

Analyzing the polarization of the output pulses at the horizontal and vertical directions the polarization seems correct, but at different directions the two-lobe structure was not clean. We developed some preliminary measurements of a full spatio-temporal and polarization characterization of these vector beams at the HCF output with a new algorithm developed by B. Alonso et al. [Alonso et al., 2020], where we observe that the polarization structure of these vector beams at the output of the HCF was different.

Considering the experimental difficulties to maintain the polarization structure of these vector beams in highly nonlinear propagation regimes and the energy loss in the conversion, we looked for some possible alternatives. According to the literature, a possibility would be to place the s-waveplate after the HCF. This way the input pulse energy would be higher and the spectral broadening more efficient since the coupling of the EH_{11} mode is less critical. However, the s-waveplate must have a broad bandwidth to obtain a pure vector beam. In Fig. 5.15 we show the measured spatial intensity distribution of the radially polarized vector beam after the s-waveplate (top left). The two lobes of the resulting intensity profile rotate with the orientation of the analyzer (indicated as black arrows), as can be observed in top right, bottom left and bottom right panels. Note that the spatial mode distribution changes in this case. Although the spectrum after the s-waveplate was broader than the spectrum shown in Fig. 5.14, we did not have time

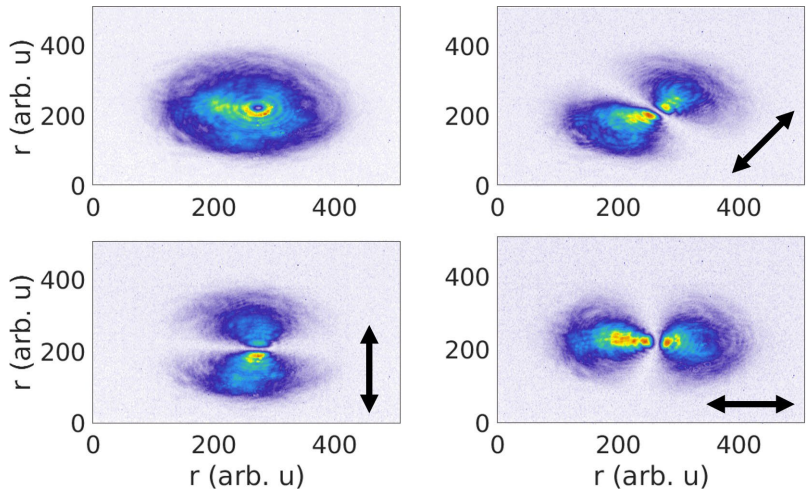

Figure 5.15: Spatial intensity distribution of the radial (TM_{01}) vector beam (top left) with the s-waveplate placed after the HCF. Top right, bottom left and bottom right panels show the intensity distribution after placing a linear polarizer in different directions (see black arrows).

to develop a full characterization of the resulting pulse to determine the polarization distribution in this case.

5.3 Conclusions

The main objective of the numerical study on the nonlinear propagation of vector beams, presented in this chapter, was the possibility of performing post-compression experiments or even achieving self-compression of these beams inside the HCF. However, in the experiments we found out that the coupling of these vector beams into the HCF in a highly nonlinear regime was challenging and, unfortunately, we did not have enough laser time to be able to explain some of the results obtained in the lab. A different strategy should be implemented to generate and post-compress vector beams in the HCF.

Nevertheless, we have learned interesting aspects related with the propagation of vector beams in HCFs from the theoretical model:

First, the self-compression of these beams is not easily accessible and we have not found any simulations where this process occurs. In principle, the main advantage of these beams is the possibility of scaling up the energy and to obtain directly at the HCF output an ultrashort and energetic structured pulse. However, if these beams propagating in the HCF are more unstable in practice, the setup of compressing the EH_{11} mode first and then perform the conversion seems more useful.

We have found that the propagation of vector beams inside the HCF results in peculiar structured profiles. This structure, or modulation, is a consequence of the intense multimode dynamics. The constructive or destructive superposition of the different spatial modes along the propagation leads to a spatial inhomogeneity and in some cases, this inhomogeneity is also translated into the spectrum of the pulse.

The propagation of the hybrid modes is more stable and in any case, the superposition of higher-order hybrid modes does not result in these complicated structured fields. They seem a better choice than vector beams in order to obtain few-cycle pulses in post-compression and self-compression processes.

We have experimentally checked that the spatial profile of vector beams inside HCFs is accurately described by Marcatili's model, at least in the linear regime. We have not observed spatial profiles similar to the one obtained with the boundary conditions from [Andreasen and Kolesik, 2013].

Chapter 6

Compression of Necklace Beams in Hollow Capillary Fibers to Obtain Ultrashort and Energetic Pulses in the Visible

In the last decades, several schemes have been developed to obtain ultrashort pulses in different bands of the visible spectral region. These ultrashort pulses are important tools for different applications, such as ultrafast spectroscopy or transient absorption image techniques in biomedical science [Domingue et al., 2017, Kobayashi et al., 2016]. There is a variety of strategies to obtain these sources. If the duration of the pulse is not a crucial factor, praseodymium ion-based mode-locked lasers are a straightforward option to obtain picosecond pulses with high average energy in red and green bands [Li et al., 2019, Luo et al., 2017]. However, if few-cycle pulses are also needed, two- or several-step setups have to be used, such as cascaded four-wave mixing [He et al., 2014, Liu and Kobayashi, 2009a,b, Silva et al., 2009, Weigand et al., 2009], nonlinear optical parametric amplification [Kobayashi et al., 2016, Okamura and Kobayashi, 2011], optical parametric chirped pulse amplification with second harmonic generation and excimer gas amplification [Clady et al., 2006], the up-conversion of different parts of the spectrum from fiber-based ultrafast systems [Domingue et al., 2017], spectral broadening in hollow capillary fibers (HCFs) [Nagy et al., 2020, Palato et al., 2020, Silva et al., 2018] or in filaments [Spokoyny et al., 2015], blue shifting solitons in single-ring photonic crystal fibers [Huang et al., 2019], or tunable dispersive waves generated during the soliton propagation, also in HCFs [Brahms et al., 2019, 2020, Travers et al., 2019]. Although the techniques described above can deliver ultrashort and energetic pulses in the visible

region of the spectrum, the complexity of most of the setups has motivated the search for alternatives.

One of the most compact setups to achieve tunable ultrashort pulses, of all those mentioned above, is the dispersive wave emission from a soliton propagation of an infrared laser pulse in HCFs filled with gas [Brahms et al., 2020, Travers et al., 2019]. This process consists of an energy transfer from the soliton, which is usually in the near or mid infrared, to a certain frequency in the normal dispersion region, which will lie in the visible or even in the ultraviolet, through a phase-matching process, as we will explain in detail in Chapter 7. However, the amount of energy transferred to the dispersive wave is still limited as a consequence of the coherent transfer of energy between the soliton and the dispersive wave. One possible solution would be to increase the input pulse energy, but this is also limited by self-focusing and the ionization of the gas inside the HCF, as we have explained in Chapter 4 [Conejero Jarque et al., 2018, Crego et al., 2019].

Another approach would be to study the nonlinear propagation of structured laser beams. These beams can be now easily generated and controlled [Forbes, 2019]. The possibility of propagating these beams in a standard post-compression setup, so the spectrum could be broadened in a controlled and efficient way to the visible region, could lead to the generation of ultrashort visible energetic pulses.

As explained in Section 2.2, necklace beams are a type of structured laser beams with amplitude and phase rotational symmetry around the propagation axis. Although they are intrinsically unstable in linear free propagation, under some circumstances they show self-trapping features which allow them to propagate with minor variations along noticeable distances in different nonlinear media such as Kerr-type media [Grow et al., 2007], thermal nonlocal media [Rotschild et al., 2006], colloidal engineered media [Silahli et al., 2015, Walasik et al., 2017], photorefractive media [Stoyanov et al., 2017], nonlinear lattice structures [Shi et al., 2019], or cubic-quintic nonlinear media [Aleksić et al., 2020]. By contrast to free propagation, necklace beams can be stable when linearly propagating inside confined structures [Fibich and Shpigelman, 2016].

In this chapter we will study the nonlinear propagation of infrared structured beams, in particular necklace beams with four, six and eight beads [Soljačić et al., 1998]. We will propagate these beams along a HCF filled with argon and study the features of the spatio-temporal dynamics. We will explore the possibility of obtaining short energetic visible pulses from its propagation and the dependence of the dynamics with some system parameters, such as the pressure and laser wavelength. We will also study the stability of these beams in the case of non-ideal input spatial profiles.

6.1 Propagation Dynamics of Necklace Beams in Hollow Capillary Fibers

There are different families of necklace beams in a HCF depending on the number of rings and beads they present, as we explained in Section 2.2. Although the spatial structure of these modes seems complex, their generation has already been demonstrated [Grow et al., 2007].

To study the nonlinear dynamics of necklace beams inside HCFs we have used the time-dependent (3+1)D numerical model presented in Section 3.3. This model includes all the spatio-temporal effects considering the azimuthal dependence, so it is able to study beams without cylindrical symmetry around the propagation axis. In this model we also include the ionization effects. Note that the Raman effect is absent in the monoatomic gases considered here.

In the (3+1)D simulation we include all the hybrid modes of the type $EH_{(-|p|)q}$ + $EH_{(|p|+2)q}$ but, since we do not decompose the electric field into the different spatial modes, we assign to all the modes the absorption and dispersion coefficients of the input mode, that is the only contribution at the entrance of the HCF and we assume it to be the dominant contribution during the whole propagation. In this case, the diffraction is solved directly with the Laplacian operator and the dispersion is solved using the propagation coefficient of the input spatial mode in the time domain, which is equivalent to include the space-time coupling term [Rothenberg, 1992].

In addition, when studying the nonlinear propagation of the input beam we immediately observe fluctuations in the spatial and temporal structure of the beam, which are signatures of the nonlinear coupling between different spatial modes [Nurhuda et al., 2003]. To check that this (3+1)D model is able to study the nonlinear propagation of a pulse through a HCF we have compared the results of the self-compression process of a pure hybrid high spatial mode with cylindrical symmetry using the (2+1)D model, presented in Section 3.2, and the (3+1)D model. We have propagated the EH_{13} hybrid mode centered at 800 nm, with 0.075 mJ of energy and 35 fs pulse duration in a HCF with a core radius of 150 μm filled with argon at 1 bar, the absorption and propagation coefficients are given by Eq. 2.67. In Fig. 6.1 we compare the propagation dynamics of this spatial mode using the (2+1)D model (orange lines) with the propagation dynamics using the (3+1)D model (blue lines). In particular, we compare the evolution of the energy (Fig. 6.1 (left)) and the temporal duration at the Full Width Half Maximum (FWHM) (Fig. 6.1 (right)), which shows a self-compression dynamics due to the anomalous dispersion response presented by the input spatial mode.

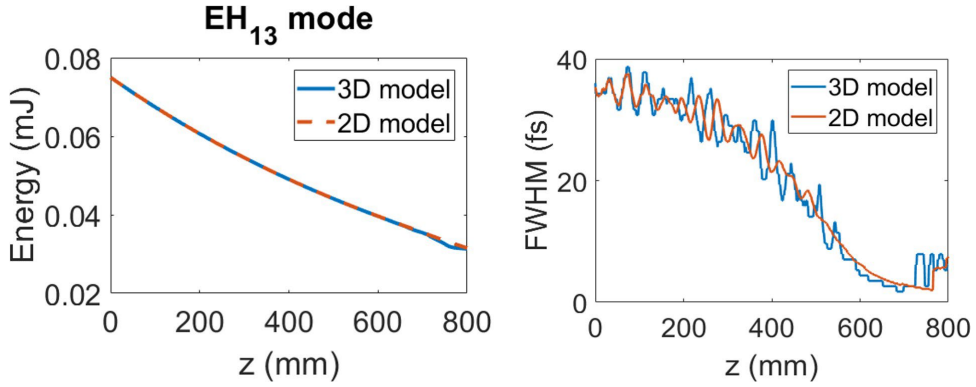

Figure 6.1: This figure shows the evolution of the energy (left) and FWHM duration (right) along the propagation of a EH_{13} hybrid mode inside a HCF. We compare the results obtained from the (2+1)D model (orange lines) with the results from the (3+1)D model (blue lines).

The results demonstrate that the new (3+1)D model recovers the main phenomena observed in the results obtained from the (2+1)D model, which includes properly all the modal dispersion and absorption. The main difference between these two models is that the modes in the (3+1)D model neither present walk-off between different modes nor modal losses, which artificially enhance their coupling. Nevertheless, in the intermediate power regime that we are using we believe that the results shown with the (3+1)D model are fully valid.

6.1.1 The Time-Dependent Model ((3+1)D Model)

We have simulated the nonlinear propagation of different necklace beams in a HCF filled with argon with the (3+1)D model. The initial condition used to solve numerically Eq. 3.18 is different depending on the number of beads of the necklace beam. We have studied the propagation of necklace beams with four, six and eight beads:

1. Necklace beam with four beads

The first necklace beam we present is a composition of the following hybrid modes: EH_{-11} and EH_{31}. So it presents one ring ($q = 1$) and four beads ($3 - (-1) = 4$). This mode composition is expressed as follows

$$EH_{-11} + EH_{31} = J_2\left(u_{31}\frac{r}{r_F}\right)\sin(2\theta) \tag{6.1}$$

The complete expression of the component of the electric field amplitude in the core of the HCF is:

$$E(r, \theta, t, z = 0) = J_2\left(u_{31}\frac{r}{r_F}\right)\sin(2\theta)e^{-t^2/t_0^2}, \tag{6.2}$$

where $u_{31} = 5.1356$ is the first zero of the Bessel J_2 function, r_F is the HCF core radius and t_0 is the input pulse duration. The combination of these two hybrid modes leads to a spatial mode with linear polarization [Marcatili and Schmeltzer, 1964]. The propagation losses of this spatial mode are represented by the absorption coefficient a_{31} defined in Eq. 2.67. We present in Fig. 6.2 (left) the beam fluence, i.e. the temporal integration of the spatio-temporal intensity of the necklace beam with four beads at the HCF input. The propagation losses of this spatial mode are represented by the absorption coefficient a_{31} defined in Eq. 2.67.

2. Necklace beam with six beads

This spatial mode is a composition of another two hybrid modes: EH_{-21} and EH_{41}. This mode also presents one ring ($q = 1$) but six beads ($4 - (-2) = 6$). The mode composition in this case is written as

$$EH_{-21} + EH_{41} = J_3\left(u_{41}\frac{r}{r_F}\right)\sin(3\theta) \tag{6.3}$$

Note that as the number of beads increases, the order of the J Bessel function also increases, and we obtain a higher-order spatial mode. The complete expression of the component of the electric field amplitude in the core of the HCF is:

$$E(r, \theta, t, z = 0) = J_3\left(u_{41}\frac{r}{r_F}\right)\sin(3\theta)e^{-t^2/t_0^2}, \tag{6.4}$$

where $u_{41} = 6.3802$ is the first zero of the Bessel J_3 function. The propagation losses of this spatial mode are represented by the absorption coefficient a_{41} defined in Eq. 2.67. In Fig. 6.2 (center) we present the beam fluence of a necklace beam with six beads at the HCF input.

3. Necklace beam with eight beads

The last case we have studied is the necklace beam with eight beads. This spatial mode is expressed as a composition of these two hybrid modes: EH_{-31} and EH_{51}. Once more, this spatial mode presents only one 1 ring ($q = 1$) and eight beads ($5 - (-3) = 8$). We can express the mode composition as

$$EH_{-31} + EH_{51} = J_4\left(u_{51}\frac{r}{r_F}\right)\sin(4\theta) \tag{6.5}$$

Including the temporal evolution, the complete expression of the component of the electric field amplitude in the core of the HCF is:

$$E(r, \theta, t, z = 0) = J_4\left(u_{51}\frac{r}{r_F}\right)\sin(4\theta)e^{-t^2/t_0^2}, \tag{6.6}$$

where u_{51} = 7.5883 is the first zero of the Bessel J_4 function. The absorption coefficient a_{51}, defined in Eq. 2.67, account for the losses in the propagation. The beam fluence of the necklace beam with eight beads at the HCF input is shown in Fig. 6.2 (right). We have not studied the propagation of necklace beams with more than eight beads due to the increase of the computing time. Also note that there is no possible combination of HCF spatial modes with the same propagation and absorption coefficients to generate a necklace beam with two beads.

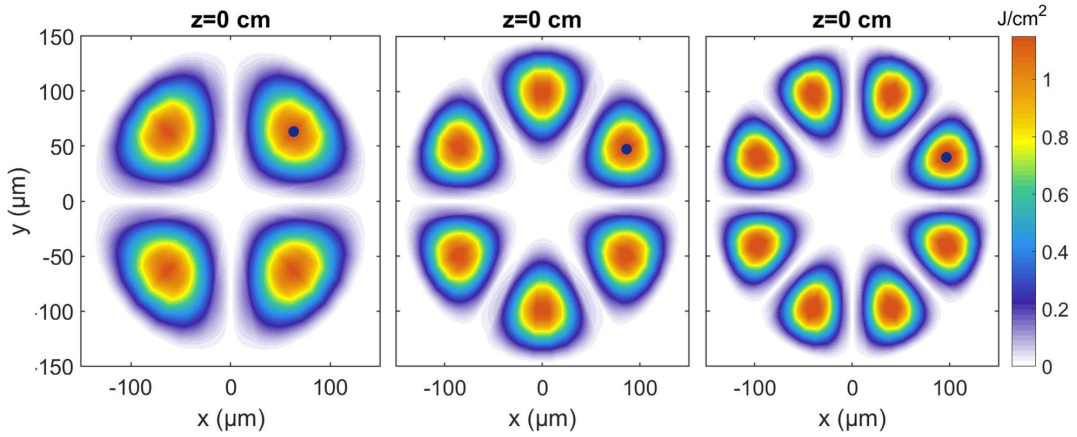

Figure 6.2: This figure shows the beam fluence, i.e. the temporal integration of the spatio-temporal intensity of a necklace beam with four (left), six (center) and eight (right) beads at the HCF input. The blue dot identify the point of maximum intensity in the first bead.

One of the main advantages of these necklace beams, that makes them an interesting alternative to hybrid modes, is that they present anomalous dispersion for standard HCF core sizes, with gas pressures close to atmospheric pressure in the wavelength region of 800 nm, which are usual conditions in the post-compression context. This feature is due to the fact that they are composed of higher spatial modes, as we have seen, and it enables the formation of a short pulse at the end of the HCF length by soliton self-compression dynamics, as shown in [López-Zubieta et al., 2018a,b]. This is very useful from the experimental point of view because there is no need of an additional compression stage as in standard post-compression setups. Moreover, the advantage of using the HCF also allows to tune the amount of linear dispersion easily just changing the gas type or pressure, but also with the HCF core size or the laser wavelength, as it is usually done in standard post-compression setups.

For the parameters used in the simulations, the input necklace beams propagate in the anomalous dispersion regime, since the zero-dispersion wavelength is 754 nm, 679 nm and 625 nm for a necklace beam with four, six and eight beads, respectively. As we have shown before, the larger the number of beads, the higher the order of the Bessel function

of the spatial mode, which corresponds to a stronger anomalous response (see the group velocity dispersion (GVD) values for each spatial mode in Table 6.1). Furthermore, we have observed that in order to increase the effect of the nonlinearity it is desirable to increase the energy rather than the pressure, due to the higher losses that these spatial modes present compared to hybrid modes (see the values of the absorption coefficient a_{pq} for each spatial mode in Table 6.1). By comparing the dispersion and absorption values of the hybrid modes with the necklace beams (Table. 6.1), we realize that the latter are an interesting choice in the dispersion region with low losses.

λ = 800 nm	EH_{11}	EH_{12}	EH_{13}	NB (4 b)	NB (6 b)	NB (8 b)
v_g (nm/fs)	299.71	299.707	299.702	299.708	299.706	299.704
GVD (fs^2/m)	15.17	-10.017	-55.34	-5.84	-20.46	-37.68
a_{pq} (m^{-1})	0.041	0.216	0.531	0.187	0.289	0.408

Table 6.1: Group velocity, GVD and absorption values for the EH_{11} mode, first two excited hybrid modes and necklace beams with 4, 6 and 8 beads at 800 nm in a HCF with 150 µm core radius and filled with argon at 1 bar.

6.1.2 Pulse Propagation of Intense Necklace Beams in Hollow Capillary Fibers

We study the propagation of 35-fs necklace beams with 0.2 mJ input energy centered at 800 nm through a HCF with 150 µm core radius filled with argon at 1 bar. We propagate necklace beams with four, six and eight beads. The HCF length will be adapted to observe properly the spectral broadening in each case. The Sellmeier equation used for the linear refractive index is again Eq. 4.10 and we use the same nonlinear refractive index for argon, n_{NL}=1.74 · 10^{23} · p (m^2/W), where p is the gas pressure. The parameters related to the ionization used in the model for all the cases are those presented in Table 4.3.

The propagation dynamics of necklace beams with four, six and eight beads inside the HCF is shown in Fig. 6.3. In this figure we show in each row the evolution of the spectral distribution in logarithmic scale (left panels), the temporal distribution in linear scale (center panels) and the temporal FWHM duration (right panels) at the point of maximum intensity of one bead (marked as a blue dot in Fig. 6.2). We present the case of a necklace beam with four beads in the top row, with six beads in the middle row and with eight beads in the bottom row.

If we look at the spectrum in each case, Fig. 6.3 (left panels), we can observe the most interesting feature of this type of propagation. The pulse begins the propagation in the anomalous dispersion region, not very far from the zero-dispersion wavelength (ZDW),

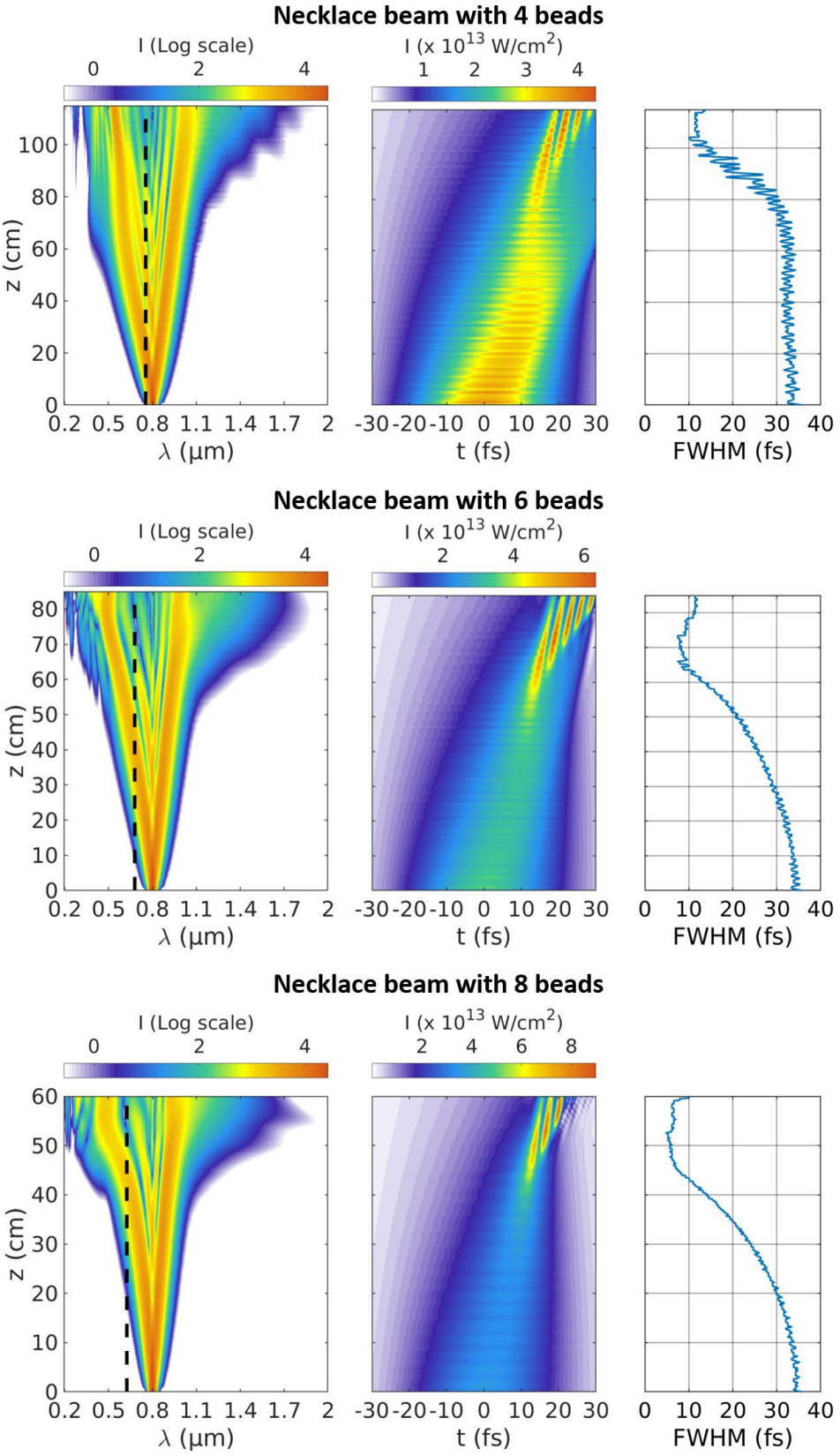

Figure 6.3: Each row shows the evolution of the spectral (left, in log scale) and temporal (center) intensity distribution and of the FWHM duration (right), at the peak intensity of one bead of a necklace beam with 4 (top), 6 (middle) and 8 beads (bottom). The dashed line in the left panels are the ZDWs, 754 nm, 679 nm and 625 nm, respectively. Note the different length of z for each case.

shown as a black dashed line in the left panels (754 nm for the necklace beam with four beads, 679 nm for six beads and 625 nm for eight beads). In this type of propagation, where the nonlinearity is very high (the soliton order N is 32, 15 and 5 for four, six and eight beads, respectively, $N \gg 1$ in all the cases) and the role of the third order dispersion is important (since the second order dispersion is small), the spectrum broadens in such a way that concentrates the energy in two spectral bands [Agrawal, 2013].

The evolution of each of the two main spectral bands during the propagation explains the evolution of the whole pulse. While the red-shifted band continues in the anomalous dispersion region, the other spectral band shifts to the visible part of the spectrum entering into the normal dispersion region of the HCF. These two spectral peaks correspond to the outermost peaks of the broadened spectrum by self-phase modulation, and in this high nonlinear propagation regime, they collect most of the energy. Since in the three cases we present here, the central wavelength of the input pulse is close to the zero-dispersion wavelength, after some distance, the blue-shifted band enters the normal dispersion region, which corresponds to the visible region here, and continues shifting towards shorter wavelengths. In the three cases presented in Fig. 6.3, the blue-shifted band reaches the visible region, and for that reason, we denote these blue bands as visible bands.

The spectral dynamics is accompanied by a temporal self-compression process (center panels), specially supported by the red band of the spectrum, which carries an important amount of energy and always propagates in the anomalous dispersion region. The generation of a soliton inside the HCF is observed around 103 cm in the case of the necklace beam with four beads, 66 cm in the case of six beads and 51 cm in the case of eight beads. This distance inside the HCF, where the soliton appears and the pulse reaches its shortest pulse duration, is called the self-compression distance. Note that during the self-compression process the peak of the intensity distribution is delayed (shifted towards positive time values) and, at the same time, the pulse is becoming slightly distorted, with the peak shifted towards the rear part of the pulse. Both effects are induced by self-steepening, which plays an important role in this self-compression process. The strong shock formation typically related to self-steepening is, in this case, dissipated by the dispersion. As a consequence of the temporal delay of the whole pulse, the high-order soliton appears at the center of the pulse but at a delayed time.

The evolution of the pulse duration at its full width half maximum (FWHM) is shown in Fig. 6.3 (right panels). We can see that the pulse reaches a minimum pulse duration of 10.1 fs at 103 cm inside the HCF in the case of the necklace beam with four beads, 7.5 fs at 66 cm inside the HCF in the case of six beads and 5.3 fs at 51 cm in the case of eight

beads. From that point on, the higher order dispersion terms cause the pulse fission, where the pulse breaks up in subpulses and there is no further spectral broadening.

If we look for the generation of ultrashort pulses at wavelengths much shorter than the input from the propagation of these necklace beams in the HCF, one mechanism would be the phase-matched coupling of the soliton with a dispersive wave inside the HCF, resulting in the emission of radiation in the blue side of the spectrum. It is well-known that the efficiency of this process, defined as the energy transferred to the blue side of the spectrum, is around 15% of the input energy resulting in dispersive waves with 10-20 μJ of energy [Travers et al., 2019]. Since in our case the energy carried by the visible band of the spectrum is basically similar to the energy of the red band that forms the soliton, one possible approach to directly obtain an energetic pulse at shorter wavelengths without a phase-matching process is through this visible band.

It is important to remark that, although the nonlinearity is high, we have not observed any spatial dynamics related to self-focusing, so the beam keeps the same intensity structure during the whole propagation. In Fig. 6.4 we show the beam fluence of the necklace beams with four beads (left), six beads (center) and eight beads (right) at the HCF output, which is only affected by the absorption losses during the propagation. Although necklace beams with a large number of beads present a higher absorption as we have seen in Table 6.1, since the propagation of the necklace beam with eight beads is shorter, the losses in this case are quite similar to the four-bead case (see Fig. 6.5).

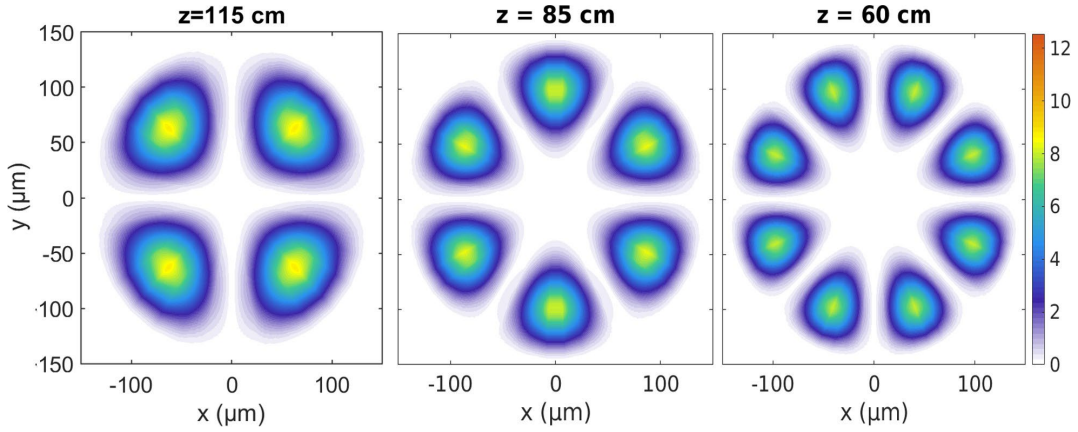

Figure 6.4: The figure shows the beam fluence (J/cm^2 of a necklace beam with 4 (left), 6 (center) and 8 (right) beads at the HCF output. Note the different length of the HCF for each case.

Finally, to find out if the ionization has a significant role in this propagation regime, bearing in mind the high nonlinearity of all the cases presented, we have simulated the propagation of one of the necklace beams, the one with six beads, without the ionization

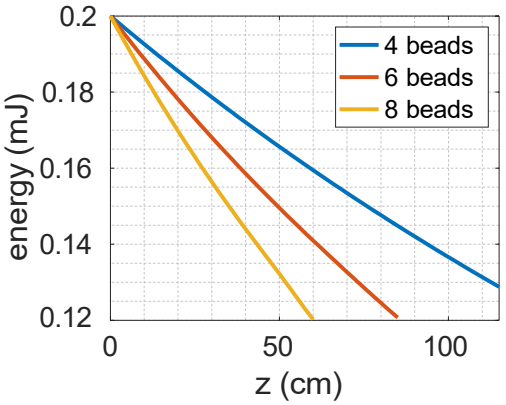

Figure 6.5: The figure shows the evolution of the energy in the case of a necklace beam with 4 (blue line), 6 (orange line) and 8 beads (yellow line) inside the HCF with the parameters used in the previous simulations.

effects. In Fig. 6.6 we show the comparison of the evolution of the energy (left) and of the FWHM duration (right). We can observe that the differences are so small that the ionization can be neglected.

One may wonder how is it possible that the ionization of the medium has such a modest role with a high N parameter. The reason is the spatial structure of this beam since the total energy is equally distributed between all the beads and it is less confined compared to the hybrid modes.

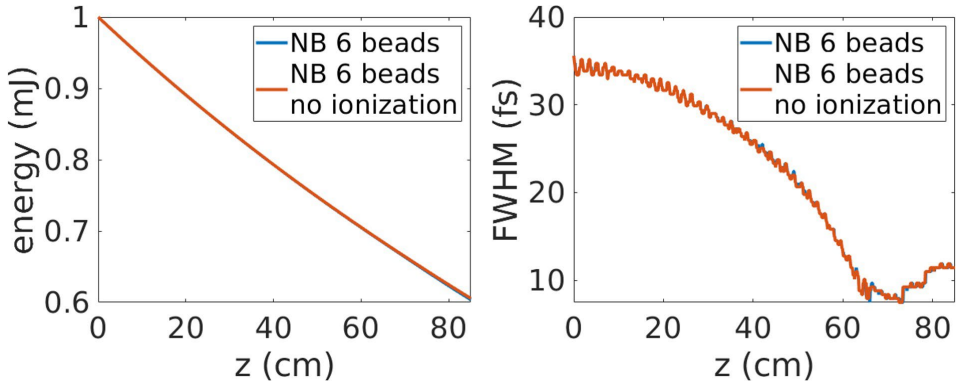

Figure 6.6: The figure shows the evolution of the energy (left) and of the FWHM duration (right) in the case of a necklace beam with 6 beads including ionization (blue line) and without it (orange line).

6.2 Ultrashort Visible Energetic Pulses from the Infrared Necklace Beam Propagation

The two-band structure of the spectrum suggests the possibility of filtering the visible band to see if we are able to obtain an ultrashort visible energetic pulse. For this purpose, we have filtered the visible band using a square dynamic filter that takes the main part of the band at each point. Since the visible band shifts to the blue side of the spectrum at each point, the filter searches for the maximum of the band and the two adjacent minima. Once we have filtered the spectral band, we calculate its energy, temporal shape and FWHM duration.

Figure 6.7 shows the filtered visible band, at the point of maximum intensity in the first bead, obtained from the propagation of a necklace beam with four beads (top row), six beads (middle row) and eight beads (bottom row). In each row of Fig. 6.7 we show the filtered spectrum (in logarithmic scale) from the propagation distance at which the band is in the normal dispersion region. As we can see, after the band crosses the zero-dispersion wavelength, it continues shifting to shorter wavelengths along the propagation without changing its width or structure, until it reaches a wavelength between 500-550 nm where the soliton fission occurs and the spectral broadening stops.

From the temporal point of view, see Fig. 6.7 (center panels), the peak intensity of the visible band is always of the same order during the whole propagation (between $3 - 6 \times 10^{13}$ W/cm^2 depending on the case) with a similar temporal structure of a few femtoseconds of duration. Figure 6.7 (right panels) shows the evolution of the energy (blue line), the FWHM duration (solid orange line) and the FWHM duration of the Fourier Limit (orange dashed line) of the filtered band in each case. We examine the energy of the band from the moment the band crosses the zero-dispersion wavelength, reaching a value around 50 μJ in the case of four and six beads and 40 μJ for the eight-bead beam. From that point on, the energy remains approximately constant without presenting relevant losses during the propagation until the soliton fission occurs. In the case of the necklace beam with eight beads, the energy presents larger variations because the dynamics occurs a few centimeters before the soliton fission process (see the central panels of Fig. 6.3), where the spectral broadening stops. A similar behaviour can also be seen in the other two cases but at longer distances (around 80 cm (100 cm) for the necklace beam with six (four) beads).

Regarding the temporal duration of the visible band, we can see that the FWHM duration is usually shorter than 10 fs and sometimes very close to its Fourier Limit, which indicates that the phase structure of the visible band is very flat. It seems that the higher the number of beads of the beam, the shorter its visible band pulse.

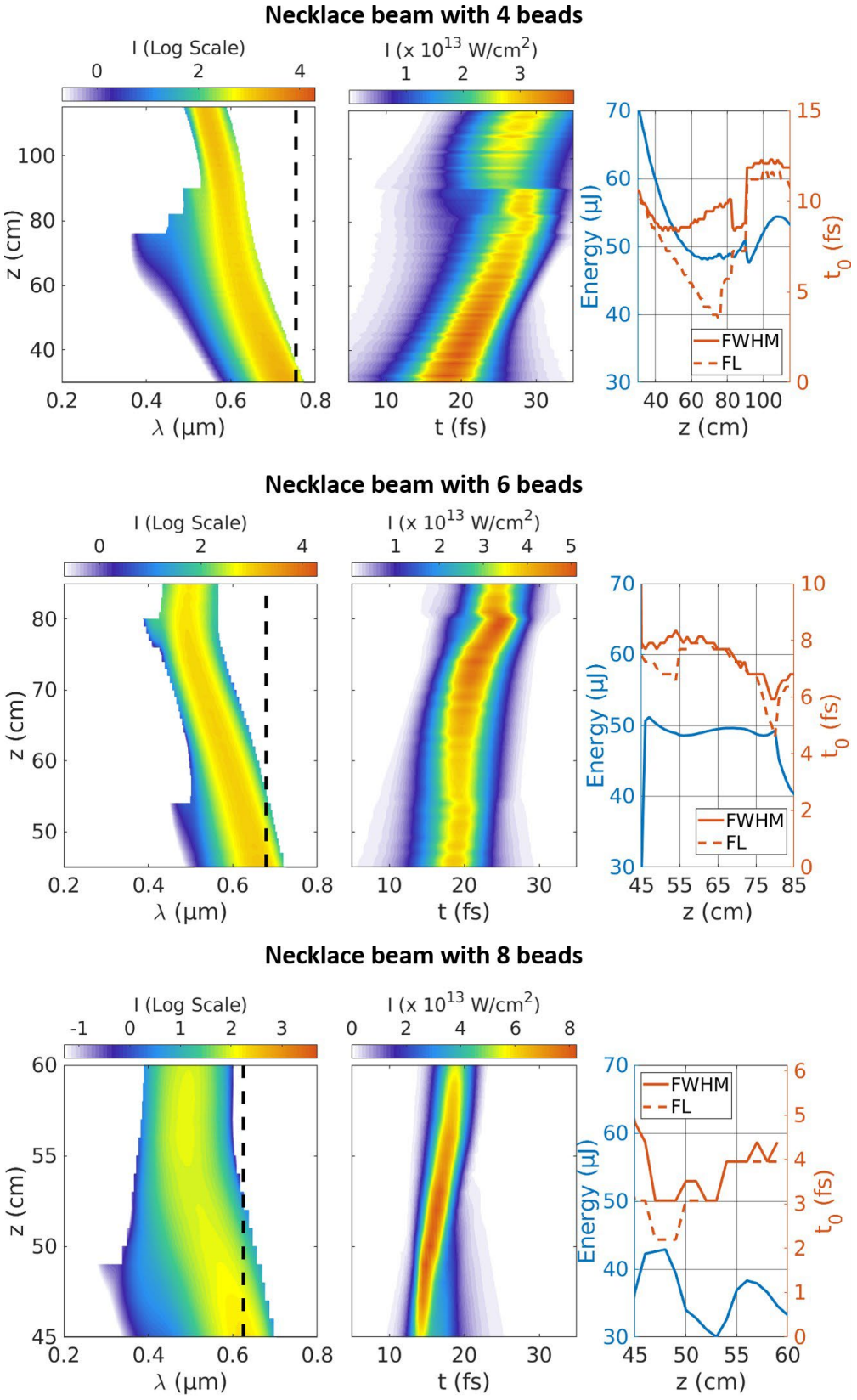

Figure 6.7: Left and center panels show the evolution of the spectral (in log scale) and of the temporal intensity distribution. Right panel shows the energy (blue line), the temporal FWHM duration (orange line) and Fourier limit (orange dashed line) of the visible band evaluated at the peak intensity of the first bead, in the case of a necklace beam with 4 (top), 6 (center) and 8 (bottom) beads. The dashed line in left panels shows the ZDWs (754, 679 and 625 nm respectively).

6.2.1 Influence of the Parameters of the Laser and the Filling Gas on the Visible Band

Even though we have simulated the nonlinear propagation of different necklace beams with four, six and eight beads in an argon-filled HCF, we will continue discussing the case of the six-bead necklace beam in this subsection, since the dynamics for a different number of beads is quite similar. We have chosen this spatial mode in particular because it has an anomalous response high enough to self-compress the pulse in a standard one meter long HCF without requiring high computational time.

Now that we have demonstrated that we are able to generate ultrashort visible energetic pulses, it would be interesting to understand its dependence with different parameters of the HCF. The easiest one to change in a real experiment is the pressure inside the HCF. For this reason we have performed the same study as in the previous section, but for different constant pressures inside the HCF for a necklace beam with six beads. We compare the visible bands of the spectrum, generated at each pressure value, at the same distance where the self-compression was optimum for the 1 bar case, at 66 cm, as if it were the actual HCF length.

Figure 6.8 (left) shows a comparison of the visible bands obtained for different pressure values inside the HCF, scanned from 0.5 to 1.2 bar. We can observe that the band suffers a blue shift as the pressure inside the HCF increases, which comes from the higher nonlinearity and the stronger induced spectral broadening. This spectral shift saturates when the band reaches the 500 nm region due to the appearance of the soliton fission dynamics, that stops the spectral shift of that band. It is not surprising that the role of the pressure in the spectral tunability of this visible pulse is the opposite to the case of dispersive wave signals, for which increasing the pressure provides longer wavelengths [Brahms et al., 2020, Travers et al., 2019], since their nonlinear origins are different.

We have also calculated the energy and the temporal duration of the bands at 66 cm inside the HCF to observe the dependence with the pressure. The blue triangles in Fig. 6.8 (right) show that the energy of the visible band is quite constant, being always around 50 μJ, which is a significant amount of energy. Calculating the efficiency in each case, the amount of energy in the visible band of the spectrum goes from 23% to 27% of the total input pulse energy and from 34% to 40% of the total pulse energy at 66 cm. The orange circles in Fig. 6.8 (right) correspond to the temporal duration at FWHM of the pulse obtained from the visible band (orange solid line) and its Fourier Limit (orange dashed line). As we can see, the pulse duration is always below 10 fs, reaching 5 fs of duration at the cases with 0.6-0.8 bar of pressure inside the HCF. Unfortunately, in

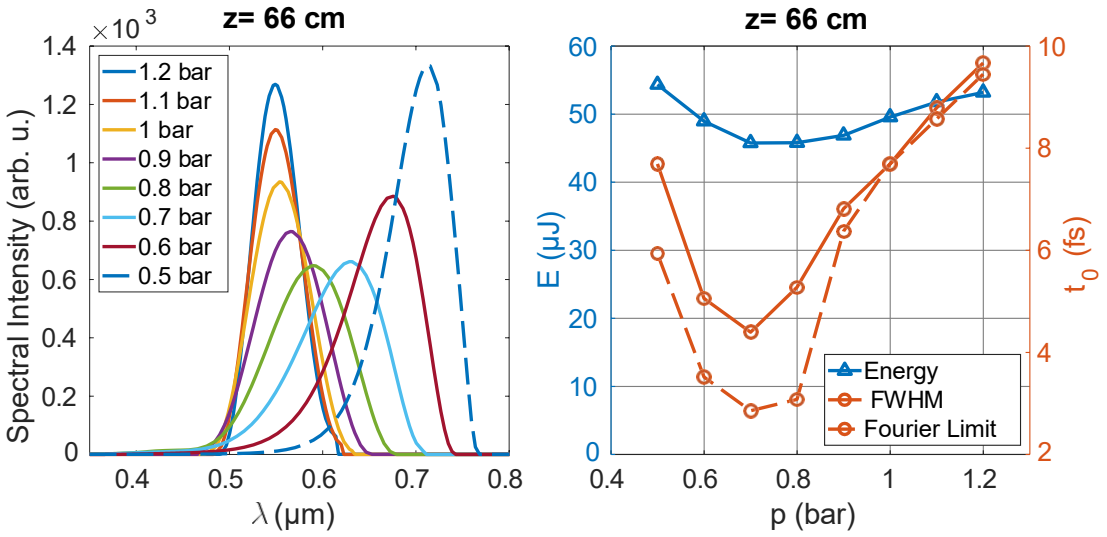

Figure 6.8: This figure shows the comparison of the spectral bands in the normal dispersion region (left) and the comparison of the energies and pulse duration of each band (right), both for different constant pressures inside the HCF at 66 cm obtained from the propagation of a necklace beam with 6 beads.

this optimal region the spectral phase of the output pulse is not perfectly balanced, and it could be post-compressed to a Fourier Limit pulse of 3 fs of duration. Nevertheless, all the pulses obtained are good ultrashort visible energetic pulses, according to the literature (see Fig. 6.9).

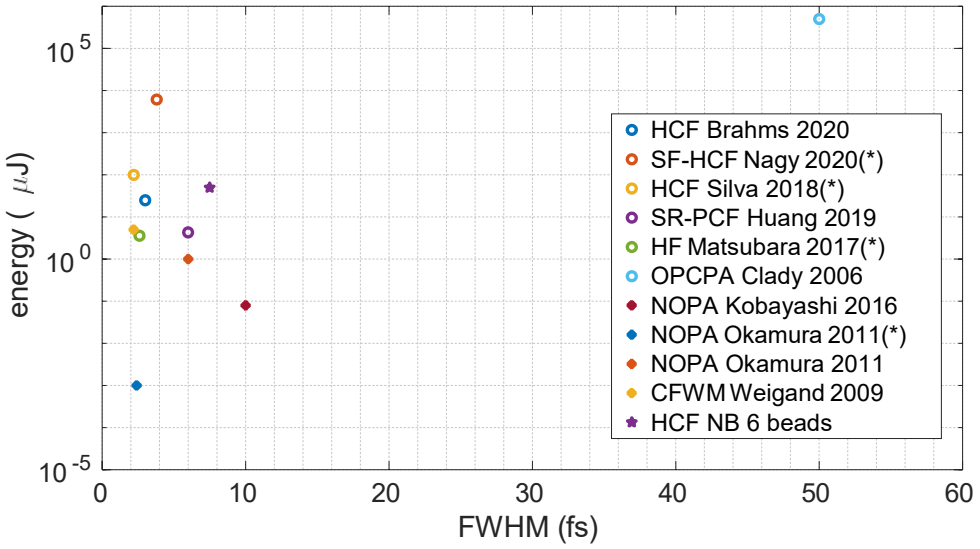

Figure 6.9: This figure shows the comparison, in log scale, of our ultrashort energetic visible pulse (purple star marker), obtained through the propagation of a necklace beam with 6 beads, with the already generated visible pulses from the literature. ((*)Energy and FWHM duration of the total pulse).

Another parameter we have explored is the laser wavelength. Since the two-band spectrum is a consequence of the important role of the third-order dispersion, we have plotted the dependence of the third order dispersion (TOD) and the second order dispersion (GVD) with the laser wavelength, for a necklace beam with six beads centered at 800 nm propagating in a HCF of 150 μm filled with argon at 1 bar. We can observe in Fig. 6.10 that at longer laser wavelengths the effect of the third-order dispersion is even larger, but also the second order dispersion increases and gets more negative, which means that the self-compression effect should be more efficient (in the sense that the linear and nonlinear phase should be balanced). To increase the effect of the third-order dispersion compared to the second order dispersion, we should use laser wavelengths close to the zero-dispersion wavelength (679 nm in this case).

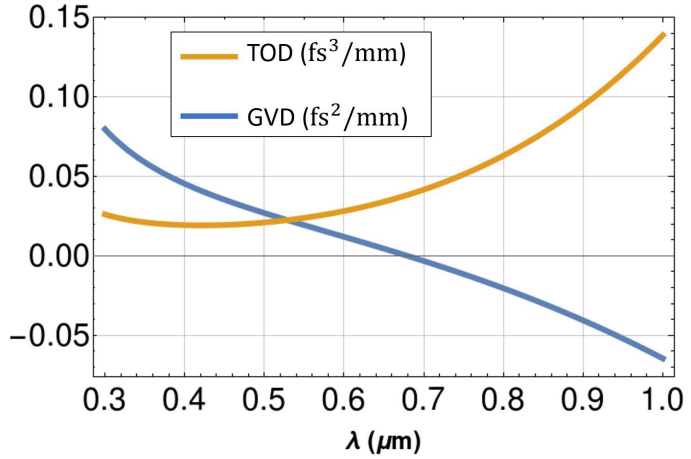

Figure 6.10: This figure shows the dependence of the second-order dispersion (GVD, blue line) and the third-order dispersion (TOD, yellow line) with the laser wavelength for a necklace beam with 6 beads centered at 800 nm propagating in a HCF of 150 μm filled with argon at 1 bar.

In Fig. 6.11 we present the propagation dynamics of the same necklace beam with six beads of 35 fs and 0.2 mJ of energy, propagating in a HCF of 150 μm core radius filled with argon at 1 bar, the same as in the previous section, but centered at 1 μm. This figure shows the evolution of the spectral intensity distribution in log scale (left), of the temporal intensity distribution in linear scale (center) and of the FWHM duration (right), at the peak intensity of the first bead. The self-compression in this case occurs at 42.5 cm inside the HCF (see 6.11 (right)), this distance is 20 cm shorter than in the 800 nm case, which means that the self-compression effect is more efficient as expected. The pulse duration at FWHM is 3.5 fs, shorter than the one obtained in the 800 nm case. On the other hand, the self-compression effect is so strong that the soliton fission occurs before the spectral band reaches the normal dispersion region and thus the blue band does not reach the visible spectral region (see 6.11 (left)). Note that in this case the central wavelength is farther from the zero-dispersion wavelength (ZDW) at 679 nm

and the spectral broadening is not enough before the soliton fission occurs, at around 43 cm.

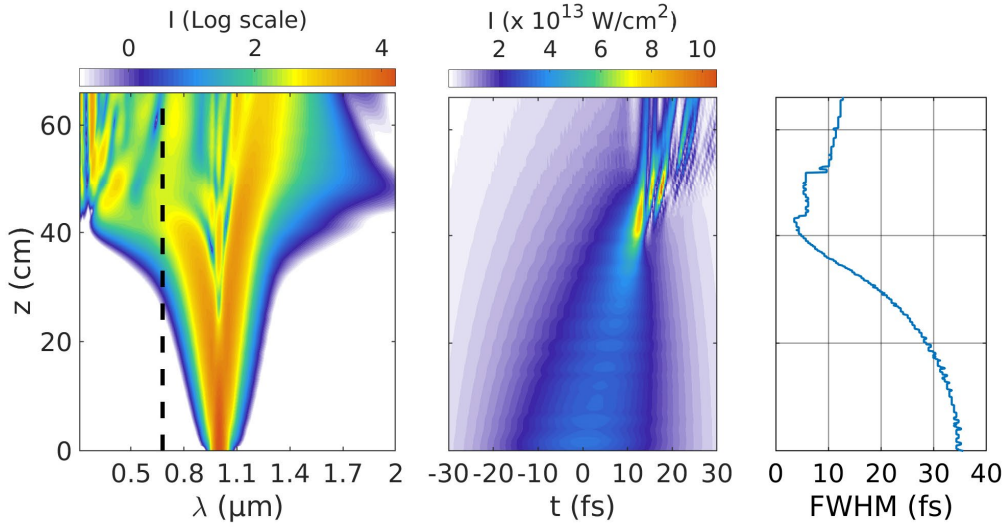

Figure 6.11: Evolution of the spectral intensity distribution in log scale (left), of the temporal intensity distribution in linear scale (center) and of the FWHM duration (right), at the peak intensity of the first bead of a necklace beam with 6 beads centered at 1 μm. The dashed line in the left panel represents the ZDW at 679 nm.

The cases with laser wavelengths close to the zero-dispersion wavelength are represented in Fig. 6.12. We present the propagation dynamics for three different laser wavelengths: 679 nm (top row), 700 nm (middle row) and 750 nm (bottom row). Each row shows the evolution of the spectral intensity distribution in log scale (left panels), of the temporal intensity distribution in linear scale (center panels) and of the FWHM duration (right panels), at the peak intensity of the first bead. The dashed line in the left panels is the zero-dispersion wavelength (ZDW) at 679 nm.

In the case where the central wavelength is 679 nm (Fig. 6.12 top row), at the beginning the dispersion is almost zero. The evolution of the FWHM duration (right panel) shows that, at the beginning of the propagation, the pulse almost maintains its duration besides some oscillations. However, as the spectrum broadens due to self-phase modulation, the pulse does not really propagate at the zero-dispersion wavelength and the pulse duration increases [Agrawal, 2013]. We can observe that, at the end of the propagation, the pulse has started to self-compress reaching 18 fs, which means the spectrum is broad enough for the anomalous dispersion to compensate the chirp from self-phase modulation.

In the case of 700 nm (Fig. 6.12 middle row), as the central wavelength is very close to the zero-dispersion wavelength, the pulse also maintains its pulse duration at the beginning of the propagation due to the small dispersion that it suffers. However, a

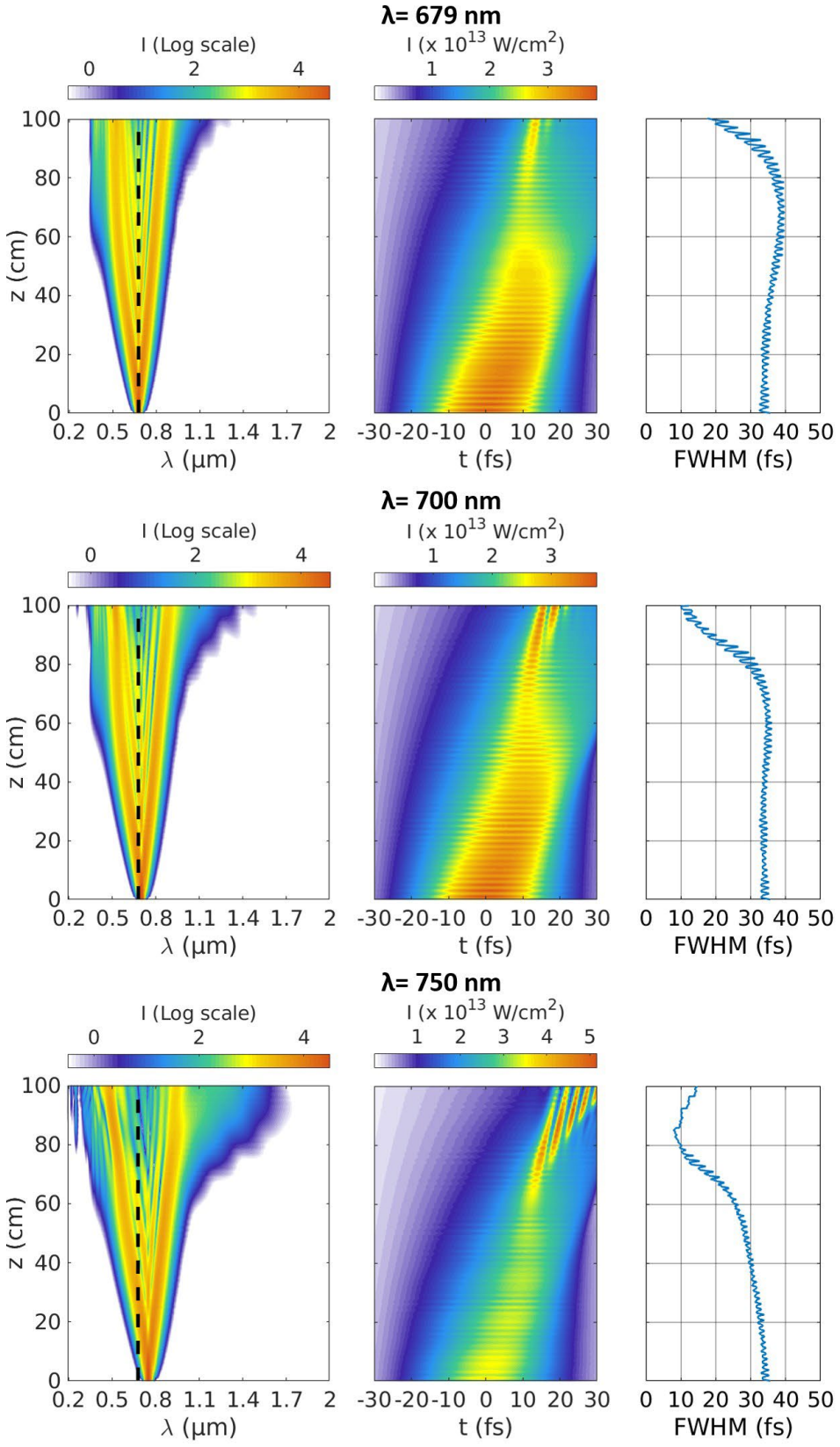

Figure 6.12: Evolution of the spectral intensity distribution in log scale (left), of the temporal intensity distribution in linear scale (center) and of the FWHM duration (right), at the peak intensity of one bead of a necklace beam centered at 679 nm (top), at 700 nm (middle) and at 750 nm (bottom). The dashed line in the left panels is the ZDW (679 nm).

self-compression effect starts at the end of the propagation, as in the previous case, and the pulse duration reaches 12 fs.

In the last case we present, at 750 nm (Fig. 6.12 bottom), the second-order dispersion is enough to compensate the chirp from the self-phase modulation from the beginning of the propagation. The pulse experiences a self-compression down to 8 fs at 85 cm inside the HCF. This dynamics is similar to the one obtained in the 800 nm case, although the self-compression distance and pulse duration are longer, as expected.

The spectral broadening in each case presents the two-band structure and it is wide enough to reach the normal dispersion region, that is the main purpose of this study. We can filter again the spectral band in the normal dispersion region in each case and compare them at the same distance where the self-compression was optimum for the 800 nm and 1 bar case, at 66 cm, as if it were the actual HCF length. In Fig. 6.13 (left) we compare the filtered visible band obtained for different laser wavelengths and we can observe that the visible bands are centered between 500 and 600 nm. The visible bands shift to the blue side of the spectrum when the laser wavelength is shorter.

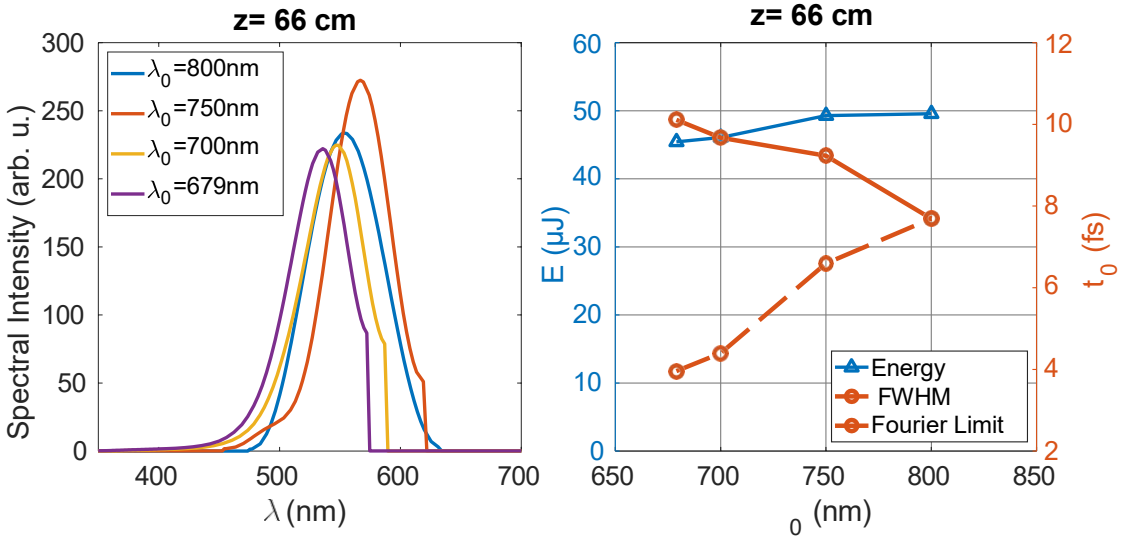

Figure 6.13: Left panel shows the comparison of the spectral bands in the normal dispersion region, and right panel shows the comparison of the energies (blue triangles) and pulse duration (orange circles) of each band, both for different laser wavelengths at 66 cm inside the HCF. The Fourier limit is represented by the orange dashed line.

We have also calculated the energy and the temporal duration of the bands at 66 cm inside the HCF to observe the dependence with the laser wavelength. The blue triangles in Fig. 6.13 (right) show that the energy of the visible band is always around 50 μJ. The temporal duration at FWHM of the pulse obtained from the visible band in each case, is represented by the orange circles in Fig. 6.13 (right), and its Fourier Limit is represented

by the orange dashed line. As we can see, the pulse duration is always between 8-10 fs. However, it seems that only the case of 800 nm is perfectly balanced, whereas for other input wavelengths the visible band could be post-compressed to a Fourier Limit pulse of 4 fs of duration. Again, all the pulses obtained are good ultrashort visible energetic pulses.

6.3 Spatial Robustness of the Beam along the Hollow Capillary Fiber

In this section we would like to see what occurs if the input necklace beam profile is not ideal. First of all, we should emphasize that we wanted to avoid any self-focusing effect, so in the energy regime that we have chosen for our necklace beams, the spectral broadening was enough to reach the visible part of the spectrum, but without entering in the self-focusing regime. For this reason, we remained below the critical power of a Gaussian beam. To calculate the critical power we use Eq. 4.2 again, $P_{cr} = N_{cr}\lambda^2/(4\pi n_L n_{NL})$, where $N_{cr} = 1.8962$, $\lambda_0 = 800$ nm and n_L and n_{NL} are the linear and nonlinear refractive indexes of argon. With these parameters, the input peak power of our necklace beams is $P = 0.96P_{cr}$, so each bead would be carrying a fraction of the total energy and would not be able to collapse, as we have already shown in Fig. 6.4 [Grow et al., 2007]. Of course, in case that the self-focusing effect appears, we could not observe the beam collapse since the ionization would inhibit it.

Under these conditions we have already demonstrated, in Subsection 6.1.2, that a pure necklace beam shows a nice spectral broadening, keeping a very good spatial quality and without any spatial collapse. According to the literature, in the situation of a non-ideal necklace input beam, it would become unstable (the stability of the beam depends on the fiber geometry and the number of beads) during the nonlinear propagation inside the HCF if the input power of each bead is above $0.06P_{cr}$ [Fibich and Shpigelman, 2016]. As we are well above this threshold, we should see an energy transfer between beads that becomes more significant as the beam propagates inside the HCF.

To test numerically how relevant this situation could be, we have simulated the propagation of the same necklace beams presented in Fig. 6.3 with four beads, six beads and eight beads, but with the first bead (labelled “B #1” in Fig. 6.14) having 5% more energy, as it is usually done in similar stability analyses [Fibich and Shpigelman, 2016]. We propagate the necklace beams centered at 800 nm with 0.2 mJ and 35 fs of duration in a HCF with 150 μm core radius filled with argon at 1 bar, the same parameters used in the previous simulations.

As expected, there is an energy transfer between beads but, in the moderate power regime that we use, the structure holds during the whole propagation distance. In Fig. 6.14 we show the results obtained for a non-ideal necklace beam with four beads (top row), six beads (middle row) and eight beads (bottom row). In each row of Fig. 6.14, the left panels show the beam fluence for the non-ideal case, at the self-compression distance (z_{sc}) of the pure input case, which is 103 cm for the necklace beam with four beads, 66 cm for six beads and 51 cm for eight beads. As it can be observed, the spatial structure is kept and, although during the propagation some of the beads acquire high peak intensity values, we have not observed any self-focusing dynamics. Comparing the beam fluence of the necklace beam with four beads and eight beads, it seems that necklace beams with a higher number of beads are more resistant to instabilities during the propagation. To confirm this apparent tendency we have also propagated a necklace beam with 16 beads. In this case the anomalous dispersion is so strong that it self-compresses from 35 fs to 1.75 fs in 25 cm of propagation inside the HCF. The beam again is stable, but since the propagation length is so short, the spectrum is not wide enough to obtain the visible band in the spectrum, which was our aim in this work. There is a visualization of the evolution of the non-ideal beam profile with six beads in [Crego et al., 2021].

In Fig. 6.14, center and right panels represent the spectral and temporal distribution of beads #1 (which initially has 5% more energy) and the opposite beam (#3 in the necklace beam with four beads, #4 in the case of six beads and #5 for the eight-bead beam) at the self-compression distance of each necklace beam and at the peak intensity point. We can see that the spectral and temporal distribution are different depending on the bead. It is clear that the spectral broadening towards the visible and the temporal self-compression are still there but, of course, not equally in all the beads of the beam. These observations are easily explained because not all beads carry the same amount of energy during the propagation. We see that there are only some beads of the beam that reach high peak intensity values during the propagation and only those are able to self-compress as the ideal beam. Moreover, these beads are located opposite to each other, so they do not self-compress at the same propagation distance.

We have calculated the weighted average spectral and temporal distribution from the non-ideal beam This weighted average is calculated taking into account the relative energy of each bead. In Fig. 6.14, center and right panels show the calculated weighted average spectral and temporal distribution in the non-ideal case at the self-compression distances (green lines) and we compare them with the spectral and temporal distribution from ideal beams (dark blue dashed lines) presented in Subsection 6.1.2. We can observe that they are quite similar, although the spectral and intensity distributions for two particular beads are different.

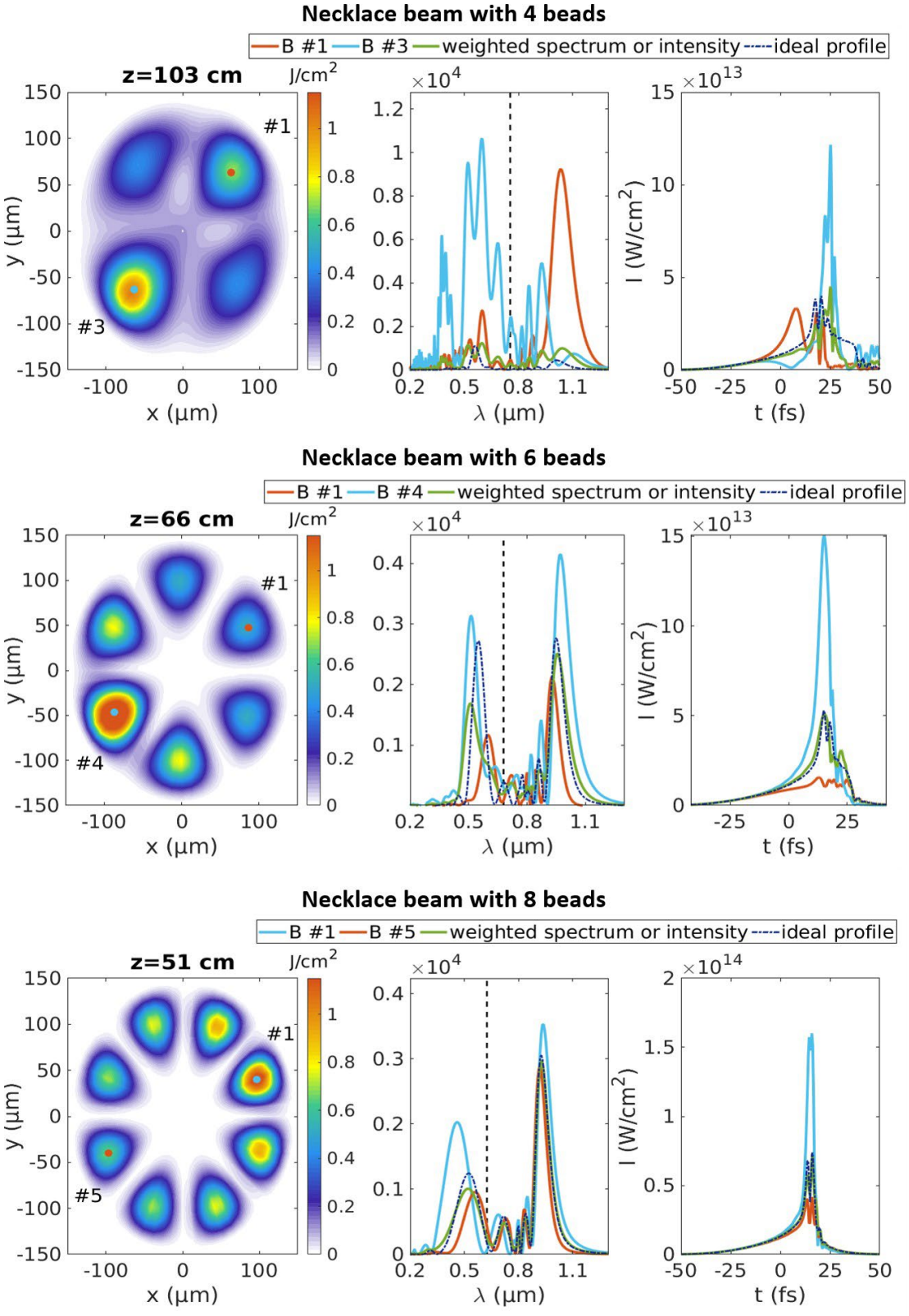

Figure 6.14: Beam fluence of a non-ideal input beam at z_{sc}=103 cm (top), 66 cm (middle) and 51 cm (bottom) for 4, 6 and 8 beads. Spectral (center) and temporal (right) profile at the intensity peak at two beads (orange and light blue markers) and the weighted average spectral and temporal intensity distribution at z_{sc} (green line). The dark blue dashed lines represent the ideal beam case. Vertical black dashed lines show the ZDWs (754, 679 and 625 nm respectively). Note the change in beads colors in the case of 8 beads.

In view of the spatial profiles at the self-compression distances shown in Fig. 6.14 (left), we can identify the optimal bead (the one with higher energy) and select it. The spatial selection of part of the beam would produce a decrease of the output energy. In the case of the necklace beam with four beads, since the blue part of the spectrum is very modulated, the energy of the visible band for bead #3 at 103 cm is 5.7 μJ. For the case of six beads the energy of the visible band for bead #4 is 14.6 μJ at z=66 cm. The last case, the necklace beam with eight beads, the energy of bead #1 is 8.06 μJ at 51 cm.

We can filter the visible band, considering the weighted average spectral distribution at the self-compression distance, and calculate the energy in the non-ideal case, not for one bead, but for the whole beam. In the case of the non-ideal necklace beam with four beads, the energy of the visible band is 9.4 μJ, which is less than a quarter of the energy of the visible band in the ideal case. In the case of non-ideal necklace beams with six beads and eight beads, we obtain an energy in the visible band of 37.3 μJ and 25.73 μJ, respectively, which are not far from the ideal cases. On the other hand, Fig. 6.14 (right) indicates that the self-compression of the selected bead could be even better compared to the ideal case, especially in the cases of six and eight beads. For that purpose, we calculate the FWHM duration of the bead with higher energy at the self-compression distance in each case. For the non-ideal necklace beam with four beads we calculate the FWHM duration of bead #3 and we obtain 8.13 fs, while the FWHM duration in the ideal case at 103 cm is 12.08 fs. In the case of the non-ideal necklace beam with six beads we obtain a FWHM duration of 6.15 fs in bead #4, while the temporal FWHM in the ideal case is 7.5 fs. In the case of the non-ideal necklace beam with eight beads we obtain a FWHM duration of 2.2 fs in bead #1, while we obtain a temporal FWHM in the ideal case of 3.5 fs. Therefore, it is true that this non-ideal situation would somehow deteriorate the output pulse, basically the output energy, but it will still be useful. We can see that this degradation is especially remarkable for beams with a low number of beads. Moreover, we must emphasize that we are in a power regime in which the instability is not large enough to couple all the energy into one bead and activate a self-focusing process.

Once again, we have checked if the ionization is significant in the case of a non-ideal beam. We have propagated the same non-ideal six-bead necklace beam but without ionization. Although at the beginning the dynamics is similar to the case with ionization, the energy transfer between the beads coming from the nonlinear instability leads to an increment of the peak power in one bead at certain moments during the propagation, overcoming the critical power at 48.5 cm, in this particular case. Therefore, the role of the ionization is crucial here since it avoids the collapse of the beam at 60 cm when one bead, #1 in this case, keeps almost all the available energy so the beam is able to collapse, as we can expect after the study on self-focusing done in Chapter 4. In Fig. 6.15

we show the beam fluence at the collapse distance (left), the evolution of the spectral intensity distribution (center) and of the FWHM duration (right) at the peak intensity at bead #1. Due to the high intensity, and hence the high nonlinearity achieved in the case of the non-ideal beam, the effect of the ionization is much more significant than in the ideal beam case.

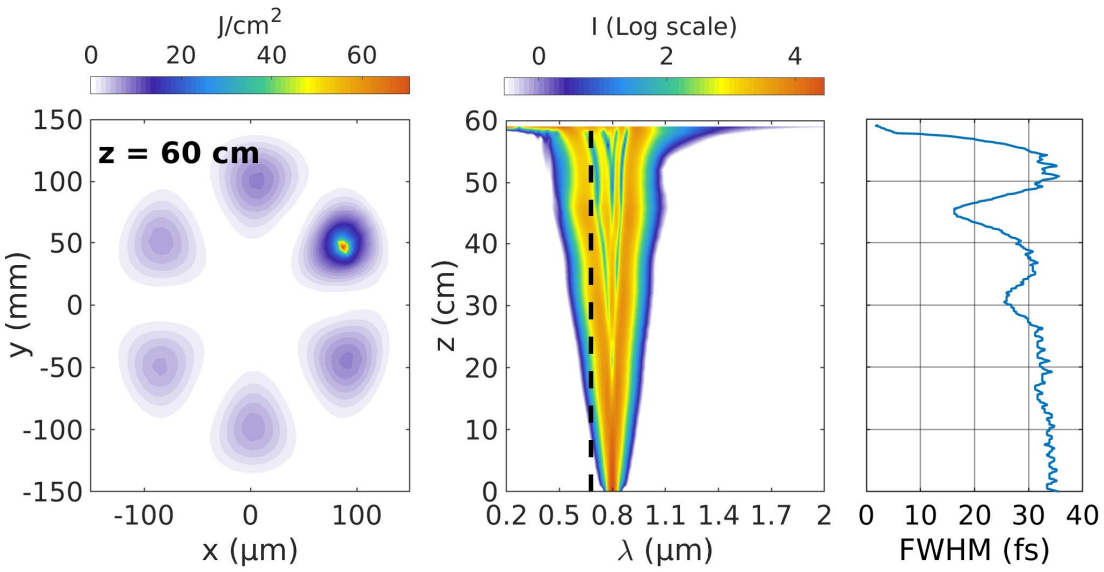

Figure 6.15: Collapse of a necklace beam with 6 beads at 60 cm without taking into account the ionization. Left panel shows the beam fluence at z_{sc}=60. Center and right panels show the evolution of the spectral intensity distribution in log scale at the peak intensity at one bead (center), marked as #1, and of the FWHM duration (right). The black dashed line shows the ZDW (679 nm)

6.4 Conclusions

In conclusion, we have found that high-energy ultrashort pulses in the visible region of the spectrum can be generated in standard HCFs using infrared necklace beams as driving pulses. The interplay between the high nonlinearity and the dispersion broadens the spectrum in such a way that the energy is mainly concentrated in two spectral bands, one of them reaching the visible part of the spectrum during the propagation. In addition, the self-compression of the pulse is observed due to the anomalous dispersion that these beams present.

Filtering this spectral band, we can obtain pulse energies of around 50 μJ and pulse durations below 10 fs using a 150 μm core radius HCF filled with argon at different constant pressures. The high efficiency (around 25% of the input energy) and the wavelength tunability of the process for different gas pressures inside the HCF, demonstrate that the soliton self-compression of infrared necklace beams in HCFs filled with gas could

be a compact tool which paves the way to new short laser pulse sources in the visible region.

We have observed that depending on the pump wavelength, the interplay between the high nonlinearity and the dispersion is different. As a result, the optimum pump wavelength is the one in which the linear and nonlinear phase balanced together, so the pulse experiences self-compression, but the spectral broadening is wide enough to reach the normal dispersion region at the end of the propagation.

We have also demonstrated that when using non-ideal input necklace beams, where there is a nonlinear energy transfer between the beads, they still present a similar spectral band and a temporal self-compression, although only in those beads that reach high peak intensity values during the propagation. Even in this non-ideal case, self-focusing does not play a role in the dynamics of the beam since the ionization prevent the beam collapse.

Chapter 7

Dispersive Wave Generation inside Hollow Capillary Fibers

Tunable ultrashort pulses in the ultraviolet are useful for different applications, such as optical frequency metrology [Ye and Cundiff, 2005] and pump-probe spectroscopy [Hockett et al., 2011]. The way of generating these sources is through frequency-conversion schemes, such as those using nonlinear crystals [Johnson et al., 2009, Ringling et al., 1993], high-harmonic generation [Durfee et al., 1997, Rundquist et al., 1998] or selecting the desired wavelength from a broadband spectrum [Jiang et al., 2015, Liu et al., 2010], which reduces the spectral brightness. In general, these techniques are limited by the optical damage of the material and the post-compression setups. In addition, they usually produce ultraviolet radiation with a narrow bandwidth, so the generation of ultrashort and energetic pulses in this spectral region with these techniques is challenging.

Hollow capillary fibers (HCFs) are an alternative system to generate ultraviolet light. Under certain conditions these systems present anomalous dispersion, which combined with the nonlinear pulse propagation dynamics, can lead to the generation of light at wavelengths shorter than the pump through the phase-matched dispersive wave emission from the propagating soliton. Wavelength-tunable dispersive wave emission from the ultraviolet to the infrared has been demonstrated in gas-filled photonic crystal fibers [Cassataro et al., 2017, Joly et al., 2011, Mak et al., 2013, Novoa et al., 2015], taking advantage of the Raman response of molecular gases for a more effective spectral broadening and pulse compression [Luan et al., 2021] and also in HCFs [Brahms et al., 2019, 2020, Travers et al., 2019]. Dispersive wave generation in HCFs presents several advantages compared to other frequency generation methods: the wavelength can be tuned through the fiber geometry, gas species and pressure, the conversion efficiency is higher than in the high-harmonic process and its duration can be of just a few femtoseconds.

In addition, HCFs have broad ultraviolet transparency and a high damage threshold, which allows to scale up the energy.

As mentioned previously, the tunability of the dispersive wave turns this emission into an important tool for different applications where a desired wavelength is needed, for instance, in atomic or nuclear clocks. Atomic clocks have been used since its first demonstration in 1949 at the National Institute of Standards and Technology in Boulder (Colorado). The procedure to measure the time is based on the interaction of microwave, optical or ultraviolet radiation with the excited states of an atom. Optical atomic clocks are the current basis of precise atomic clocks, reaching accuracies of 10^{-18}, which means not losing or gaining one second in 30 billion years [von der Wense and Chuankun., 2020]. The accuracy of this time measurement is important to achieve a greate temporal precision in scientific experiments and in different applications, such as telecommunications and satellites [Boulder Atomic Clock Optical Network (BACON) Collaboration*, 2021].

Since higher frequencies increase the precision, one of the most challenging goals in this research area is the pursuit of a nuclear clock. The operation principle is the same, however, the difference is using a nuclear transition instead of a transition between electronic energy levels for time measurement. The difficulty to implement this theory lies in the very high frequency and thus energy, necessary for nuclear transitions, which is not accessible with present narrow bandwidth laser sources. However, there is an exception, the excitation energy to the first nuclear excited state in ^{229}Th thorium isomer, is comparable to typical electronic transitions in the atomic shell, which could be used for a nuclear clock with better precision [Campbell et al., 2012, Peik and Tamm, 2003]. The excitation energy between the ground state and the first excited state has been measured recently to be about 8.3 eV, which corresponds to a wavelength of 149.7 ± 3.1 nm [Seiferle et al., 2019]. Since there is no broadband gain medium available in the ultraviolet region, a laser oscillator is not possible at the moment. This wavelength can be generated through nonlinear conversion in nonlinear crystals, high-harmonic generation or frequency comb technology. Nevertheless, it is possible to generate radiation at this wavelength through the dispersive wave generation process in HCFs, a more compact and efficient process.

In this chapter we will study the generation of dispersive waves through the soliton self-compression effect in HCFs. First, we will study the dispersion properties of HCFs and the phase-matching condition between the soliton and the dispersive wave. We will obtain the theoretical formulas that estimate the wavelength of the dispersive wave. We will study the dependence of the phase-matching condition with different parameters, such as gas pressure and the laser wavelength.

In the second section of this chapter, we will study the nonlinear propagation of the fundamental mode EH_{11} and the dispersive wave emission using the (2+1)D model, explained in Section 3.2 in Chapter 3, and a simplified version of this model that only includes the temporal dynamics (time-dependent (1+1)D model). We will give a complete description of the dispersive wave generation process, its tunability and calculate its duration and energy. We will also try to gain some insight into the effect of the multimode nature of the HCF in the dispersive wave emission process. Although in the (1+1)D simulations the generation of the dispersive wave is quite clean, the multimode nature of the HCF emerges with the (2+1)D simulations, showing a more structured dispersive wave emission. In the last section of this chapter we will introduce the scaling rules to choose the right laser and HCF parameters to obtain a dispersive wave at a desired wavelength, for instance, 150 nm that is related to the excitation energy in ^{229}Th. We will perform a pump wavelength scan with the time-dependent (1+1)D and (2+1)D models, achieving the same nonlinear dynamics in each case.

7.1 Properties of the Dispersive Wave Emitted in Hollow Capillary Fibers

The dispersion in a HCF is the combination of the material dispersion, the filling gas in our case, and the HCF dispersion itself. The gas dispersion is usually small due to the low density, but one of the advantages of the HCF is the possibility of tuning the HCF dispersion easily through the gas pressure and species and make the overall dispersion anomalous ($D < 0$). This makes HCFs ideal for ultrafast applications. The dispersion is usually calculated from the frequency dependence of the propagation coefficient β_{pq} of each spatial modes [Marcatili and Schmeltzer, 1964], defined in Eq. 2.67, and it depends on the gas pressure through the linear refractive index of the gas. The expression for the dispersion of each spatial mode is defined in Eq. 2.36, where the propagation coefficient k is replaced by β_{pq}.

$$D(\omega) = \sum_{m\geq 2} \frac{1}{m!}(\beta_{pq})_m(\omega - \omega_0)^m \tag{7.1}$$

During the pulse propagation inside HCFs, the anomalous dispersion that the pulse experiences, combined with the self-phase modulation, leads to soliton formation and soliton self-compression process resulting in an ultrashort pulse with a high intensity peak. This self-compression process is accompanied by an important spectral expansion. In general, solitons are stable but in the presence of certain perturbations they become unstable, which can cause the break-up of the soliton into its fundamental components,

a phenomenon known as soliton fission. Some of these perturbations are the higher-order dispersion [Höök and Karlsson, 1993, Wai et al., 1990] and the non-instantaneous nonlinear response of the medium. The instability of the soliton due to the third-order dispersion is manifested as a shed of energy to a certain frequency in the normal dispersion regime, produced under perfect phase matching conditions, separated from the soliton spectrum [Akhmediev and Karlsson, 1995]. This emitted radiation from the soliton in the normal dispersion region is usually known as dispersive wave emission.

7.1.1 Phase-Matching Condition of the Dispersive Wave

In this section we are going to obtain the theoretical formulas for the phase-matching condition between the soliton and the emitted dispersive wave. While the soliton propagates nonlinearly in the anomalous dispersion region, the dispersive wave propagates linearly in the normal dispersion region. We can express the propagation coefficients and calculate the frequency of the dispersive wave, which is determined by the phase-matching between them:

$$\begin{aligned} \beta_{sol}(\omega) &= \beta_{pq}(\omega_{sol}) + (\beta_{pq})_1(\omega_{sol})(\omega - \omega_{sol}) + \frac{\omega_{sol} n_{NL} I_{sol}}{2c} \\ \beta_{DW}(\omega) &= \beta_{pq}(\omega) \approx \beta_{pq}(\omega_{sol}) + (\beta_{pq})_1(\omega_{sol})(\omega - \omega_{sol}) + D(\omega) \\ \Delta\beta &= \beta_{DW}(\omega) - \beta_{sol}(\omega) = 0 \end{aligned} \tag{7.2}$$

where we have considered that the soliton and the dispersive wave propagate as the pq-spatial mode of the HCF. Subscripts indicate frequency derivatives and $D(\omega)$ denotes the higher-order dispersion terms, as defined in Eq. 7.1. The parameter I_{sol} is the self-compressed peak intensity and ω_{sol} is the soliton frequency. The soliton propagates with the group velocity of the HCF spatial mode with an additional small nonlinear phase that is often small compared to the other terms [Akhmediev and Karlsson, 1995]. The dispersive wave propagates linearly at a different frequency, experiencing the normal dispersion of a HCF spatial mode.

Considering the anomalous propagation of the fundamental mode in the HCF, and not taking into account the energy transfer from the fundamental mode to a dispersive wave in a higher-order mode, we can calculate the phase-matching condition by finding the frequency that solves the following equation:

$$D(\omega) - \frac{\omega_{sol} n_{NL} I_{sol}}{2c} = 0 \tag{7.3}$$

As mentioned above, these dispersive waves are tuneable changing the pressure and hence the dispersion of the medium, which changes the phase-matching relation. In

Fig. 7.1 we show the dependence of the phase-matching condition $\Delta\beta$ with the gas pressure for neon (top) and argon (bottom) in two different systems. In the case of neon, this is the phase-matching condition for a pulse centered at 800 nm propagating in the fudamental mode of a HCF with 100 μm core radius, while in the case of argon the pulse propagates as the fundamental mode, centered at 1800 nm through a HCF with a core radius of 150 μm. We can observe that the phase-matching occurs in the ultraviolet region of the spectrum in the case of neon for different pressures. For a 800 nm laser beam, phase-matched solutions can be achieved from 160 to 240 nm. In argon the dependence with the pressure is stronger.

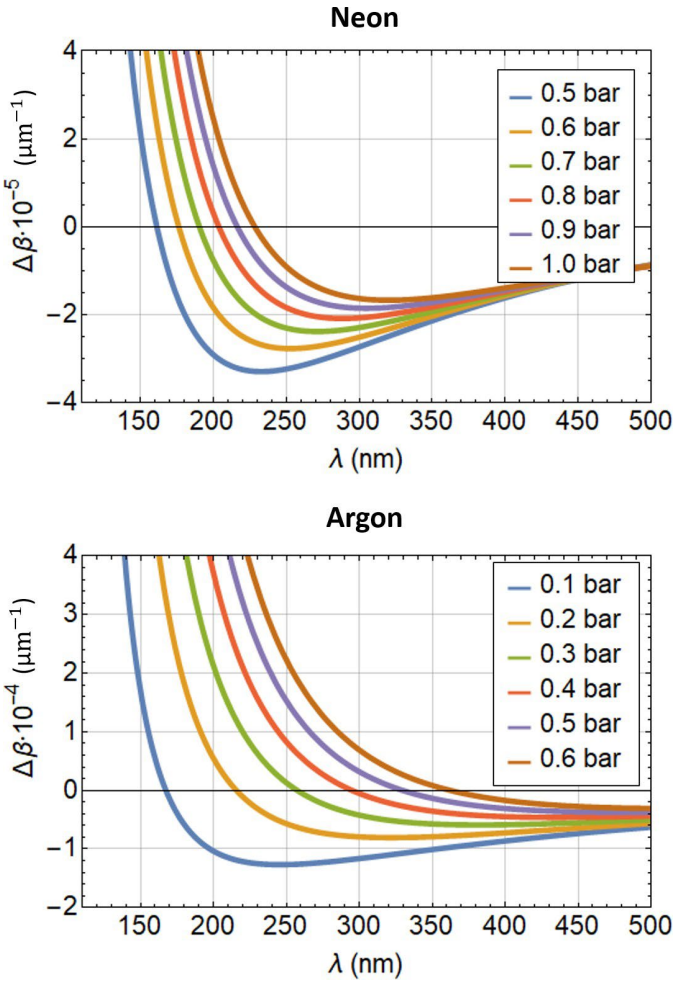

Figure 7.1: Top panel represents the phase-matching condition of a dispersive wave pumped by a 800 nm pulse propagating in a HCF with 100 μm core radius filled with Ne as a function of the gas pressure. Bottom panel represents the phase-matching condition of a dispersive wave pumped by a 1800 nm pulse propagating in a HCF with 150 μm core radius filled with Ar as a function of the gas pressure.

7.2 Dispersive Wave Generation Process

In this section we will give a complete description of the dispersive wave generation process. For this purpose we will propagate through the HCF a laser pulse with anomalous dispersion. Consequently, we expect to observe the soliton self-compression process and the emission of the dispersive wave in the propagation dynamics. We will study the tunability of the dispersive wave wavelength, its energy and the temporal duration. In this study we have performed simulations with the time-dependent (1+1)D model and the (2+1)D model. The initial condition to solve numerically Eq. 3.12 is again 4.8.

We simulate the propagation of a 50-fs laser pulse with 0.62 mJ input energy and centered at 1800 nm inside a 2-meter long HCF with 150 μm core radius filled with Ar at 0.2 bar (we choose the parameters based on the phase-matching condition results shown in Fig. 7.1 (bottom)). The expression for the linear refractive index of argon is the same as presented in Eq. 4.10 and the nonlinear refractive index is $n_{NL} = 1.74 \cdot 10^{-23} \cdot p$ (m²/W), where p is the gas pressure [Couairon et al., 2008]. We assume that the pulse is coupled to the fundamental mode of the HCF, EH_{11} mode. For these particular parameters the zero-dispersion wavelength is 737 nm, which means that the dispersion is anomalous. In Fig. 7.2 we show the (1+1)D propagation dynamics. The top left panel shows the evolution of the on-axis temporal intensity distribution, while the top right panel shows the evolution of the on-axis spectral intensity distribution. Both panels represent the characteristic propagation dynamics in a self-compression process. It is clear from Fig. 7.2 (top left), that the pulse duration, which is initially 50 fs, becomes shorter along the propagation until it reaches 2.18 fs, below one-cycle duration for a pump wavelength of 1800 nm due to the spectral broadening achieved. This optimal pulse self-compression occurs at z_{sc}=150 cm inside the HCF. During the propagation, the dispersion and the self-phase modulation balance each other, leading to the formation of the soliton at 140 cm inside the HCF. On the other hand, in the evolution of the spectrum shown in Fig. 7.2 (top right), we can observe a symmetric spectral broadening due to self-phase modulation and, at the point of optimal pulse self-compression (z_{sc}=150 cm), the spectrum expands shedding energy in the ultraviolet region around 204 nm, in good agreement with the dispersive wave predicted from the phase matching condition and depicted in Fig. 7.1. This emission is the dispersive wave, resulting from an energy transfer from the soliton to this particular frequency placed in the normal dispersion region. In Fig. 7.2, bottom left and right panels represent the temporal and spectral intensity profile at the point of maximum self-compression (150 cm). In Fig. 7.2 (bottom left) the self-compressed pulse presents an intensity profile with features from a soliton self-compression process. It has a long front tail with the peak of the pulse located at the trailing part. The generated dispersive wave propagates at a different group velocity and, at some point, it interferes

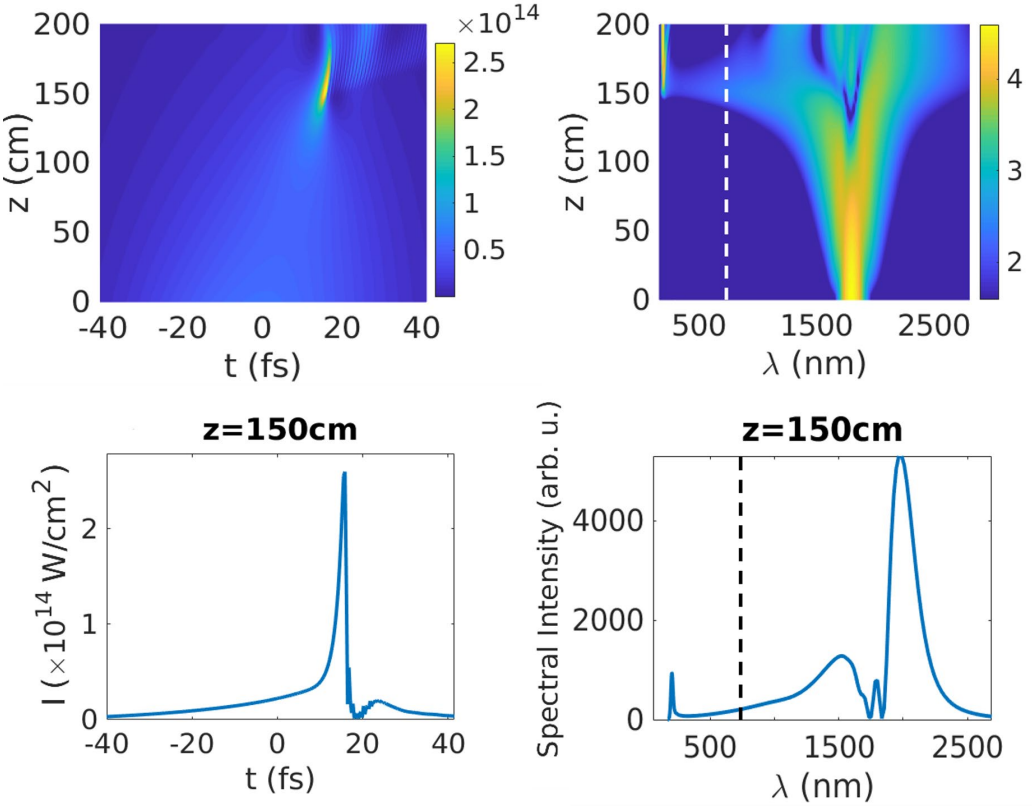

Figure 7.2: Temporal intensity (W/cm^2) evolution (top left) and spectral intensity evolution in log scale (top right) of a 50-fs pulse centered in 1800 nm with 0.62 mJ, propagating inside a HCF with 150 µm core radius filled with Ar at 0.2 bar using the (1+1)D model. Temporal and spectral intensity profile (bottom left and bottom right respectively) at the point of maximum self-compression (150 cm). The ZDW is represented as dashed lines. We use the (1+1)D model.

with the soliton causing the appearance of some amplitude oscillations at the trailing part of the pulse, as one can find in the literature [Köttig et al., 2017, Travers et al., 2019]. In the spectral intensity evolution (Fig. 7.2 bottom right) we can observe the spectral broadening and at the optimal pulse compression at z_{sc}=150 cm, the spectrum expands leading to the formation of a dispersive wave at 204 nm.

Since this dispersive wave lies within the normal dispersion region, it broadens as it propagates away from the soliton, which explains the second structure behind the main peak observed in Fig. 7.2 (bottom left). As a consequence of this dynamics, the soliton is unstable and these perturbations cause the soliton fission and the saturation of the spectral broadening, as can be seen in the top panels from 150 cm until the HCF output.

7.2.1 Features of the Dispersive Wave

To use this ultraviolet emission as an ultrashort laser source, one may wonder what the features of this dispersive wave are. For this reason, we are going to study its tunability

with the wavelength and the gas pressure, but also the energy and the pulse duration of this radiation.

For simplicity, we use again the (1+1)D model to perform a wavelength scan from 1400 nm to 1800 nm. We propagate the same pulse of 50 fs and 0.62 mJ inside a HCF with 150 μm core radius filled with Ar at 0.2 bar, but changing the pump wavelength. As expected, the phase-matching condition is different for each case and the emission of the dispersive wave occurs at a different wavelength. In Fig. 7.3 (left), we plot the spectral intensity profile of the dispersive waves obtained from different pump wavelengths, at the point of optimal self-compression in each case. The wavelength of the dispersive waves obtained with the theoretical formulas in this case are: 216 nm pumped by 1800 nm, 228 nm pumped by 1700 nm, 241.5 nm pumped by 1600 nm, 258 nm pumped by 1500 nm and 278.5 nm pumped by 1400 nm. Comparing these estimations with the numerical values from Fig. 7.3 (left), the agreement is satisfactory. We can observe that the distance where the dispersive wave is generated varies in each case (see the legend), being longer for shorter pump wavelengths, which is consistent with a lower anomalous response since they are closer to the zero-dispersion wavelength. According to the tunability, we can see that the wavelength of the dispersive wave depends on the pump wavelength in such a way that it blue-shifts for longer pump wavelengths.

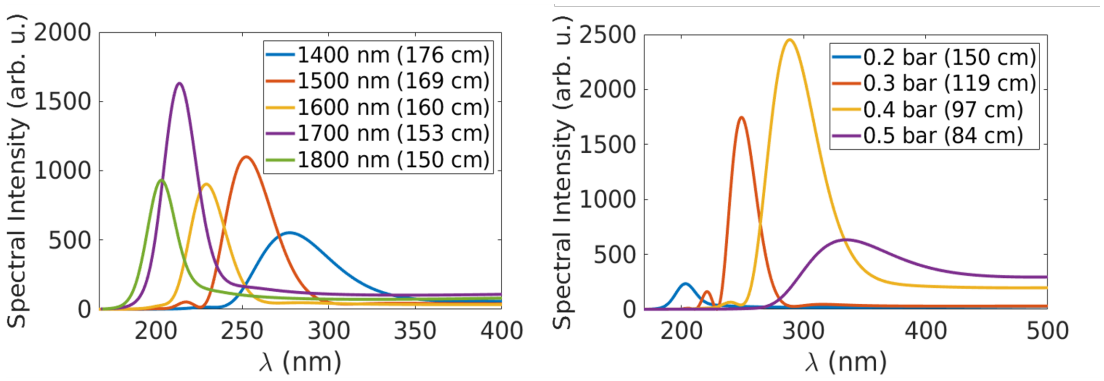

Figure 7.3: Spectral intensity profiles of the dispersive waves generated from different pump wavelengths (left) or different constant pressures inside the HCF (right) at the point of optimal self-compression in each case (indicated in the legend). We use the (1+1)D model.

Another parameter we can easily change in a real experiment to tune the dispersive wave is the gas pressure. We propagate the same pulse, centered at 1800 nm, changing the constant argon pressure inside the HCF. We perform a pressure scan from 0.1 to 0.5 bar. In Fig. 7.3 (right), we plot the spectral intensity profile of the dispersive waves obtained for different constant pressures in the HCF, at the point of optimal self-compression in each case. The wavelength of the dispersive waves with these parameters obtained with the theoretical prediction from Fig. 7.1 are: 215.5 nm for 0.2 bar, 257.5 nm for 0.3 bar,

295 nm for 0.4 bar and 328 nm for 0.5 bar. The agreement of these estimations with the results from the (1+1)D model shown in 7.3 (right) is again fairly good. A lower pressure means also a lower nonlinearity, so we can observe that for lower pressures the dispersive wave is generated at longer distances (see legend). In fact, the case of 0.1 bar is not plotted since we have not observed the dispersive wave emission in the HCF length (2 m). Related to the tunability, it is clear that a higher pressure red-shifts the dispersive wave wavelength with a dependence that seems stronger than changing the pump wavelength.

Since we know that the spectral tuning of the dispersive wave is easily accessible, if we want to use this emission as an ultrashort source we have to calculate its duration and the amount of energy transferred to it from the soliton. For this reason, we have filtered the dispersive wave spectrally and reconstructed the temporal structure of the ultraviolet pulse for the case presented in Fig. 7.2 (1800 nm, 50 fs, 0.62 mJ and Ar at 0.2 bar). In Fig. 7.4 (left) we show the FWHM duration of the dispersive wave (purple line) and the corresponding Fourier Limit (green line) from z=150 cm, the point where the dispersive wave is generated. At this point, the FWHM duration has a value of 1.87 fs, the same as the Fourier Limit and also similar to the FWHM duration of the soliton at this point. However, despite the low pressure, as the dispersive wave propagates in the normal dispersion region of the HCF it broadens reaching 26.75 fs at the HCF output.

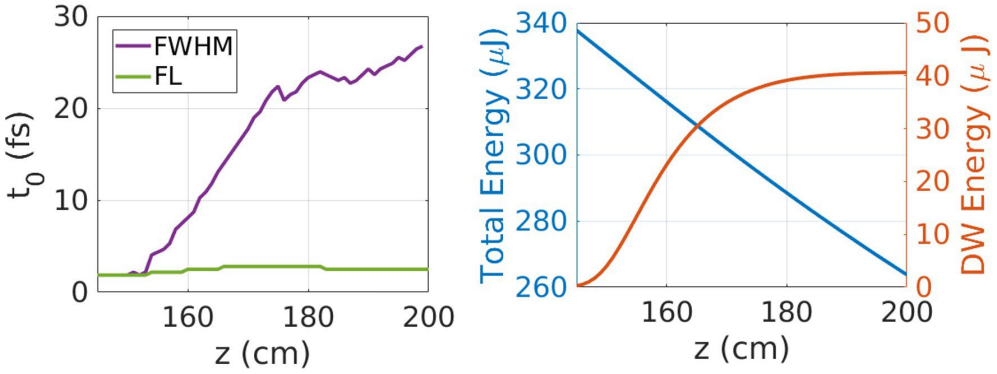

Figure 7.4: Left panel shows the evolution of the FWHM (purple line) and Fourier Limit duration (green line) of the generated dispersive wave. Right panel shows the evolution of the total pulse energy (blue line) and the energy of the dispersive wave (orange line) from the point where it is generated.

On the other hand, Fig. 7.4 (right) shows the energy of the dispersive wave (orange line) together with the total energy of the pulse (blue line). We can see that at the point of the dispersive wave emission (150 cm) the energy is low, less than 4 µJ, but as it propagates in the HCF more energy is transferred to it reaching 40.62 µJ at the HCF output. We can calculate the efficiency of the process as the amount of the energy that goes to the dispersive wave from the total pulse energy at the HCF input. We obtain

an efficiency of 0.65% at 150 cm, but an efficiency of 6.6% at the HCF output. From this discussion we can deduce that it is possible to obtain an ultrashort source from the dispersive wave, if the emission occurs near the HCF output, but the energy would be low. On the contrary, if we are interested in an energetic dispersive wave, the more it propagates inside the HCF the more energy it gains, but its duration grows along the propagation.

One last feature we can study is the multimode nature of the dispersive wave generation process and the influence of the spatial dynamics and the ionization of the medium. So far, we have studied the nonlinear propagation and the dispersive wave generation process with the time-dependent (1+1)D model. This model does not include neither the spatial dynamics nor the ionization, so the simulations are single mode and the energy transfer between the soliton and the dispersive wave is always in the same spatial mode, the fundamental one in this case. However, taking into account the spatial dynamics could lead to the emission of different dispersive waves that might be related with the appearance of other spatial modes besides the fundamental mode [López-Zubieta et al., 2018b] and the generation of plasma.

We have propagated with the (2+1)D model the 50-fs pulse with 0.62 mJ centered at 1800 nm in a HCF filled with 0.2 bar of Ar. Figure 7.5 shows the comparison of the nonlinear propagation obtained with the (1+1)D (orange lines) and the (2+1)D model (blue lines). In Fig. 7.5 (right) we have plotted the evolution of the FWHM duration and we can see that it is quite similar with both models, meaning that neither the spatial dynamics nor the ionization are significant during the propagation. However, there is a small disagreement near the dispersive wave generation point (150 cm).

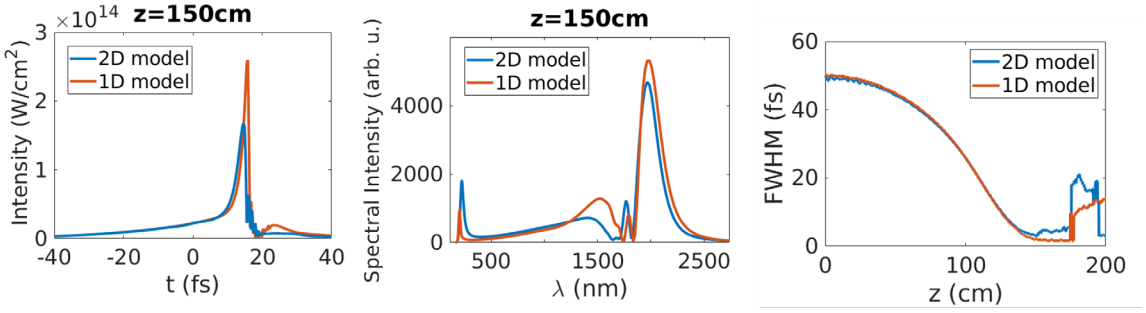

Figure 7.5: Comparison of the results from the (1+1)D model (orange lines) and the (2+1)D model (blue lines). Left panel shows the on axis temporal intensity profile, center panel shows the on axis spectral intensity profile and right panel shows the evolution of the FWHM duration of a 50 fs pulse centered in 1800 nm with 0.62 mJ, propagating inside a HCF filled with Ar at 0.2 bar.

Left and center panels of Fig. 7.5 show the comparison of the temporal and spectral intensity profile at the dispersive wave generation point. There, we can observe that

the dynamics is practically the same, however the intensity peak is lower in the (2+1)D model and the dispersive wave is slightly shifted to 224 nm, which presents the same difference with respect to the theoretical formulas and the (1+1)D model. The origin of the frequency shift of the dispersive wave in the (1+1)D model and the (2+1)D model could be the effect of the generated plasma, but we have not found a complete explanation of this shift.

Figure 7.6 shows a comparison of the spectral intensity profile of the dispersive wave from the (1+1)D model and the (2+1)D model at 150 cm (left) and at the HCF output (center). We have already discussed that there is a red shift of the wavelength of the dispersive wave obtained from the (2+1)D model with respect to the one obtained from the (1+1)D model at the generation point (at 150 cm, Fig. 7.6 (left)). The differences between both dispersive waves are more important at the HCF output (Fig. 7.6 (center)) because the dispersive wave obtained from the (2+1)D model is significantly more structured than the one obtained with the (1+1)D model. Although it is hard to identify exactly the origin of this structure it must be related to the ionization and the multimode nature of the propagation, that is only kept by the (2+1)D model.

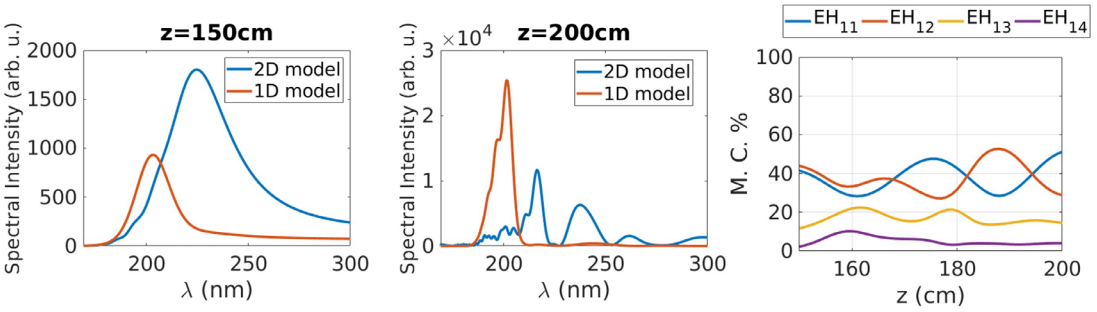

Figure 7.6: Spectral intensity profile of the dispersive wave from the (1+1)D model (orange line) and the spectral intensity profile from the (2+1)D model (blue line) at 150 cm (left) and at the HCF output (center). Right panel shows the mode contribution of the first four spatial modes to the dispersive wave.

To expose the relevance of the higher spatial modes in this particular situation, Fig. 7.6 (right) shows the mode decomposition of the dispersive wave, illustrating the substantial contribution of different spatial modes to the emission during the process of emission of the dispersive wave along the propagation. We have filtered the dispersive wave to calculate the evolution of its energy and FWHM duration. In this case, the energy and the FWHM duration obtained with the (1+1)D model and the (2+1)D model match at the generation point (less than 2 fs and 4 μJ at 150 cm), but as the dispersive wave propagates the evolution differs, due to the multimode nature of the beam reaching a lower energy and a longer FWHM duration at the end of the HCF with the (2+1)D model (33 fs and 27 μJ at 200 cm). Note that although the spectra shown in Fig. 7.5 (left) indicates that the dispersive wave generated from the (2+1)D models is more

intense than the one obtained with the (1+1)D model, these two spectra are just on-axis spectra. Therefore, to calculate the energy of the whole dispersive wave we have to take into account the complete spatio-spectral distribution, which finally results in a lower energetic dispersive wave from the (2+1)D model.

7.3 Route to Dispersive Wave Generation at a Fixed Wavelength

Once we have studied in detail the dispersive wave emission process, in this section we will try to gain some insight into the choice of the particular laser and HCF parameters to obtain a dispersive wave at a desired wavelength.

As mentioned before, deep and vacuum ultraviolet sources have several applications in spectroscopy and photochemistry [Reinert and Hüfner, 2005, Sansone et al., 2010]. Broadband ultraviolet sources could be used to produce ultrashort pulses for precise temporal, spectral and spatial measurements of the electronic and vibrational dynamics of molecules [Galli et al., 2019, Polli et al., 2008] and in particular, we already mentioned the interest in nuclear clocks. For all these reasons, we will focus on the generation of a dispersive wave centered in 150 nm, in the region of the vacuum ultraviolet (100-200 nm).

First we have to choose the laser wavelength and the gas species. From the phase-matching condition shown in Fig. 7.1 we can infer that neon with a pump wavelength at 800 nm is suitable for the dispersive wave generation in vacuum ultraviolet, since in argon the pressure is quite low in this region and it presents a resonance at 105 nm. In fact, from Fig. 7.1 we can obtain precisely the gas pressure to achieve the dispersive wave at the desired wavelength, which will be close to 0.5 bar. We are going to propagate the fundamental mode EH_{11} with 35 fs and 0.33 mJ inside a HCF with 100 μm of core radius filled with neon at 0.5 bar. Using the (1+1)D model as a first approximation, we perform a pressure scan around 0.5 bar to obtain the right pressure for generating the dispersive wave at 150 nm we find that 0.468 bar is a very good choice. The nonlinear refractive index of neon is $n_{NL} = 0.14 \cdot 10^{-23} \cdot p$ (m²/W) in the core [Couairon et al., 2008], p being the gas pressure, and for the linear refractive index we use the following expression [Dalgarno and Kingston, 1960]

$$n_L(\lambda, p) = \sqrt{1 + p \cdot 1.335 \cdot 10^{-4} \left(1 + \frac{2.24 \cdot 10^5}{\lambda^2} + \frac{8.09 \cdot 10^{10}}{\lambda^4} + \frac{3.56 \cdot 10^{16}}{\lambda^6}\right)} \tag{7.4}$$

With the chosen parameters the zero-dispersion wavelength (419 nm) is shorter than the pump wavelength and we expect to activate the self-compression process, the subsequent soliton formation and the generation of the dispersive wave. The (1+1)D propagation dynamics of the pulse at 800 nm in a 3.5 m long HCF is the following:

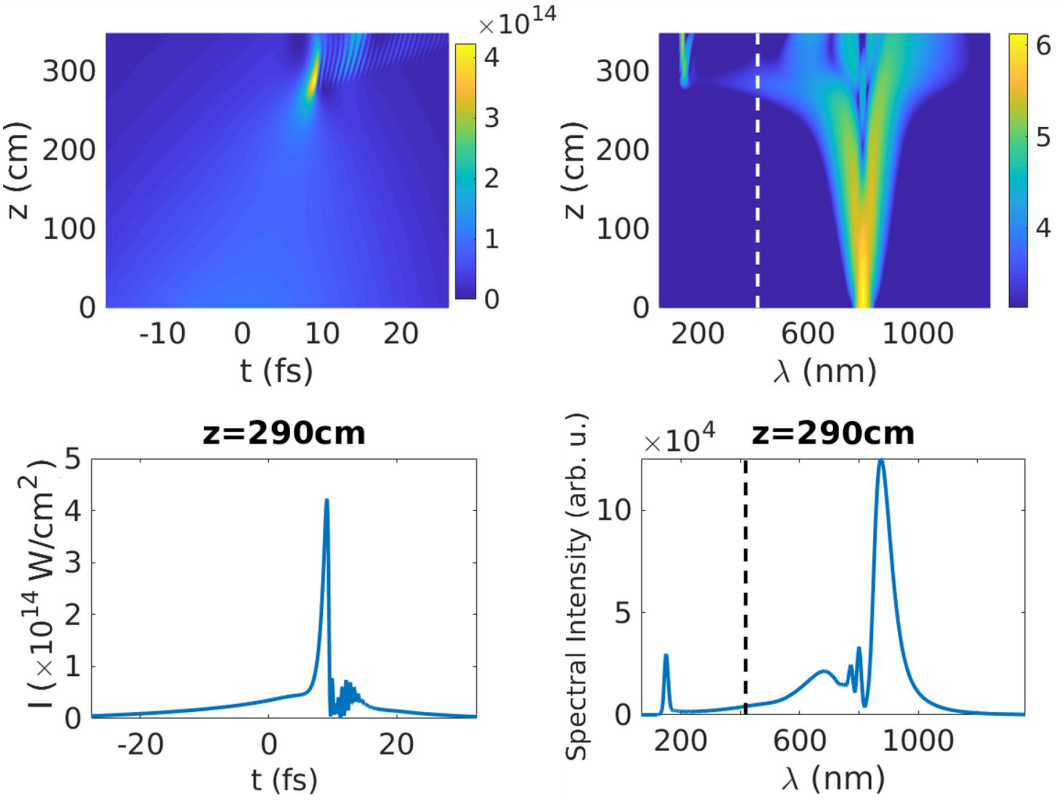

Figure 7.7: Temporal intensity (W/cm^2) evolution (top left) and on spectral intensity evolution (arb. u.) in log scale (top right) of a 35-fs pulse centered in 800 nm with 0.33 mJ, propagating inside a HCF with 100 µm core radius filled with Ne at 0.468 bar using the (1+1)D model. Temporal and spectral intensity (bottom left and bottom right respectively) at the point of maximum self-compression (290 cm). The ZDW is represented as dashed lines.

Figure 7.7 shows the distinctive propagation dynamics in a self-compression process, as we have already explained in the previous section. We can observe the soliton formation and the self-compression process in the evolution of the on-axis temporal intensity distribution (Fig. 7.7). The evolution of the spectral broadening is clearly represented in Fig. 7.7 (top right). At the point of optimal pulse compression at z_{sc}=290 cm, the spectrum shows the emission of a dispersive wave at 150 nm, in agreement with the theoretical predictions. As can be seen in the spectral intensity profile at 290 cm shown in Fig. 7.7 bottom right, the dispersive wave generation process is quite clean. Figure 7.7 (bottom left) shows the temporal intensity profile at 290 cm. The self-compressed pulse has the characteristic long front tail and the intensity peak at the trailing part of the pulse. Once more, we can observe the amplitude oscillations at the trailing part due to the interference between the self-compressed pulse and the dispersive wave.

7.3.1 Scaling Rules for Dispersive Wave Generation at a Fixed Wavelength

The nonlinear propagation dynamics depends on the dispersion of the HCF and its dependence with the laser parameters and gas pressure. The propagation dynamics is different depending on the interaction between nonlinearity and dispersion. One may wonder if it is possible to obtain the same dynamics using another pump wavelength. The answer to this question is that we can find the same dynamics we have observed at 800 nm using another pump wavelength, but the remaining laser and HCF parameters must be chosen carefully. In this subsection we determine the scaling rules to obtain the same dispersive wave generation process for different pump wavelengths in approximately the same distance in the HCF . The method we have followed consists in several steps:

1. Pulse duration

The first thing we change is the pulse duration t_0 to match the number of cycles (n_c) of the new pump wavelength ($\lambda^{(2)}$) with the 800 nm case ($\lambda^{(1)}$).

$$t_0^{(2)} = n_c^{(1)} \frac{c}{\lambda^{(2)}} = \frac{\lambda^{(2)}}{\lambda^{(1)}} t_0^{(1)} \tag{7.5}$$

where c is the velocity of light in vacuum. Therefore, the duration of the new pulse will be fixed and related with the duration of the reference one.

2. HCF core radius

Assuming that the losses of the pulse during the propagation correspond to the HCF itself and they do not depend on the pressure of the filling gas, the next parameter we have to change is the HCF size. This way we obtain the same propagation losses with the new pump wavelength as in the 800 nm case. The HCF losses are given by the absorption coefficient a_{pq} defined in Eq. 2.67. From this equation we assume that the losses are related with the pump wavelength and the HCF core radius as

$$a \approx \frac{\lambda^2}{r_F^3} \tag{7.6}$$

Matching the absorption coefficients of the new pump wavelength with the coefficient of the 800 nm case, we obtain the corresponding relation between the HCF core radii

$$r_F^{(2)} = \left(\frac{\lambda^{(2)}}{\lambda^{(1)}}\right)^{\frac{2}{3}} r_F^{(1)} \tag{7.7}$$

Therefore, the size of the new HCF must be related to the size of the HCF used with the reference pump wavelength. Until this point, Eqs. 7.5 and 7.7 suggest that the scaling parameter could be $(\lambda^{(2)}/\lambda^{(1)})$.

3. Gas pressure

Once we have scaled the HCF core radius, the next parameter we adjust is the pressure. By changing the pressure we adjust the dispersion of the new wavelength to be the same as the reference case. A different pressure modifies the location of the zero-dispersion wavelength, but not the location of the phase-matching wavelength for the dispersive wave emission since we have already scaled the core radius too.

Since longer wavelengths induce a blue shift and higher pressures lead to a red shift in the dispersive wave emission, following the same reasoning as in the previous parameters, we change the pressure according to the wavelength as follows

$$p^{(2)} = \frac{\lambda^{(2)}}{\lambda^{(1)}} p^{(1)} \tag{7.8}$$

Note that a longer wavelength means a higher pressure inside the HCF, which shifts the zero-dispersion wavelength to the red side of the spectrum, as we have already observed in the previous section.

4. Pulse energy

With the scaling of the pulse duration, the core radius and the pressure we have adjusted the dispersion of the pulse. To obtain the same dynamics for different wavelengths the interplay between the dispersion and the nonlinearity should be the same too. To achieve this we need to scale the energy. One possible solution to establish the input energy would be to compare the nonlinear phase accumulated during the propagation through the B-integral

$$\begin{aligned} B^{(1)} &= B^{(2)} \\ \frac{2\pi}{\lambda^{(1)}} \int_0^{L_F} (n_{NL} \cdot {}^{(1)}) I_0^{(1)} dz &= \frac{2\pi}{\lambda^{(2)}} \int_0^{L_F} (n_{NL} \cdot {}^{(2)}) I_0^{(2)} \\ I_0^{(2)} &= \frac{\lambda^{(2)}}{\lambda^{(1)}} \frac{p^{(1)}}{p^{(2)}} I_0^{(1)} \end{aligned} \tag{7.9}$$

where we have assumed that the nonlinear refractive index n_{NL} is proportional to the pressure, which is a good approximation at low and moderate pressures. We use the input pulse intensity as an estimation and we assume it to be constant along the propagation, since we do not know how the intensity evolves in advance. We can describe the intensity

as a function of the energy of the pulse calculating the energy as

$$E = I(r,\theta,t)\,dr d\theta dt = r\, J_0(u_{0m} r/r_F)^2\, dr d\theta\, I(t)\,dt = \\ = \pi r_F^2\, (J_1(u_{01}))^2\, I_0 I_t \tag{7.10}$$

where I_t is the integral of the temporal intensity distribution. For simplicity we assume a Gaussian distribution $I_t = \sqrt{\pi/2}\, t_0$. So the relation between the input energies can be written as

$$E^{(2)} = \frac{\lambda^{(2)}}{\lambda^{(1)}} \left(\frac{r_F^{(2)}}{r_F^{(1)}}\right)^2 \frac{p^{(1)}}{p^{(2)}} \frac{I_t^{(2)}}{I_t^{(1)}} E^{(1)} = \frac{\lambda^{(2)}}{\lambda^{(1)}} \left(\frac{r_F^{(2)}}{r_F^{(1)}}\right)^2 \frac{p^{(1)}}{p^{(2)}} \frac{t_0^{(2)}}{t_0^{(1)}} E^{(1)} = \left(\frac{\lambda^{(2)}}{\lambda^{(1)}}\right)^{\frac{7}{3}} E^{(1)} \tag{7.11}$$

Again, for longer wavelengths the input energy is higher, which is translated into a blue-shift of the dispersive wave.

Note that this method can be adapted to any available pulse duration, wavelength or HCF size. We have developed this scaling route to obtain the same nonlinear dynamics in the HCF and it works within our model. Let us remember that there are other strategies to implement similar parameter scaling in the literature to obtain the same nonlinear propagation [Chen and Kelley, 2002, Heyl et al., 2016, Travers et al., 2019].

λ_{pump} (nm)	t_0 (fs)	r_F µm	p (bar)	E_{in} (mJ)	λ_{ZDW} (nm)
500	22.04	73.10	0.33	0.10	332
600	26.45	82.55	0.35	0.17	340
800	35.26	100.00	0.47	0.33	419
1030	45.48	118.35	0.61	0.59	484
1100	48.56	123.65	0.65	0.69	503
1200	52.98	131.04	0.69	0.86	525

Table 7.1: Laser and HCF parameters to obtain the same nonlinear dynamics and the dispersive wave emission at 150 nm for different pump wavelengths. We scale the input FWHM duration (t_0), HCF core radius (r_F), Ne pressure (p) and input pulse energy (E_{in}) for each pump wavelength (λ_{pump}). The last column shows the zero-dispersion wavelength in each case.

Using these scaling rules we have performed a wavelength scan from 500 to 1200 nm. In Table 7.1 we show the different laser and HCF parameters obtained for each pump wavelength. In Fig. 7.8 we can observe a comparison of the nonlinear propagation dynamics for all the pump wavelengths, laser properties and HCF parameters presented in Table 7.1. We show the evolution of the spectral intensity distribution in log scale in each case. We observe that the spectral broadening dynamics is almost identical and between 300 and 350 cm the dispersive wave is emitted at 150 nm (we will see that the dispersive wave generated with shorter pump wavelengths is slightly red-shifted).

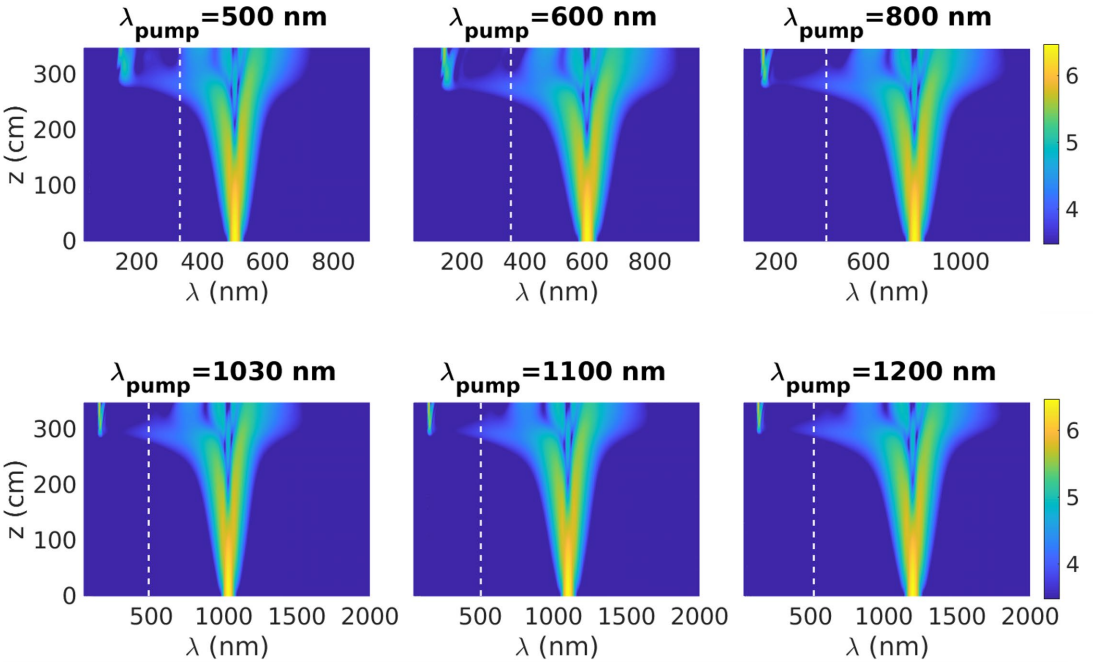

Figure 7.8: Spectral intensity evolution in log scale along the propagation in the HCF for different pump wavelengths using the (1+1)D model. The ZDWs are represented as dashed lines.

Since the input pulse with different pump wavelengths experiences anomalous dispersion at the beginning of the propagation, a soliton self-compression effect is observed in each case. As the dispersive wave is generated almost at the same distance inside the HCF in each case, we assume that the optimal self-compression point is the same for every pump wavelength (290 cm).

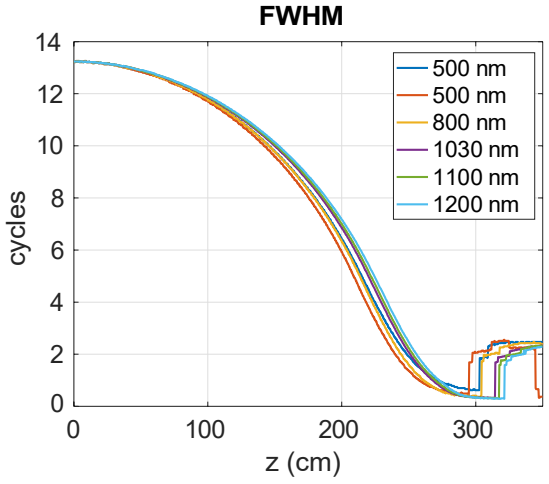

Figure 7.9: Evolution of the FWHM duration for different pump wavelengths, obtained with the time-dependent (1+1)D model. Note that the y axis represents the number of cycles of the pump wavelength in each case.

To check this assumption, we compare in Fig. 7.9 the evolution of the FWHM duration of the pulse (shown in number of cycles of the pump wavelength in each case) with

different pump wavelengths. The self-compression process is always activated and it barely depends on the pump wavelength. For each wavelength, the dispersive wave generation process occurs at similar distances inside the HCF, as expected.

To explore if the dispersive waves are clean and if they shift to other wavelengths along the propagation, we represent their evolution at different distances inside the HCF from the point they are generated until they reach the HCF output. In Fig. 7.10 we show the dispersive waves at three different distances inside the HCF, after they are generated at 300 cm, at 324 cm and very close to the HCF output (at 348 cm). We can observe that at 300 cm almost all the dispersive waves are centered at 150 nm, except in the case of 500 nm as pump wavelength.

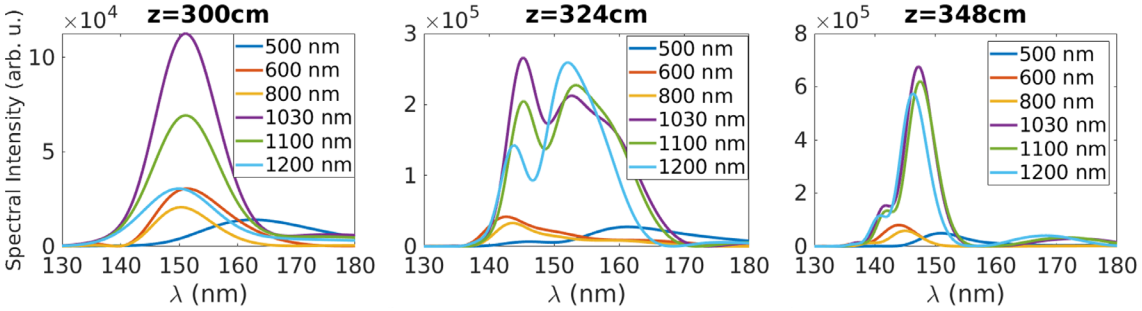

Figure 7.10: Spectral intensity profile of the dispersive waves for different pump wavelengths at 300 cm, 324 cm and 348 cm, obtained with the (1+1)D model.

We have filtered each dispersive wave with a square filter to reconstruct the ultraviolet pulses, and we have calculated their energy along the propagation. Figure 7.11 shows the evolution of the energy of each dispersive wave. The energy increases from the point they are generated until the HCF output.

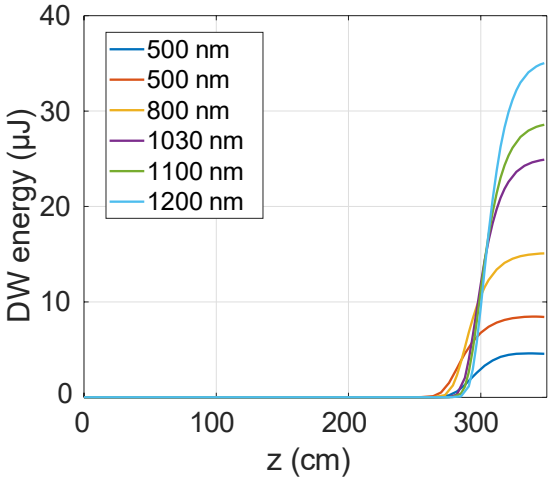

Figure 7.11: Evolution of the energy of the dispersive wave along the propagation distance for different pump wavelengths. The results were obtained with the time-dependent (1+1)D model.

The energy of the dispersive wave is higher for longer wavelengths, but since the input energy is also higher, a more realistic parameter would be the efficiency of the process. We achieve efficiencies between 4-5% , which is a normal efficiency although, recently, an efficiency of 15% of the input energy has been reported with HCFs filled with helium [Travers et al., 2019].

To complete this study on the dispersive wave generation at a desired wavelength, it is convenient to validate the results we have obtained with the (2+1)D simulations, including all the spatio-temporal effects and the plasma that could appear during the propagation. For this reason, we have performed the same simulations done with the time-dependent (1+1)D model, but with the (2+1)D model.

In Fig. 7.12 we show the comparison between the results from the (1+1)D model (solid lines) and the (2+1)D model (dashed lines). We only represent the cases of 500 nm, 800 nm, 1030 nm and 1200 nm for clarity. Figure 7.12 (left) represents the evolution of the FWHM duration, and we can observe that the self-compression dynamics obtained with the (2+1)D model is identical to the one observed with the (1+1)D model, even though we have taken into account the spatial effects and the ionization. We can deduce that neither the ionization nor the spatial dynamics are very significant in this regime, so the propagation dynamics does not change dramatically from what we have already obtained with the (1+1)D model.

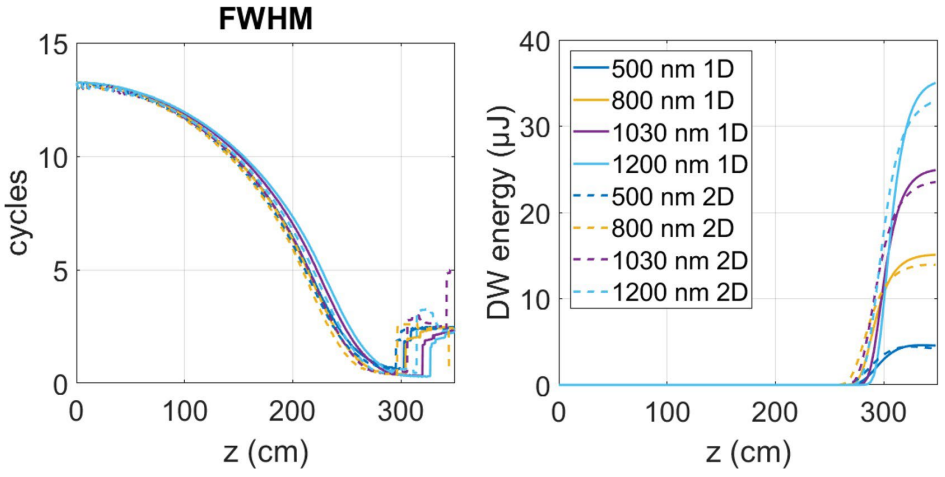

Figure 7.12: Comparison of the evolution of the FWHM duration of the pulse (left) and the energy of the dispersive wave (right), obtained with the (1+1)D model (solid lines) and with the (2+1)D model (dashed lines) for different pump wavelengths.

If we pay attention to the dispersive wave generation process, they are all emitted at 150 nm again for different pump wavelengths. However, they present a more complex structure than in the (1+1)D case. We have filtered spectrally the dispersive waves obtained with the (2+1)D model and we have calculated the amount of energy transferred

to them from the soliton (see Fig. 7.12 (right)). We can observe that the energy of the dispersive waves achieved with both models is similar and the efficiency is also around 4-5% with the (2+1)D model.

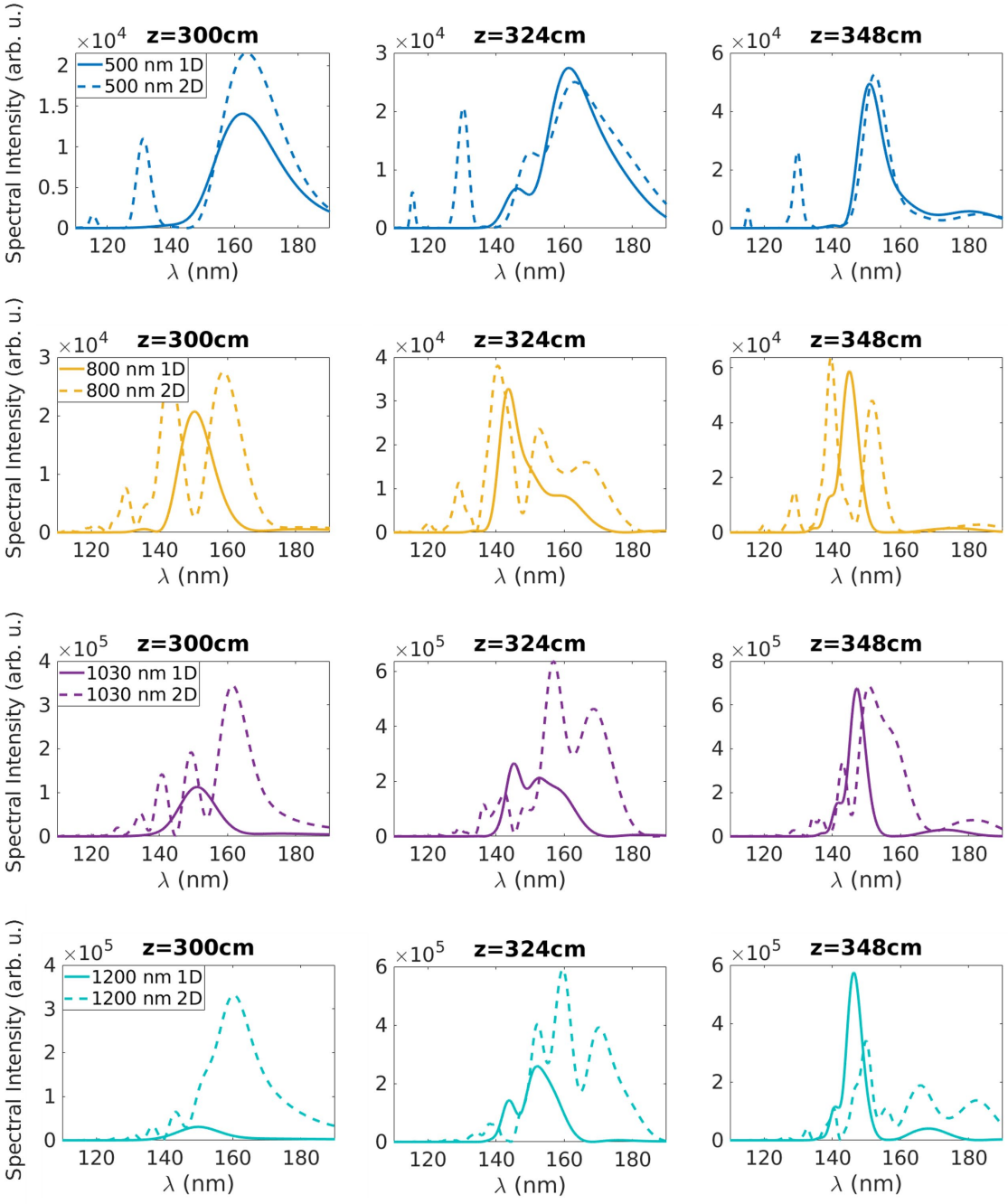

Figure 7.13: Comparison of the spectral intensity of the dispersive waves obtained with the (1+1)D model (solid lines) and with the (2+1)D model (dashed lines) at 300, 324 and 348 cm inside the HCF for different pump wavelengths.

As mentioned above, the dispersive waves obtained with the (2+1)D model present a complex spectral structure, which is the first signature of the multimode nature of these nonlinear propagation cases. In Fig. 7.13 we show the spectral intensity profiles

obtained with the (1+1)D model (solid lines) and with the on-axis spectral intensity profiles obtained with the (2+1)D model (dashed lines) for different pump wavelengths at 300 cm, 324 cm and 348 cm inside the HCF. We can see that while the (1+1)D simulations are single mode and we obtained a clean dispersive wave, in the (2+1)D model, different structures appear in the range from 110 to 180 nm. These new spectral structures that appear in the dispersive waves obtained with the (2+1)D model have been interpreted as dispersive waves emitted from the soliton to other higher-order spatial modes [López-Zubieta et al., 2018a].

We can decompose the pulse resulting from the dispersive wave into the spatial modes of the HCF to determine the mode composition for different pump wavelengths. Figure 7.14 shows the mode composition of the dispersive wave generated with a pump wavelength of 500 nm (left), 800 nm (center) and 1200 nm (right). Note that the x axis corresponds to the distance that the dispersive waves propagate inside the HCF since its generation. We can see that in the 500 nm case the contribution of the EH_{12} is less than 20%, which explains that the dispersive waves obtained in this case with both numerical models present the most similar structure. In the rest of the cases, for longer pump wavelengths the influence of higher-order spatial modes becomes significant making the structure of the dispersive waves more complex.

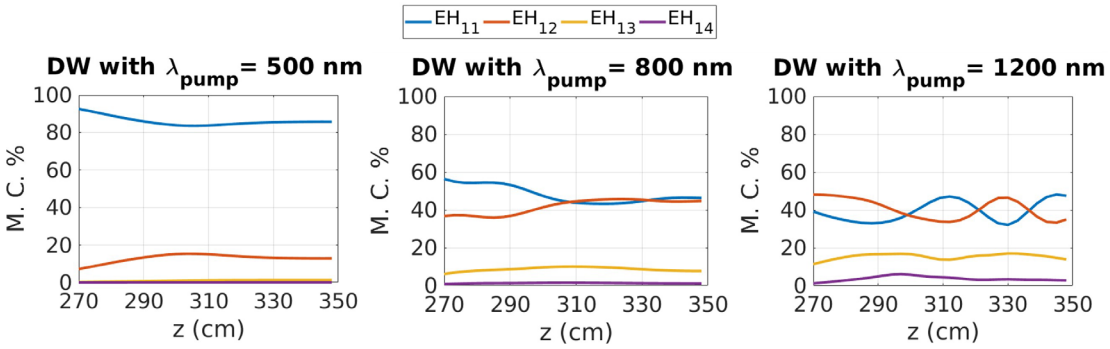

Figure 7.14: Mode contributions to the dispersive waves obtained with the (2+1)D model (solid lines) since its generation until the HCF output for a pump wavelength of 500 nm (left), 800 nm (center) and 1200 nm (right).

Now that we have identified which spatial modes have the most significant contributions, we can calculate when the phase-matching condition, defined in Eq. 7.2, between the soliton in the fundamental mode and the dispersive wave in a higher-order mode is fulfilled following the strategy presented in [López-Zubieta et al., 2018b]. This way we can corroborate the structures present in the spectral intensity profiles from the (2+1)D model, shown in Fig. 7.13. In the case of a pump wavelength of 500 nm, we obtain with the theoretical relations a dispersive wave at 133.72 nm coming from the EH_{12} mode and at 117.1 nm coming from the EH_{13} mode, which are in good agreement with

the first two peaks observed in Fig. 7.13 (top left) at 300 cm. In the case of a pump wavelength of 800 nm, we obtain with the theoretical relations a dispersive wave at 143.44 nm coming from the EH_{12} mode, at 131.45 nm coming from the EH_{13} mode and at 121.85 nm coming from the EH_{14} mode, again these results are in conformity with the first three peaks observed in Fig. 7.13 (center) at 300 cm. The last case we will check is the case with 1200 nm pump wavelength, which presents a more structured dispersive wave. In this case, we obtain theoretically a dispersive wave at 151.48 nm coming from the EH_{12} mode which can be represented by the irregular broadening of the main peak, at 143.81 nm coming from the EH_{13} mode and at 136.34 nm coming from the EH_{14} mode, which can correspond to the second and third small peaks observed in Fig. 7.13 (bottom) at 300 cm. This way we have verified the multimode nature of the dispersive wave.

To conclude this study we can calculate the pulse duration of the dispersive wave. The pulse duration of this ultraviolet light can be ultrashort at the moment of its generation, as we have already seen in the previous section, but since it propagates in the normal dispersion region, it stretches along its propagation. We have calculated the FWHM duration at 300 cm, when it is emitted, and we have obtained a FWHM duration of 1.40-1.20 fs for pump wavelengths between 1200-1030 nm, while with pump wavelengths of 800 nm and 500 nm the FWHM duration are 6.26 fs and 2.95 fs, respectively.

We have checked that the phase-matching equation (Eq 7.2) is a good estimation to identify the emission of the dispersive wave, even from different spatial modes in the HCF. This theoretical approach is enough to represent the results obtained with our numerical models. It is true that a certain amount of disagreement has been observed between the theory and the simulations in some cases, but the deviation is not very significant. However, at high intensities the disagreement could become significant and a correction to the propagation coefficient of the soliton in the form of a nonlinear wavenumber was proposed by Austin et al. [Austin et al., 2006]. The fairly good agreement obtained without this correction in our cases indicates that we are not in such a high intensity regime.

7.4 Conclusions

It is well-known that if we propagate a laser pulse inside a HCF in the anomalous dispersion region with the proper intensity, the interaction between dispersion and nonlinearity will form a soliton during the propagation. The higher-order dispersion terms, and also some other nonlinear effects, perturb this soliton leading to the generation of a dispersive wave in the normal dispersion region. In this work we have shown that dispersive

wave emission in HCFs is a feasible alternative to other frequency-conversion processes to generate ultrashort tunable pulses at wavelengths which are not accessible by current laser systems.

We have studied the dependence of the phase-matching condition between the soliton and the dispersive wave with different parameters in the HCF. Maintaining the pulse duration, the input pulse energy and the core size of the HCF, we explore the features of the dispersive wave emission for different pump wavelengths or constant gas pressures inside the HCF. According to the numerical results, the dispersive wave blue-shifts for longer pump wavelengths, but it red-shifts for higher pressures of the filling gas.

We have found that the possibility of obtaining an ultrashort but also energetic dispersive wave is challenging. The shortest pulse duration is achieved at the moment when the dispersive wave is generated, but since it propagates in the normal dispersion region, it will stretch during the propagation. However, the energy grows with the propagation in the HCF.

We have studied the influence of the multimode nature of HCF systems and the presence of higher-order modes during the propagation. We have found that the appearance of higher-order spatial modes leads to different dispersive waves contributions, resulting in a complex structure in certain cases. We have found that higher-order modes generate dispersive waves at shorter wavelengths.

Finally, we have implemented a parameter scaling route to obtain the same nonlinear dynamics for different pump wavelengths but maintaining the HCF length. As a consequence, the rest of the laser and HCF parameters will change as well to balance the dispersion and nonlinearity in each case. Related to this scaling, we have shown that it is possible to obtain a dispersive wave at a desired wavelength for different pump wavelengths. As an example of these scaling rules, we have generated a dispersive wave at 150 nm, which is a promising laser source for nuclear clocks, in a HCF filled with neon for a wide range of pump wavelengths, always choosing carefully the rest of the parameters involved.

Chapter 8

Conclusions and Perspectives

8.1 Conclusions

We have presented in this thesis a numerical study on nonlinear propagation of ultrashort laser pulses in hollow capillary fibers (HCFs). We have used different numerical models, (1+1)D, (2+1)D and (3+1)D models, where the (1+1)D and (3+1)D models have been developed in the frame of this thesis.

Our starting point was to understand the spatial dynamics and the multimode nature of HCFs in different propagation regimes, since the input energy will be limited by the nonlinear effects. Our objective was to find these limits to avoid the activation of undesirable higher-order nonlinear effects (such as spatial collapse or noticeable ionization), which may distort the spectral phase of the output pulse making it useless for post-compression applications.

In a first set of simulations, we have compared the propagation dynamics of a laser pulse in a HCF using a time-independent model ((1+1)D model) which includes only the spatial dynamics, with a complete spatio-temporal model ((2+1)D model) developed previously in the group. We have demonstrated that the spatial confinement in a HCF of the fundamental spatial mode, EH_{11} mode, plays a key role in the self-focusing process, minimizing the diffraction and enhancing self-focusing. In particular, we have identified two different self-focusing regions in the HCF depending on the input power: for input peak powers slightly greater than the critical power, the collapse appears at shorter distances than in the free space case and independently of the pulse duration. For input peak powers below the critical power, we have obtained spatial collapses induced mainly by the energy transfer between spatial modes, only observable in the (2+1)D model. The spatial collapse dynamics explained in Chapter 4 can be used to identify the energy

limits in any power region when using standard post-compression schemes. In other words, it gives guidance about the optimal length of the HCF that one should use to avoid a strong nonlinear response at the HCF output.

By studying the interplay between the spatial modes, we have found that the energy transfer between the fundamental and the higher-order modes occurs close to the intensity peak of the pulse. Consequently, the generated higher-order modes present a shorter pulse duration and their spectrum is broader. This process can be understood as a compression effect in the energy transfer process itself, which could be an interesting topic for a future research.

Following on the study of the energy scaling in these post-compression setups, we have developed numerical models to study the propagation of structured beams in the HCF in chapters 5 and 6, such as vector beams and necklace beams. One of the main advantages that this type of beams present is that the intensity is more distributed within the core area, so it is possible to couple higher input pulse energies into the HCF. Besides, the possibility of obtaining short structured pulses is very promising for different applications. The numerical study on the nonlinear propagation of vector beams in the HCF has resulted in a very complex dynamics, where the interplay between the spatial modes modulates the intensity and spectrum distribution of the full pulse.

While the spatio-temporal profile of an input EH_{11} beam is almost maintained along the propagation in the HCF despite the appearance of higher-order modes, in the case of an input vector beam the spatio-temporal profile evolves to a complex spatio-temporal distribution. Furthermore, the different polarization signs of the rings from the higher-order modes lead to a constructive or destructive superposition of all of them when they overlap. These spatio-temporal modulations are transferred to the spectrum which shows also a similar spatial inhomogeneity. In the case of the hybrid modes of the EH_{1q} type, the mode superposition is always constructive in the optical axis so the coupling between the modes does not hinder the propagation, which is more stable.

We have generated and propagated vector beams through a HCF at the laser facility in the University of Salamanca with the collaboration of the experimental team in the group. The agreement of the spatial profile of the vector beam measured in experiments with our numerical simulations has served to validate our theoretical model. Nevertheless, we have found coupling issues and lack of polarization maintenance at the HCF output for nonlinear propagation of vector beams. In conclusion, these vector beams could support a higher input energy, but since their propagation in the HCF is less stable, the polarization conversion after the HCF output seems a more robust approach for future investigation.

The second type of structured beams propagating in HCFs that we have considered in this work are necklace beams. In comparison to vector beams, these necklace beams were more stable during the propagation. We have found that the high nonlinearity broadens the spectrum in such a way that the energy is concentrated in two bands, one of them reaching the visible part of the spectrum during the propagation. Filtering this spectral band, it is possible to obtain high-energy ultrashort pulses in the visible region of the spectrum using infrared necklace beams as driving pulses. The high efficiency of the process (25%) and the wavelength tunability for different gas pressures inside the HCF, demonstrate that the soliton self-compression of infrared necklace beams in HCFs filled with gas could be a compact tool to obtain new short laser pulse sources in the visible region. We have also demonstrated that when using non-ideal input necklace beams, where there is a nonlinear energy transfer between the beads, they still present a similar spectral band and temporal self-compression, although only in those beads that reach high peak intensity values during the propagation. Even in this non-ideal case, self-focusing does not play a relevant role in the dynamics of the beam.

From the results obtained with the propagation of necklace beams in HCF, we have explored the idea of generating short pulses in regions of the spectrum which are not directly accessible with current laser systems, such as the visible or the ultraviolet. In the last part of this thesis, we have studied the dispersive wave emission in a HCF as a feasible alternative to other frequency-conversion processes to generate ultrashort tunable pulses at non-conventional wavelengths. We have studied the dependence of the phase-matching condition between the soliton and the dispersive wave with different parameters. According to our numerical results, the dispersive wave blue-shifts for longer pump wavelengths and it red-shifts for higher pressures inside the HCF.

We have examined the relation between the energy and the duration of the generated ultraviolet pulse, concluding that the possibility of obtaining an ultrashort but also energetic dispersive wave is challenging. The shortest pulse duration is achieved when the dispersive wave is generated, but since it propagates in the normal dispersion region, it stretches during the propagation. On the other hand, the energy grows since its generation until the HCF output. As we have already observed through the different chapters, the presence of higher-order modes during the propagation leads to different dispersive wave contributions, in particular, higher-order modes generate dispersive waves at shorter wavelengths. In the cases of HCF with large mode area, the dispersive wave will become more structured along the propagation due to the larger contribution of higher-order spatial modes.

Finally, we have implemented a parameters scaling route to obtain the same nonlinear dynamics for different pump wavelengths. By means of this scaling, we have shown that

it is possible to obtain a dispersive wave at a desired wavelength for different laser and HCF parameters.

8.2 Outlook

The possibility of obtaining few-cycle energetic pulses delivered from compact laser sources is an achievement of great relevance. Hollow capillary fibers (HCFs), flexible HCFs, multi-pass cells, photonic crystal fibers and filaments are well-established post-compression techniques. The perspectives in the use of post-compression schemes are related to the energy up-scaling, which is hindered by ionization and self-focusing, the pulse duration and the wavelength tunability of the output pulses. At the moment, the only post-compression technique able to reach energies above mJ-level and sub-3-cycle pulse duration is based in HCF. However, the improvements of these parameters is under constant study.

A further energy scaling with these techniques is possible by increasing the length of the compressor, which is possible with flexible HCFs and multi-pass cells, but it may be a problem when reaching almost tens of meters. In addition, an approach to obtain shorter pulse durations is to increase the compression ratio. This development would enable using a longer input pulse with a higher input energy but keeping the peak power below the critical values. This could be achieved combining different techniques.

Moreover, it is necessary to find a viable route to couple and propagate structured beams in post- and self-compression schemes, since they have the potential to achieve laser pulses of a higher energy than conventional beams, also in interesting spectral regions.

Apart from few-cycle pulses in the near infrared, the compression of laser pulses at different wavelengths, such as ultraviolet or visible has a great implication in different applications. One of the most remarkable processes to obtain ultrashort pulses is the dispersive wave generation process. The promising short pulse duration, considerable energy and tunability from the ultraviolet to the infrared make this technique a suitable alternative, although it is still under development at present [Brahms et al., 2020].

Conclusiones

En esta tesis hemos realizado un estudio numérico sobre la propagación no lineal de un pulso láser en una fibra hueca. Para ello hemos utilizado distintos modelos numéricos, (1+1)D, (2+1)D y (3+1)D, de los cuales el (1+1)D y el (3+1)D han sido desarrollados en este trabajo.

Nuestro punto de partida ha sido entender la dinámica espacial y la naturaleza multimodal de las fibras huecas en diferentes regímenes de propagación, ya que la energía de entrada del pulso estará limitada por los distintos efectos no lineales que aparecen durante la propagación del pulso en la fibra hueca. Nuestro objetivo ha sido encontrar dichos límites para así evitar la activación de efectos no lineales de orden alto (como el colapso espacial o la ionización), que pueden empeorar la fase espectral del pulso a la salida complicando su posible post-compresión.

En las primeras simulaciones realizadas, hemos comparado la dinámica de la propagación de un pulso láser en una fibra hueca usando un modelo independiente del tiempo (modelo (1+1)D), el cual incluye únicamente la dinámica espacial, con un modelo espacio-temporal (modelo (2+1)D) que fue desarrollado previamente por el grupo. En este estudio hemos demostrado que el confinamiento espacial dentro de la fibra hueca del modo fundamental, modo EH_{11}, juega un papel muy relevante en el proceso de auto-focalización, minimizando la difracción y favoreciendo la auto-focalización. En concreto, hemos identificado dos regiones diferentes de auto-focalización en la fibra hueca dependiendo de la potencia de entrada del pulso: para pulsos con potencias pico por debajo de la potencia crítica, hemos obtenido colapsos espaciales inducidos principalmente por la transferencia de energía entre los distintos modos espaciales, solo presente en el modelo (2+1)D. La dinámica de colapso espacial explicada en el Capítulo 4 puede ser útil a la hora de identificar los límites de energía en cualquier región de potencia en los esquemas de post-compresión. En otras palabras, este estudio puede servir como guía para encontrar la longitud de la fibra hueca óptima para evitar una respuesta no lineal muy intensa a la salida.

Mediante el estudio de la interacción entre los modos espaciales en la fibra hueca, hemos encontrado que la transferencia de energía entre el modo fundamental y los modos de orden alto se produce cerca del pico de intensidad del pulso. Por consiguiente, los modos espaciales de orden alto que se generan presentan una duración temporal más corta y un espectro más ancho. Este fenómeno se puede entender como un efecto de compresión temporal en el propio proceso de transferencia de energía, lo que puede ser interesante para futuras investigaciones.

Siguiendo con el estudio sobre el posible escalado de la energía en los esquemas de post-compresión, hemos adaptado y desarrollado modelos numéricos para poder simular la propagación de haces estructurados en la fibra hueca en los capítulos 5 y 6, como haces vectoriales y haces tipo "necklace". Una de las principales ventajas que este tipo de haces presenta es que la intensidad está más distribuida en el área transversal del núcleo de la fibra y por lo tanto, es posible acoplar pulsos con una energía mayor en la fibra hueca. Además, la posibilidad de obtener pulsos estructurados ultracortos es muy prometedora y de gran utilidad para diversas aplicaciones. El estudio numérico sobre la propagación no lineal de los haces vectoriales en la fibra hueca ha dado como resultado una dinámica muy compleja, donde la interacción entre los distintos modos espaciales modula la intensidad y el espectro del pulso. Mientras que el perfil espacio-temporal de un haz tipo EH_{11} se mantiene prácticamente igual a lo largo de la propagación en la fibra hueca a pesar de la aparición de modos de orden alto, en el caso de un haz vectorial el perfil espacio-temporal evoluciona de manera compleja. Debido a que los anillos de los diferentes modos altos espaciales que aparecen en la propagación presentan distinto signo en la polarización del campo, su acoplamiento puede llevar a una superposición constructiva o destructiva. Estas modulaciones espacio-temporales en el perfil del pulso se transfieren al espectro mostrando también la misma distribución espacial no homogénea. En el caso de los modos híbridos de tipo EH_{1q}, la superposición de los modos siempre es constructiva en eje y el acoplamiento entre los distintos modos altos no dificulta la propagación, siendo mucho más estable.

Hemos generado y propagado haces vectoriales a través de una fibra hueca en las instalaciones láser de la Universidad de Salamanca en colaboración con el grupo experimental. El acuerdo entre el perfil espacial del haz medido en los experimentos y el haz de nuestras simulaciones numéricas ha servido para validar el modelo teórico. Sin embargo, hemos encontrado problemas en el acoplamiento de los haces vectoriales a la fibra y la polarización de estos no se mantiene al final de la fibra hueca en régimen de propagación no lineal. En conclusión, estos haces vectoriales pueden soportar una mayor energía de entrada, pero como su propagación en la fibra hueca es menos estable, la conversión de polarización lineal al haz vectorial después de la fibra hueca parece una propuesta más robusta para futuras investigaciones.

El segundo tipo de haz estructurado que hemos propagado a través de la fibra hueca son los haces tipo ”necklace”. En comparación con los haces vectoriales, estos haces tipo ”necklace” son más estables en la propagación. Durante este estudio hemos encontrado que la no linealidad en este caso ensancha el espectro de manera que la energía del pulso se concentra en dos bandas espectrales, una de ellas alcanzando la parte visible del espectro en la propagación. Mediante el filtrado espectral de esta banda, es posible obtener pulsos energéticos y ultracortos en el rango visible a partir de pulsos infrarrojos tipo ”necklace”. La alta eficiencia de este proceso (alrededor del 25%) y la posible sintonización de la longitud de onda de la banda a través de la presión del gas en el interior de la fibra hueca, demuestran que la auto-compresión solitónica de haces infrarrojos tipo ”necklace” en fibras huecas llenas de gas puede ser una herramienta compacta para obtener pulsos láser cortos en la región visible. También hemos demostrado que para haces de entrada no ideales tipo ”necklace”, donde tiene lugar una transferencia de energía entre las distintas cuentas del haz debido a esa asimetría espacial, se mantiene la estructura espectral de dos bandas y la auto-compresión temporal, aunque solamente en aquellas cuentas que alcanzan una intensidad pico alta durante la propagación. Incluso en el caso de un haz no ideal, la auto-focalización no juega un papel importante en la dinámica del haz.

A partir de los resultados obtenidos en la propagación de haces tipo ”necklace” en la fibra hueca, hemos explorado la idea de generar pulsos cortos en otras zonas del espectro que no son accesibles directamente con los sistemas láser actuales, como el visible o el ultravioleta. En la última parte de esta tesis, hemos estudiado la emisión de ondas dispersivas en la fibra hueca como una alternativa factible a otros procesos de conversión de frecuencias para generar pulsos ultracortos y sintonizables a longitudes de onda no convencionales. Hemos estudiado la dependencia de la condición de ajuste de fase entre el solitón y la onda dispersiva en función de distintos parámetros, como la presión o la longitud de onda del láser. De acuerdo con nuestras simulaciones, la onda dispersiva se desplaza hacia el azul cuando el láser tiene una longitud de onda mayor y se desplaza hacia los rojos cuando la presión dentro de la fibra hueca aumenta.

Para completar este estudio hemos examinado la relación entre la energía y la duración del pulso ultravioleta generado, concluyendo que la posibilidad de obtener una onda dispersiva ultracorta y a la vez energética es exigente. La duración temporal más corta se logra en el momento en el que se genera la onda dispersiva, pero como se propaga en la región de dispersión normal, se ensancha a medida que se propaga hasta el final de la fibra hueca. Por otra parte, la energía crece durante la propagación pudiendo llegar a alcanzar decenas de microjulios. Como ya hemos observados a través de los diferentes capítulos, la presencia de modos espaciales de orden alto en la propagación influye en la dinámica y en este caso conlleva a diferentes contribuciones de la onda dispersiva, en

concreto, los modos altos generan ondas dispersivas en longitudes de onda más cortas. En el caso de fibras huecas con un tamaño de núcleo grande, la onda dispersiva estará más estructurada debido a la contribución de los modos espaciales de orden alto.

Finalmente hemos implementado un escalado de parámetros para obtener la misma dinámica no lineal para diferentes longitudes de onda para el pulso de entrada. Mediante este escalado hemos mostrado que es posible obtener una onda dispersiva en una longitud de onda concreta para distintos parámetros del láser y de la fibra hueca.

Bibliography

G. P. Agrawal. *Nonlinear Fiber Optics*. Academic Press, 5th edition, 2013.

N. Akhmediev and M. Karlsson. Cherenkov radiation emitted by solitons in optical fibers. *Phys. Rev. A*, 51:2602–2607, 1995. doi: 10.1103/PhysRevA.51.2602. URL https://link.aps.org/doi/10.1103/PhysRevA.51.2602.

N. B. Aleksić, A. I. Strinić, M. M. Petroski, and M. S. Petrović. Necklace beams in media with cubic-quintic nonlinearity. *Opt Quant Electron*, 52:73, 2020. doi: 10.1007/s11082-019-2189-x. URL https://doi.org/10.1007/s11082-019-2189-x.

B.Alonso, I. Lopez-Quintas, W. Holgado, R. Drevinskas, P. G. Kazansky, C. Hernández-Garc´ıa, and ´I. J. Sola. Complete spatiotemporal and polarization characterization of ultrafast vector beams. *Commun Phys*, 3:151, 2020. doi: 10.1038/s42005-020-00419-w. URL https://doi.org/10.1038/s42005-020-00419-w.

M. V. Ammosov, N. B. Delone, and V. P. Krainov. Tunnel ionization of complex atoms and of atomic ions in an alternating electromagnetic field. *JETP*, 64:1191, 1986. URL http://www.jetp.ac.ru/cgi-bin/e/index/e/64/6/p1191?a=list.

A. Anderson, F. Lücking, T. Prikoszovits, M. Hofer, Z. Cheng, C. C. Neacsu, M. Scharrer, S. Rammler, P. St. J. Russell, G. Tempea, and A. Assion. Multi-mJ carrier envelope phase stabilized few-cycle pulses generated by a tabletop laser system. *Appl. Phys. B*, 103:531–536, 2011. doi: 10.1007/s00340-011-4592-2. URL https://doi.org/10.1007/s00340-011-4592-2.

J. Andreasen and M. Kolesik. Nonlinear propagation of light in structured media: Generalized unidirectional pulse propagation equations. *Phys. Rev. E*, 86:036706, 2012. doi: 10.1103/PhysRevE.86.036706. URL https://link.aps.org/doi/10.1103/PhysRevE.86.036706.

J. Andreasen and M. Kolesik. Midinfrared femtosecond laser pulse filamentation in hollow waveguides: A comparison of simulation methods. *Phys. Rev. E*, 87:053303, 2013. doi: 10.1103/PhysRevE.87.053303. URL https://link.aps.org/doi/10.1103/PhysRevE.87.053303.

C.L. Arnold, B. Zhou, S. Akturk, S. Chen, A. Couairon, and A. Mysyrowicz. Pulse compression with planar hollow waveguides: a pathway towards relativistic intensity with table-top lasers. *New Journal of Physics*, 12(7):073015, 2010. doi: 10.1088/1367-2630/12/7/073015. URL https://hal-polytechnique.archives-ouvertes.fr/hal-00510589.

D. R. Austin, C. Martijn de Sterke, B. J. Eggleton, and T. G. Brown. Dispersive wave blue-shift in supercontinuum generation. *Opt. Express*, 14(25):11997–12007, 2006. doi: 10.1364/OE.14.011997. URL http://www.opticsexpress.org/abstract.cfm?URI=oe-14-25-11997.

M. Azhar, G. K. L. Wong, W. Chang, N. Y. Joly, and P. St. J. Russell. Raman-free nonlinear optical effects in high pressure gas-filled hollow core PCF. *Opt. Express*, 21(4):4405–4410, 2013. doi: 10.1364/OE.21.004405. URL http://www.opticsexpress.org/abstract.cfm?URI=oe-21-4-4405.

P. Balla, A. B. Wahid, I. Sytcevich, C. Guo, A-L. Viotti, L. Silletti, A. Cartella, S. Alisauskas, H. Tavakol, U. Grosse-Wortmann, A. Schönberg, M. Seidel, A. Trabattoni, B. Manschwetus, T. Lang, F. Calegari, A.Couairon, A. L'Huillier, C. L. Arnold, I.Hartl, and C. M. Heyl. Postcompression of picosecond pulses into the few-cycle regime. *Opt. Lett.*, 45(9):2572–2575, 2020. doi: 10.1364/OL.388665. URL http://ol.osa.org/abstract.cfm?URI=ol-45-9-2572.

J. E. Beetar, S. Gholam-Mirzaei, and M. Chini. Spectral broadening and pulse compression of a 400 µJ, 20 W Yb:KGW laser using a multi-plate medium. *Appl. Phys. Lett.*, 112:051102, 2018. doi: 10.1063/1.5018758. URL https://doi.org/10.1063/1.5018758.

J. E. Beetar, F. Rivas, S. Gholam-Mirzaei, Y. Liu, and M. Chini. Hollow-core fiber compression of a commercial yb:kgw laser amplifier. *J. Opt. Soc. Am. B*, 36(2):A33–A37, 2019. doi: 10.1364/JOSAB.36.000A33. URL http://josab.osa.org/abstract.cfm?URI=josab-36-2-A33.

J. E. Beetar, M. Nrisimhamurty, T-Ch. Truong, G. C. Nagar, Y. Liu, J. Nesper, O. Suarez, F. Rivas, Y. Wu, B. Shim, and M. Chini. Multioctave supercontinuum generation and frequency conversion based on rotational nonlinearity. *Science Advances*, 6(34), 2020. doi: 10.1126/sciadv.abb5375. URL https://advances.sciencemag.org/content/6/34/eabb5375.

F. Benabid, J. C. Knight, G. Antonopoulos, and P. St. J. Russell. Stimulated raman scattering in hydrogen-filled hollow-core photonic crystal fiber. *Science*, 298(5592):399–402, 2002. doi: 10.1126/science.1076408. URL https://science.sciencemag.org/content/298/5592/399.

T. A. Birks, W. J. Wadsworth, and P. St. J. Russell. Supercontinuum generation in tapered fibers. *Opt. Lett.*, 25(19):1415–1417, 2000. doi: 10.1364/OL.25.001415. URL http://ol.osa.org/abstract.cfm?URI=ol-25-19-1415.

M. Blanco, F. Cambronero, M. T. Flores-Arias, E. Conejero Jarque, L. Plaja, and C. Hernández-Garc´ıa. Ultraintense femtosecond magnetic nanoprobes induced by azimuthally polarized laser beams. *ACS Photonics*, 6(1):38–42, 2019. doi: 10.1021/acsphotonics.8b01312. URL https://doi.org/10.1021/acsphotonics.8b01312.

N. Bloembergen. The influence of electron plasma formation on superbroadening in light filaments. *Optics Communications*, 8(4):285–288, 1973. doi: https://doi.org/10.1016/0030-4018(73)90196-X. URL https://www.sciencedirect.com/science/article/pii/003040187390196X.

S. Bohman, A. Suda, T. Kanai, S. Yamaguchi, and K. Midorikawa. Generation of 5.0 fs, 5.0 mJ pulses at 1 kHz using hollow-fiber pulse compression. *Opt. Lett.*, 35(11):1887–1889, 2010. doi: 10.1364/OL.35.001887. URL http://ol.osa.org/abstract.cfm?URI=ol-35-11-1887.

Boulder Atomic Clock Optical Network (BACON) Collaboration*. Frequency ratio measurements at 18-digit accuracy using an optical clock network. *Nature*, 591:564–569, 2021. doi: 10.1038/s41586-021-03253-4. URL https://doi.org/10.1038/s41586-021-03253-4.

R. Boyd. *Nonlinear Optics*. Academic Press, 4th edition, 2020.

T. Brabec and F. Krausz. Nonlinear optical pulse propagation in the single-cycle regime. *Phys. Rev. Lett.*, 78:3282–3285, 1997. doi: 10.1103/PhysRevLett.78.3282. URL https://link.aps.org/doi/10.1103/PhysRevLett.78.3282.

T. Brabec and F. Krausz. Intense few-cycle laser fields: Frontiers of nonlinear optics. *Rev. Mod. Phys.*, 72:545–591, 2000. doi: 10.1103/RevModPhys.72.545. URL https://link.aps.org/doi/10.1103/RevModPhys.72.545.

C. Brahms, T. Grigorova, F. Belli, and J. C. Travers. High-energy ultraviolet dispersive-wave emission in compact hollow capillary systems. *Opt. Lett.*, 44(12):2990–2993, 2019. doi: 10.1364/OL.44.002990. URL http://ol.osa.org/abstract.cfm?URI=ol-44-12-2990.

C. Brahms, F. Belli, and J. C. Travers. Infrared attosecond field transients and UV to IR few-femtosecond pulses generated by high-energy soliton self-compression. *Phys. Rev. Research*, 2:043037, 2020. doi: 10.1103/PhysRevResearch.2.043037. URL https://link.aps.org/doi/10.1103/PhysRevResearch.2.043037.

A. Braun, G. Korn, X. Liu, D. Du, J. Squier, and G. Mourou. Self-channeling of high-peak-power femtosecond laser pulses in air. *Opt. Lett.*, 20(1):73–75, 1995. doi: 10.1364/OL.20.000073. URL http://ol.osa.org/abstract.cfm?URI=ol-20-1-73.

C. J. Campbell, A. G. Radnaev, A. Kuzmich, V. A. Dzuba, V. V. Flambaum, and A. Derevianko. Single-ion nuclear clock for metrology at the 19th decimal place. *Phys. Rev. Lett.*, 108:120802, 2012. doi: 10.1103/PhysRevLett.108.120802. URL https://link.aps.org/doi/10.1103/PhysRevLett.108.120802.

H. Cao, R. S. Nagymihaly, V. Chvykov, N. Khodakovskiy, and M. Kalashnikov. Multipass-cell-based post-compression of radially and azimuthally polarized pulses to the sub-two-cycle regime. *J. Opt. Soc. Am. B*, 36(9):2517–2525, 2019. doi: 10.1364/JOSAB.36.002517. URL http://josab.osa.org/abstract.cfm?URI=josab-36-9-2517.

S. Carbajo, E. Granados, D. Schimpf, A. Sell, K-H. Hong, J. Moses, and F. X. Kärtner. Efficient generation of ultra-intense few-cycle radially polarized laser pulses. *Opt. Lett.*, 39(8):2487–2490, 2014. doi: 10.1364/OL.39.002487. URL http://ol.osa.org/abstract.cfm?URI=ol-39-8-2487.

M. Cassataro, D. Novoa, M. C. Günendi, N. N. Edavalath, M. H. Frosz, J. C. Travers, and P. St.J. Russell. Generation of broadband mid-IR and UV light in gas-filled single-ring hollow-core PCF. *Opt. Express*, 25(7):7637–7644, 2017. doi: 10.1364/OE.25.007637. URL http://www.opticsexpress.org/abstract.cfm?URI=oe-25-7-7637.

C-M. Chen and P. L. Kelley. Nonlinear pulse compression in optical fibers: scaling laws and numerical analysis. *J. Opt. Soc. Am. B*, 19(9):1961–1967, 2002. doi: 10.1364/JOSAB.19.001961. URL http://josab.osa.org/abstract.cfm?URI=josab-19-9-1961.

X. Chen, P. Polynkin, and M. Kolesik. Raman effect in self-focusing of few-cycle laser pulses in air. *Opt. Lett.*, 38(12):2017–2019, 2013. doi: 10.1364/OL.38.002017. URL http://ol.osa.org/abstract.cfm?URI=ol-38-12-2017.

Y. Cheng, H. Xie, Z. Wang, G. Li, B. Zeng, F. He, W. Chu, J. Yao, and L. Qiao. Onset of nonlinear self-focusing of femtosecond laser pulses in air: Conventional vs spatiotemporal focusing. *Phys. Rev. A*, 92:023854, 2015. doi: 10.1103/PhysRevA.92.023854. URL https://link.aps.org/doi/10.1103/PhysRevA.92.023854.

R. Y. Chiao, E. Garmire, and C. H. Townes. Self-trapping of optical beams. *Phys. Rev. Lett.*, 13:479–482, 1964. doi: 10.1103/PhysRevLett.13.479. URL https://link.aps.org/doi/10.1103/PhysRevLett.13.479.

R. Y. Chiao, T.K. Gustafson, and P.L. Kelley. Self-focusing of optical beams. In R. W. Boyd, S. G. Lukishova, and Y.R. Shen, editors, *Self-focusing: Past and Present: Fundamentals and Prospects*, pages 129–143. Springer New York, 2009. ISBN 978-0-387-34727-1. doi: 10.1007/978-0-387-34727-1 4. URL https://doi.org/10.1007/978-0-387-34727-1_4.

R. Clady, G. Coustillier, M. Gastaud, M. Sentis, P. Spiga, V. Tcheremiskine, O. Uteza, L. D. Mikheev, V. Mislavskii, J. P. Chambaret, and G. Cheriaux. Architecture of a blue high contrast multiterawatt ultrashort laser. *Appl. Phys. B*, 82:347–358, 2006. doi: 10.1007/s00340-005-2081-1. URL https://doi.org/10.1007/s00340-005-2081-1.

E. Conejero Jarque, J. San Roman, F. Silva, R. Romero, W. Holgado, M. A. Gonzalez-Galicia, I. J. Sola, and H. Crespo. Universal route to optimal few- to single-cycle pulse generation in hollow-core fiber compressors. *Sci. Reports*, 8:2256, 2018. doi: https://doi.org/10.1038/s41598-018-20580-1. URL https://doi.org/10.1038/s41598-018-20580-1.

P. B. Corkum. Plasma perspective on strong field multiphoton ionization. *Phys. Rev. Lett.*, 71:1994–1997, 1993. doi: 10.1103/PhysRevLett.71.1994. URL https://link.aps.org/doi/10.1103/PhysRevLett.71.1994.

A. Couairon and L. Bergé. Modeling the filamentation of ultra-short pulses in ionizing media. *Physics of Plasmas*, 7:193–209, 2000. doi: 10.1063/1.873794. URL https://aip.scitation.org/doi/10.1063/1.873794.

A. Couairon and A. Mysyrowicz. Femtosecond filamentation in transparent media. *Physics Reports*, 441(2):47–189, 2007. doi: 10.1016/j.physrep.2006.12.005. URL http://www.sciencedirect.com/science/article/pii/S037015730700021X.

A. Couairon, S. Tzortzakis, L. Bergé, M. Franco, B. Prade, and A. Mysyrowicz. Infrared femtosecond light filaments in air: simulations and experiments. *J. Opt. Soc. Am. B*, 19(5):1117–1131, 2002. doi: 10.1364/JOSAB.19.001117. URL http://josab.osa.org/abstract.cfm?URI=josab-19-5-1117.

A. Couairon, H. S. Chakraborty, and M. B. Gaarde. From single-cycle self-compressed filaments to isolated attosecond pulses in noble gases. *Phys. Rev. A*, 77:053814, 2008. doi: 10.1103/PhysRevA.77.053814. URL https://link.aps.org/doi/10.1103/PhysRevA.77.053814.

A. Couairon, E. Brambilla, T. Corti, D. Majus, O. de J. Ramírez-Góngora, and M. Kolesik. Practitioner's guide to laser pulse propagation models and simulation. *Eur. Phys. J. Special Topics*, 199:5–76, 2011. doi: 10.1140/epjst/e2011-01503-3. URL https://doi.org/10.1140/epjst/e2011-01503-3.

J. Crank and P. Nicolson. A practical method for numerical evaluation of solutions of partial differential equations of the heat-conduction type. *Mathematical Proceedings of the Cambridge Philosophical Society*, 43(1):50–67, 1947. doi: 10.1017/S0305004100023197.

R. F. Cregan, B. J. Mangan, J. C. Knight, T. A. Birks, P. St. J. Russell, P. J. Roberts, and D. C. Allan. Single-mode photonic band gap guidance of light in air. *Science*, 285 (5433):1537–1539, 1999. doi: 10.1126/science.285.5433.1537. URL https://science.sciencemag.org/content/285/5433/1537.

A. Crego, E. Conejero Jarque, and J. San Roman. Influence of the spatial confinement on the self-focusing of ultrashort pulses in hollow-core fibers. *Sci Rep*, 9: 9546, 2019. doi: 10.1038/s41598-019-45940-3. URL https://doi.org/10.1038/s41598-019-45940-3.

A. Crego, E. Conejero Jarque, and J. San Roman. Ultrashort visible energetic pulses generated by nonlinear propagation of necklace beams in capillaries. *Opt. Express*, 29 (2):929–937, 2021. doi: 10.1364/OE.411338. URL http://www.opticsexpress.org/abstract.cfm?URI=oe-29-2-929.

A. Dalgarno and A. E. Kingston. The refractive indices and verdet constants of the inert gases. *Proc. R. Soc. Lond. A*, 259:424–431, 1960. doi: 10.1098/rspa.1960.0237. URL https://royalsocietypublishing.org/doi/10.1098/rspa.1960.0237.

E. L. Dawes and J. H. Marburger. Computer studies in self-focusing. *Phys. Rev.*, 179: 862–868, 1969. doi: 10.1103/PhysRev.179.862. URL https://link.aps.org/doi/10.1103/PhysRev.179.862.

S. R. Domingue, R. A. Bartels, A. J. Chicco, and J. W. Wilson. Transient absorption imaging of hemes with 2-color, independently tunable visible-wavelength ultrafast source. *Biomed. Opt. Express*, 8(6):2807–2821, 2017. doi: 10.1364/BOE.8.002807. URL http://www.osapublishing.org/boe/abstract.cfm?URI=boe-8-6-2807.

R. Dorn, S. Quabis, and G. Leuchs. Sharper focus for a radially polarized light beam. *Phys. Rev. Lett.*, 91:233901, 2003. doi: 10.1103/PhysRevLett.91.233901. URL https://link.aps.org/doi/10.1103/PhysRevLett.91.233901.

C. G. Durfee, S. Backus, M. M. Murnane, and H. C. Kapteyn. Ultrabroadband phase-matched optical parametric generation in the ultraviolet by use of guided waves. *Opt. Lett.*, 22(20):1565–1567, 1997. doi: 10.1364/OL.22.001565. URL http://ol.osa.org/abstract.cfm?URI=ol-22-20-1565.

C. G. Durfee, S. Backus, Henry C. Kapteyn, and M. M. Murnane. Intense 8-fs pulse generation in the deep ultraviolet. *Opt. Lett.*, 24(10):697–699, 1999. doi: 10.1364/OL.24.000697. URL http://ol.osa.org/abstract.cfm?URI=ol-24-10-697.

A. Ermolov, C. Heide, P. Dienstbier, F. Köttig, F. Tani, P. Hommelhoff, and P. St. J. Russell. Carrier-envelope-phase-stable soliton-based pulse compression to 4.4 fs and ultraviolet generation at the 800 kHz repetition rate. *Opt. Lett.*, 44(20):5005–5008, 2019. doi: 10.1364/OL.44.005005. URL http://ol.osa.org/abstract.cfm?URI=ol-44-20-5005.

G. Fan, P. A. Carpeggiani, Z. Tao, G. Coccia, R. Safaei, E. Kaksis, A. Pugzlys, F. Lẽgarẽ, B. E. Schmidt, and A. Baltu˘ska. 70 mJ nonlinear compression and scaling route for an Yb amplifier using large-core hollow fibers. *Opt. Lett.*, 46(4):896–899, 2021. doi: 10.1364/OL.412296. URL http://ol.osa.org/abstract.cfm?URI=ol-46-4-896.

R. L. Farrow, D. A. V. Kliner, G. R. Hadley, and A. V. Smith. Peak-power limits on fiber amplifiers imposed by self-focusing. *Opt. Lett.*, 31(23):3423–3425, 2006. doi: 10.1364/OL.31.003423. URL http://ol.osa.org/abstract.cfm?URI=ol-31-23-3423.

G. Fibich and A. L. Gaeta. Critical power for self-focusing in bulk media and in hollow waveguides. *Opt. Lett.*, 25(5):335–337, 2000. doi: 10.1364/OL.25.000335. URL http://ol.osa.org/abstract.cfm?URI=ol-25-5-335.

G. Fibich and B. Ilan. Self-focusing of elliptic beams: an example of the failure of the aberrationless approximation. *J. Opt. Soc. Am. B*, 17(10):1749–1758, 2000. doi: 10.1364/JOSAB.17.001749. URL http://josab.osa.org/abstract.cfm?URI=josab-17-10-1749.

G. Fibich and G. C. Papanicolaou. Self-focusing in the presence of small time dispersion and nonparaxiality. *Opt. Lett.*, 22(18):1379–1381, 1997. doi: 10.1364/OL.22.001379. URL http://ol.osa.org/abstract.cfm?URI=ol-22-18-1379.

G. Fibich and D. Shpigelman. Positive and necklace solitary waves on bounded domains. *Physica D: Nonlinear Phenomena*, 315:13–32, 2016. doi: 10.1016/j.physd.2015.09.015. URL http://www.sciencedirect.com/science/article/pii/S0167278915001888.

G. Fibich, S. Eisenmann, B. Ilan, Y. Erlich, M. Fraenkel, Z. Henis, A. L. Gaeta, and A. Zigler. Self-focusing distance of very high power laser pulses. *Opt. Express*, 13(15):5897–5903, 2005. doi: 10.1364/OPEX.13.005897. URL http://www.opticsexpress.org/abstract.cfm?URI=oe-13-15-5897.

A. Forbes. Structured light from lasers. *Laser & Photonics Reviews*, 13(11):1900140, 2019. doi: 10.1002/lpor.201900140. URL https://onlinelibrary.wiley.com/doi/abs/10.1002/lpor.201900140.

R. L. Fork, C. H. Brito Cruz, P. C. Becker, and C. V. Shank. Compression of optical pulses to six femtoseconds by using cubic phase compensation. *Opt. Lett.*, 12(7):483–485, 1987. doi: 10.1364/OL.12.000483. URL http://ol.osa.org/abstract.cfm?URI=ol-12-7-483.

P. A. Franken, A. E. Hill, C. W. Peters, and G. Weinreich. Generation of optical harmonics. *Phys. Rev. Lett.*, 7:118–119, 1961. doi: 10.1103/PhysRevLett.7.118. URL https://link.aps.org/doi/10.1103/PhysRevLett.7.118.

M. Frigo and S. G. Johnson. The design and implementation of FFTW3. *Proceedings of the IEEE*, 93(2):216–231, 2005. doi: 10.1109/JPROC.2004.840301. URL https://ieeexplore.ieee.org/document/1386650.

J. G. Fujimoto, A. M. Weiner, and E. P. Ippen. Generation and measurement of optical pulses as short as 16 fs. *Appl. Phys. Lett.*, 44:832–834, 1984. doi: 10.1063/1.94957. URL https://aip.scitation.org/doi/10.1063/1.94957.

M. Galli, V. Wanie, D. Pereira Lopes, E. P. Månsson, A. Trabattoni, L. Colaizzi, K. Saraswathula, A. Cartella, F. Frassetto, L. Poletto, F. Légaré, S. Stagira, M. Nisoli, R. Martínez Vázquez, R. Osellame, and F. Calegari. Generation of deep ultraviolet sub-2-fs pulses. *Opt. Lett.*, 44(6):1308–1311, 2019. doi: 10.1364/OL.44.001308. URL http://ol.osa.org/abstract.cfm?URI=ol-44-6-1308.

S. Ghimire, B. Shan, C. Wang, and Z. Chang. High-energy 6.2-fs pulses for attosecond pulse generation. *Laser physics*, 15(6):838–842, 2005. URL https://perg.phys.ksu.edu/dh/zchang/004-chang-laser-physics-15-6-838.pdf.

P. G. Gobbi and G. C. Reali. A novel unstable resonator configuration with a self filtering aperture. *Optics Communications*, 52(3):195–198, 1984. doi: https://doi.org/10.1016/0030-4018(84)90357-2. URL http://www.sciencedirect.com/science/article/pii/0030401884903572.

E. Goulielmakis, S. Koehler, B. Reiter, M. Schultze, A. J. Verhoef, E. E. Serebryannikov, A. M. Zheltikov, and F. Krausz. Ultrabroadband, coherent light source based on self-channeling of few-cycle pulses in helium. *Opt. Lett.*, 33(13):1407–1409, 2008. doi: 10.1364/OL.33.001407. URL http://ol.osa.org/abstract.cfm?URI=ol-33-13-1407.

T. D. Grow, A. A. Ishaaya, L. T. Vuong, and A. L. Gaeta. Collapse and stability of necklace beams in Kerr media. *Phys. Rev. Lett.*, 99:133902, 2007. doi: 10.1103/

PhysRevLett.99.133902. URL https://link.aps.org/doi/10.1103/PhysRevLett.99.133902.

C. Guclu, M. Veysi, and F. Capolino. Photoinduced magnetic nanoprobe excited by an azimuthally polarized vector beam. *ACS Photonics*, 3(11):2049–2058, 2016. doi: 10.1021/acsphotonics.6b00329. URL https://doi.org/10.1021/acsphotonics.6b00329.

M. Guizar-Sicairos and J. C. Gutiérrez-Vega. Computation of quasi-discrete Hankel transforms of integer order for propagating optical wave fields. *J. Opt. Soc. Am. A*, 21(1):53–58, 2004. doi: 10.1364/JOSAA.21.000053. URL http://josaa.osa.org/abstract.cfm?URI=josaa-21-1-53.

S. Hädrich, A. Klenke, A. Hoffmann, T. Eidam, T. Gottschall, J. Rothhardt, J. Limpert, and A. Tünnermann. Nonlinear compression to sub-30-fs, 0.5 mJ pulses at 135 W of average power. *Opt. Lett.*, 38(19):3866–3869, 2013. doi: 10.1364/OL.38.003866. URL http://ol.osa.org/abstract.cfm?URI=ol-38-19-3866.

S. Hädrich, M. Kienel, M. Müller, A. Klenke, J. Rothhardt, R. Klas, T. Gottschall, T. Eidam, A. Drozdy, P. Jójárt, Z. Várallyay, E. Cormier, K. Osvay, A. Tünnermann, and J. Limpert. Energetic sub-2-cycle laser with 216 W average power. *Opt. Lett.*, 41(18):4332–4335, 2016. doi: 10.1364/OL.41.004332. URL http://ol.osa.org/abstract.cfm?URI=ol-41-18-4332.

J.-M. Halbout and D. Grischkowsky. 12-fs ultrashort optical pulse compression at a high repetition rate. *Appl. Phys. Lett.*, 45:1281–1283, 1984. doi: 10.1063/1.95112. URL https://aip.scitation.org/doi/10.1063/1.95112.

L. E. Hargrove, R. L. Fork, and M. A. Pollack. Locking of He-Ne laser modes induced by synchronous intracavity modulation. *Appl. Phys. Lett.*, 5:4–5, 1964. doi: 10.1063/1.1754025. URL https://aip.scitation.org/doi/10.1063/1.1754025.

A. Hasegawa and F. Tappert. Transmission of stationary nonlinear optical pulses in dispersive dielectric fibers. I. Anomalous dispersion. *Appl. Phys. Lett.*, 23:142–144, 1973. doi: 10.1063/1.1654836. URL https://aip.scitation.org/doi/10.1063/1.1654836.

C. P. Hauri, W. Kornelis, F. W. Helbing, A. Heinrich, A. Couairon, A. Mysyrowicz, J. Biegert, and U. Keller. Generation of intense, carrier-envelope phase-locked few-cycle laser pulses through filamentation. *Appl Phys B*, 79:673–677, 2004. doi: 10.1007/s00340-004-1650-z. URL https://doi.org/10.1007/s00340-004-1650-z.

F. He, C. Ruiz, and A. Becker. Absorbing boundaries in numerical solutions of the time-dependent Schrödinger equation on a grid using exterior complex scaling. *Phys.*

Rev. A, 75:053407, 2007. doi: 10.1103/PhysRevA.75.053407. URL https://link.aps.org/doi/10.1103/PhysRevA.75.053407.

J. He, J. Liu, and T. Kobayashi. Tunable multicolored femtosecond pulse generation using cascaded four-wave mixing in bulk materials. *Applied Sciences*, 4(3):444–467, 2014. doi: 10.3390/app4030444. URL https://www.mdpi.com/2076-3417/4/3/444.

R. W. Hellwarth. Theory of the pulsation of fluorescent light from ruby. *Phys. Rev. Lett.*, 6:9–12, 1961. doi: 10.1103/PhysRevLett.6.9. URL https://link.aps.org/doi/10.1103/PhysRevLett.6.9.

C. Hernández-Garc´ıa, A. Turpin, J. San Román, A. Picón, R. Drevinskas, A. Cerkauskaite, P. G. Kazansky, C. G. Durfee, and I. J. Sola. Extreme ultraviolet vector beams driven by infrared lasers. *Optica*, 4(5):520–526, 2017. doi: 10.1364/OPTICA.4.000520. URL http://www.osapublishing.org/optica/abstract.cfm?URI=optica-4-5-520.

G. D. Hesketh, F. Poletti, and P. Horak. Spatio-temporal self-focusing in femtosecond pulse transmission through multimode optical fibers. *Journal of Lightwave Technology*, 30(17):2764–2769, 2012. doi: 10.1109/JLT.2012.2206796. URL http://eprints.soton.ac.uk/id/eprint/342422.

C. M. Heyl, H. Coudert-Alteirac, M. Miranda, M. Louisy, K. Kovacs, V. Tosa, E. Balogh, K. Varjú, A. L'Huillier, A. Couairon, and C. L. Arnold. Scale-invariant nonlinear optics in gases. *Optica*, 3(1):75–81, 2016. doi: 10.1364/OPTICA.3.000075. URL http://www.osapublishing.org/optica/abstract.cfm?URI=optica-3-1-75.

P. Hockett, C. Z. Bisgaard, O. J. Clarkin, and A. Stolow. Time-resolved imaging of purely valence-electron dynamics during a chemical reaction. *Nature Physics*, 7:612–615, 2011. doi: 10.1038/nphys1980. URL https://doi.org/10.1038/nphys1980.

D. Homoelle and A. L. Gaeta. Nonlinear propagation dynamics of an ultrashort pulse in a hollow waveguide. *Opt. Lett.*, 25(10):761–763, 2000. doi: 10.1364/OL.25.000761. URL http://ol.osa.org/abstract.cfm?URI=ol-25-10-761.

A. H ö ö k and M. Karlsson. Ultrashort solitons at the minimum-dispersion wavelength: effects of fourth-order dispersion. *Opt. Lett.*, 18(17):1388–1390, 1993. doi: 10.1364/OL.18.001388. URL http://ol.osa.org/abstract.cfm?URI=ol-18-17-1388.

O. Hort, A. Dubrouil, A. Cabasse, S. Petit, E. M ē vel, D. Descamps, and E. Constant. Postcompression of high-energy terawatt-level femtosecond pulses and application to high-order harmonic generation. *J. Opt. Soc. Am. B*, 32(6):1055–1062, 2015. doi: 10.1364/JOSAB.32.001055. URL http://josab.osa.org/abstract.cfm?URI=josab-32-6-1055.

Z. Huang, Y. Chen, F. Yu, D. Wu, D. Wang, R. Zhao, Y. Zhao, S. Gao, Y. Wang, P. Wang, and Y. Leng. Highly-tunable, visible ultrashort pulses generation by soliton-plasma interactions in gas-filled single-ring photonic crystal fibers. *Opt. Express*, 27(21):30798–30809, 2019. doi: 10.1364/OE.27.030798. URL http://www.opticsexpress.org/abstract.cfm?URI=oe-27-21-30798.

E. P. Ippen. Low-power quasi-CW Raman oscillator. *Appl. Phys. Lett.*, 16:303–305, 1970. doi: 10.1063/1.1653204. URL https://aip.scitation.org/doi/10.1063/1.1653204.

A. A. Ishaaya, C. J. Hensley, B. Shim, S. Schrauth, K. W. Koch, and A. L. Gaeta. Highly-efficient coupling of linearly- and radially-polarized femtosecond pulses in hollow-core photonic band-gap fibers. *Opt. Express*, 17(21):18630–18637, 2009. doi: 10.1364/OE.17.018630. URL http://www.opticsexpress.org/abstract.cfm?URI=oe-17-21-18630.

A. Jarnac, F. Brizuela, C. M. Heyl, P. Rudawski, F. Campi, B. Kim, L. Rading, P. Johnsson, A. Mysyrowicz, A. L'Huillier, A. Houard, and C. L. Arnold. Compression of TW class laser pulses in a planar hollow waveguide for applications in strong-field physics. *Eur. Phys. J. D*, 68(373), 2014. doi: 10.1140/epjd/e2014-50558-7. URL https://doi.org/10.1140/epjd/e2014-50558-7.

Y-G. Jeong, R. Piccoli, D. Ferachou, V. Cardin, M. Chini, S. Hädrich, J. Limpert, R. Morandotti, F. Légaré, B. E. Schimdt, and L. Razzari. Direct compression of 170-fs 50-cycle pulses down to 1.5 cycles with 70% transmission. *Sci Rep*, 8: 11794, 2018. doi: 10.1038/s41598-018-30198-y. URL https://doi.org/10.1038/s41598-018-30198-y.

X. Jiang, N. Y. Joly, M. A. Finger, F. Babic, G. K. L. Wong, J. C. Travers, and P. St. J. Russell. Deep-ultraviolet to mid-infrared supercontinuum generated in solid-core ZBLAN photonic crystal fibre. *Nat. Photonics*, 9:133–139, 2015. doi: 10.1038/nphoton.2014.320. URL https://doi.org/10.1038/nphoton.2014.320.

P. J. M. Johnson, V. I. Prokhorenko, and R. J. D. Miller. Stable UV to IR supercontinuum generation in calcium fluoride with conserved circular polarization states. *Opt. Express*, 17(24):21488–21496, 2009. doi: 10.1364/OE.17.021488. URL http://www.opticsexpress.org/abstract.cfm?URI=oe-17-24-21488.

N. Y. Joly, J. Nold, W. Chang, P. Hölzer, A. Nazarkin, G. K. L. Wong, F. Biancalana, and P. St. J. Russell. Bright spatially coherent wavelength-tunable deep-UV laser source using an Ar-filled photonic crystal fiber. *Phys. Rev. Lett.*, 106:203901, 2011. doi: 10.1103/PhysRevLett.106.203901. URL https://link.aps.org/doi/10.1103/PhysRevLett.106.203901.

K. C. Kao and G. A. Hockham. Dielectric-fibre surface waveguides for optical frequencies. *IEE Proceedings*, 133:191–198, 1966. doi: 10.1049/piee.1966.0189. URL https://digital-library.theiet.org/content/journals/10.1049/piee.1966.0189.

V. I. Karpman. Radiation by solitons due to higher-order dispersion. *Phys. Rev. E*, 47:2073–2082, 1993. doi: 10.1103/PhysRevE.47.2073. URL https://link.aps.org/doi/10.1103/PhysRevE.47.2073.

M. Kaumanns, V. Pervak, D. Kormin, V. Leshchenko, A. Kessel, M. Ueffing, Y. Chen, and T. Nubbemeyer. Multipass spectral broadening of 18 mJ pulses compressible from 1.3 ps to 4 fs. *Opt. Lett.*, 43(23):5877–5880, 2018. doi: 10.1364/OL.43.005877. URL http://ol.osa.org/abstract.cfm?URI=ol-43-23-5877.

L. V. Keldysh. Ionization in the field of a strong electromagnetic wave. *J. Exp. Theor. Phys.*, 20(5):1307–1314, 1965. URL http://www.jetp.ac.ru/cgi-bin/dn/e_020_05_1307.pdf.

P. L. Kelley. Self-focusing of optical beams. *Phys. Rev. Lett.*, 15:1005–1008, 1965. doi: 10.1103/PhysRevLett.15.1005. URL https://link.aps.org/doi/10.1103/PhysRevLett.15.1005.

J. C. Knight, T. A. Birks, P. St. J. Russell, and D. M. Atkin. All-silica single-mode optical fiber with photonic crystal cladding. *Opt. Lett.*, 21(19):1547–1549, 1996. doi: 10.1364/OL.21.001547. URL http://ol.osa.org/abstract.cfm?URI=ol-21-19-1547.

T. Kobayashi, A. Yabushita, and Y. Kida. Development of sub 10 fs visible-NIR, UV, and DUV pulses and their applications to ultrafast spectroscopy. *Photonics*, 3(4):64, 2016. doi: 10.3390/photonics3040064. URL https://www.mdpi.com/2304-6732/3/4/64.

F. Kong, H. Larocque, E. Karimi, P. B. Corkum, and C. Zhang. Generating few-cycle radially polarized pulses. *Optica*, 6(2):160–164, 2019. doi: 10.1364/OPTICA.6.000160. URL http://www.osapublishing.org/optica/abstract.cfm?URI=optica-6-2-160.

F. Köttig, F. Tani, J. C. Travers, and P. St. J. Russell. Self-focusing below the critical power in gas-filled hollow-core PCF. In *2017 European Conference on Lasers and Electro-Optics and European Quantum Electronics Conference*. Optical Society of America, 2017. URL http://www.osapublishing.org/abstract.cfm?URI=EQEC-2017-EE_2_5.

F. Köttig, D. Schade, J. R. Koehler, P. St. J. Russell, and F. Tani. Efficient single-cycle pulse compression of an ytterbium fiber laser at 10 MHz repetition rate. *Opt. Express*, 28(7):9099–9110, 2020. doi: 10.1364/OE.389137. URL http://www.opticsexpress.org/abstract.cfm?URI=oe-28-7-9099.

M. Kretschmar, C. Brée, T. Nagy, A. Demircan, H. G. Kurz, U. Morgner, and M. Kovačev. Direct observation of pulse dynamics and self-compression along a femtosecond filament. *Opt. Express*, 22(19):22905–22916, 2014. doi: 10.1364/OE.22.022905. URL http://www.opticsexpress.org/abstract.cfm?URI=oe-22-19-22905.

J. Lapointe and R. Kashyap. A simple technique to overcome self-focusing, filamentation, supercontinuum generation, aberrations, depth dependence and waveguide interface roughness using fs laser processing. *Sci Rep*, 7:499, 2017. doi: 10.1038/s41598-017-00589-8. URL https://doi.org/10.1038/s41598-017-00589-8.

L. Lavenu, M. Natile, F. Guichard, Y. Zaouter, M. Hanna, E. Mottay, and P. Georges. High-energy few-cycle Yb-doped fiber amplifier source based on a single nonlinear compression stage. *Opt. Express*, 25(7):7530–7537, 2017. doi: 10.1364/OE.25.007530. URL http://www.opticsexpress.org/abstract.cfm?URI=oe-25-7-7530.

L. Lavenu, M. Natile, F. Guichard, Y. Zaouter, X. Delen, M. Hanna, E. Mottay, and P. Georges. Nonlinear pulse compression based on a gas-filled multipass cell. *Opt. Lett.*, 43(10):2252–2255, 2018. doi: 10.1364/OL.43.002252. URL http://ol.osa.org/abstract.cfm?URI=ol-43-10-2252.

L. Lavenu, M. Natile, F. Guichard, X. Délen, M. Hanna, Y. Zaouter, and P. Georges. High-power two-cycle ultrafast source based on hybrid nonlinear compression. *Opt. Express*, 27(3):1958–1967, 2019. doi: 10.1364/OE.27.001958. URL http://www.opticsexpress.org/abstract.cfm?URI=oe-27-3-1958.

N. Li, J. Huang, B. Xu, Y. Cai, J. Lu, L. Zhan, Z. Luo, H. Xu, Z. Cai, and W. Cai. Direct generation of an ultrafast vortex beam in a CVD-graphene-based passively mode-locked Pr:$LiYF_4$ visible laser. *Photon. Res.*, 7(11):1209–1213, 2019. doi: 10.1364/PRJ.7.001209. URL http://www.osapublishing.org/prj/abstract.cfm?URI=prj-7-11-1209.

C. Lin and R. H. Stolen. New nanosecond continuum for excited-state spectroscopy. *Appl. Phys. Lett.*, 28:216–218, 1976. doi: 10.1063/1.88702. URL https://aip.scitation.org/doi/10.1063/1.88702.

J. Liu and T. Kobayashi. Generation of sub-20-fs multicolor laser pulses using cascaded four-wave mixing with chirped incident pulses. *Opt. Lett.*, 34(16):2402–2404, 2009a. doi: 10.1364/OL.34.002402. URL http://ol.osa.org/abstract.cfm?URI=ol-34-16-2402.

J. Liu and T. Kobayashi. Generation of μJ multicolor femtosecond laser pulses using cascaded four-wave mixing. *Opt. Express*, 17(7):4984–4990, 2009b. doi: 10.1364/OE.17.004984. URL http://www.opticsexpress.org/abstract.cfm?URI=oe-17-7-4984.

J. Liu, Y. Kida, T. Teramoto, and T. Kobayashi. Generation of stable sub-10 fs pulses at 400 nm in a hollow fiber for UV pump-probe experiment. *Opt. Express*, 18(5):4664–4672, 2010. doi: 10.1364/OE.18.004664. URL http://www.opticsexpress.org/abstract.cfm?URI=oe-18-5-4664.

B. A. López-Zubieta, E. Conejero Jarque, I. J. Sola, and J. San Roman. Theoretical analysis of single-cycle self-compression of near infrared pulses using high-spatial modes in capillary fibers. *Opt. Express*, 26(5):6345–6350, 2018a. doi: 10.1364/OE.26.006345. URL http://www.opticsexpress.org/abstract.cfm?URI=oe-26-5-6345.

B. A. López-Zubieta, E. Conejero Jarque, I. J. Sola, and J. San Roman. Spatiotemporal-dressed optical solitons in hollow-core capillaries. *OSA Continuum*, 1(3):930–938, 2018b. doi: 10.1364/OSAC.1.000930. URL http://www.osapublishing.org/osac/abstract.cfm?URI=osac-1-3-930.

C-H. Lu, Y-J. Tsou, H-Y. Chen, B-H. Chen, Y-C. Cheng, S-D. Yang, M-C. Chen, C-C. Hsu, and A. H. Kung. Generation of intense supercontinuum in condensed media. *Optica*, 1(6):400–406, 2014. doi: 10.1364/OPTICA.1.000400. URL http://www.osapublishing.org/optica/abstract.cfm?URI=optica-1-6-400.

C-H. Lu, W-H. Wu, S-H. Kuo, J-Y. Guo, M-C. Chen, S-D. Yang, and A. H. Kung. Greater than 50 times compression of 1030 nm Yb:KGW laser pulses to single-cycle duration. *Opt. Express*, 27(11):15638–15648, 2019. doi: 10.1364/OE.27.015638. URL http://www.opticsexpress.org/abstract.cfm?URI=oe-27-11-15638.

J. Luan, P. St. J. Russell, and D. Novoa. Efficient self-compression of ultrashort near-UV pulses in air-filled hollow-core photonic crystal fibers. *Opt. Express*, 29(9):13787–13793, 2021. doi: 10.1364/OE.422815. URL http://www.opticsexpress.org/abstract.cfm?URI=oe-29-9-13787.

F. Lücking, A. Trabattoni, S. Anumula, G. Sansone, F. Calegari, M. Nisoli, T. Oksenhendler, and G. Tempea. In situ measurement of nonlinear carrier-envelope phase changes in hollow fiber compression. *Opt. Lett.*, 39(8):2302–2305, 2014. doi: 10.1364/OL.39.002302. URL http://ol.osa.org/abstract.cfm?URI=ol-39-8-2302.

S. Luo, B. Xu, H. Xu, and Z. Cai. High-power self-mode-locked Pr:YLF visible lasers. *Appl. Opt.*, 56(34):9552–9555, 2017. doi: 10.1364/AO.56.009552. URL http://ao.osa.org/abstract.cfm?URI=ao-56-34-9552.

G. Machavariani, Y. Lumer, I. Moshe, A. Meir, and S. Jackel. Efficient extracavity generation of radially and azimuthally polarized beams. *Opt. Lett.*, 32(11):1468–1470, 2007. doi: 10.1364/OL.32.001468. URL http://ol.osa.org/abstract.cfm?URI=ol-32-11-1468.

T. H. Maiman. Stimulated optical radiation in ruby. *Nature*, 187:493–494, 1960. doi: 10.1038/187493a0. URL https://doi.org/10.1038/187493a0.

K. F. Mak, J. C. Travers, P. Hölzer, N. Y. Joly, and P. St. J. Russell. Tunable vacuum-UV to visible ultrafast pulse source based on gas-filled Kagome-PCF. *Opt. Express*, 21(9): 10942–10953, 2013. doi: 10.1364/OE.21.010942. URL http://www.opticsexpress.org/abstract.cfm?URI=oe-21-9-10942.

I. H. Malitson. Interspecimen comparison of the refractive index of fused silica. *J. Opt. Soc. Am.*, 55(10):1205–1209, 1965. doi: 10.1364/JOSA.55.001205. URL http://www.osapublishing.org/abstract.cfm?URI=josa-55-10-1205.

J. H. Marburger. Self-focusing: Theory. *Progress in Quantum Electronics*, 4:35–110, 1975. doi: https://doi.org/10.1016/0079-6727(75)90003-8. URL https://www.sciencedirect.com/science/article/pii/0079672775900038.

E. A. J. Marcatili and R. A. Schmeltzer. Hollow metallic and dielectric wave-guides for long distance optical transmission and lasers. *Bell Labs Technical Journal*, 43:1783–1809, 1964. doi: 10.1002/j.1538-7305.1964.tb04108.x. URL https://ieeexplore.ieee.org/document/6773550.

G. L. McAllister, J. H. Marburger, and L. G. DeShazer. Observation of optical pulse shaping by the self-focusing effects. *Phys. Rev. Lett.*, 21:1648–1649, 1968. doi: 10.1103/PhysRevLett.21.1648. URL https://link.aps.org/doi/10.1103/PhysRevLett.21.1648.

F. J. McClung and R. W. Hellwarth. Giant optical pulsations from ruby. *Appl. Opt.*, 1(S1):103–105, 1962. doi: 10.1364/AO.1.S1.000103. URL http://ao.osa.org/abstract.cfm?URI=ao-1-101-103.

R. B. Miles, G. Laufer, and G. C. Bjorklund. Coherent anti-Stokes Raman scattering in a hollow dielectric waveguide. *Appl. Phys. Lett.*, 30:417–419, 1977. doi: 10.1063/1.89426. URL https://aip.scitation.org/doi/10.1063/1.89426.

M. Miranda, T. Fordell, C. Arnold, A. L'Huillier, and H. Crespo. Simultaneous compression and characterization of ultrashort laser pulses using chirped mirrors and glass wedges. *Opt. Express*, 20(1):688–697, 2012. doi: 10.1364/OE.20.000688. URL http://www.opticsexpress.org/abstract.cfm?URI=oe-20-1-688.

S. Y. Mironov, S. Fourmaux, P. Lassonde, V. N. Ginzburg, S. Payeur, J.-C. Kieffer, E. A. Khazanov, and G. Mourou. Thin plate compression of a sub-petawatt Ti:Sa laser pulses. *Appl. Phys. Lett.*, 116:241101, 2020. doi: 10.1063/5.0008544. URL https://aip.scitation.org/doi/10.1063/5.0008544.

A. V. Mitrofanov, A. A. Voronin, D. A. Sidorov-Biryukov, S. I. Mitryukovsky, A. B. Fedotov, E. E. Serebryannikov, D. V. Meshchankin, V. Shumakova, S. Ališauskas, A. Pugžlys, V. Y. Panchenko, A. Baltuška, and A. M. Zheltikov. Subterawatt few-cycle mid-infrared pulses from a single filament. *Optica*, 3(3):299–302, 2016. doi: 10.1364/OPTICA.3.000299. URL http://www.osapublishing.org/optica/abstract.cfm?URI=optica-3-3-299.

F. M. Mitschke and L. F. Mollenauer. Discovery of the soliton self-frequency shift. *Opt. Lett.*, 11(10):659–661, 1986. doi: 10.1364/OL.11.000659. URL http://ol.osa.org/abstract.cfm?URI=ol-11-10-659.

K. D. Moll, A. L. Gaeta, and G. Fibich. Self-similar optical wave collapse: Observation of the Townes profile. *Phys. Rev. Lett.*, 90:203902, 2003. doi: 10.1103/PhysRevLett.90.203902. URL https://link.aps.org/doi/10.1103/PhysRevLett.90.203902.

L. F. Mollenauer, R. H. Stolen, and J. P. Gordon. Experimental observation of picosecond pulse narrowing and solitons in optical fibers. *Phys. Rev. Lett.*, 45:1095–1098, 1980. doi: 10.1103/PhysRevLett.45.1095. URL https://link.aps.org/doi/10.1103/PhysRevLett.45.1095.

T. Nagy, M. Forster, and P. Simon. Flexible hollow fiber for pulse compressors. *Appl. Opt.*, 47(18):3264–3268, 2008. doi: 10.1364/AO.47.003264. URL http://ao.osa.org/abstract.cfm?URI=ao-47-18-3264.

T. Nagy, S. Hädrich, P. Simon, A. Blumenstein, N. Walther, R. Klas, J. Buldt, H. Stark, S. Breitkopf, P. Jójárt, I. Seres, Z. Várallyay, T. Eidam, and J. Limpert. Generation of three-cycle multi-millijoule laser pulses at 318 W average power. *Optica*, 6(11):1423–1424, 2019. doi: 10.1364/OPTICA.6.001423. URL http://www.osapublishing.org/optica/abstract.cfm?URI=optica-6-11-1423.

T. Nagy, M. Kretschmar, M. J. J. Vrakking, and A. Rouzée. Generation of above-terawatt 1.5-cycle visible pulses at 1 kHz by post-compression in a hollow fiber. *Opt. Lett.*, 45(12):3313–3316, 2020. doi: 10.1364/OL.395830. URL http://ol.osa.org/abstract.cfm?URI=ol-45-12-3313.

T. Nagy, P. Simon, and L. Veisz. High-energy few-cycle pulses: post-compression techniques. *Advances in Physics: X*, 6(1):1845795, 2021. doi: 10.1080/23746149.2020.1845795. URL https://doi.org/10.1080/23746149.2020.1845795.

M. Nisoli, S. De Silvestri, and O. Svelto. Generation of high energy 10 fs pulses by a new pulse compression technique. *Appl. Phys. Lett.*, 68(20):2793–2795, 1996. doi: 10.1063/1.116609. URL https://doi.org/10.1063/1.116609.

M. Nisoli, S. De Silvestri, O. Svelto, R. Szipöcs, K. Ferencz, Ch. Spielmann, S. Sartania, and F. Krausz. Compression of high-energy laser pulses below 5 fs. *Opt. Lett.*, 22 (8):522–524, 1997. doi: 10.1364/OL.22.000522. URL http://ol.osa.org/abstract.cfm?URI=ol-22-8-522.

M. Nisoli, G. Sansone, S. Stagira, and S. De Silvcstri. Ultrabroadband continuum generation by hollow fiber cascading. In *Conference on Lasers and Electro-Optics*, page CThL4. Optical Society of America, 2002. URL http://www.osapublishing.org/abstract.cfm?URI=CLEO-2002-CThL4.

D. Novoa, M. Cassataro, J. C. Travers, and P. St. J. Russell. Photoionization-induced emission of tunable few-cycle midinfrared dispersive waves in gas-filled hollow-core photonic crystal fibers. *Phys. Rev. Lett.*, 115:033901, 2015. doi: 10.1103/PhysRevLett.115.033901. URL https://link.aps.org/doi/10.1103/PhysRevLett.115.033901.

M. Nurhuda, A. Suda, K. Midorikawa, M. Hatayama, and K. Nagasaka. Propagation dynamics of femtosecond laser pulses in a hollow fiber filled with argon: constant gas pressure versus differential gas pressure. *J. Opt. Soc. Am. B*, 20(9):2002–2011, 2003. doi: 10.1364/JOSAB.20.002002. URL http://josab.osa.org/abstract.cfm?URI=josab-20-9-2002.

M. Nurhuda, A. Suda, S. Bohman, S. Yamaguchi, and K. Midorikawa. Optical pulse compression of ultrashort laser pulses in an argon-filled planar waveguide. *Phys. Rev. Lett.*, 97:153902, 2006. doi: 10.1103/PhysRevLett.97.153902. URL https://link.aps.org/doi/10.1103/PhysRevLett.97.153902.

K. Okamura and T. Kobayashi. Octave-spanning carrier-envelope phase stabilized visible pulse with sub-3-fs pulse duration. *Opt. Lett.*, 36(2):226–228, 2011. doi: 10.1364/OL.36.000226. URL http://ol.osa.org/abstract.cfm?URI=ol-36-2-226.

M. Ouillé, A. Vernier, F. Böhle, M. Bocoum, A. Jullien, M. Lozano, J-P. Rousseau, Z. Cheng, D. Gustas, A. Blumenstein, P. Simon, S. Haessler, J. Faure, T. Nagy, and R. Lopez-Martens. Relativistic-intensity near-single-cycle light waveforms at kHz repetition rate. *Light Sci Appl*, 9(47), 2020. doi: 10.1038/s41377-020-0280-5. URL https://doi.org/10.1038/s41377-020-0280-5.

S. Palato, H. Seiler, H. Baker, C. Sonnichsen, R. Zifkin, J. McGowan, and P. Kambhampati. An analysis of hollow-core fiber for applications in coherent femtosecond spectroscopies. *Journal of Applied Physics*, 128(10):103107, 2020. doi: 10.1063/1.5113691. URL https://doi.org/10.1063/1.5113691.

E. Peik and Chr. Tamm. Nuclear laser spectroscopy of the 3.5 eV transition in Th-229. *Europhys. Lett.*, 61(2):181–186, 2003. doi: 10.1209/epl/i2003-00210-x. URL https://iopscience.iop.org/article/10.1209/epl/i2003-00210-x.

A. M. Perelomov, V. S. Popov, and M. V. Terentev. Ionization of atoms in an alternating electric field. *Sov. Phys. JETP*, 23(5):924–934, 1966. URL http://www.jetp.ac.ru/cgi-bin/dn/e_023_05_0924.pdf.

D. Polli, M. R. Antognazza, D. Brida, G. Lanzani, G. Cerullo, and S. De Silvestri. Broadband pump-probe spectroscopy with sub-10-fs resolution for probing ultrafast internal conversion and coherent phonons in carotenoids. *Chemical Physics*, 350(1): 45–55, 2008. doi: https://doi.org/10.1016/j.chemphys.2007.12.021. URL https://www.sciencedirect.com/science/article/pii/S0301010407005617.

W. H. Press, S. A. Teukolsky, W. T. Vetterling, and B. P. Flannery. *Numerical Recipes, The Art of Scientific Computing*. Cambridge University Press, 3rd edition, 2007.

J. K. Ranka, R. S. Windeler, and A. J. Stentz. Visible continuum generation in air–silica microstructure optical fibers with anomalous dispersion at 800 nm. *Opt. Lett.*, 25(1): 25–27, 2000. doi: 10.1364/OL.25.000025. URL http://ol.osa.org/abstract.cfm?URI=ol-25-1-25.

F. Reinert and S. Hüfner. Photoemission spectroscopy—from early days to recent applications. *New J. Phys.*, 7:97–97, 2005. doi: 10.1088/1367-2630/7/1/097. URL https://doi.org/10.1088/1367-2630/7/1/097.

J. Ringling, O. Kittelmann, F. Noack, G. Korn, and J. Squier. Tunable femtosecond pulses in the near vacuum ultraviolet generated by frequency conversion of amplified Ti:sapphire laser pulses. *Opt. Lett.*, 18(23):2035–2037, 1993. doi: 10.1364/OL.18.002035. URL http://ol.osa.org/abstract.cfm?URI=ol-18-23-2035.

C. Rolland and P. B. Corkum. Compression of high-power optical pulses. *J. Opt. Soc. Am. B*, 5(3):641–647, 1988. doi: 10.1364/JOSAB.5.000641. URL http://josab.osa.org/abstract.cfm?URI=josab-5-3-641.

J. E. Rothenberg. Space–time focusing: breakdown of the slowly varying envelope approximation in the self-focusing of femtosecond pulses. *Opt. Lett.*, 17(19):1340–1342, 1992. doi: 10.1364/OL.17.001340. URL http://ol.osa.org/abstract.cfm?URI=ol-17-19-1340.

C. Rotschild, M. Segev, Z. Xu, Y. V. Kartashov, L. Torner, and O. Cohen. Two-dimensional multipole solitons in nonlocal nonlinear media. *Opt. Lett.*, 31(22):3312–3314, 2006. doi: 10.1364/OL.31.003312. URL http://ol.osa.org/abstract.cfm?URI=ol-31-22-3312.

C. Ruiz, J. San Roman, C. Mêndez, V. D´ıaz, L. Plaja, I. Arias, and L. Roso. Observation of spontaneous self-channeling of light in air below the collapse threshold. *Phys. Rev. Lett.*, 95:053905, 2005. doi: 10.1103/PhysRevLett.95.053905. URL https://link.aps.org/doi/10.1103/PhysRevLett.95.053905.

A. Rundquist, C. G. Durfee, Z. Chang, C. Herne, S. Backus, M. M. Murnane, and H. C. Kapteyn. Phase-matched generation of coherent soft X-rays. *Science*, 280 (5368):1412–1415, 1998. doi: 10.1126/science.280.5368.1412. URL https://science.sciencemag.org/content/280/5368/1412.

P. Russbueldt, J. Weitenberg, J. Schulte, R. Meyer, C. Meinhardt, H. D. Hoffmann, and R. Poprawe. Scalable 30 fs laser source with 530 W average power. *Opt. Lett.*, 44(21): 5222–5225, 2019. doi: 10.1364/OL.44.005222. URL http://ol.osa.org/abstract.cfm?URI=ol-44-21-5222.

P. St. J. Russell, P. Hölzer, W. Chang, A. Abdolvand, and J. C. Travers. Hollow-core photonic crystal fibres for gas-based nonlinear optics. *Nat. Photonics*, 8:278–286, 2014. doi: 10.1038/nphoton.2013.312. URL https://doi.org/10.1038/nphoton.2013.312.

G. Sansone, F. Kelkensberg, J. F. Pérez-Torres, F. Morales, M. F. Kling, W. Siu, O. Ghafur, P. Johnsson, M. Swoboda, E. Benedetti, F. Ferrari, F. Lépine, J. L. Sanz-Vicario, S. Zherebtsov, I. Znakovskaya, A. L'Huillier, M. Y. Ivanov, M. Nisoli, F. Mart´ın, and M. J. J. Vrakking. Electron localization following attosecond molecular photoionization. *Nature*, 465(7299):763–766, 2010. doi: 10.1038/nature09084. URL https://doi.org/10.1038/nature09084.

B. Schenkel, J. Biegert, U. Keller, C. Vozzi, M. Nisoli, G. Sansone, S. Stagira, S. De Silvestri, and O. Svelto. Generation of 3.8-fs pulses from adaptive compression of a cascaded hollow fiber supercontinuum. *Opt. Lett.*, 28(20):1987–1989, 2003. doi: 10.1364/OL.28.001987. URL http://ol.osa.org/abstract.cfm?URI=ol-28-20-1987.

W. Schweinberger, A. Sommer, E. Bothschafter, J. Li, F. Krausz, R. Kienberger, and M. Schultze. Waveform-controlled near-single-cycle milli-joule laser pulses generate sub-10 nm extreme ultraviolet continua. *Opt. Lett.*, 37(17):3573–3575, 2012. doi: 10.1364/OL.37.003573. URL http://ol.osa.org/abstract.cfm?URI=ol-37-17-3573.

B. Seiferle, L. von der Wense, P. V. Bilous, I. Amersdorffer, C. Lemell, F. Libisch, S. Stellmer, T. Schum, C. E. Düllmann, A. Pálffy, and P. G. Thirolf. Energy of the 229th nuclear clock transition. *Nature*, 573:243–246, 2019. doi: 10.1038/s41586-019-1533-4. URL https://doi.org/10.1038/s41586-019-1533-4.

C. V. Shank and E. P. Ippen. Subpicosecond kilowatt pulses from a mode-locked cw dye laser. *Appl. Phys. Lett.*, 24:373–375, 1974. doi: 10.1063/1.1655222. URL https://aip.scitation.org/doi/10.1063/1.1655222.

C. V. Shank, R. L. Fork, R. Yen, R. H. Stolen, and W. J. Tomlinson. Compression of femtosecond optical pulses. *Appl. Phys. Lett.*, 40:761–763, 1982. doi: 10.1063/1.93276. URL https://aip.scitation.org/doi/10.1063/1.93276.

Z. Shi, H. Li, and X. Zhu. Necklacelike solitons formed by manipulating vortex beams in a synthetic structure. *J. Opt. Soc. Am. B*, 36(8):2007–2012, 2019. doi: 10.1364/JOSAB.36.002007. URL http://josab.osa.org/abstract.cfm?URI=josab-36-8-2007.

V. Shumakova, P. Malevich, S. Ališauskas, A. Voronin, A. M. Zheltikov, D. Faccio, D. Kartashov, A. Baltuška, and A. Pugžlys. Multi-millijoule few-cycle mid-infrared pulses through nonlinear self-compression in bulk. *Nat Commun*, 7(1):12877, 2016. doi: 10.1038/ncomms12877. URL https://doi.org/10.1038/ncomms12877.

S. Z. Silahli, W. Walasik, and N. M. Litchinitser. Necklace beam generation in nonlinear colloidal engineered media. *Opt. Lett.*, 40(24):5714–5717, 2015. doi: 10.1364/OL.40.005714. URL http://ol.osa.org/abstract.cfm?URI=ol-40-24-5714.

F. Silva, B. Alonso, W. Holgado, R. Romero, J. San Roman, E. Conejero Jarque, H. Koop, V. Pervak, H. Crespo, and I. J. Sola. Strategies for achieving intense single-cycle pulses with in-line post-compression setups. *Opt. Lett.*, 43(2):337–340, 2018. doi: 10.1364/OL.43.000337. URL http://ol.osa.org/abstract.cfm?URI=ol-43-2-337.

J. L. Silva, R. Weigand, and H. M. Crespo. Octave-spanning spectra and pulse synthesis by nondegenerate cascaded four-wave mixing. *Opt. Lett.*, 34(16):2489–2491, 2009. doi: 10.1364/OL.34.002489. URL http://ol.osa.org/abstract.cfm?URI=ol-34-16-2489.

M. Soljačić, S. Sears, and M. Segev. Self-trapping of "Necklace" beams in self-focusing Kerr media. *Phys. Rev. Lett.*, 81:4851–4854, 1998. doi: 10.1103/PhysRevLett.81.4851. URL https://link.aps.org/doi/10.1103/PhysRevLett.81.4851.

B. Spokoyny, C. J. Koh, and E. Harel. Stable and high-power few cycle supercontinuum for 2D ultrabroadband electronic spectroscopy. *Opt. Lett.*, 40(6):1014–1017,

2015. doi: 10.1364/OL.40.001014. URL http://ol.osa.org/abstract.cfm?URI=ol-40-6-1014.

M. Stalder and M. Schadt. Linearly polarized light with axial symmetry generated by liquid-crystal polarization converters. *Opt. Lett.*, 21(23):1948–1950, 1996. doi: 10.1364/OL.21.001948. URL http://ol.osa.org/abstract.cfm?URI=ol-21-23-1948.

D. S. Steingrube, M. Kretschmar, D. Hoff, E. Schulz, T. Binhammer, P. Hansinger, G. G. Paulus, U. Morgner, and M. Kovačev. Sub-1.5-cycle pulses from a single filament. *Opt. Express*, 20(21):24049–24058, Oct 2012. doi: 10.1364/OE.20.024049. URL http://www.opticsexpress.org/abstract.cfm?URI=oe-20-21-24049.

R. H. Stolen and C. Lin. Self-phase-modulation in silica optical fibers. *Phys. Rev. A*, 17:1448–1453, 1978. doi: 10.1103/PhysRevA.17.1448. URL https://link.aps.org/doi/10.1103/PhysRevA.17.1448.

R. H. Stolen, E. P. Ippen, and A. R. Tynes. Raman oscillation in glass optical waveguide. *Appl. Phys. Lett.*, 20:62–64, 1972. doi: 10.1063/1.1654046. URL https://aip.scitation.org/doi/10.1063/1.1654046.

L. Stoyanov, N. Dimitrov, I. Stefanov, D. N. Neshev, and A. Dreischuh. Optical waveguiding by necklace and azimuthon beams in nonlinear media. *J. Opt. Soc. Am. B*, 34(4):801–807, 2017. doi: 10.1364/JOSAB.34.000801. URL http://josab.osa.org/abstract.cfm?URI=josab-34-4-801.

D. Strickland and G. Mourou. Compression of amplified chirped optical pulses. *Optics Communications*, 56(3):219–221, 1985. doi: 10.1016/0030-4018(85)90120-8. URL https://www.sciencedirect.com/science/article/pii/0030401885901208.

A. Suda, M. Hatayamab, K. Nagasaka, and K. Midorikawa. Generation of sub-10-fs, 5-mJ-optical pulses using a hollow fiber with a pressure gradient. *Appl. Phys. Lett.*, 86:111116, 2005. doi: 10.1063/1.1883706. URL https://aip.scitation.org/doi/10.1063/1.1883706.

R. Szipöcs and A. Köházi-Kis. Theory and design of chirped dielectric laser mirrors. *Appl Phys B*, 65:115–135, 1997. doi: 10.1007/s003400050258. URL https://doi.org/10.1007/s003400050258.

R. Szipöcs, K. Ferencz, C. Spielmann, and F. Krausz. Chirped multilayer coatings for broadband dispersion control in femtosecond lasers. *Opt. Lett.*, 19(3):201–203, 1994. doi: 10.1364/OL.19.000201. URL http://ol.osa.org/abstract.cfm?URI=ol-19-3-201.

V. I. Talanov. Self Focusing of Wave Beams in Nonlinear Media. *Soviet Journal of Experimental and Theoretical Physics Letters*, 2:138, 1965. URL https://ui.adsabs.harvard.edu/abs/1965JETPL...2..138T. Provided by the SAO/NASA Astrophysics Data System.

F. Tani, J. C. Travers, and P. St. J. Russell. PHz-wide supercontinua of nondispersing subcycle pulses generated by extreme modulational instability. *Phys. Rev. Lett.*, 111: 033902, 2013. doi: 10.1103/PhysRevLett.111.033902. URL https://link.aps.org/doi/10.1103/PhysRevLett.111.033902.

G. Tempea and T. Brabec. Theory of self-focusing in a hollow waveguide. *Opt. Lett.*, 23(10):762–764, 1998. doi: 10.1364/OL.23.000762. URL http://ol.osa.org/abstract.cfm?URI=ol-23-10-762.

S. C. Tidwell, D. H. Ford, and W. D. Kimura. Generating radially polarized beams interferometrically. *Appl. Opt.*, 29(15):2234–2239, 1990. doi: 10.1364/AO.29.002234. URL http://ao.osa.org/abstract.cfm?URI=ao-29-15-2234.

W. J. Tomlinson, R. H. Stolen, and C. V. Shank. Compression of optical pulses chirped by self-phase modulation in fibers. *J. Opt. Soc. Am. B*, 1(2):139–149, 1984. doi: 10.1364/JOSAB.1.000139. URL http://josab.osa.org/abstract.cfm?URI=josab-1-2-139.

J. C. Travers, W. Chang, J. Nold, N. Y. Joly, and P. St. J. Russell. Ultrafast nonlinear optics in gas-filled hollow-core photonic crystal fibers. *J. Opt. Soc. Am. B*, 28(12): A11–A26, 2011. doi: 10.1364/JOSAB.28.000A11. URL http://josab.osa.org/abstract.cfm?URI=josab-28-12-A11.

J. C. Travers, T. F. Grigorova, C. Brahms, and F. Belli. High-energy pulse self-compression and ultraviolet generation through soliton dynamics in hollow capillary fibres. *Nat. Photonics*, 13:547–554, Aug 2019. doi: 10.1038/s41566-019-0416-4. URL https://doi.org/10.1038/s41566-019-0416-4.

E. Treacy. Optical pulse compression with diffraction gratings. *IEEE Journal of Quantum Electronics*, 5(9):454–458, 1969. doi: 10.1109/JQE.1969.1076303. URL https://ieeexplore.ieee.org/document/1076303.

E. B. Treacy. Compression of picosecond light pulses. *Physics Letters A*, 28(1):34–35, 1968. doi: 10.1016/0375-9601(68)90584-7. URL https://www.sciencedirect.com/science/article/pii/0375960168905847.

E. Ugaitz, L. Maidment, L. Vamos, F. Tani, D. Novoa, M. H. Frosz, V. Badikov, D. Badikov, V. Petrov, P. St. J. Russell, and J. Biegert. Seven-octave high-brightness and carrier-envelope-phase-stable light source. *Nat. Photonics*, 15:277–280, 2021. doi: 10.1038/s41566-020-00735-1. URL https://doi.org/10.1038/s41566-020-00735-1.

L. von der Wense and Z. Chuankun. Concepts for direct frequency-comb spectroscopy of 229mth and an internal-conversion-based solid-state nuclear clock. *Eur. Phys. J. D*, 74:146, 2020. doi: 10.1140/epjd/e2020-100582-5. URL https://doi.org/10.1140/epjd/e2020-100582-5.

A. A. Voronin and A. M. Zheltikov. Soliton-number analysis of soliton-effect pulse compression to single-cycle pulse widths. *Phys. Rev. A*, 78:063834, 2008. doi: 10.1103/PhysRevA.78.063834. URL https://link.aps.org/doi/10.1103/PhysRevA.78.063834.

N. L. Wagner, E. A. Gibson, T. Popmintchev, I. P. Christov, M. M. Murnane, and H. C. Kapteyn. Self-compression of ultrashort pulses through ionization-induced spatiotemporal reshaping. *Phys. Rev. Lett.*, 93:173902, 2004. doi: 10.1103/PhysRevLett.93.173902. URL https://link.aps.org/doi/10.1103/PhysRevLett.93.173902.

J. K. Wahlstrand, Y.-H. Cheng, Y.-H. Chen, and H. M. Milchberg. Optical nonlinearity in Ar and N_2 near the ionization threshold. *Phys. Rev. Lett.*, 107:103901, 2011. doi: 10.1103/PhysRevLett.107.103901. URL https://link.aps.org/doi/10.1103/PhysRevLett.107.103901.

P. K. A. Wai, H. H. Chen, and Y. C. Lee. Radiations by "solitons" at the zero group-dispersion wavelength of single-mode optical fibers. *Phys. Rev. A*, 41:426–439, 1990. doi: 10.1103/PhysRevA.41.426. URL https://link.aps.org/doi/10.1103/PhysRevA.41.426.

W. Walasik, S. Z. Silahli, and N. M. Litchinitser. Dynamics of necklace beams in nonlinear colloidal suspensions. *Sci Rep*, 7:11709, 2017. doi: 10.1038/s41598-017-12169-x. URL https://doi.org/10.1038/s41598-017-12169-x.

Y. Wan and W. Chang. Effect of decreasing pressure on soliton self-compression in higher-order modes of a gas-filled capillary. *Opt. Express*, 29(5):7070–7083, 2021. doi: 10.1364/OE.418217. URL http://www.opticsexpress.org/abstract.cfm?URI=oe-29-5-7070.

D. Wang, L. Qiao, R. Zhao, Y. Zhao, and Y. Leng. Propagation dynamics of radially polarized pulses in a gas-filled hollow-core fiber. *Opt. Express*, 25(4):3083–3091, 2017.

doi: 10.1364/OE.25.003083. URL http://www.opticsexpress.org/abstract.cfm?URI=oe-25-4-3083.

R. Weigand, J. T. Mendon¸ca, and H. M. Crespo. Cascaded nondegenerate four-wave-mixing technique for high-power single-cycle pulse synthesis in the visible and ultraviolet ranges. *Phys. Rev. A*, 79:063838, 2009. doi: 10.1103/PhysRevA.79.063838. URL https://link.aps.org/doi/10.1103/PhysRevA.79.063838.

M. Wen, Y. I. Salamin, and C. H. Keitel. Electron acceleration by a radially-polarized laser pulse in a plasma micro-channel. *Opt. Express*, 27(2):557–566, 2019. doi: 10.1364/OE.27.000557. URL http://www.opticsexpress.org/abstract.cfm?URI=oe-27-2-557.

L. G. Wright, D. N. Christodoulides, and F. Wise. Controllable spatiotemporal nonlinear effects in multimode fibres. *Nat. Photonics*, 9:306–310, 2015. doi: 10.1038/nphoton.2015.61. URL https://doi.org/10.1038/nphoton.2015.61.

J. Ye and S. T. Cundiff. *Femtosecond Optical Frequency Comb: Principle, Operation and Applications*. Springer US, 1st edition, 2005.

Q. Zhan. Cylindrical vector beams: from mathematical concepts to applications. *Adv. Opt. Photon.*, 1(1):1–57, 2009. doi: 10.1364/AOP.1.000001. URL http://aop.osa.org/abstract.cfm?URI=aop-1-1-1.

J. Zhang, Z. H. Lu, and L. J. Wang. Precision refractive index measurements of air, N2, O2, Ar, and CO2 with a frequency comb. *Appl. Opt.*, 47(17):3143–3151, 2008. doi: 10.1364/AO.47.003143. URL http://ao.osa.org/abstract.cfm?URI=ao-47-17-3143.